

LEVEL III

A031388



AFWAL-TR-80-3032

VOLUME I

AD A099330

PREDICTION OF SUPERSONIC STORE SEPARATION
CHARACTERISTICS INCLUDING FUSELAGE AND
STORES OF NONCIRCULAR CROSS SECTION.
VOLUME I - THEORETICAL METHODS AND COMPARISONS
WITH EXPERIMENT

Frederick K. Goodwin
Marnix F. E. Dillenius
Joseph Mullen, Jr.
Nielsen Engineering & Research, Inc.
Mountain View, California 94043

November 1980

TECHNICAL REPORT AFWAL-TR-80-3032, VOLUME I
FINAL REPORT FOR PERIOD JUNE 1975 - JANUARY 1980

Approved for Public Release, Distribution Unlimited

DTIC
ELECTE
MAY 27 1981
A

FLIGHT DYNAMICS LABORATORY
AIR FORCE WRIGHT AERONAUTICAL LABORATORIES
AIR FORCE SYSTEMS COMMAND
WRIGHT-PATTERSON AIR FORCE BASE, OHIO 45433

81 5 26 052

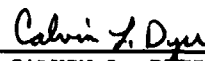
FILE COPY

NOTICE

When Government drawings, specifications, or other data are used for any purpose other than in connection with a definitely related Government procurement operation, the United States Government thereby incurs no responsibility nor any obligation whatsoever; and the fact that the government may have formulated, furnished, or in any way supplied the said drawings, specifications, or other data, is not to be regarded by implication or otherwise as in any manner licensing the holder or any other person or corporation, or conveying any rights or permission to manufacture, use, or sell any patented invention that may in any way be related thereto.

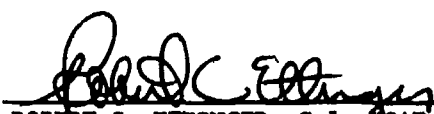
This report has been reviewed by the Office of Public Affairs (ASD/PA) and is releasable to the National Technical Information Service (NTIS). At NTIS, it will be available to the general public, including foreign nations.

This technical report has been reviewed and is approved for publication.


CALVIN L. DYER
Project Engineer


RONALD O. ANDERSON, Chief
Control Dynamics Branch

FOR THE COMMANDER


ROBERT C. ETTINGER, Col, USAF, Chief
Flight Control Division

"If your address has changed, if you wish to be removed from our mailing list, or if the addressee is no longer employed by your organization please notify AFWAL/FIGC, W-PAFB, OH 45433 to help us maintain a current mailing list."

Copies of this report should not be returned unless return is required by security considerations, contractual obligations, or notice on the specific document.

(14) TR-80-3032-VOL-4

SECURITY CLASSIFICATION OF THIS PAGE (When Data Entered)

REPORT DOCUMENTATION PAGE		READ INSTRUCTIONS BEFORE COMPLETING FORM
1. REPORT NUMBER AFWAL-TR-80-3032, Volume I	2. GOVT ACCESSION NO. AD-A099	3. RECIPIENT'S CATALOG NUMBER 330
4. TITLE (or Subtitle) PREDICTION OF SUPERSONIC STORE SEPARATION CHARACTERISTICS INCLUDING FUSELAGE AND STORES OF NONCIRCULAR CROSS SECTION, Volume I Theoretical Methods and Comparisons with Experiment	5. TYPE OF REPORT & PERIOD COVERED Final Report June 1975 - January 1980	6. PERFORMING ORG. REPORT NUMBER NEAR-TR-210-VOL-4
7. AUTHOR(s) Frederick K./Goodwin Marnix F. E./Dillenius Joseph Mullen, Jr.	8. PERFORMING ORGANIZATION NAME AND ADDRESS Nielsen Engineering & Research, Inc. 510 Clyde Avenue Mountain View, CA 94043	9. PROGRAM ELEMENT, PROJECT, TASK AREA & WORK UNIT NUMBERS Project 2403 Task 240305 Work Unit 240309
10. CONTROLLING OFFICE NAME AND ADDRESS Flight Dynamics Laboratory Air Force Wright Aeronautical Laboratories Air Force Systems Command Wright-Patterson Air Force Base, Ohio 45433	11. REPORT DATE November 1980	12. NUMBER OF PAGES 330
13. MONITORING AGENCY NAME & ADDRESS (if different from Controlling Office)	14. SECURITY CLASS. (of this report) Unclassified	15. DECLASSIFICATION/DOWNGRADING SCHEDULE
16. DISTRIBUTION STATEMENT (of this Report)		
17. DISTRIBUTION STATEMENT (of the abstract entered in Block 20, if different from Report) Approved for public release; distribution unlimited		
18. SUPPLEMENTARY NOTES		
19. KEY WORDS (Continue on reverse side if necessary and identify by block number) Aerodynamic Loads Flow Fields Aerodynamic Interference Store Separation External Stores Supersonic Flow		
20. ABSTRACT (Continue on reverse side if necessary and identify by block number) The primary objective of this report is to describe an investigation conducted to develop a method for predicting the trajectory of a store separated from an aircraft flying at supersonic speeds. The aircraft model can include a circular or noncircular fuselage, engine inlets, wing, pylon, ejector rack, and circular and noncircular stores. The linear, potential flow methods used to model the aircraft components are described as are nonlinear corrections which are made to position shock waves more accurately. The methods used to calculate		

DD FORM 1 JAN 73 1473 EDITION OF 1 NOV 65 IS OBSOLETE

SECURITY CLASSIFICATION OF THIS PAGE (When Data Entered)

387183

20. (continued)

the nonuniform flow field, the store forces and moments, and the store trajectory are presented. Comparisons between theory and experiment for flow fields, store loading distributions, store forces and moments, and store trajectories are shown and discussed.

Approved For	
Class	CS/CI
Form	TAB
Approved	11
Classification	11
Distribution/	
Availability Codes	
Dist	Avail and/or Special
A	

FOREWORD

This report "Prediction of Supersonic Store Separation Characteristics Including Fuselage and Stores of Noncircular Cross Section," describes a combined theoretical-experimental program directed toward developing a computer program for predicting the trajectory of an external store separated from an aircraft flying at supersonic speed. It describes improvements to the previous work described in AFFDL-TR-76-41 and extensions to include more realistic modeling of fuselage shapes including noncircular cross sections and ramp type engine air inlets, and to include modeling store shapes with elliptic cross section with multiple sets of arbitrarily oriented fins. This volume, Volume I, "Theoretical Methods and Comparisons with Experiment," describes the theoretical approach and presents extensive comparisons with experimental data. Volume II, "Users Manual for the Computer Program," presents detailed instructions on the use of the computer program with emphasis on preparation of input data and interpretation of output. Volume III, "Appendices A and B, Details of Program I," provides additional descriptions of the individual subroutines and program variables passed between modules in the first of two programs. Volume IV, "Appendices C and D, Details of Program II," provides additional descriptions of the individual subroutines and program variables passed between modules in the second program.

This work was carried out by Nielsen Engineering & Research, Inc., 510 Clyde Avenue, Mountain View, California, 94043, under Contract No. F33615-76-C-3077. The contract was initiated under Project 2403, Task 240305, of the Air Force Flight Dynamics Laboratory. The Air Force Project Engineer on the contract was Calvin L. Dyer, AFWAL/FIGC. The report number assigned by Nielsen Engineering & Research, Inc. is NEAR TR 210.

TABLE OF CONTENTS

<u>Section</u>	<u>Page No.</u>
1. INTRODUCTION	1
2. GENERAL APPROACH	4
3. FLOW MODELS	7
3.1 Description of Aircraft Components and Flight Conditions	7
3.1.1 Fuselage	8
3.1.2 Wing	8
3.1.3 Pylon	9
3.1.4 Ejector Rack	9
3.1.5 Store	9
3.1.6 Flight Conditions	10
3.2 Flow Models for the Fuselage, Ejector Rack, and Store Bodies	10
3.2.1 Circular Fuselage	11
3.2.2 Noncircular Fuselage	20
3.2.3 Fuselage Mounted Engine Inlets	21
3.2.4 Ejector Rack Body	28
3.2.5 Circular Store Body	28
3.2.6 Elliptic Store Body	28
3.3 Flow Model for Wing-Pylon Combination and Interference Shell on Fuselage	29
3.3.1 Geometrical Layout	30
3.3.2 Constant u-Velocity and Constant Source Panel Solutions	31
3.3.3 Flow Tangency Boundary Condition	32
3.3.4 Aerodynamic Influence Coefficients	35
3.3.5 Symmetry Considerations	40
3.3.6 Solution for Constant u-Velocity Panel Strengths	45
3.3.7 Superposition Scheme for Flow-Field Calculations	45

TABLE OF CONTENTS (Continued)

<u>Section</u>	<u>Page No.</u>
4. NONLINEAR CORRECTIONS TO FLOW MODELS	49
4.1 Body Shock Wave Shape	49
4.1.1 Circular Body	49
4.1.2 Noncircular Body	54
4.2 Inlet Shock Wave Shape	56
4.3 Wing Shock Wave System	60
4.4 Store Imaging	64
4.4.1 Circular Store Imaging	65
4.4.2 Elliptic Store Imaging	70
5. PARENT AIRCRAFT FLOW-FIELD CALCULATION	73
5.1 Circular Fuselage	73
5.2 Ejector Rack and Circular Stores	75
5.3 Noncircular Fuselage	76
5.4 Engine Inlets	76
5.5 Elliptic Stores	79
5.6 Wing, Pylon, and Fuselage Interference Shell	79
6. STORE FORCE AND MOMENT CALCULATION	81
6.1 Velocity Field as Seen by Store	81
6.2 Circular Store Forces and Moments	86
6.2.1 Body Forces and Moments	86
6.2.2 Empennage Forces and Moments	89
6.3 Elliptic Store Forces and Moments	90
6.3.1 Body Forces and Moments	90
6.3.2 Empennage Forces and Moments	94
6.3.3 Trailing Edge Vortex Interference	98
7. TRAJECTORY CALCULATION	102
8. COMPARISONS WITH EXPERIMENTAL DATA	108
8.1 Wind-Tunnel Model Description	108
8.2 Flow Fields	109
8.3 Store Load Distributions	115
8.4 Store Forces and Moments	120
8.5 Store Trajectories	124

TABLE OF CONTENTS (Concluded)

<u>Section</u>	<u>Page No.</u>
9. CONCLUDING REMARKS	128
APPENDIX A - NORMAL- AND SIDE-FOR E DISTRIBUTIONS ACTING ON AN AXISYMMETRIC STORE IN SUPERSONIC, NONUNIFORM FLOW	276
APPENDIX B - EQUATIONS OF MOTION OF A RIGID BODY WITH MASS AND INERTIA ASYMMETRIES	299
REFERENCES	326

LIST OF ILLUSTRATIONS

<u>Figure</u>	<u>Page No.</u>
1. Flow field below a circular arc body ($L/D=5$), $M_{\infty} = 1.5$, $\alpha = 0^{\circ}$.	132
2. Flow field below a circular arc body ($L/D=5$), $M_{\infty} = 1.5$, $\alpha = 5^{\circ}$.	134
3. Isometric view of typical layout of body source panels on the surface of a body with elliptical cross section, 11 rings with 16 panels each.	136
4. Triple ejection rack, TER.	137
5. Simplified layout of panels for wing-pylon fuselage combination.	138
6. Flow tangency boundary conditions for the wing and pylon.	139
7. Layout of semi-infinite triangular shape and associated coordinate system.	140
8. Prediction of shock wave shape; $M_{\infty} = 2.0$, $\alpha = 0^{\circ}$.	141
9. Prediction of shock wave shape; $M_{\infty} = 1.5$, $\alpha = 0^{\circ}$.	142
10. Shock angle of attack correction factor, ϵ_{α} .	143
11. Circular store wing imaging.	144
12. Circular store fuselage imaging.	145
13. Coordinate systems fixed in separated store and used in force and moment calculation.	146
14. Coordinate systems used in trajectory calculation.	147
15. Pressure distribution on top of store in presence of wing-fuselage; $M_{\infty} = 1.5$, $\alpha = 0^{\circ}$, $y_F = -4$ in., $z_F = 1.47$ in.	148
16. Pressure distribution on inboard side of store in presence of wing-fuselage; $M_{\infty} = 1.5$, $\alpha = 0^{\circ}$, $y_F = -4$ in., $z_F = 1.47$ in.	149
17. Pressure distribution on bottom of store in presence of wing-fuselage; $M_{\infty} = 1.5$, $\alpha = 0^{\circ}$, $y_F = -4$ in., $z_F = 1.47$ in.	150
18. Pressure distribution on outboard side of store in presence of wing-fuselage; $M_{\infty} = 1.5$, $\alpha = 0^{\circ}$, $y_F = -4$ in., $z_F = 1.47$ in.	151
19. Coordinate systems and typical panel layout shown for one fin and quarter of the interface shell.	152
20. Geometrical angles associated with case involving fins on body with elliptical cross section and force coefficients associated with fins and body inter- ference panel.	153

LIST OF ILLUSTRATIONS (Continued)

Figure	Page No.
21. Configuration N_1B_2W .	154
22. Short fuselage, B_1 .	155
23. Noncircular nose, N_3 .	156
24. Noncircular fuselage adapter, A_3 .	157
25. Duct assembly for $M_\infty = 1.5$, A_4 .	159
26. Ogive-cylinder force and moment store in the carriage position at the fuselage centerline, 1/3 semispan, and 2/3 semispan pylon stations.	161
27. Double-wedge pylon, P_2 .	162
28. Swept pylon, P_3 .	163
29. Dummy ogive-cylinder store, S_{DOC} , S_{DOC2} , or S_{DOC3} .	164
30. Comparison of calculated radial velocity with experimental data for configuration N_1B_1 ; $M_\infty = 1.5$, $\alpha_F = 0^\circ$, $r_B = 2.87$ in.	165
31. Effect of axial density of source panels on flow field of configuration N_1B_1 ; $M_\infty = 1.5$, $\alpha_F = 0^\circ$.	166
32. Comparison of calculated radial velocity with experimental data for configuration N_1B_1 ; $M_\infty = 1.5$, $\alpha_F = 0^\circ$, $r_B = 5.86$ in.	167
33. Comparison of calculated upwash velocity with experimental data 5.86 inches below the centerline of configuration N_1B_1 ; $M_\infty = 1.5$, $\alpha_F = 5^\circ$.	168
34. Upwash velocity below the centerline of configuration $N_3B_1A_3$; $M_\infty = 1.5$, $\alpha_F = 0^\circ$.	169
35. Upwash and sidewash velocities at $y_F = -2.49$ in. and $z_F = 4.36$ in. for configuration $N_3B_1A_3$; $M_\infty = 1.5$, $\alpha_F = 0^\circ$.	170
36. Flow field under the wing at the one-third semispan location; $M_\infty = 1.5$, $\alpha_F = 0^\circ$, $z_F = 1.37$ in.	171
37. Flow field under the wing at the one-third semispan location; $M_\infty = 1.5$, $\alpha_F = 0^\circ$, $z_F = 2.12$ in.	174
38. Flow field under the wing at the one-third semispan location; $M_\infty = 1.5$, $\alpha_F = 0^\circ$, $z_F = 4.37$ in.	176
39. Flow field under the wing at the two-third semispan location; $M_\infty = 1.5$, $\alpha_F = 0^\circ$, $z_F = 1.37$ in.	178
40. Flow field under the fuselage centerline; $M_\infty = 1.5$, $\alpha_F = 0^\circ$, $z_F = 2.87$ in.	181
41. Flow field under the wing at the one-third semispan location; $M_\infty = 2.0$, $\alpha_F = 0^\circ$, $z_F = 1.37$ in.	183

LIST OF ILLUSTRATIONS (Continued)

<u>Figure</u>	<u>Page No.</u>
42. Flow field under the wing at the one-third semispan location; $M_\infty = 2.5$, $\alpha_F = 0^\circ$, $z_F = 1.37$ in.	185
43. Flow field under the wing at the one-third semispan location; $M_\infty = 1.5$, $\alpha_F = 5^\circ$, $z_F = 1.37$ in.	187
44. Flow field under the wing at the one-third semispan location; $M_\infty = 1.5$, $\alpha_F = 5^\circ$, $z_F = 4.37$ in.	189
45. Effect of the pylon on the flow field under the left wing panel at the one-third semispan location; $M_\infty = 1.5$, $\alpha_F = 0^\circ$, $z_F = 1.37$ in.	191
46. Flow field under the pylon at the one-third semispan location; $M_\infty = 1.5$, $\alpha_F = 0^\circ$, $z_F = 2.87$ in.	194
47. Flow field under the pylon at the one-third semispan location; $M_\infty = 1.5$, $\alpha_F = 5^\circ$, $z_F = 1.37$ in.	197
48. Flow field under the TER at the one-third semispan location; $M_\infty = 1.5$, $\alpha_F = 0^\circ$, $z_F = 2.12$ in.	200
49. Flow field under the TER at the one-third semispan location; $M_\infty = 1.5$, $\alpha_F = 0^\circ$, $z_F = 3.62$ in.	203
50. Flow field under the fuselage centerline of the configuration with inlets; $M_\infty = 1.5$, $\alpha_F = 5^\circ$, $z_F = 2.87$ in.	206
51. Experimental flow fields below the fuselage centerline for various configurations; $M_\infty = 1.5$, $\alpha = 0^\circ$, $z_F = 2.87$ in.	208
52. Ogive-cylinder pressure distribution model.	210
53. Store load distributions under the wing at the one-third semispan location; $M_\infty = 1.5$, $\alpha_F = 0^\circ$, $z_F = 1.47$ in.	211
54. Store load distributions under the wing at the one-third semispan location; $M_\infty = 1.5$, $\alpha_F = 0^\circ$, $z_F = 2.87$ in.	213
55. Store normal-force distribution under the fuselage centerline; $M_\infty = 1.5$, $\alpha_F = 0^\circ$.	215
56. Store load distributions under the wing at the one-third semispan location; $M_\infty = 1.5$, $\alpha_F = 5^\circ$, $z_F = 1.47$ in.	217
57. Store load distributions under the wing at the one-third semispan location; $M_\infty = 1.5$, $\alpha_F = 5^\circ$, $z_F = 1.47$ in.	219
58. Effect of pylon on load distributions on store at one-third semispan location; $M_\infty = 1.5$, $\alpha_F = 0^\circ$, $z_F = 1.47$ in.	221

LIST OF ILLUSTRATIONS (Continued)

<u>Figure</u>	<u>Page No.</u>
59. Effect of pylon on load distributions on store at one-third-semispan location; $M_\infty = 1.5$, $\alpha_F = 0^\circ$, $z_F = 2.12$ in.	223
60. Effect of pylon on normal-force distributions on store below fuselage centerline; $M_\infty = 1.5$, $\alpha_F = 0^\circ$, $z_F = 2.94$ in.	225
61. Effect of pylon on load distribution on store at one-third semispan location; $M_\infty = 1.5$, $\alpha_F = 5^\circ$, $z_F = 1.47$ in.	226
62. Elliptic force and moment model.	228
63. Pressure distributions on the top and bottom of the elliptic store; $M_\infty = 1.5$, $\alpha_C = 10^\circ$, $\phi_S = 0^\circ$.	229
64. Normal-force distribution on the elliptic store in free-stream; $M_\infty = 1.5$, $\alpha_C = 10^\circ$, $\phi_S = 0^\circ$	230
65. Load distributions on the elliptic store in the free-stream; $M_\infty = 1.5$, $\alpha_C = 10^\circ$, $\phi_S = 45^\circ$.	231
66. Side-force distribution on the elliptic store in the free-stream; $M_\infty = 1.5$, $\alpha_C = 10^\circ$, $\phi_S = 90^\circ$.	233
67. Forces and moments on the ogive-cylinder store at the one-third semispan location; $M_\infty = 1.5$, $\alpha_F = 0^\circ$.	234
68. Forces and moments on the ogive-cylinder store under the fuselage centerline; $M_\infty = 1.5$, $\alpha_F = 0^\circ$.	236
69. Forces and moments on the ogive-cylinder store at the two-third semispan location; $M_\infty = 1.5$, $\alpha_F = 0^\circ$.	237
70. Forces and moments on the ogive-cylinder store at the one-third semispan location; $M_\infty = 1.5$, $\alpha_F = 5^\circ$.	239
71. Forces and moments on the ogive-cylinder store under the pylon at the one-third semispan location; $M_\infty = 1.5$, $\alpha_F = 0^\circ$.	241
72. Forces and moments on the ogive-cylinder store under the pylon at the fuselage centerline; $M_\infty = 1.5$, $\alpha_F = 0^\circ$.	243
73. Forces and moments on the ogive-cylinder store under the pylon at the one-third semispan location; $M_\infty = 1.5$, $\alpha_F = 5^\circ$.	244
74. Triform ogive-cylinder store.	246
75. Forces and moments on triform store in free stream; $M_\infty = 1.5$.	247
76. Forces and moments on elliptic store with wing and tail in the free stream; $M_\infty = 1.5$.	252

LIST OF ILLUSTRATIONS (Concluded)

<u>Figure</u>	<u>Page No.</u>
77. Configuration for trajectory of ogive-cylinder store with cruciform fins.	254
78. Cruciform ogive-cylinder store.	255
79. Trajectory of ogive-cylinder store with cruciform fins released at one-third semispan location; $M_{\infty} = 1.5$, $\alpha_F = 5^\circ$.	256
80. Configuration for trajectory of elliptic store.	258
81. Trajectory of elliptic store released under the fuselage centerline; $M_{\infty} = 1.5$, $\alpha_F = 5^\circ$.	259

LIST OF SYMBOLS

The following list contains most of the symbols used in the report. Other symbols are used in isolated sections of the report and they are defined as they are used.

a	length of horizontal semi-axis of an ellipse
A_i	area of a fin or body-interference-shell u-velocity panel
A_{ij}	aerodynamic influence coefficient of body source panel i on source panel j
$[A]$	direction cosine matrix given by Equation (86)
$[A]'$	transpose of direction cosine matrix of Equation (86)
b	length of vertical semi-axis of an ellipse
c	length of local wing chord
C_A	axial-force coefficient, axial force/ $q_{\infty} S_R$
C_F	force coefficient normal to a fin or body interference shell u-velocity panel, positive as shown in Figure 20; force/ $q_{\infty} S_R$
C_ℓ	rolling-moment coefficient, rolling moment/ $q_{\infty} S_R \ell_R$
C_m	pitching-moment coefficient, pitching moment/ $q_{\infty} S_R \ell_R$
C_n	yawing-moment coefficient, yawing moment/ $q_{\infty} S_R \ell_R$
C_N	normal-force coefficient, normal force/ $q_{\infty} S_R$
C_P	pressure coefficient, $(p - p_{\infty})/q_{\infty}$
C_Y	side-force coefficient, side force/ $q_{\infty} S_R$
F_{ex}, F_{ey}, F_{ez}	ejector forces; positive in the x, y, z directions shown in Figure 13
F_t	thrust force; positive in the x direction shown in Figure 13

LIST OF SYMBOLS (Continued)

F_u, F_v, F_w	aerodynamic influence functions defined by Equation (27)
$F_{u_t}, F_{v_t}, F_{w_t}$	aerodynamic influence functions defined by Equation (29)
F_x, F_y, F_z	sums of all forces acting on ejected store; positive in the x, y, z directions shown in Figure 13
g	gravitational acceleration
g_x, g_y, g_z	gravitational acceleration components in x, y, z directions of Figure 13
i_w	wing incidence angle relative to fuselage longitudinal axis, positive leading edge up
I_{xx}, I_{yy}, I_{zz}	moments of inertia about x, y, z axes of Figure 13; taken about store moment center
I_{yz}, I_{xz}, I_{xy}	products of inertia about x, y, z axes of Figure 13; taken about store moment center
ℓ_R	reference length; store maximum diameter for circular stores, diameter of a circle with the same area as the frontal area of an elliptical store
ℓ_s	store length
m	mass of ejected store
M	Mach number
$M_{e_x}, M_{e_y}, M_{e_z}$	moments due to ejector forces; positive in the positive C_ℓ , C_m , and C_n moment directions shown in Figure 13
M_x, M_y, M_z	sum of all moments acting on ejected store; positive in the positive C_ℓ , C_m , and C_n directions shown in Figure 13
p	static pressure
p, q, r	rotational velocities about x, y, z axes of Figure 13; positive as shown in Figure 14
$\dot{p}, \dot{q}, \dot{r}$	rotational accelerations; time derivatives of p, q, r
q	dynamic pressure

LIST OF SYMBOLS (Continued)

r	radial distance from a body
S_R	reference area taken as store frontal area
t	time
u, v, w	perturbation velocities positive in the positive x, y, z directions of a Cartesian coordinate system
u_B, v_B, w_B	perturbation velocities positive in the x_B, r_B, θ directions of the cylindrical coordinate system associated with a body of revolution
u_{si}, v_{si}, w_{si}	perturbation velocities induced by the image store(s) at a point on the separated store; positive in the x_s, y_s, z_s directions shown in Figure 13
u_{sp}, v_{sp}, w_{sp}	perturbation velocities induced by the parent aircraft at a point on the separated store; positive in the x_s, y_s, z_s directions shown in Figure 13
u_W, v_W, w_W	perturbation velocities induced at a u-velocity panel control point in all u-velocity panels; positive in the x_W, y_W, z_W directions shown in Figure 5
u_{wi}, v_{wi}, w_{wi}	interference velocities induced at wing and pylon u-velocity panel control points by the fuselage at wing and pylon thickness; positive in the x_W, y_W, z_W directions shown in Figure 5
u_ξ, u_η, u_ζ	sum of all perturbation velocities in ξ, η, ζ directions of Figure 14
u_+/V_∞	strength of u-velocity panel with u_+ equal to the axial velocity in the panel
U_s, V_s, W_s	total velocities as seen by store, positive in x_s, y_s, z_s directions of Figure 13
U_s^*, V_s^*, W_s^*	$U_s/V_{\infty_s}, V_s/V_{\infty_s}, W_s/V_{\infty_s}$
$U_{\infty_s, x}, V_{\infty_s, y}, W_{\infty_s, z}$	free-stream velocity components as seen by store; positive in x, y, z directions shown in Figure 13
$U_{\infty_s, x_s}, V_{\infty_s, y_s}, W_{\infty_s, z_s}$	free-stream velocity components as seen by store; positive in x_s, y_s, z_s directions shown in Figure 13

LIST OF SYMBOLS (Continued)

v_{sy}, w_{se}	velocities induced by external vortices; positive in the y_s, z_s directions shown in Figure 13
V	total velocity
w_N	velocity normal to a body source panel at the panel control point
x, y, z	panel coordinate system shown in Figures 5 and 7 or store coordinate system shown in Figures 13 and 14
$\bar{x}, \bar{y}, \bar{z}$	location of store center of mass relative to store moment center
x_B, y_B, z_B	body coordinate system with positive directions as shown in Figure 3
x_B, r_B, θ	body cylindrical coordinate system used in Section 3.2.1 and Appendix A
x_f, y_f, z_f	fin coordinate system shown in Figure 19
x_F, y_F, z_F	fuselage coordinate system shown in Figure 5
x_{le}, x_{te}	x_w coordinate of the wing leading-edge and trailing-edge shock wave locations
x_L	body length
x_s, y_s, z_s	store coordinate system with positive direction as shown in Figure 13
$x_{s,m}$	x_s location of store moment center
x_w, y_w, z_w	wing coordinate system shown in Figure 5
Δz	vertical location of store measured from carriage position on the pylon
α	angle of attack
α_c	combined angle of attack; angle between store longitudinal axis and free-stream velocity vector
α_l	local angle of attack due to wing twist and camber
β	$\sqrt{M^2 - 1}$

LIST OF SYMBOLS (Continued)

β_I	value of β associated with an inlet source panel
γ	ratio of specific heats, $\gamma = 1.4$ for air
γ_f	flight-path angle of parent aircraft
γ_j	strength of j^{th} source panel modeling a body
ϵ_α	shock wave angle of attack correction factor, see Figure 10
θ	local slope of wing or pylon thickness envelope in Section 3.3.4; elsewhere, polar angle measured as defined in the various sections
$\Delta\theta, \Delta\psi$	changes in store pitch and yaw angles from carriage position values
ξ, η, ζ	inertial coordinate system fixed in fuselage nose, positive forward along longitudinal axis, positive laterally to the right, and positive vertically downward, respectively
$\Delta\xi, \Delta\eta, \Delta\zeta$	location of store center of moments in inertial coordinate system relative to the carriage position on pylon
$\dot{\xi}, \dot{\eta}, \dot{\zeta}$	velocity components of store center of moments in inertial system
$\ddot{\xi}, \ddot{\eta}, \ddot{\zeta}$	acceleration components of store center of moments in inertial system
ν	Prandtl-Meyer angle
$\Delta\nu$	change in Prandtl-Meyer angle
ρ	air density
ϕ_f	fin orientation angle defined as shown in Figure 20
ϕ	complete potential for an axisymmetric body; Section 3.2 and Appendix A
ϕ_s	store roll angle, positive right wing down
ψ, θ, ϕ	store yaw, pitch and roll angles specifying angular orientation of store x, y, z coordinate system relative to ξ, η, ζ inertial system, see Figure 14

LIST OF SYMBOLS (Concluded)

$\dot{\psi}, \dot{\theta}, \dot{\phi}$ time rates of change of ψ , θ , and ϕ

Subscripts

F of the fuselage

l local conditions

le, LE quantities associated with the wing leading-edge shock wave

te, TE quantities associated with the wing trailing-edge shock wave

W of the wing

∞ free-stream conditions as seen by the parent aircraft

∞_s free-stream conditions as seen by the separated store

PREDICTION OF SUPERSONIC STORE SEPARATION CHARACTERISTICS
INCLUDING FUSELAGE AND STORES OF NONCIRCULAR
CROSS SECTION

Volume I.- Theoretical Methods and Comparisons
with Experiment

1. INTRODUCTION

This report presents the results of a combined theoretical/experimental research program, the purpose of which is to extend and improve the supersonic store separation prediction method described in References 1 and 2. This volume presents the theoretical methods used and compares predictions with experiment. The computer programs developed during the present investigation are described in Volumes II through IV of this report, References 3 through 5.

The aircraft configuration treated in References 1 and 2 was limited to an axisymmetric fuselage, a wing without dihedral or incidence relative to the fuselage, a single pylon under the wing or fuselage, and single axisymmetric store which could have planar or cruciform fins. The forces and moments acting on the store were calculated using slender-body theory.

In the present work the axisymmetric, or circular, fuselage has been retained as an option. A second option has been added in order that a fuselage which is noncircular in cross section can be modeled with or without engine inlets. The wing model has been generalized to include dihedral, which may vary across the span, and wing incidence relative to the fuselage. Incidence is only included in the wing boundary condition for reasons to be discussed. The pylon model has been extended to allow for breaks in leading-edge and trailing-edge sweep. The option of adding an ejector rack to the pylon

has been added. Up to seven stores may now be used on the parent aircraft. They may be circular or elliptic in cross section. In the trajectory calculation, a store modeled using the circular option may have one set of planar or cruciform fins. If the elliptic option is used, two sets of fins may be included with one, two, three, or four fins in each set. For certain fin arrangements tracking of the trailing-edge vortices from the forward set of fins to the aft set may be performed so their influence can be included in the loads on the aft set of fins.

The experimental program carried out in conjunction with the present work will not be described in this report. It is fully documented in Reference 6. The purpose of the program was to provide systematic data at supersonic speeds for use in evaluating and improving analytical techniques for predicting store separation trajectories. The program was conducted under Air Force Contract F33615-75-C-3053 and the present contract. Five wind-tunnel entries were made during the period from June 1975 through February 1978. The test program was conducted in Tunnel A of the von Kármán Gas Dynamics Facility (VKF) at Arnold Engineering Development Center (AEDC) at nominal Mach numbers of 1.5, 1.6, 2.0, and 2.5 with most testing done at 1.5 and 2.0. Four types of data were obtained; flow-field survey data, store pressure-distribution data, store force-and-moment data, and store separation trajectories. Numerous parent aircraft configurations were used. They varied from a simple circular fuselage with or without a wing to a complex noncircular fuselage with engine inlets, pylon, rack, and stores. The parent aircraft configurations were built up component by component in order to isolate interference effects.

The next two sections of this report describe the general approach to the problem and the flow models based on linear, potential flow theory used for the aircraft components and the stores. The work of Reference 1 will be heavily referenced with

only modifications and additions described in detail. This will be followed by a section which describes nonlinear corrections made to the flow models in order to place shock waves more nearly in their correct positions.

The last sections of the report describe the parent aircraft flow field calculation, the store force and moment calculation, including store-aircraft interference effects, and the store trajectory calculation. Many comparisons between experiment and theory are also presented.

2. GENERAL APPROACH

It is possible to determine the forces and moments acting on an external store in the presence of a parent aircraft in the following manner. Consider first the entire airframe excluding the store in question. The nonuniform flow field, induced by the flow model representing the airframe, is computed in the region occupied by the store. If the store is now placed in this nonuniform flow field, then the calculated loading acting on it includes primary interference. The primary interference can be viewed as the first term in an iterative procedure. Higher-order solutions would be generated as follows. After modeling the store subjected to the primary interference flow field, its effects on the airframe can be determined. These effects, in terms of velocities normal to the wing, pylon, and fuselage, must then be cancelled by an additional set of singularities distributed over these components. A new nonuniform flow field can now be computed in the region occupied by the store, and the loading acting on it can be recalculated. At this stage, the result is associated with the second term in the iteration procedure. The difference between the results of the second and the first loading calculation is due to additional interference. This process can be continued until the effects of additional interference becomes negligible.

In the work of Reference 1, a modification to the first iteration was used to account for aircraft-store mutual interference. This consisted of including in the first iteration the effects of the store in the boundary condition applied to the aircraft flow model. This approach has two difficulties. First, it is impractical to include enough panels in modeling the aircraft to describe accurately the multiple reflections of the store shock wave between the store and the airplane. Second, the separating store moves relative to the aircraft and the point at which its shock wave strikes the aircraft moves,

changing the boundary conditions. This requires that the strengths of the singularities modeling the wing-pylon-fuselage combination be recalculated at each point in the trajectory, a lengthy process. It was recommended that store effects be removed from the aircraft boundary condition and store-aircraft interference be accounted for by imaging. The wing and/or fuselage are treated as reflection planes; that is, an image store is placed on the other side of the wing and/or inside the fuselage. This approach has been adopted in the present work.

The approach taken in the present work is to model all bodies (fuselage, ejector rack, and stores) as isolated bodies. Singularities are used to model both volume and angle-of-attack effects. Wing and pylon thickness are modeled by source panels and the lifting surfaces are modeled by u-velocity panels. Mutual interference between wing and pylon is accounted for and their mutual interference with the fuselage is included by placing an interference shell of u-velocity panels on the fuselage.

With the singularity distributions which represent the various aircraft components determined, the trajectory of the separated store can be calculated. This requires that the forces and moments acting on the store, including damping, be calculated at each point in the trajectory. This is done by calculating the three-dimensional flow field in which the store is located. To do this the separated store is removed from the flow field and the perturbation velocity field due to the aircraft components is calculated at specified points in the region the store had occupied. These points are the control points to be used in modeling the store in the non-uniform flow field. The store is then put back in the flow field and the image store(s) is located relative to the store. The free-stream velocity components that the store sees and the

velocities due to store angular motion are added to the perturbation velocities.

The solution for the store singularity strengths begins at the store nose and works its way aft one axial station at a time. As soon as an image store influence is felt at a control point, the image store induced velocities are added to the previously calculated velocities. After all of the singularity strengths have been calculated, the store surface pressure distribution is calculated using the full Bernoulli equation. These pressures are integrated radially and axially to determine the forces and moments acting on the store. A similar procedure is used to calculate the empennage forces and moments.

3. FLOW MODELS

In general, the flow models for the components to be described are based on linear theory for steady, inviscid flow. Because the flow regime considered here is supersonic, the associated potential flow is governed by the wave equation. In a rectangular coordinate system (x,y,z) with the x -axis in the direction of the free-stream vector, the potential ϕ is given by

$$(M_{\infty}^2 - 1) \frac{\partial^2 \phi}{\partial x^2} - \frac{\partial^2 \phi}{\partial y^2} - \frac{\partial^2 \phi}{\partial z^2} = 0 \quad (1)$$

This equation is valid if the perturbation velocities u,v,w given below in terms of the potential are small.

$$\begin{aligned} u &= \frac{\partial \phi}{\partial x} \\ v &= \frac{\partial \phi}{\partial y} \\ w &= \frac{\partial \phi}{\partial z} \end{aligned} \quad (2)$$

Because of the linearity of the potential ϕ in Equation (1), it is possible to make use of superposition. This principle allows for the representation of the aircraft components by distributions of potentials or singularities. Flow conditions at a given field point are given by the summed influences of all the singularities. Before describing the flow models, the aircraft components, the store, and flight conditions will be summarized.

3.1 Description of Aircraft Components and Flight Conditions

The configuration of interest consists of a wing attached to a fuselage. A pylon can be positioned under the wing or

under the fuselage centerline. An ejector rack can be attached to the pylon. Up to seven stores can be positioned relative to the aircraft.

The geometric parameters of the aircraft components described below are accounted for in the computer program. Flight conditions cover the supersonic speed regime and are specified below together with the expected range of validity of the present method.

3.1.1 Fuselage

Two options exist for modeling the fuselage. These options will be referred to throughout this report as the "circular" fuselage option and the "noncircular" fuselage option.

In the circular fuselage option, the body is axisymmetric and its axial radius distribution is specified by a set of polynomials.

The noncircular fuselage may have an arbitrary cross section which may vary over the length of the fuselage. A number of options exist in the computer program for specifying the cross-sectional shape as a function of axial location. All of the options provide information such that quadrilateral panels can be laid out on the fuselage surface. This option also allows for the inclusion of external-compression-ramp inlets on the sides of the fuselage. The mass-flow ratio through the inlets is varied by specifying panels on the face of the inlet as "open" or "closed".

3.1.2 Wing

The wing may have twist and camber and the leading and trailing edges can have breaks in sweep. Dihedral angle is also variable across the wing span and incidence relative to the fuselage centerline may be specified and is included in the wing boundary condition. Vertical location of the wing

attachment on the fuselage is not limited to the midplane. Effects of wing thickness are included in the program. The wing leading edge can be blunt or sharp.

3.1.3 Pylon

Leading and trailing edges may be swept with breaks in sweep across the span. The length of the pylon root chord need not equal the local wing chord. Thickness is accounted for and the leading edge can be blunt or sharp. The pylon can be located under the wing or fuselage but is aligned with the free stream.

3.1.4 Ejector Rack

The ejector rack is assumed to be attached to the pylon and can only be used with a pylon. Only the rack body is modeled and this is modeled as an axisymmetric body. Its axial radius distribution is specified by a set of polynomials.

3.1.5 Stores

Two options exist for modeling stores. They will be referred to throughout this report as the "circular" store option and the "elliptical" store option. Up to seven stores can be included in the parent aircraft model, including the store to be separated.

The circular store body shape is described by a set of polynomials which gives its radius as a function of axial location. Up to seven different shapes may be used. A particular shape may be used for more than one store.

The elliptical store option is restricted to two different shapes; again, more than one store can be modeled with a given shape. Several options exist for describing the shape of the elliptic body. They all provide information which allow computation of the body cross-sectional shape as a

function of axial location. This information allows quadrilateral panels to be laid out on the body surface.

The store to be separated may have fins. If the circular store option is used, it can have one set of fins. They may be planar or cruciform and may be located axially anywhere on the store body. Use of the elliptic store option allows up to two sets of fins to be placed on the store at arbitrary locations. Each set can consist of one, two, three, or four fins. The fins can be located anywhere on the circumference of the body.

All of the stores may be at arbitrary pitch angle relative to the aircraft but must be at zero yaw angle. Stores using the circular body option must be at zero roll angle while those using the elliptic option may be at arbitrary roll angle.

At the beginning of the trajectory the store may have arbitrary translational and rotational velocities relative to the aircraft. The store may be ejected with an ejector force versus time or displacement history. There can be one or two ejector feet. The store can be powered by specifying a thrust force versus time history. Store mass and moments and products of inertia are constant and the center of gravity may be located off the store longitudinal axis.

3.1.6 Flight Conditions

The flight path is straight but not necessarily horizontal, angle of attack is constant, and angle of sideslip is zero. The Mach number should lie between 1.2 and 3.0. The angle of attack should be in the 0° - 10° range.

3.2 Flow Models for the Fuselage, Ejector Rack, and Store Bodies

This section will describe the flow models of the fuselage, rack, and stores as they comprise part of the parent aircraft.

In the present work they are modeled as isolated bodies. The modeling of the separated store during its trajectory when forces and moments must be calculated will be presented in Section 6.

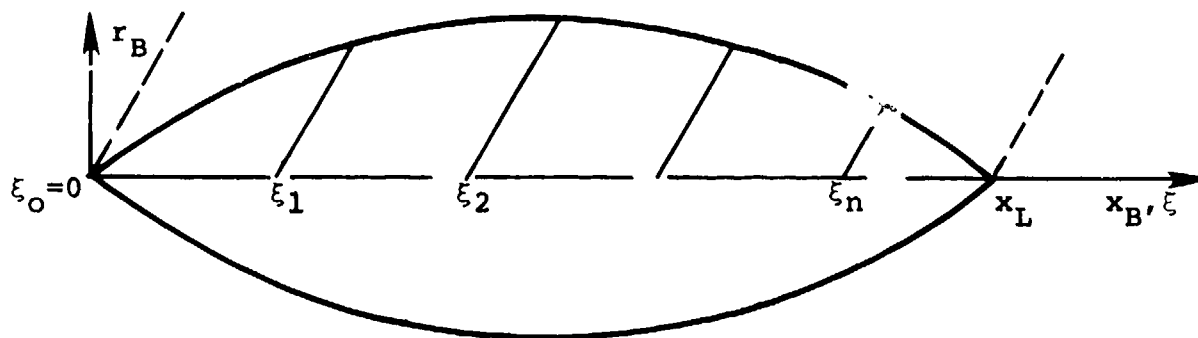
3.2.1 Circular Fuselage

The potential flow method used to model the circular fuselage is the one which was used in Reference 1 with one modification which will be discussed later. The method is described in Section 3.2 and Appendix I of that reference. Fundamentally, an axisymmetric body in supersonic flow can be represented by a distribution of line sources or sinks and doublets on the body centerline to account for volume and angle of attack effects, respectively. The strengths of these singularities are determined from the flow tangency conditions applied at points on the body surface. The source strength constants are determined using Equations (I-14) and (I-17) and the doublet strength constants using Equations (I-27) and (I-28) of Appendix I of Reference 1. The strengths of the singularities vary linearly with length. The perturbation velocities produced by the line singularities at a field point are given by Equation (I-30) in the appendix.

During the course of the present investigation it was found that this flow model worked well as long as the field point at which the velocities were to be calculated was not downstream of the point at which the last singularities modeling the body began influencing the flow field. As the field point moved downstream of the point at which the last singularities were "felt", the induced velocities increased without bound due to the linearly varying strengths of the singularities. To eliminate this problem additional singularities are introduced at the body base to cancel the effects caused by the singularities modeling the body. The potential and velocity equations will now be derived, first for the sources and sinks

and then for the doublets. The derivations parallel those in Appendix I of Reference 1.

The following sketch shows a body of revolution of length x_L .



Line sources and sinks of linearly increasing strength modeling the body volume start at $\xi_0 = 0, \xi_1, \xi_2, \dots, \xi_n$ with known source constants of $K_0, K_1, K_2, \dots, K_n$. At the base of the body, $x = x_L$, the source strengths are $K_0 x_L, K_1(x_L - \xi_1), K_2(x_L - \xi_2), \dots, K_n(x_L - \xi_n)$. Therefore, the function representing the singularities to be introduced at the body base to cancel the singularities behind the base is

$$f_L(\xi) = -K_0 \xi - K_1(\xi - \xi_1) - K_2(\xi - \xi_2) \dots - K_n(\xi - \xi_n) \quad (3)$$

The potential for these sources and sinks starting at $x_B = \xi = x_L$ is

$$\phi_a(x_B, r_B) = - \int_{x_L}^{x_B - \beta r_B} \frac{f_L(\xi) d\xi}{\sqrt{(x_B - \xi)^2 - \beta^2 r_B^2}} \quad (4)$$

Since the integrand is singular at the upper limit of integration, the procedures described on page 108 of Reference 1 can be followed and the axial potential rewritten as

$$\phi_a(x_B, r_B) = - \int_0^{\cosh^{-1} \left(\frac{x_B - x_L}{\beta r_B} \right)} f_L(x_B - \beta r_B \cosh \sigma) d\sigma \quad (5)$$

For the n^{th} term in Equation (3) where $f_{L,n} = -K_n(\xi - \xi_n)$, Equation (5) becomes

$$\phi_a(x_B, r_B) = \int_0^{\cosh^{-1} \left(\frac{x_B - x_L}{\beta r_B} \right)} (K_n x_B - K_n \beta r_B \cosh \sigma - K_n \xi_n) d\sigma \quad (6)$$

and after integrating

$$\begin{aligned} \phi_a(x_B, r_B) = & K_n(x_B - \xi_n) \cosh^{-1} \left(\frac{x_B - x_L}{\beta r_B} \right) \\ & - K_n \sqrt{(x_B - x_L)^2 - \beta^2 r_B^2} \end{aligned} \quad (7)$$

The total potential for all the source-sink singularities originating at the body base is obtained by summing the right side of Equation (7) over the N singularities.

The axial and radial perturbation velocities can be determined by differentiation of the potential

$$\left. \begin{aligned} \frac{u_{B,a}}{V_\infty} &= \frac{\partial \phi_a}{\partial x_B} \\ \frac{v_{B,a}}{V_\infty} &= \frac{\partial \phi_a}{\partial r_B} \end{aligned} \right\} \quad (8)$$

From Equation (7)

$$\left. \begin{aligned} \frac{u_{B,a}}{V_\infty} &= \cosh^{-1} \left(\frac{x_B - x_L}{\beta r_B} \right) K_n + \frac{K_n (x_L - \xi_n)}{\beta r_B \sqrt{\left(\frac{x_B - x_L}{\beta r_B} \right)^2 - 1}} \\ \frac{v_{B,a}}{V_\infty} &= -\beta \sqrt{\left(\frac{x_B - x_L}{\beta r_B} \right)^2 - 1} K_n \\ &\quad + \frac{\beta \left(\frac{x_B - x_L}{\beta r_B} \right)}{\beta r_B \sqrt{\left(\frac{x_B - x_L}{\beta r_B} \right)^2 - 1}} K_n (x_L - \xi_n) \end{aligned} \right\} \quad (9)$$

Similar expressions can be derived for the line doublets introduced at the body base. Referring to the preceding sketch, line doublets modeling the body angle of attack effects start at $\xi_0 = 0, \xi_1, \xi_2, \dots, \xi_n$ with known doublet constants $K_{d,0}, K_{d,1}, K_{d,2}, \dots, K_{d,n}$. At the base of the body, $x = x_L$, the doublet strengths are $K_{d,0} x_L, K_{d,1} (x_L - \xi_1), K_{d,2} (x_L - \xi_2), \dots, K_{d,n} (x_L - \xi_n)$. The function representing the doublet singularities to be introduced at the body base is

$$d_L(\xi) = -K_{d,0} \xi - K_{d,1} (\xi - \xi_1) - K_{d,2} (\xi - \xi_2), \dots - K_{d,n} (\xi - \xi_n) \quad (10)$$

The potential for these doublets starting at $x_B = \xi = x_L$ is

$$\phi_C(x_B, r_B, \theta) = \frac{\cos \theta}{r_B} \int_{x_L}^{x_B - \beta r_B} \frac{d_L(\xi)(x_B - \xi)}{\sqrt{(x_B - \xi)^2 - \beta^2 r_B^2}} d\xi \quad (11)$$

This potential is integrated following the same procedure used for the sources to give

$$\begin{aligned} \phi_C(x_B, r_B, \theta) = & -\cos \theta \left[\frac{\beta}{2} K_{d,n}(x_B - x_L) \sqrt{\left(\frac{x_B - x_L}{\beta r_B} \right)^2 - 1} \right. \\ & + \beta K_{d,n}(x_L - \xi_n) \sqrt{\left(\frac{x_B - x_L}{\beta r_B} \right)^2 - 1} \\ & \left. - \frac{\beta^2 r_B}{2} K_{d,n} \cosh^{-1} \left(\frac{x_B - x_L}{\beta r_B} \right) \right] \quad (12) \end{aligned}$$

The total potential due to all the doublets introduced at the body base is obtained by summing the right side of Equation (12) over the N singularities.

The axial, radial, and tangential perturbation velocities are obtained by differentiating the potential,

$$\left. \begin{aligned} \frac{u_{B,d}}{V_\infty} &= \frac{\partial \phi_C}{\partial x_B} \\ \frac{v_{B,d}}{V_\infty} &= \frac{\partial \phi_C}{\partial r_B} \\ \frac{w_{B,d}}{V_\infty} &= \frac{1}{r_B} \frac{\partial \phi_C}{\partial \theta} \end{aligned} \right\} \quad (13)$$

From Equation (12)

$$\begin{aligned}
 \frac{u_{B,d}}{V_\infty} &= -\cos \theta \left[\beta K_{d,n} \sqrt{\left(\frac{x_B - x_L}{\beta r_B} \right)^2 - 1} \right. \\
 &\quad \left. + \frac{1}{r_B} K_{d,n} (x_L - \xi_n) \frac{\left(\frac{x_B - x_L}{\beta r_B} \right)}{\sqrt{\left(\frac{x_B - x_L}{\beta r_B} \right)^2 - 1}} \right] \\
 \frac{v_{B,d}}{V_\infty} &= \cos \theta \left[\frac{\beta^2}{2} K_{d,n} \cosh^{-1} \left(\frac{x_B - x_L}{\beta r_B} \right) \right. \\
 &\quad + \frac{\beta^2}{2} K_{d,n} \left(\frac{x_B - x_L}{\beta r_B} \right) \sqrt{\left(\frac{x_B - x_L}{\beta r_B} \right)^2 - 1} \\
 &\quad \left. + \frac{\beta}{r_B} K_{d,n} (x_L - \xi_n) \frac{\left(\frac{x_B - x_L}{\beta r_B} \right)^2}{\sqrt{\left(\frac{x_B - x_L}{\beta r_B} \right)^2 - 1}} \right] \\
 \frac{w_{B,d}}{V_\infty} &= \sin \theta \left[-\frac{\beta^2}{2} K_{d,n} \cosh^{-1} \left(\frac{x_B - x_L}{\beta r_B} \right) \right. \\
 &\quad + \frac{\beta^2}{2} K_{d,n} \left(\frac{x_B - x_L}{\beta r_B} \right) \sqrt{\left(\frac{x_B - x_L}{\beta r_B} \right)^2 - 1} \\
 &\quad \left. + \frac{\beta}{r_B} K_{d,n} (x_L - \xi_n) \sqrt{\left(\frac{x_B - x_L}{\beta r_B} \right)^2 - 1} \right]
 \end{aligned} \tag{14}$$

The velocities induced by all of the line sources and doublets starting at the body base are obtained by summing Equations (9) and (14) over the N singularities.

An examination of Equations (9) and (14) shows that the last terms in the equations for u_B and v_B are singular on the Mach cone originating at the body base, $(x_B - x_L)/\beta r_B = 1$. The singular terms in Equation (9) for the source induced velocities are multiplied by the source strength $K_n(x_L - \xi_n)$. For a closed body the sum of the source strengths is zero, that is

$$\sum_{n=0}^{N-1} K_n(x_L - \xi_n) = 0 \quad (15)$$

Making use of this fact, the singular terms in Equation (9) have been set to zero.

For the doublets the requirement that the sum of their strengths be zero does not apply. Thus, the singular terms in Equation (14) cannot be eliminated for this reason. A numerical study of the relative magnitudes of the singular and nonsingular terms was performed. It was found that in a short distance downstream of the Mach cone originating at the body base the singular terms were small compared to the nonsingular terms. Thus, to avoid numerical difficulties on or very near the base Mach cone, the singular terms in the $u_{B,d}$ and $v_{B,d}$ expressions in Equation (14) have been set to zero. The last term in the $w_{B,d}$ equation, which is proportional to the sum of the doublet strengths $\sum_n K_{d,n}(x_L - \xi_n)$ has been set to zero since it was also found to be small.

The total axial, radial, and tangential body induced perturbation velocities at field point (x_B, r_B, θ) are obtained by adding the velocities given by Equation (I-30) of Appendix I of Reference 1 to those given by Equations (9) and (14) after

summing these latter two equations over the number, NXBODY, line sources and doublets. The resulting equations are

$$\begin{aligned}
 \frac{u_B}{V_\infty} &= \sum_{n=0}^{NXBODY-1} \left\{ -K_n \left[\cosh^{-1} \left(\frac{x_B - \xi_n}{\beta r_B} \right) - \cosh^{-1} \left(\frac{x_B - x_L}{\beta r_B} \right) \right] \right. \\
 &\quad \left. + \beta \cos \theta K_{d,n} \left[\sqrt{\left(\frac{x_B - \xi_n}{\beta r_B} \right)^2 - 1} - \sqrt{\left(\frac{x_B - x_L}{\beta r_B} \right)^2 - 1} \right] \right\} \\
 \frac{v_B}{V_\infty} &= \sum_{n=0}^{NXBODY-1} \left\{ \beta K_n \left[\sqrt{\left(\frac{x_B - \xi_n}{\beta r_B} \right)^2 - 1} - \sqrt{\left(\frac{x_B - x_L}{\beta r_B} \right)^2 - 1} \right] \right. \\
 &\quad - \frac{\beta^2}{2} \cos \theta K_{d,n} \left[\cosh^{-1} \left(\frac{x_B - \xi_n}{\beta r_B} \right) - \cosh^{-1} \left(\frac{x_B - x_L}{\beta r_B} \right) \right. \\
 &\quad \left. \left. + \left(\frac{x_B - \xi_n}{\beta r_B} \right) \sqrt{\left(\frac{x_B - \xi_n}{\beta r_B} \right)^2 - 1} - \left(\frac{x_B - x_L}{\beta r_B} \right) \sqrt{\left(\frac{x_B - x_L}{\beta r_B} \right)^2 - 1} \right] \right\} \\
 \frac{w_B}{V_\infty} &= \sum_{n=0}^{NXBODY-1} \left\{ \frac{\beta^2}{2} \sin \theta K_{d,n} \left[\cosh^{-1} \left(\frac{x_B - \xi_n}{\beta r_B} \right) \right. \right. \\
 &\quad - \cosh^{-1} \left(\frac{x_B - x_L}{\beta r_B} \right) - \left(\frac{x_B - \xi_n}{\beta r_B} \right) \sqrt{\left(\frac{x_B - \xi_n}{\beta r_B} \right)^2 - 1} \\
 &\quad \left. \left. + \left(\frac{x_B - x_L}{\beta r_B} \right) \sqrt{\left(\frac{x_B - x_L}{\beta r_B} \right)^2 - 1} \right] \right\}
 \end{aligned}$$

(16)

where

$$\begin{aligned}
 \beta^2 &= M_\infty^2 - 1 \\
 \xi_n &= x_{Bd_n} - \beta r_{Bd_n}
 \end{aligned}$$

and

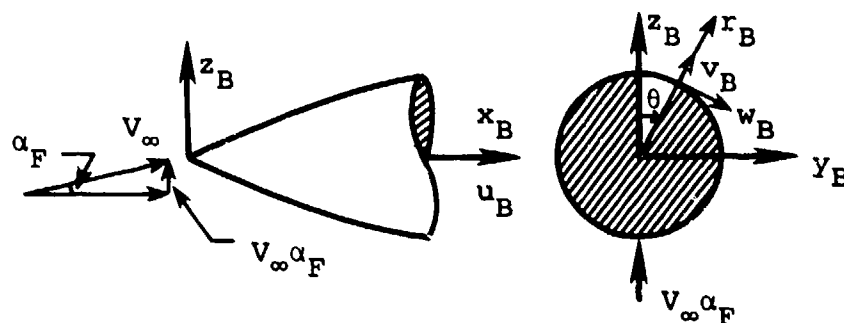
x_{Bd_n}, r_{Bd_n} = coordinates of the n^{th} body definition point

u_B = axial perturbation velocity component

v_B = radial perturbation velocity component

w_B = tangential perturbation velocity component

The positive directions are shown again for convenience in the following sketch.



To show how the introduction of the source and doublet singularities at the body base improves the flow-field predictions behind the body base, calculations were performed for a circular arc body of length to diameter ratio (L/D) of 5. For zero degrees angle of attack, sources only, the results of including these singularities are shown in Figure 1. The dashed curves are the velocities without including the sources starting at the body base and the solid curves include these singularities. As can be seen, when the singularities are included the velocities return to the free-stream values.

Similar results for an angle of attack of 5° are shown in Figure 2. Here, the dashed curves have only source singularities starting at the body base. The solid curves have doublet singu-

larities also starting there. With the doublets, the velocities again return to the free-stream values downstream of the body base

3.2.2 Noncircular Fuselage

The method used in the present work to model a noncircular fuselage is an adaptation of program WDYBDY used in the work of Reference 7. This program was extracted from the advanced paneling program described in References 8 and 9. The method is used to model both the noncircular fuselage and the elliptic store body which will be described in Section 3.2.6.

The theoretical approach is based on representing the non-circular fuselage body alone by supersonic, linear flow theory. The body is modeled using quadrilateral supersonic body source panels which can be inclined to the flow. In this way the panels account for both volume and angle of attack effects. A typical panel layout on an elliptic body is shown in Figure 3. The inclination of a panel with respect to the body axis is limited to the semiapex angle of the Mach cone associated with the free-stream Mach number. This limits the local body surface slope which can be modeled. An approximate method for modeling engine inlets where the inclination angle is greater than the Mach cone semiapex angle is described in the next section. In the noncircular fuselage model a vertical plane of symmetry is assumed, the cross-sectional shape is arbitrary and may vary over the fuselage length, and the sideslip angle is zero.

The panel strengths are determined by solving the following set of simultaneous algebraic equations for N panels for the γ_j 's.

$$\sum_{j=1}^N A_{ij} \gamma_j = \left(\frac{w_N}{V_\infty} \right)_i \quad i = 1, 2, \dots, N \quad (17)$$

The quantity A_{ij} is the aerodynamic influence coefficient of panel i on panel j , γ_j is the unknown strength of panel j , and

$(W_N/V_\infty)_i$ is the component of the free-stream velocity normal of the panel control point, its centroid of area.

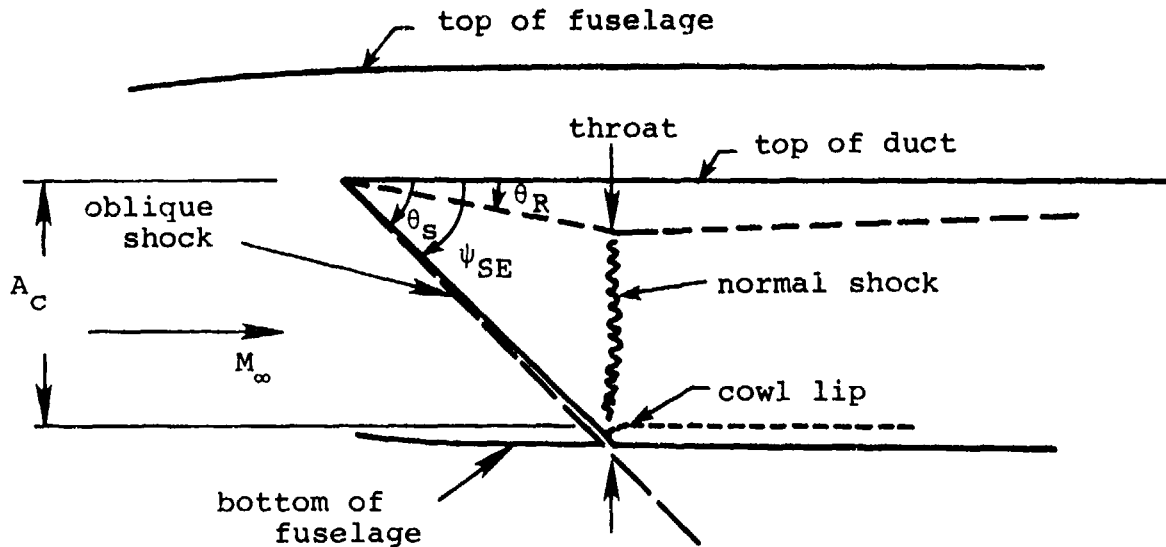
The calculation of the A_{ij} matrix is described in Reference 8. All the fuselage panels have unswept leading and trailing edges so that Equations (88) through (95) of that reference give the basic velocity expressions for one corner of the panel used in calculating the A_{ij} 's. The superposition of the four corners of the panel is given by Equations (21), (22), and (23) of Reference 8. Equation (13) of Reference 7 is the expression used for $(W_N/V_\infty)_i$.

3.2.3 Fuselage Mounted Engine Inlets

This section is concerned with the flow modeling of supersonic, ramp type engine air inlets mounted to the sides of the parent aircraft fuselage. The primary objective is to determine the effects of the inlets on the flow fields in which the separated store may be immersed. Effects of the inlets are also included in accounting for fuselage/wing interference. The inlet is assumed to operate at on-design condition with or without flow blockage. In either case, the contribution to the flow field from the inlet is characterized by the presence of a shock system. The method described below is an approximate one and is based on the supersonic source panels used for modeling the noncircular fuselage of the parent aircraft and the store body if the elliptical store option is used.

First, a description is given of the inlet of interest and the flow conditions. Then, the technical approach is discussed. The method used to generate the shock system external to the supersonic inlet will be discussed in Section 4.2.

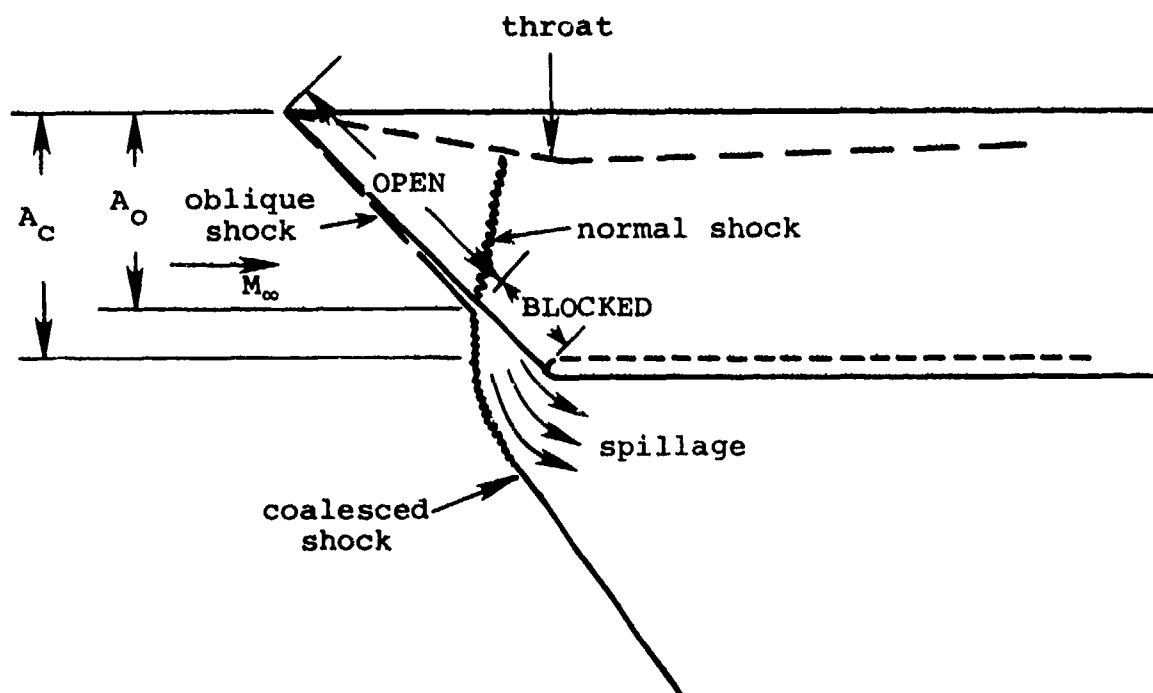
The configuration treated here is a fuselage mounted, two-dimensional, external compression type engine air inlet as shown in the following sketch. For this type of inlet, the



leading edges of the sideplates are swept back at angle $90^\circ - \psi_{SE}$. The sharp unswept leading edge of the compression ramp is at angle θ_R which extends into the inlet duct, and the opposite edge forms the cowl with a rounded or sharp edge or lip.

The oncoming flow is assumed at free-stream Mach number, M_∞ , and can be inclined with respect to the duct center line. The inlet is shown "on-design" and operates at "critical flow" condition. The first designation indicates that the oblique shock emanating from the ramp leading edge falls on the intake opening. Angle θ_S is the oblique shock angle corresponding to ramp angle θ_R and free-stream Mach number M_∞ . For the on-design case, $\theta_S = \psi_{SE}$. For critical flow, a normal shock stands in the throat. If the oncoming Mach number is below design, the oblique shock still originates from the ramp edge but stands ahead of the cowl lip. When the inlet sees higher than design Mach number, the oblique shock may be turned inside the duct. In this effort, only the on-design condition will be considered. An on-design inlet can operate subcritically, critically, or supercritically. When the mass flow rate in the duct is less than that contained in the stream tube ahead of the inlet, some flow spillage occurs. Under this partial blockage

condition, the normal shock moves ahead of the throat and the inlet operates at subcritical condition. This situation is depicted in the following sketch. The prediction method is aimed at being able to handle the zero and partial blockage case.



Length A_C is the height of the stream tube containing the maximum mass flow which can enter the inlet. Length A_O is the height of the stream tube actually entering the inlet under a partial blockage condition. The mass flow ratio MFR is defined as

$$\text{MFR} = \frac{A_O}{A_C} \quad (18)$$

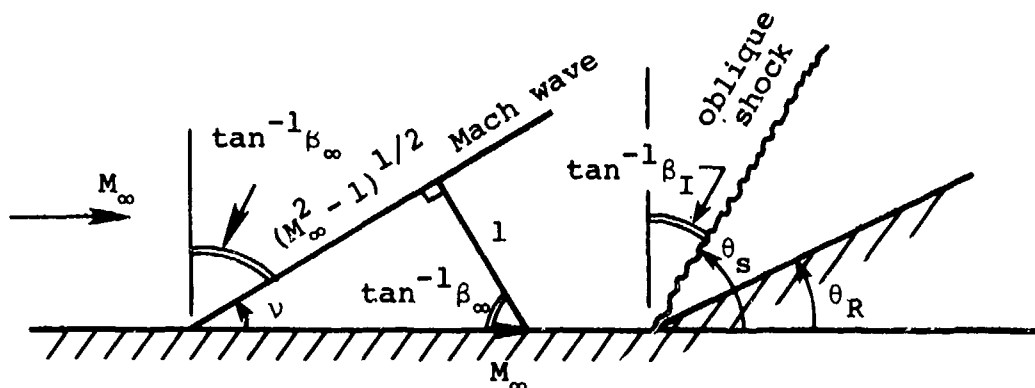
The normal and oblique shocks combine to form the indicated coalesced shock, and the stream tube containing the spilled flow is deflected from the intake.

The descriptions of the inlet and its flow features given above are by no means complete. They are intended only to provide the nomenclature and parameters used in the prediction method discussed below. More detailed description of supersonic, external compression inlet characteristics are available, for example refer to Reference 10.

The method described here for modeling the inlets makes use of the supersonic source panels already employed to model the noncircular fuselage. The slant area of the intake opening is covered by the source panels. These inlet panels have a special boundary condition treatment to account for flow blockage. The steps in the procedure are as follows. The first step concerns the solution for the panel strengths. Then, the shock shape is determined. Finally, the contributions to the flow field are calculated. These latter two are discussed in Sections 4.2 and 5.4.

The fuselage source panels and the inlet panels are treated integrally by one set of simultaneous equations, accounting for a vertical plane of symmetry, to solve for their strengths subject to the boundary conditions to be subsequently discussed. In this process, the Mach cones determining the region of influence of the inlet panels require special treatment. This is necessary because the angles of incidence of the inlet panels are such that the panel planes usually lie outside the Mach cones from their corners based on the free-stream Mach number. In fact, they are superinclined panels. The present source panel solution cannot handle such a case. To alleviate this problem the oblique shock-wave angle is employed to specify an effective Mach number for use in the calculation of the contributions from the inlet panels such that the panels lie behind their Mach cones. The Prandtl-Glauert factor β_I for the source panels on the inlet face is calculated as follows. For given free-stream Mach number, M_∞ ,

and specified ramp angle θ_R , the oblique shock angle θ_s is obtained from Reference 11. For the Mach wave triangle we have



$$\beta_\infty = \tan (90^\circ - \nu) = \sqrt{M_\infty^2 - 1} \quad (19)$$

In an analogous manner, replacing the Mach wave with the oblique shock leads to

$$\beta_I = \tan (90^\circ - \theta_s) \quad (20)$$

In effect, the on-design oblique shock is used to position a "Mach wave" slightly ahead of the inlet panels. It is this modified "Mach wave" that determines the region of influence of the inlet panels. Above all, this scheme allows the source panels placed on the inlet panels to have a solution; that is, generate perturbation velocities at other panel control points.

The original flow tangency boundary condition associated with the source panels used for modeling a body in supersonic flow is described on page 52 of Reference 8. A modified version allowing for pitch and roll is discussed in Reference 7, Equation (13). However, the boundary condition applied at control points of the source panels on the inlet requires special treatment to reflect specified mass flow ratio, MFR, Equation (18).

In the source panel solution, the flow tangency condition is expressed in terms of velocity, not mass flow, normal to the plane of the source panels. It is clear, however, that fully blocked panels have zero mass flow and zero normal velocity at their control points. Open panels allow mass flow at free-stream velocity to pass through at their control points. Thus, in these two limits, the boundary condition can be expressed in either velocity or mass flow normal to the panel.

Refer now to the first two sketches in this section. In the first, all of the mass flow contained in the stream tube of height A_c enters the inlet and the mass flow ratio, MFR, equals 1. The boundary condition assigned to the inlet source panels for this case states that the perturbation velocities induced by all source panels must cancel one another. To accomplish this, the right-hand side of the inlet source panel flow tangency condition is set equal to zero. Equation (17), Equation (138) in Reference 8, is modified for the full flow situation to

$$\left. \begin{aligned} \sum_{j=1}^N A_{ij} \gamma_j &= 0, \quad i = \text{index of source panels on inlet} \\ N &= \text{total number of source panels} \\ &\quad \text{on fuselage and inlet} \end{aligned} \right\} \quad (21)$$

Here, A_{ij} represents the aerodynamic influence coefficients and γ_j are the source panel strengths. Consequently, all the source panels modeling the fuselage and inlets cause the resultant velocity at the control point of the inlet panels to be equal to that of the free stream. Note that with the vertical plane of symmetry assumption, the effects of the "image" inlet is included in all of the above. Any effects of the wing thickness or lifting panels on the inlet velocity are neglected.

The second sketch in this section depicts the partial blockage case. Now, only the stream tube with height A_0 enters the inlet. The remaining stream tube with height $(A_C - A_0)$ is spilled from the intake. For this case, the region designated "OPEN" on the intake opening is made to act as if there is no blockage. The panels in this region have the boundary condition given by Equation (21) with changed limits on the index i .

$$\sum_{j=1}^N A_{ij} \gamma_j = 0, \quad i = \text{index of OPEN source panels on inlet} \quad (22)$$

Now, the source panels in the region designated "BLOCKED" are made to block the flow and actually become a continuation of the upper stream surface forming the stream tube containing the spilled flow. The flow tangency condition is applied to these panels.

$$\sum_{j=1}^N A_{ij} \gamma_j = \left(\frac{W_N}{V_\infty} \right)_i, \quad i = \text{index of BLOCKED source panels on inlet} \quad (23)$$

Quantity W_N/V_∞ is given by Equation (13) in Reference 7 and represents the contribution from the free stream. Regions OPEN and BLOCKED are determined by the intersections of the stream tubes and the plane of the inlet. As such, the lengths of the two regions are proportional to the heights of the stream tubes, A_0 and $(A_C - A_0)$, respectively. Thus, the ratio of the inlet area covered by the OPEN source panels to the total inlet area reflects the mass flow ratio MFR, Equation (18).

To solve for the source panel strengths modeling a non-circular fuselage with engine inlets, the set of equations given by Equation (17) is modified in accordance with Equation (21) or Equations (22) and (23). In calculating the aerodynamic

influence coefficient for an inlet panel acting on another panel, β_I given by Equation (20) is used.

3.2.4 Ejector Rack Body

A sketch of a triple ejection rack, TER, wind tunnel model is shown in Figure 4. It consists of the rack body with two stubby pylons at the shoulder locations and a long pylon at the bottom location. This same configuration exists at the two longitudinal stations on a multiple ejection rack, MER. In the present work the pylons are not modeled and the rack body is modeled as a body of revolution.

The rack body is modeled as if no parent aircraft were present, that is as a body in free-stream flow at angle of attack only. Volume effects are modeled by a distribution of line sources along the body axis and angle of attack effects by a distribution of line doublets along the axis. The method of calculating the singularity strengths and the perturbation velocity field is identical to that described in Section 3.2.1 for the circular fuselage.

3.2.5 Circular Store Body

The circular store body option is restricted to a body of revolution. As in the case of the circular fuselage and the ejector rack bodies, the circular store is modeled in the free-stream at angle of attack. A distribution of line sources along the store axis models the volume effects and a distribution of line doublets models the angle of attack effects. The method of calculating the singularity strengths and the perturbation velocity field is identical to that described in Section 3.2.1 for the circular fuselage.

3.2.6 Elliptic Store Body

The elliptic store body option models a body of elliptic cross section. The ratio of major axis length to minor axis

can vary over the store length. This option can also be used to model a circular store which is to be separated. In the circular store option, the separated store can have only one set of fins and they must be planar or cruciform. The elliptic store option allows the separated store to have one or two sets of fins with 1, 2, 3, or 4 fins in each set. The fins may be oriented circumferentially anywhere on the body. Also, they do not have to be perpendicular to the tangent to the body surface.

The elliptic store body is modeled using the same method as was described in Section 3.2.2 for the noncircular fuselage. The body is modeled by supersonic source panels and their strengths are calculated using Equation (17).

The elliptic store model does not assume a vertical plane of symmetry as was done for the noncircular fuselage. Source panels are laid out on the entire body. This is done since, even though the store is being modeled in the free-stream, it can be rolled as well as pitched relative to the free-stream velocity vector. An example of this is an elliptic store on one of the shoulder locations on a TER.

3.3 Flow Model for Wing-Pylon Combination and Interference Shell on Fuselage

This section describes the representation of the wing-pylon in terms of elements from linear, potential flow theory. Also, the methods used to account for mutual interference between the wing-pylon and the fuselage are discussed. Specifically, constant u-velocity panels are distributed over the wing, pylon, and part of the fuselage. In addition, constant s-velocity panels distributed over the wing and pylon account for thickness effects. The constant u-velocity panels laid out on the fuselage form the interference shell and serve primarily to cancel interference effects from the wing-pylon

combination. The flow model is an extension to that described in Section 3.3 of Reference 1 in that wing dihedral and wing incidence are now included.

3.3.1 Geometrical Layout

The left wing and pylon and the left half of the fuselage are divided up into area panels of trapezoidal shape. The right half of the airframe is accounted for by employing symmetry properties discussed later. Figure 5 shows a swept-wing, swept-pylon combination attached to a circular fuselage above its midplane. The rectangular coordinate systems associated with the fuselage (x_F, y_F, z_F) and the wing (x_W, y_W, z_W) are shown. The origin of the former is at the fuselage nose. The wing coordinate system has its origin in the $y_F = 0$ plane at the point where it is intersected by the line connecting the leading edges of the root chords of the left and right wing panels. The coordinate system (x, y, z) with its origin at corner 1 of the cross-hatched panel is associated with a semi-infinite triangle which is part of the solution for the panel to be described later. The panel lies in the x, y plane.

A distribution of constant u-velocity type panels to model loading and a distribution of constant source type panels to model thickness will be laid out on the wing and pylon. The distributions of the two types of panels need not be the same in the chordwise direction or in the spanwise direction. The sides of both types of panels are taken parallel to the centerline of the fuselage. Their leading and trailing edges are swept along constant percent chordlines of the wing or pylon. A leading or trailing edge is called subsonic or supersonic depending on whether or not the component of the free-stream velocity perpendicular to the edge in question is subsonic or supersonic, respectively. Figure 5 shows a simplified layout of 2 chordwise by 6 spanwise panels on the

left wing half. A distribution of 2 chordwise by 2 spanwise panels covers the pylon. Generally, more panels are required to obtain accurate results.

Constant u-velocity panels only are laid out over part of the fuselage and designated body interference panels. The leading and trailing edges of these panels are unswept. Only the left half of the aircraft configuration needs to be covered because of symmetry about the $y_F = 0$ plane provided that the effects of the other half are accounted for as discussed later. The length of fuselage covered by the body interference panels is determined by the range of influence of the wing and pylon. This range is taken as the length along the body measured from the leading edge of the wing-fuselage junction, or root chord, to the trailing edge of the wing for a supersonic wing trailing edge. For the case of a subsonic trailing edge, the length should extend back further. In this case, the interference shell is sufficient to account for most of the wing-pylon to fuselage interference. In the simplified layout of Figure 5, the body interference shell consists of 5 circumferential rings with 4 panels per half ring. The interference shell shape is constant over its length. For a noncircular fuselage it must be on or outside the source panel representation of the body, see Section 3.2.2, and is not circular as shown in Figure 5.

Each constant u-velocity panel contains a control point placed at the 95-percent location on the chord containing the panel centroid as shown in Figure 5. The flow tangency condition is applied at these points.

3.3.2 Constant u-Velocity and Constant Source Panel Solutions

An explanation of the basic solutions for the two types of panels will not be presented in this report. They are discussed in detail in Section 3.3.2 and Appendix II of Reference 1.

With the induced velocity expressions, or solutions, for the two types of panels known, it is possible to formulate the influence of a constant u-velocity panel of unknown strength and the influence of a constant source panel with known strength at any control point accounting for the region of influence inherent in supersonic flight. By considering interactions between all constant u-velocity panels laid out on the wing, pylon, and body interference shell, there results a set of simultaneous equations from which the unknown constant u-velocity panel strengths can be determined. This formulation will now be discussed.

3.3.3 Flow Tangency Boundary Condition

The flow tangency boundary condition states that there is no flow through the constant u-velocity panels on the wing, pylon, and interference shell at the control points. A few control points are shown in Figure 5. The tangency condition for a wing panel with dihedral, ϕ_v , is shown in Figure 6 and can be written in the wing coordinate system shown in Figure 5 as

$$\sum_{n=1}^{NPTOT} \left(\frac{w_{Wv,n}}{V_\infty} \cos \phi_v - \frac{v_{Wv,n}}{V_\infty} \sin \phi_v \right) = (\alpha_F + i_W + \alpha_{\ell_v}) \cos \phi_v$$

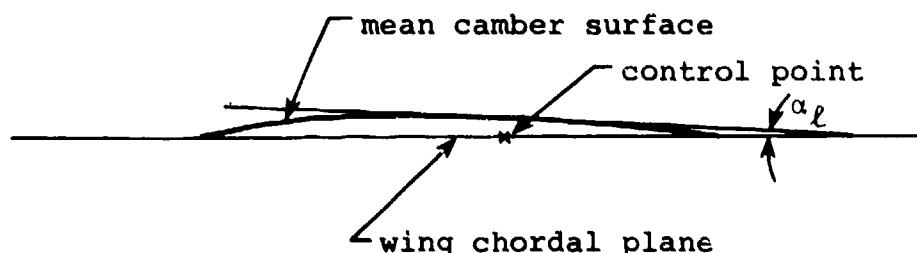
$$+ \frac{v_{Wi,v}}{V_\infty} \sin \phi_v - \left(\frac{u_{Wi,v}}{V_\infty} + \frac{w_{Wi,v}}{V_\infty} \right) \cos \phi_v$$

(24)

$$v = 1, 2, \dots, NPANLS$$

In the above equation NPTOT is the total number of u-velocity panels on the wing, pylon, and fuselage interference shell and NPANLS is the number on the wing.

The free-stream components are the fuselage angle of attack, α_F , and the wing incidence angle, i_W . Wing incidence is only included in the boundary condition in the computer program. The wing is not placed at incidence geometrically relative to the fuselage interference shell since Mach cones on the shell and the wing must be parallel to get a valid solution. This restricts the incidence to small angles. The angle $\alpha_{\ell v}$ is the local angle of attack due to wing twist and/or camber at the v^{th} control point as shown in the following sketch. The velocities $u_{Wi,v}$, $v_{Wi,v}$, $w_{Wi,v}$ are interference



velocities induced at the control points by the circular fuselage line sources and doublets or the noncircular fuselage source panels, wing thickness source panels when there is wing dihedral, and pylon thickness source panels. The velocities $v_{Wv,n}$, $w_{Wv,n}$ on the left-hand side of the equation are perturbation velocities induced at the control point by the constant u -velocity panels distributed over the wing, pylon, and fuselage interference shell.

The pylon boundary condition, also shown in Figure 6, is

$$\sum_{n=1}^{NPTOT} \frac{v_{Wv,n}}{V_{\infty}} = - \frac{v_{Wi,v}}{V_{\infty}} \quad (25)$$

$$v = NPNLS+1, NPNLS+2, \dots, NPNLS+MP$$

in the wing coordinate system. The velocities $v_{Wv,n}$ are perturbation velocities induced at the control point by the

u-velocity panels. The velocity v_{wi} is the sum of the interference velocities due to the circular fuselage line sources and doublets or the noncircular fuselage source panels and wing thickness source panels. The index MP is the number of u-velocity panels on the pylon.

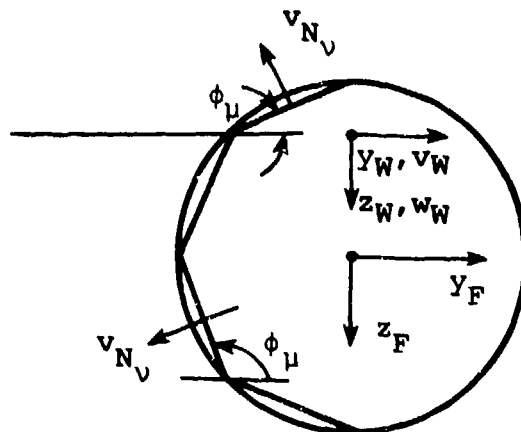
Similarly, letting $v_{Nv,n}$ be the perturbation velocity in the direction normal to the v^{th} body interference panel, the flow tangency condition states that the net velocity normal to the body interference panel is zero.

$$\sum_{n=1}^{NPTOT} \frac{v_{Nv,n}}{V_{\infty}} = \left(\frac{w_{wi,v}}{V_{\infty}} \cos \phi_{\mu} - \frac{v_{wi,v}}{V_{\infty}} \sin \phi_{\mu} \right) \quad (26)$$

$$v = NPANLS+MP+1, NPANLS+MP+2, \dots, NPTOT$$

$$\mu = v - NPANLS - MP$$

The right-hand side of the above equation represents the external induced perturbation velocity normal to the body interference panel under consideration. It contains interference velocities induced by source panels laid out on the wing and the pylon to model thickness. In this way, interference on the fuselage due to wing-pylon thickness is accounted for. Angle ϕ_{μ} is called the body panel orientation angle measured relative to a plane parallel to the (x_F, y_F) or (x_W, y_W) plane as indicated in the following sketch looking in



the positive x_F direction. The angle ϕ_μ shown in the sketch is a negative angle. Finally, the summation on the left-hand side of Equation (26) represents the perturbation velocity normal to the interference panel under consideration induced by all constant u-velocity panels. So far, the strengths of these panels are still unknown.

In the boundary conditions formulated above, advantage is taken of the fact that the $y_F = 0$ or $y_W = 0$ plane is a plane of symmetry. Panels are laid out over the left wing and pylon and only the left half of the fuselage is covered with interference panels. Perturbation velocities on both sides of Equations (24), (25), and (26) are induced not only by the panels to the left of the symmetry plane but also must contain contributions from the right half. The required procedure is discussed below in connection with the aerodynamic influence coefficients.

Next, it will be shown how the perturbation velocities are expressed in terms of aerodynamic influence coefficients. These coefficients relate the perturbation velocity components induced at some point by a constant u-velocity panel to its strength u_+/V_∞ and the coordinates of the point relative to the panel corners. A similar procedure relates the perturbation velocities at a field point to the known strength of a source panel.

3.3.4 Aerodynamic Influence Coefficients

Appendix II of Reference 1 contains the results of the theory for determining the perturbation velocities induced by a semi-infinite triangle subject to a constant jump condition in axial velocity. The appendix also specifies the perturbation velocities induced by a semi-infinite triangle with a constant strength source distribution. The results are given below in symbolic form. In terms of the coordinate system associated with the triangle shown in Figure 7, the perturbation

velocities due to a triangle with sweptback leading edge and with constant jump in u -velocity are expressed as follows.

$$\left. \begin{aligned} \frac{u}{V_{\infty}} &= \frac{1}{\pi} \left(\frac{u_+}{V_{\infty}} \right) F_u(x, y, z, \beta, \psi_{LE}) \\ \frac{v}{V_{\infty}} &= \frac{1}{\pi} \left(\frac{u_+}{V_{\infty}} \right) F_v(x, y, z, \beta, \psi_{LE}) \\ \frac{w}{V_{\infty}} &= \frac{1}{\pi} \left(\frac{u_+}{V_{\infty}} \right) F_w(x, y, z, \beta, \psi_{LE}) \end{aligned} \right\} \quad (27)$$

The quantity u_+/V_{∞} is the constant strength of the singularity distributed over the triangle. In fact, it is proportional to the axial velocity u_+ in the plane of the triangle ($z = 0$). The computer program has been arranged to predict axial velocity u_+ in the zero plane and requires a very small negative value for z to produce axial velocity u_- shown in Figure 7. The complete expressions for the perturbation velocities are given in Appendix II of Reference 1. Functions F_u, F_v, F_w are called influence functions and depend on coordinates x, y, z of the point at which the velocities are computed relative to the apex of the semi-infinite triangle shown in Figure 7. The influence functions can be determined from Appendix II of Reference 1, Equations (II-4) and (II-12), and depend on the leading-edge sweep ψ_{LE} and the factor β given in terms of the free-stream Mach number by

$$\beta = \sqrt{M_{\infty}^2 - 1} \quad (28)$$

Perturbation velocities induced by the semi-infinite triangle with constant source strength are related to a surface tangent, $\tan \theta$, to be discussed later, and the coordinates of the field point relative to the triangle apex. Employing the subscript t to indicate association with thickness, the perturbation velocities are expressed as

$$\left. \begin{aligned} \frac{u_t}{V_\infty} &= \frac{\tan \theta}{\pi} F_{u_t}(x, y, z, \beta, \psi_{LE}) \\ \frac{v_t}{V_\infty} &= \frac{\tan \theta}{\pi} F_{v_t}(x, y, z, \beta, \psi_{LE}) \\ \frac{w_t}{V_\infty} &= \frac{\tan \theta}{\pi} F_{w_t}(x, y, z, \beta, \psi_{LE}) \end{aligned} \right\} \quad (29)$$

Functions $F_{u_t}, F_{v_t}, F_{w_t}$ are the influence functions associated with the thickness and depend on coordinates x, y, z of the field point relative to the apex of the semi-infinite triangle such as the one with sweptback leading edge shown in Figure 7. These functions can be determined from Appendix II of Reference 1, Equations (II-15) and (II-16), and depend on the leading-edge sweep ψ_{LE} and the factor β given by Equation (28).

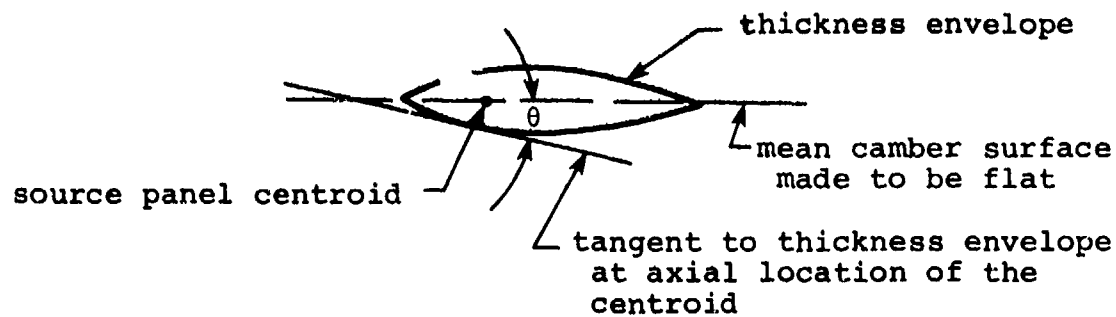
In order to formulate the perturbation velocities induced by a trapezoidal constant u-velocity panel, the superposition principle described in Section 3.3.2 of Reference 1 and depicted in Figure 4 of that reference must be employed. For example, for a panel with sweptback leading and trailing edges on the left wing, the upwash at the v^{th} control point induced by the n^{th} constant u-velocity panel in the coordinate system of the n^{th} panel is expressed as

$$\begin{aligned} \frac{w_{v,n}}{V_\infty} &= \frac{1}{\pi} \left(\frac{u_+}{V_\infty} \right) \left[F_{w_n}(x_{2,v}, -y_{2,v}, z_{2,v}, \beta, \psi_{LE}) \right. \\ &\quad - F_{w_n}(x_{1,v}, -y_{1,v}, z_{1,v}, \beta, \psi_{LE}) - F_{w_n}(x_{4,v}, -y_{4,v}, z_{4,v}, \beta, \psi_{TE}) \\ &\quad \left. + F_{w_n}(x_{3,v}, -y_{3,v}, z_{3,v}, \beta, \psi_{TE}) \right] \end{aligned} \quad (30)$$

The subscripted coordinates represent the coordinates of the control point relative to one of the four panel corner points. The numbering sequence of the corner points is kept consistent in its relation to the directions of the coordinate systems shown in Figure 4 of Reference 1. The leading-edge, and trailing-edge sweep angles of the panel are designated ψ_{LE} and ψ_{TE} , respectively. Here function F_w is defined in Equation (27). Similar expressions can be written for $u_{v,n}$ and $v_{v,n}$ using F_u and F_v , respectively. The left-hand sides of Equations (24), (25), and (26) require the velocities in the wing coordinate system. The transformation is

$$\left. \begin{aligned} \frac{u_{w,v,n}}{V_\infty} &= - \frac{u_{v,n}}{V_\infty} \\ \frac{v_{w,v,n}}{V_\infty} &= \frac{v_{v,n}}{V_\infty} \cos \phi_n + \frac{w_{v,n}}{V_\infty} \sin \phi_n \\ \frac{w_{w,v,n}}{V_\infty} &= \frac{v_{v,n}}{V_\infty} \sin \phi_n - \frac{w_{v,n}}{V_\infty} \cos \phi_n \end{aligned} \right\} \quad (31)$$

In a similar manner, the perturbation velocities induced by a trapezoidal constant source panel are obtained by means of a superposition scheme using the solutions for four semi-infinite triangles with their apexes at each of the panel corners. The source strength for one panel is given by the surface slope of the wing or pylon thickness distribution at the panel centroid. It is expressed as the tangent of the angle θ associated with the thickness envelope as shown in the following sketch. Therefore, the upwash due to thickness at the v^{th}



control point induced by the constant source panel with index nt on the left wing is expressed in the coordinate system of the nt^{th} panel as

$$\begin{aligned} \frac{w_{t,v,nt}}{V_\infty} = & \frac{\tan \theta}{\pi} F_{w_t,nt} \left(x_{2,v}, -y_{2,v}, z_{2,v}, \beta, \psi_{t,LE} \right) \\ & - F_{w_t,nt} \left(x_{1,v}, -y_{1,v}, z_{1,v}, \beta, \psi_{t,LE} \right) \\ & - F_{w_t,nt} \left(x_{4,v}, -y_{4,v}, z_{4,v}, \beta, \psi_{t,TE} \right) \\ & + F_{w_t,nt} \left(x_{3,v}, -y_{3,v}, z_{3,v}, \beta, \psi_{t,TE} \right) \end{aligned} \quad (32)$$

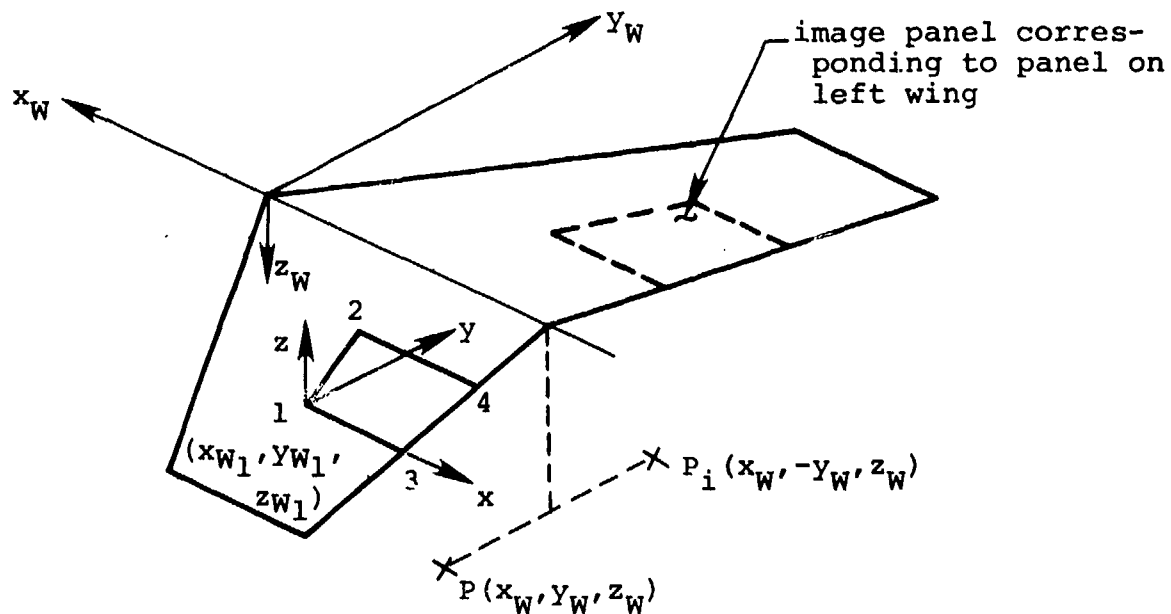
Here ψ_t pertains to the leading-edge or trailing-edge sweep of the constant source panel accounting for thickness. Similar expressions can be written for $u_{t,v,nt}$ and $v_{t,v,nt}$ in Equation (29) using F_{u_t} and F_{v_t} . The thickness panel induced velocities make up part of the $u_{wi,v}$, $v_{wi,v}$, and $w_{wi,v}$ terms on the right-hand sides of Equations (24), (25), and (26) in the wing coordinate system. The same transformation as was used in Equation (31) can be used to put $u_{t,v,nt}$, $v_{t,v,nt}$, and $w_{t,v,nt}$ into that system.

The bracketed terms in Equations (30) and (32) are the upwash aerodynamic influence coefficients associated with a

constant u-velocity panel and a constant source panel, respectively.

3.3.5 Symmetry Considerations

In order to account for the effects of the constant u-velocity and wing thickness source panels on the right half of the aircraft configuration, the perturbation velocity components induced by a panel on the left are augmented by a contribution from its image panel on the right. However, the following simplification is used. The effect of the image panel at a given point can be obtained using the panel on the left with a change in sign of the y_W or y_F coordinate of the point. The sidewash calculated this way at $P_i(x_W, -y_W, z_W)$ is then transformed back by a change in sign. The procedure is shown in the following sketch for a panel on the left wing half of a wing-alone configuration. The coordinate system (x, y, z)



associated with the semi-infinite triangle with its apex at corner 1 will be used. The panel lies in the x, y plane. It is the same as the coordinate system of Figure 7. The coordinates of point P relative to corner 1 (x_{W1}, y_{W1}, z_{W1}) are then given in the wing system by

$$\left. \begin{aligned} \Delta x_W &= x_W - x_{W1} \\ \Delta y_W &= y_W - y_{W1} \\ \Delta z_W &= z_W - z_{W1} \end{aligned} \right\} \quad (33)$$

Let the panel be at dihedral angle, ϕ_i , with respect to the y_W axis. Then the location of point P relative to corner 1 in the panel (x, y, z) system is

$$\left. \begin{aligned} x &= -\Delta x_W \\ y &= \Delta y_W \cos \phi_i + \Delta z_W \sin \phi_i \\ z &= \Delta y_W \sin \phi_i - \Delta z_W \cos \phi_i \end{aligned} \right\} \quad (34)$$

With these local coordinates, the direct influence of corner 1 at point P can be calculated. The influences of the other corners of the panel are added in accordance with the superposition scheme as indicated for the w component in Equations (30) and (32).

The location of the image point, P_i , in the wing coordinate system is

$$\left. \begin{aligned} \Delta x_W &= x_W - x_{W1} \\ \Delta y_W &= -y_W - y_{W1} \\ \Delta z_W &= z_W - z_{W1} \end{aligned} \right\} \quad (35)$$

and Equation (34) can again be used to locate this point in the panel system. The influence of corner 1 is now calculated at point P_i . The influences of the other corners of the panel are added in accordance with the superposition scheme. The resulting velocity components u, v, w in the panel system represent the influence of the panel on the left wing-half on the point P_i . With a change in the sign of the sidewash, v , they also represent the influence of the image panel on the point P . Thus, at a given point P there will be a direct influence induced by a constant u -velocity or constant source panel and an indirect effect induced by the image of the panel under consideration.

This method of accounting for symmetry is also applied to constant u -velocity and constant source panels on a wing-mounted pylon and the constant u -velocity panels on the fuselage interference shell. The influence functions required in Equations (30) and (32) and defined by Equations (27) and (29) for these panels are obtained from Appendix II of Reference 1, Equations (II-4), (II-12), and Equations (II-15), (II-16), using suitable transformations. For the pylon, a 90° counter-clockwise rotation about the x -axis (viewing upstream) places the semi-infinite triangles in the vertical plane and the influence functions can be determined. The superposition scheme gives the solution for a trapezoidal panel on the pylon. Effects of the image wing-mounted pylon panel are obtained in the manner described above for a panel on the wing. The same procedure is applied to the pylon source panels. The influence functions associated with a body interference panel are also obtained after performing a rotation about the x -axis. The angle of rotation is different for each panel and is related to the body orientation angle ϕ_μ mentioned earlier in connection with the boundary conditions. Image panel effects are accounted for using the same procedure as used for a panel on the wing.

The terms on both sides of Equations (24), (25), and (26) can now be specified. Equation (30) for w/V_∞ and a similar expression for v/V_∞ are used on the left-hand sides. These expressions give velocities in the coordinate system of the n^{th} panel while Equations (24), (25), and (26) require velocities in the wing coordinate system. The velocity transformation from the panel system to the wing system is

$$\left. \begin{aligned} \frac{u_{w,v,n}}{V_\infty} &= - \frac{u_{v,n}}{V_\infty} \\ \frac{v_{w,v,n}}{V_\infty} &= \frac{v_{v,n}}{V_\infty} \cos \phi_n + \frac{w_{v,n}}{V_\infty} \sin \phi_n \\ \frac{w_{w,v,n}}{V_\infty} &= \frac{v_{v,n}}{V_\infty} \sin \phi_n - \frac{w_{v,n}}{V_\infty} \cos \phi_n \end{aligned} \right\} \quad (36)$$

The $u_{wi,v}$, $v_{wi,v}$, and $w_{wi,v}$ terms in Equations (24), (25), and (26) are externally induced perturbation velocities. In Equation (24) for the wing they are the sums of the velocities induced at the v^{th} control point by the circular fuselage line sources and doublets or the noncircular fuselage source panels, the wing thickness source panels, and the pylon thickness source panels.

The circular fuselage induced velocities in the axial, radial, and tangential directions are given by Equation (16). The positive directions are shown in the sketch following the equation. The velocities are transformed into the wing coordinate system shown in Figure 5 using

$$\left. \begin{aligned}
 \frac{u_{Wi,v}}{V_\infty} &= - \frac{u_B}{V_\infty} \\
 \frac{v_{Wi,v}}{V_\infty} &= \frac{v_B}{V_\infty} \sin \theta + \frac{w_B}{V_\infty} \cos \theta \\
 \frac{w_{Wi,v}}{V_\infty} &= - \frac{v_B}{V_\infty} \cos \theta + \frac{w_B}{V_\infty} \sin \theta
 \end{aligned} \right\} \quad (37)$$

The noncircular fuselage induced velocities due to the source panels are calculated using the superposition scheme given by Equations (21) through (23) of Reference 8 and the velocity expressions given by Equations (88) through (95) which are multiplied by the panel strength. These velocities are in the panel coordinate system. The program extracted from Reference 7 rotates them into the body coordinate system shown in Figure 3 of this report. The signs on the u and w velocity components are changed to put them in the wing or fuselage coordinate system shown in Figure 5.

Wing and pylon source panel effects are given by Equation (32) for $w_{t,v,nt}$. Similar expressions can be written for $u_{t,v,nt}$ and $v_{t,v,nt}$ using F_{u_t} and F_{v_t} . These are velocities induced at the v^{th} control point by the nt^{th} panel in the coordinate system of the nt^{th} panel. They can be resolved into the wing system by

$$\left. \begin{aligned}
 \frac{u_{Wv,nt}}{V_\infty} &= - \frac{u_{v,nt}}{V_\infty} \\
 \frac{v_{Wv,nt}}{V_\infty} &= \frac{v_{v,nt}}{V_\infty} \cos \phi_{nt} + \frac{w_{v,nt}}{V_\infty} \sin \phi_{nt} \\
 \frac{w_{Wv,nt}}{V_\infty} &= \frac{v_{v,nt}}{V_\infty} \sin \phi_{nt} - \frac{w_{v,nt}}{V_\infty} \cos \phi_{nt}
 \end{aligned} \right\} \quad (38)$$

The total perturbation velocity induced at the v^{th} u-velocity panel control point by all of the wing and pylon thickness source panels are obtained by summing Equation (38) over all of the source panels.

The $v_{Wi,v}$ velocities appearing on the right-hand side of Equation (25), the pylon u-velocity boundary condition, are the sums of those induced by the circular fuselage line sources and doublets or noncircular fuselage source panels and the wing thickness source panels. The $v_{Wi,v}$ and $w_{Wi,v}$ velocities appearing in the fuselage interference shell boundary condition, Equation (26), are the sums of the wing and pylon thickness source panel velocities. These velocities are calculated in the manner just described for the wing.

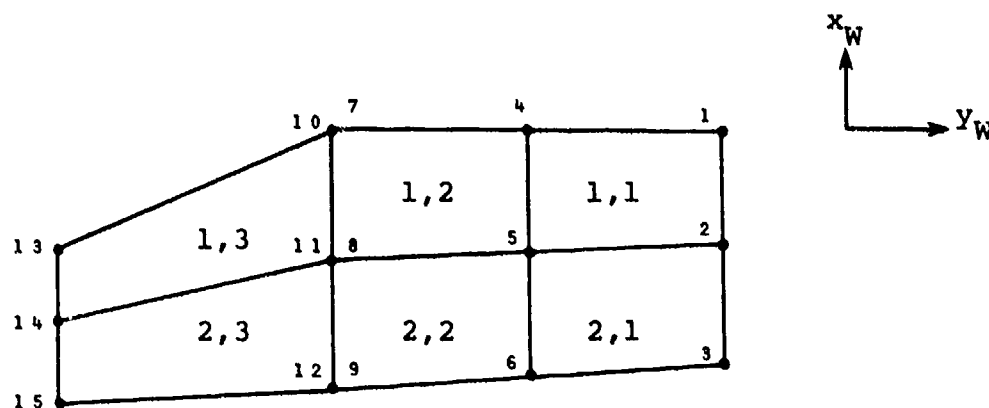
3.3.6 Solution for Constant u-Velocity Panel Strengths

After recasting the perturbation velocities on the left side of Equations (24), (25), and (26) in terms of the influence functions specified by Equation (27) and accounting for symmetry, there results a set of simultaneous equations in which the unknowns are the NPTOT values of panel strengths u_+/V_∞ . The values can be obtained through a matrix solution for given angle of attack, α_F , wing incidence angle, i_W , and Mach number, M_∞ .

3.3.7 Superposition Scheme for Flow-Field Calculations

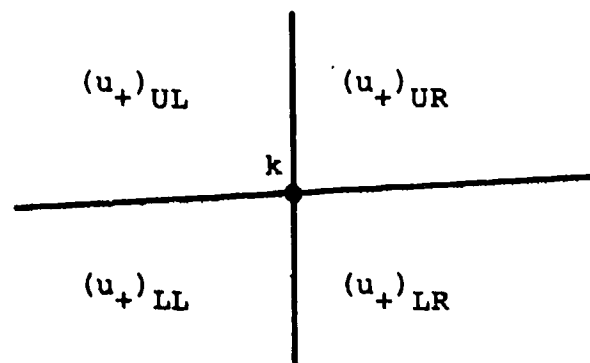
In the preceeding sections the solution for a constant u-velocity panel or thickness constant source panel, such as the cross-hatched one shown in Figure 5, is obtained through a superposition scheme using four semi-infinite triangles with their apexes at each of the four corners of the panel. At a given field point relative to the panel, the influence functions due to the triangles at the corners of a panel are calculated, summed, and multiplied by the panel strength. This is repeated sequentially for all panels. This scheme must be used when determining the strengths of the u-velocity panels.

Once the constant u-velocity panel strengths are known, a different superposition scheme can be used which eliminates many redundant influence function calculations. Consider the wing shown in the following sketch. Corner 5 is associated



with four panels so that using the four corner superposition scheme requires calculating the influence functions for that corner four times, once for each of the surrounding panels. This redundant calculation can be eliminated if the wing is represented by a series of corners and a net singularity strength calculated for that corner. In calculating velocities at a field point, the influence functions for the corner are calculated once and multiplied by the net strength.

The following sketch shows a corner k surrounded by four panels of known strength. The net strength of the u-velocity



panel singularity associated with this corner is

$$(\Delta u_+)_k = (u_+)_{UR} - (u_+)_{LR} - (u_+)_{UL} + (u_+)_{LL} \quad (39)$$

and for corner 5 in the previous sketch

$$(u_+)_5 = (u_+)_{1,1} - (u_+)_{2,1} - (u_+)_{1,2} + (u_+)_{2,2}$$

For corners which do not have panels in some of the quadrants surrounding the point, the strengths in those quadrants are treated as zero. Thus, for corner 1, for example,

$$(u_+)_1 = (u_+)_{LL} = (u_+)_{1,1}$$

and for corner 6

$$(u_+)_6 = (u_+)_{UR} - (u_+)_{UL} = (u_+)_{2,1} - (u_+)_{2,2}$$

The wing shown in the first sketch in this section has a break in leading edge sweep. Since the influence functions are functions of this angle, two rows of corner points are defined at this location, one associated with the panels to the left and the other associated with the panels to the right. In calculating the net strengths of corners 7, 8, and 9, the strengths of panels 1,3 and 2,3 are assumed to be zero. For example,

$$(u_+)_8 = (u_+)_{UR} - (u_+)_{LR} = (u_+)_{1,2} - (u_+)_{2,2}$$

Similarly, for corners 10, 11, and 12, the strengths of panels 1,2 and 2,2 are assumed zero. For corner 12

$$(u_+)_{12} = -(u_+)_{UL} = -(u_+)_{2,3}$$

This same procedure is followed at points where breaks in trailing-edge sweep angle or wing dihedral angle occur.

The procedure just described for the wing is followed for the pylon and fuselage u-velocity panel interference shell. The latter is treated like a wing with a change in wing dihedral angle at each panel side edge.

The superposition scheme just described for the constant u-velocity panels is also used for the wing and pylon thickness source panels. A net source panel strength is calculated for each corner.

4. NONLINEAR CORRECTION TO FLOW MODELS

The flow models described in Section 3 for the various parent aircraft components are based on supersonic, linear flow theory. Linear theory causes disturbances to travel along Mach waves determined only by the free-stream Mach number which was used in the solution for the singularity strengths. In actuality, the disturbances travel along curved Mach waves whose shapes are determined by the local Mach number variation along the waves. If straight linear theory is used in calculating the flow field under the aircraft in the region in which a separated store is immersed, parent aircraft disturbances will strike the store in the wrong location. This will cause errors in the calculated forces and moments.

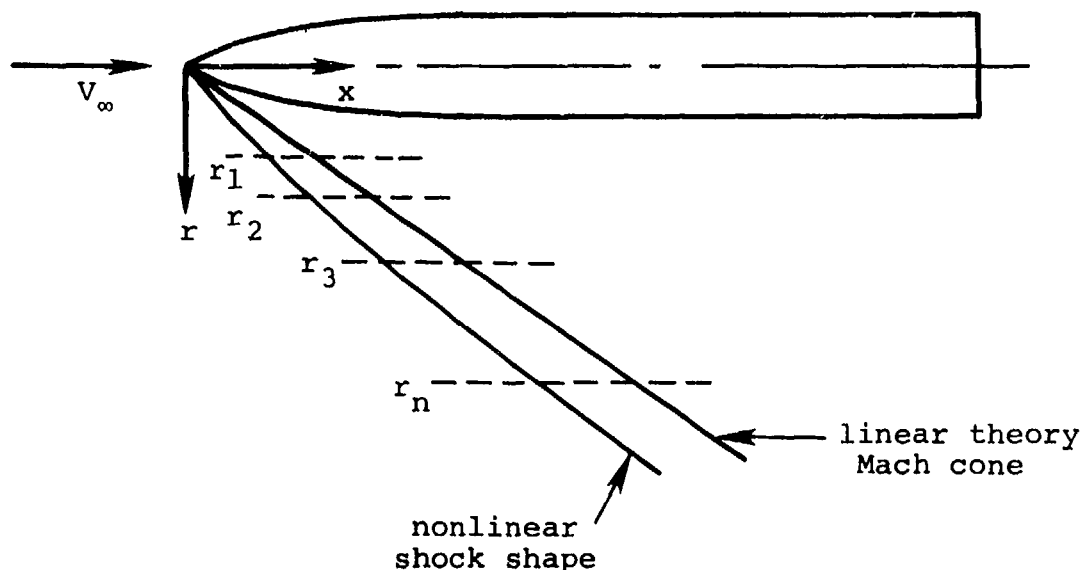
In order to place the disturbances, particularly shock waves, close to their correct locations a series of nonlinear corrections are made to the linear theory solutions. They are engineering corrections and have been selected because they require little computer time and seem to be quite accurate.

4.1 Body Shock Wave Shape

4.1.1 Circular Body

The procedure used to determine the shock wave shape for a circular or axisymmetric body will now be described. This method is used for the circular fuselage, the ejector rack, and the circular stores which are modeled by line sources, sinks, and doublets. Experimental data in Reference 6 show that a good approximation to the shock wave shape at angle of attack is to calculate it for the body at zero degrees angle of attack. This aligns the longitudinal axis of the axisymmetric shock wave with the free stream. The data show that at five degrees angle of attack there is little movement of the shock relative to the free stream.

The nonlinear axisymmetric shock wave shape is calculated in the manner which will now be described. Consider the following sketch which shows an axisymmetric body and the linear theory Mach cone originating at the body nose. The source-sink distribution modeling the body is calculated as



described in Section 3.2.1. The nonlinear shock shape is also shown in the sketch. It is curved. The slope of the shock at any radial point r is assumed to be determined by the stream-wise component, M_ℓ , of the Mach number immediately behind the shock. If the slope, β_ℓ , is known as a function of r , then the shape of the shock wave can be calculated from the following integral

$$x = \int_0^r \beta_\ell(r) dr \quad (40)$$

where $\beta_\ell = \sqrt{M_\ell^2 - 1}$. At the tip of the nose, $x = r = 0$, β_ℓ is determined from the shock wave angle for a cone with the

same angle as that at the tip of the nose of the body. This shock angle, θ , can be determined from Chart 5 of Reference 11. Then

$$(\beta_\ell)_{r=0} = \tan (90^\circ - \theta) \quad (41)$$

The values of β_ℓ at other values of r are determined from $M_\ell(r)$. At a given value of r , M_ℓ is calculated in a manner similar to that used in Section 3.4.1 of Reference 1 for the wing leading-edge shock wave. At a radial distance from the body axis, for example r_1 in the preceding sketch, the velocity field induced by the source-sink distribution is calculated beginning at the linear theory Mach cone location and extending a short distance downstream. From this velocity field, the maximum change in flow angle, Δv , is determined. It can be calculated using the source terms in Equation (16) and is

$$\tan \Delta v = \frac{|v_B/V_\infty|}{U/V_\infty} \quad (42)$$

where

$$\frac{U}{V_\infty} = 1 + \frac{u_B}{V_\infty} \quad (43)$$

The velocities u_B and v_B are the axial and radial perturbation velocities which are positive aft and outward, respectively. The change in flow angle, Δv , corresponds to a compression of the free-stream flow. Assuming that this compression is isentropic, the Prandtl-Meyer angle, v_1 , at the point where the maximum Δv occurs is

$$v_1 = v_\infty - \Delta v \quad (44)$$

Prandtl-Meyer angle ν_∞ is associated with the free-stream Mach number, M_∞ , and is given by Equation (171c) of Reference 11.

$$\nu_\infty = 2.4495 \tan^{-1} \left[0.40825 (M_\infty^2 - 1)^{1/2} \right] - \tan^{-1} (M_\infty^2 - 1)^{1/2} \quad (45)$$

In accordance with Reference 12, the Mach number associated with Prandtl-Meyer angle ν_1 can be determined most conveniently as follows:

$$\left. \begin{aligned} M_1 &= \frac{1 + 1.3604 p + 0.0962 p^2 - 0.5127 p^3}{1 - 0.6722 p - 0.3278 p^2} \\ p &= \left(\frac{\nu_1}{\nu_{\max}} \right)^{2/3} \\ \nu_{\max} &= \frac{\pi}{2} \left(\sqrt{\frac{\gamma+1}{\gamma-1}} - 1 \right) = \frac{\pi}{2} (\sqrt{6} - 1) \text{ for } \begin{matrix} M = \infty \\ \gamma = 1.4 \end{matrix} \end{aligned} \right\} \quad (46)$$

The author of Reference 12 claims 0.05-percent accuracy over the entire range of Mach number ($1 < M_1 < \infty$). The component of the Mach number, M_1 , in the axial free-stream direction, M_ℓ , is then given by

$$M_\ell = M_1 \cos \Delta\nu \quad (47)$$

The above calculation is repeated for a series of radial locations, such as r_2, r_3, \dots, r_n shown in the preceeding sketch, and then the nonlinear shock wave shape is calculated using Equation (40).

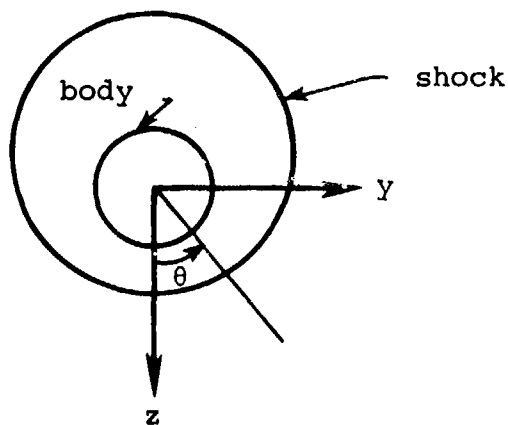
Shock wave shapes for an ogive-cylinder body calculated using the method just described are shown by the dashed curves in Figures 8 and 9. Also shown are the linear theory Mach cone and the shock wave shape calculated using an Euler equation computer program, Reference 13. The present method agrees

well with the Euler equation solution. In Figure 8 the horizontal bars show the shock wave location as estimated from the experimental flow-field data of Reference 6. Flow field measurements were made every 0.25 inch. The bars represent the two bracketing data points. The present method shows good agreement with the data. The crosses in Figures 8 and 9 are shock wave shapes calculated using the source panel method. This will be described in the next section.

It was mentioned previously that with a body at angle of attack there is little movement of the shock wave relative to the free-stream when compared with the shock wave produced by the body at zero degrees angle of attack. Since the shock wave shape calculated in the manner just described is for the body at zero degrees angle of attack, a transformation is required to locate a point on the shock wave in the body coordinate system with the body at angle of attack. Let x_0 and r_0 be the coordinates of a point on the shock at $\alpha = 0^\circ$. The coordinates x_α and r_α in the body system at angle of attack are

$$\left. \begin{aligned} x_\alpha &= x_0 \cos(\alpha \cos \theta) + r_0 \sin(\alpha \cos \theta) \\ r_\alpha &= -x_0 \sin(\alpha \cos \theta) + r_0 \cos(\alpha \cos \theta) \end{aligned} \right\} \quad (48)$$

where θ is measured as shown in the following sketch



The $\cos \theta$ variation is used so that correct motion of the shock relative to the body is obtained.

4.1.2 Noncircular Body

The shock wave shape for a noncircular body, noncircular fuselage or elliptic store, is calculated in the same manner as was just described for a circular body. The circular body shock wave is axisymmetric so the shape is only calculated in one meridian plane. For a noncircular body the shape is not axisymmetric so it is calculated in a number of meridian planes.

The shock wave shape for the noncircular fuselage is calculated from the velocities induced by the body source panels whose strengths are determined with the fuselage at angle of attack. Thus, a transformation similar to that given by Equation (48) is not required. The velocities used in the shock shape calculation are in the wind axis system. Let these be u' , v' , and w' . They are determined from those calculated in the body axis system of Figure 3 by

$$\left. \begin{aligned} u' &= u \cos \alpha + w \sin \alpha \\ v' &= v \\ w' &= -u \sin \alpha + w \cos \alpha \end{aligned} \right\} \quad (49)$$

Then Equations (42) and (43) are replaced by

$$\tan \Delta v = \frac{\sqrt{v'^2 + w'^2}/V_\infty}{U/V_\infty} \quad (50)$$

where

$$\frac{U}{V_\infty} = 1 + \frac{u'}{V_\infty} \quad (51)$$

The shock wave shape for the elliptic store is calculated with the store at $\alpha = 0^\circ$, that is, the source panel strengths were calculated for $\alpha = 0^\circ$. Thus, the velocities in the wind axis system are equal to those in the body system of Figure 3.

$$\left. \begin{aligned} u' &= u \\ v' &= v \\ w' &= w \end{aligned} \right\} \quad (52)$$

The shock shape is calculated using the method of Section 4.1.1 with Equation (50) and (51) replacing Equations (42) and (43).

Since the elliptic store shock wave shape is calculated for $\alpha = 0^\circ$, a transformation is required to locate a point on the store shock wave in the body coordinate system when the store is at angle of attack. The transformation used is

$$\left. \begin{aligned} x_\alpha &= x_0 \cos \alpha' + r_0 \sin \alpha' \\ r_\alpha &= -x_0 \sin \alpha' + r_0 \cos \alpha' \end{aligned} \right\} \quad (53)$$

where

$$\alpha' = \alpha(1 - \epsilon_\alpha) \cos \theta \quad (54)$$

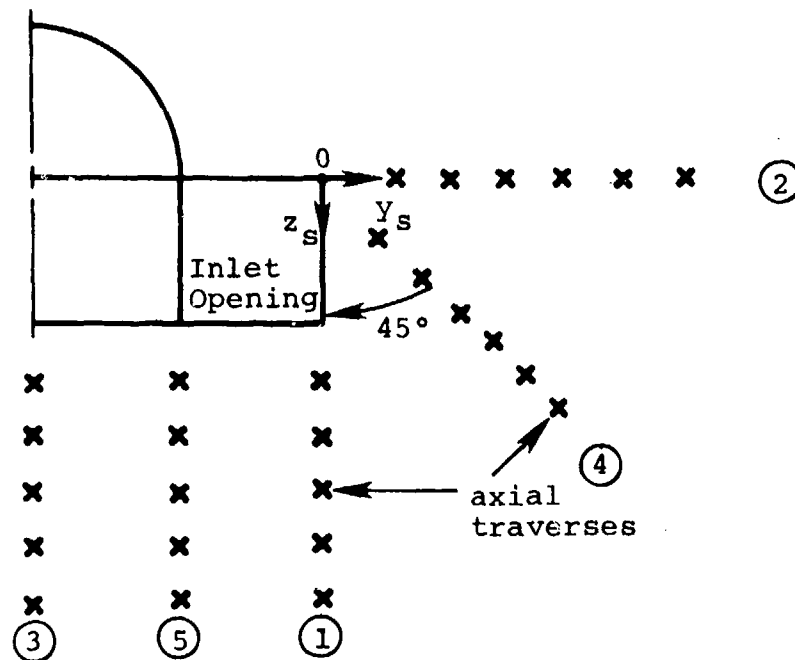
and is similar to Equation (48). The additional factor $(1 - \epsilon_\alpha)$ appearing in the expression for α' is taken from Reference 14. The parameter ϵ_α defines the amount of deviation from a full rotation of the shock about store nose as it goes to angle of attack. This factor is strictly applicable only to a cone. A plot of ϵ_α as a function of cone semi-apex angle, δ_c , and Mach number, M_∞ , is presented in Figure 10.

The accuracy of the shock wave shape calculated for a body modeled by source panels is shown in Figures 8 and 9. The ogive-cylinder body was modeled by source panels. The shock wave shapes are well predicted.

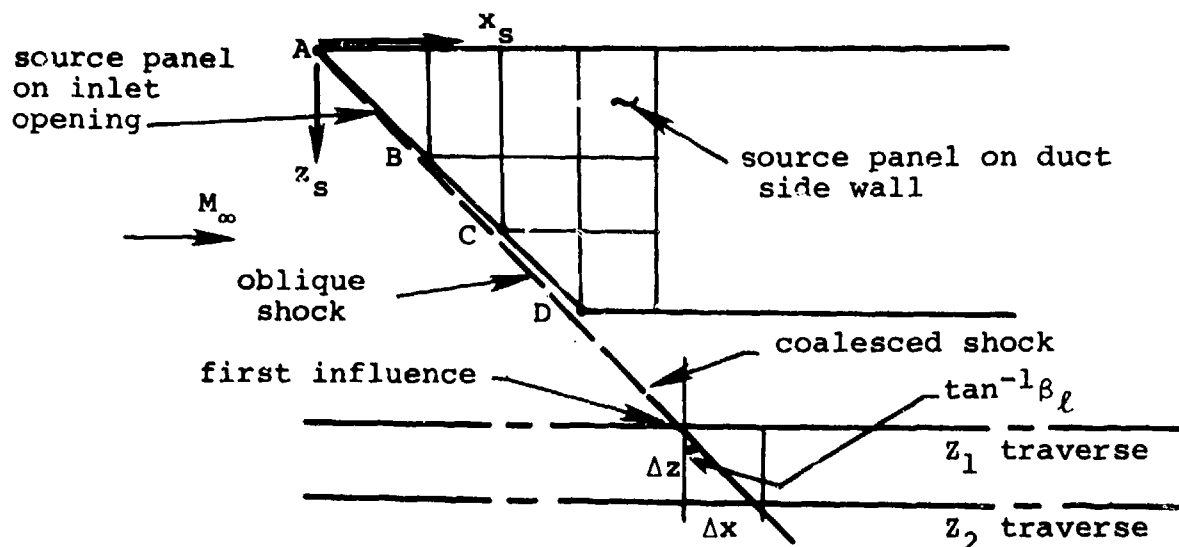
4.2 Inlet Shock Wave Shape

The noncircular fuselage and engine inlets are modeled by source panels as described in Sections 3.2.3 and 3.2.4. Once the panel strengths are known, an approximate shape of the shock system associated with the inlets can be determined in a way which will now be described. It will be assumed that the flow ahead of the inlets is at free stream conditions and that the shock shape depends on the local inlet configuration details only. Inlet induced effects are scanned along strategically located axial traverses for the maximum downwash velocity component. The approximate shape of the shock system is then determined from an integration scheme. The objective is to generate a table containing coordinates of the shock shape for the inlet flow conditions at hand.

Consider first the zero-blockage case, i.e., the inlets are "flowing full" and operate on design. The flow field is calculated at points along traverses laid out parallel to the centerline of the parent aircraft. A set of planes containing axial traverses are shown in the cross flow plane for a simplified fuselage inlet in the following sketch. Plane ①



contains traverses parallel to the duct outboard wall, in plane ② they are outboard along the extension of the ramp leading edge, and in plane ③ the traverses run parallel to the fuselage centerline. Traverses are located in plane ④ passing through the upper outboard corner of the inlet opening and those traverses in plane ⑤ lie in the plane of the inboard duct wall. The length of the traverses are made to cover the range of influence of the inlets. In these flow field calculations, the only effects included are those of the source panels laid out on the inlet opening and the panels on the upper, lower, and outboard duct walls sharing corner points with the panels on the opening. The object is to proceed along each traverse and determine the first influence from inlet source panels. The Prandtl-Glauert factor, β_I , associated with the inlet panels and their immediate neighbors on the duct walls is given by Equation (20) so that the region of influence of a given shared corner (A,B,C, or D) is the same. In the sketch below, the first influence comes from corner A. It is followed



in rapid succession by influences from corners B, C, and D. Over this short range, the maximum in the quantity $V_{C_{max}}^2$ is searched for.

$$V_{C_{max}}^2 = \frac{(v^2 + w^2)}{V_{\infty}^2} \quad (55)$$

Here, v and w are the perturbation velocities induced by the set of source panels on the inlet and the panels on the side walls nearest the inlet face. The shock "surface" for the full flow case is then laid as follows. In the region below the fuselage and inlets, the shock is assumed to be attached to the cowl lip and its inboard extension. Actually, it is the continuation of the oblique shock which is taken slightly ahead of the cowl lip. In planes 2 and 4, the shock starts from corner O shown in the first sketch. The shape of the shock surface in the vertical and other planes is then computed from the calculated "shock slope."

$$\text{slope} = \left. \frac{\Delta x_s}{\Delta z_s} \right|_{\text{shock}} = \beta_{\ell} \equiv \sqrt{M_{\text{local}}^2 - 1} \quad (56)$$

Referring to the preceeding sketch, the perturbation velocities associated with $V_{C_{max}}$, Equation (55), are used to compute a local Mach number for a given traverse. The approximate method used to accomplish this is based on Prandtl-Meyer compression and is described in Section 4.1.1. Knowing the local Prandtl-lauert factor, β_{ℓ} , for several traverses allows the calculation of the shock shapes in a given plane in accordance with the following integration

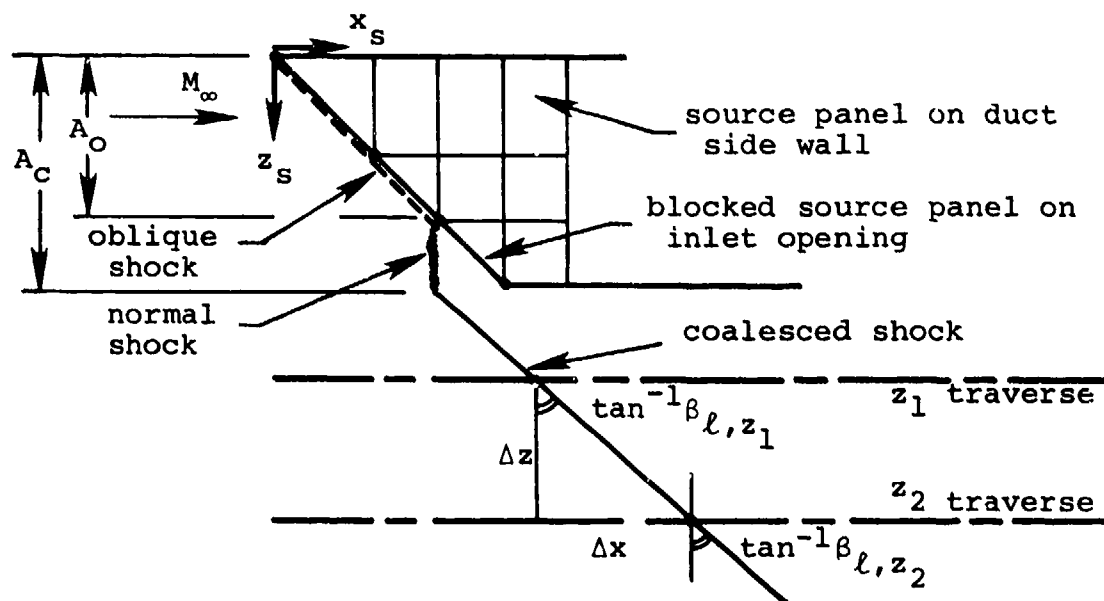
$$x_s = \int_{z_1}^{z_2} \beta_{\ell, \text{average}} dz_s \quad (57)$$

For the first step, β_ℓ calculated for the first traverse is used in Equation (57). The shock shape integration is continued up to a specified number of traverses in the planes ① through ⑤ and continued until β_ℓ equals approximately β_∞ . In Equation (57), $\beta_{\ell, \text{average}}$ is obtained from

$$\beta_{\ell, \text{average}} = \frac{\beta_{\ell, z_1} + \beta_{\ell, z_2}}{2} \quad (58)$$

It is clear that in essence this shock determination method is analogous to the method for computing body nose shocks described in the preceding sections of this report. Tables containing (x_s, y_s, z_s) coordinates are calculated for all 5 traverse planes shown in an earlier sketch. Interpolation schemes are set up to specify the shock surfaces in between the traverse planes. Above the traverse plane ②, the inlet effects are assumed to propagate along free-stream Mach cones.

Now consider the partial blockage case with the inlet operating on design over the upper portion of the inlet opening. We will first treat the shock shapes in the vertical planes ①, ③, and ⑤. Refer to the following sketch and the first sketch in this section. In the inlet opening, the lowest



panel is blocked and has associated with it the flow tangency condition, Equation (23). The following simplifying assumption is made. The normal shock protrudes down from the most forward leading edge of the blocked panels. From its intersection with the extension of the duct wall, the coalesced shock surfaces are determined in the manner described above for the unblocked or full flow case. In planes ② and ④, the shock shapes are obtained from the integration starting from the upper outboard corner O.

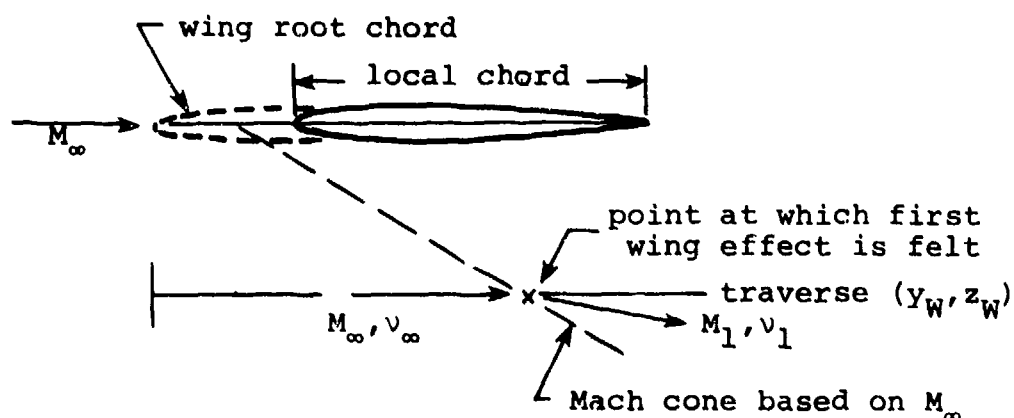
4.3 Wing Shock Wave System

The nonlinear correction used to position the wing shock wave system is a modification and extension to that described in Section 3.4 of Reference 1. In that reference only the wing leading-edge shock wave was considered. In the present work a correction is also made to position the expansion associated with the wing trailing-edge in the correct location. The assumption is made, as in Reference 1, that the shock patterns from the leading and trailing edges depend on wing thickness only and rotate with the wing at angle of attack. This assumption is based on experimental evidence as discussed in Section 5.2 of Reference 1.

The wing coordinate system is shown in Figure 5. For a given field point (x_w, y_w, z_w) under the wing at which the flow field is to be calculated, an axial traverse is laid out parallel to the x_w axis at coordinates y_w, z_w . The nonlinear correction to linear theory to be described determines the Mach number behind the leading-edge shock wave and determines the shock location along the traverse as well as the Mach number just ahead of the trailing edge shock and the shock location along the traverse. Let us first consider the leading edge correction.

The perturbation velocities due to wing thickness are calculated using the linear theory method described in Section 3.3.4. For example, the upwash velocity due to one source

panel is given by Equation (32). The velocities are calculated along the traverse beginning at the root-chord leading edge and extending to the point where the wing effect is first felt as shown in the following sketch. Once this point is found a



careful search is made downstream of this point for the maximum flow angle Δv where

$$\tan \Delta v = \frac{\sqrt{v_W^2 + w_W^2}}{U} \quad (59)$$

and the total axial velocity, U , is given by

$$\frac{U}{V_\infty} = 1 - \frac{u_W}{V_\infty} \quad (60)$$

The velocities u_W , v_W , and w_W are the wing thickness induced velocities positive in the x_W , y_W , and z_W directions, respectively, shown in Figure 5. With Δv determined, Equations (44), (45), and (46) are used to calculate M_1 . The component of M_1 in the axial direction, which is associated with the wing leading edge, is then

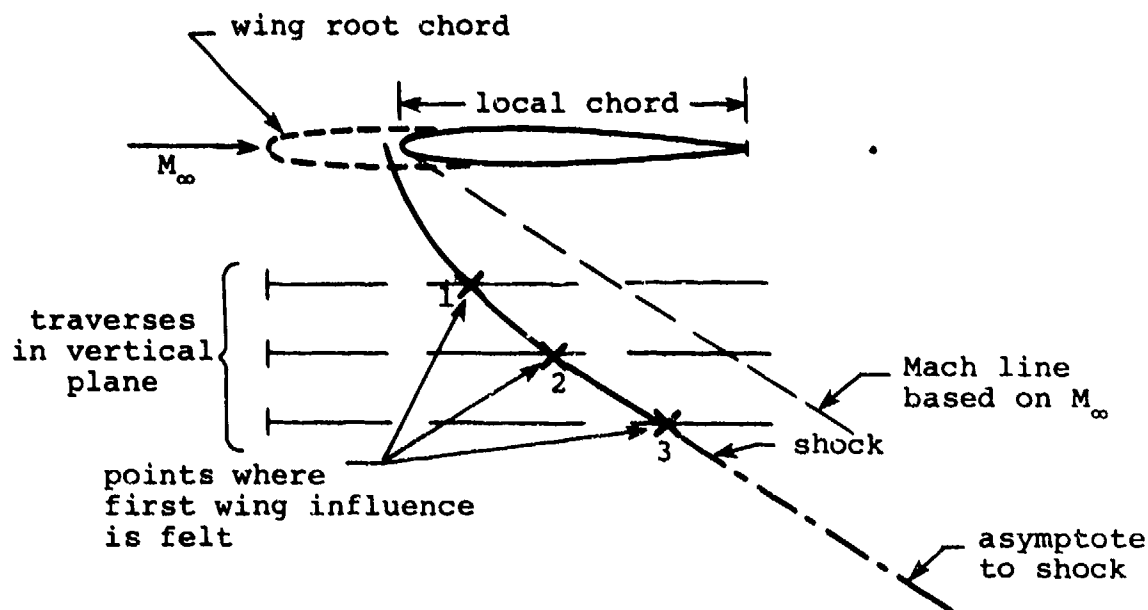
$$M_{le} = M_1 \cos \Delta v \quad (61)$$

This is the local Mach number which will be associated with the flow immediately behind the leading edge shock wave at this y_W, z_W location.

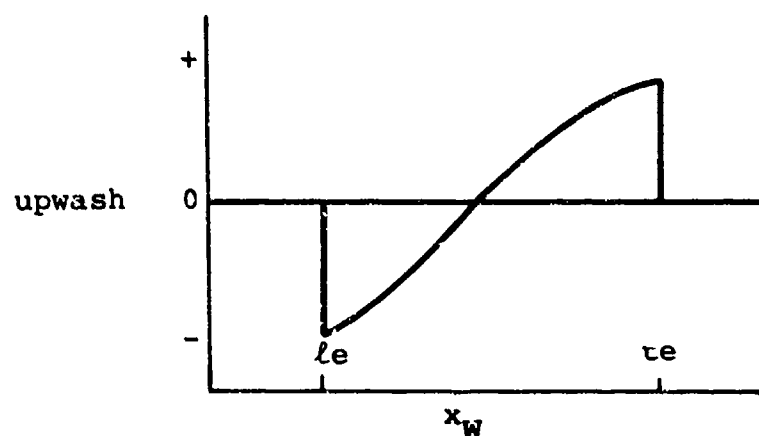
Under the assumption that the shape of the shock associated with the wing leading edge depends on wing thickness only, the scheme to be described next allows for the determination of the shock location. The assumption is justified by evidence offered by comparison with experimental data in Section 5.2 of Reference 1.

The summed effects of the source panels on the wing are computed again at points along the same axial traverse discussed previously. However, the Mach number used in this calculation is M_{le} calculated above instead of the free-stream value. The result is a velocity component profile similar in shape to the profile obtained on the basis of the free-stream Mach number but shifted in the upstream direction. In other words, the point on the x_W traverse where the first wing thickness effects are felt, x_{le} , now lies ahead of the point shown in the previous sketch.

Different local Mach numbers, M_{le} , can be calculated for additional traverses parallel to the x_W traverse and located in the same y_W plane using the method just described. After re-computing the flow field due to wing thickness along the traverses with the appropriate local Mach numbers, M_{le} , the points where the first influence is felt describe a locus which is taken as the shock shape. A typical result is indicated in the sketch below. Points 1, 2, and 3 are the locations where wing thickness effects are first calculated on the basis of local Mach numbers, M_{le1} , M_{le2} , and M_{le3} , respectively. The asymptote of the locus determined this way runs parallel to the Mach line based on the free-stream Mach number.



The Mach number just ahead of the wing trailing edge shock wave and the shock location at y_W, z_W are determined in a manner very similar to that used for the leading edge. The thickness induced upwash velocity distribution under a wing at constant y_W, z_W has the characteristic shape shown in the following sketch. Just behind the leading edge shock a down-



wash (negative upwash) exists which reduces with downstream distance. As the trailing edge shock wave is approached, upwash is produced which abruptly returns to zero after passing

through the shock. To determine the Mach number just ahead of the shock the linear theory wing thickness velocities are calculated along the x_w traverse and a search is made for the maximum flow angle, Δv , prior to the sudden drop in upwash velocity. Equation (59) and (60) are used to calculate Δv . This change in flow angle is treated as an expansion of the free-stream flow and the Prandtl-Meyer angle at this point is

$$v_1 = v_\infty + \Delta v \quad (62)$$

where v_∞ is given by Equation (45). Equation (46) is used to determine M_1 . The component of M_1 in the axial direction just ahead of the wing trailing-edge shock wave is taken to be

$$M_{te} = M_1 \cos \Delta v \quad (63)$$

The location of the trailing-edge shock wave is found by repeating the above search using Mach number M_{te} in the thickness velocity calculation. This time the point at which the upwash velocity drops, x_{te} , is searched for rather than the maximum flow angle. Since the flow is an expansion of the free-stream flow, $M_{te} > M_\infty$, x_{te} is downstream of the corresponding point calculated using straight linear theory. Comparisons with data to be presented later show the wing trailing-edge influence location to be well predicted.

The complete wing trailing-edge shock wave shape at a particular y_w can be determined by repeating the above calculations for a series of z_w positions as was done for the leading-edge shock wave.

4.4 Store Imaging

In the work of Reference 1 store-aircraft interference was accounted for by including store effects in the wing-fuselage-pylon u-velocity panel boundary condition. It was

found that to model accurately the reflection of the store nose shock wave an extremely large number of panels had to be distributed over the affected areas of the aircraft. In addition, the u-velocity panel strengths would have to be recalculated at each point in the trajectory since the point at which the store shock wave strikes the wing-fuselage-pylon combination would move and thus change the boundary condition.

To circumvent these situations an imaging scheme has been adopted in which the store shock-wave reflection is accounted for by imaging the store above the wing and/or inside the fuselage. The imaging schemes will now be described. The methods of imaging the circular store modeled by line singularities with respect to the wing and fuselage will first be discussed. This will be followed by a similar discussion for the elliptic store which is modeled by source panels.

4.4.1 Circular Store Imaging

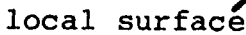
A sketch of the circular store wing imaging method is shown in Figure 11. This sketch shows the method for zero degrees angle of attack. At angle of attack the shock wave shape is assumed to be the same as at zero degrees angle of attack with the shock wave axis aligned with the free-stream velocity vector. The imaging scheme places the image store in a mirror image position relative to the local wing chordal plane. The first step is to determine the location at which the calculated store shock wave intersects the surface of the local airfoil section, that is, the section immediately above the store. To do this, the vertical distance, z_s shown in Figure 11, from the store nose to the local wing chordal plane is determined. Next, the point at which the store shock wave, calculated as described in Section 4.1.1, intersects this plane is found. If this point lies ahead of the local wing leading edge or behind the trailing edge, the store is not imaged. With this intersection point, x_{ws} , determined, the wing thickness slope distribution, $\tan \theta$, is integrated to determine the airfoil section half thickness at this point.

(64)

3

(65)

ir



De

(66)

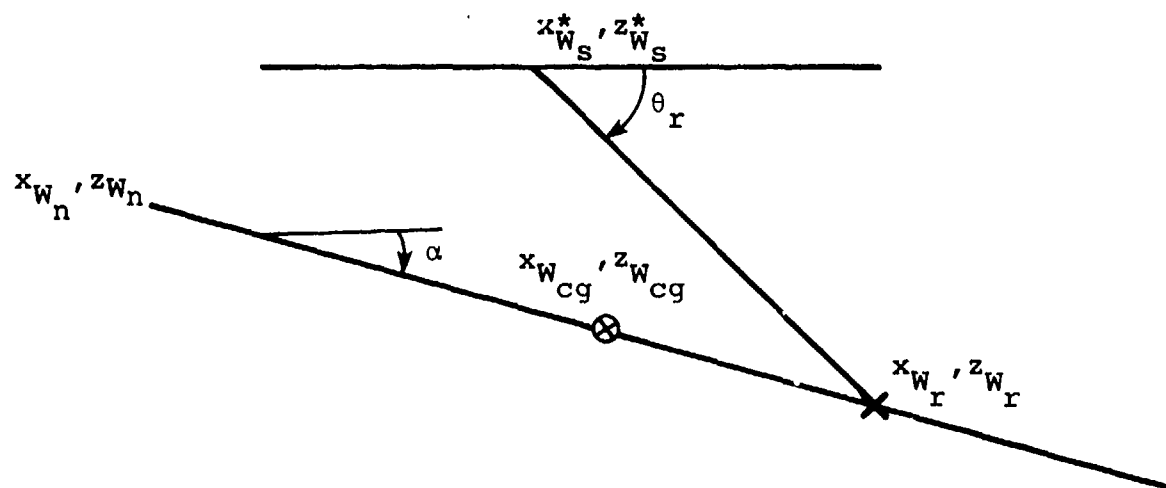
and

$$\theta_i = 90^\circ - \theta_s - \theta_t \quad (67)$$

The shock wave is assumed to reflect back at angle θ_i' , which is equal to θ_i . The reflection angle relative to the local x_W axis is

$$\theta_r = \theta_s + 2\theta_t \quad (68)$$

The point at which the reflected shock wave strikes the axis of the real store is determined in the following manner. In the local airfoil coordinate system the store nose is located at x_{Wn}, y_{Wn}, z_{Wn} as shown in the following sketch



The store center of gravity is also located in this system assuming zero yaw angle of the store, that is $y_{Wcg} = y_{Wn}$. Then with $z_{Ws}^* = t/2$, the equation of the straight reflected shock wave is

$$z_{Wr} = z_{Ws}^* + (x_{Ws}^* - x_{Wr}) \tan \theta_r \quad (69)$$

The equation of the line representing the store axis is

$$z_{W_r} = z_{W_n} + (x_{W_n} - x_{W_r}) \tan \alpha \quad (70)$$

where

$$\tan \alpha = \frac{z_{W_{cg}} - z_{W_n}}{x_{W_n} - x_{W_{cg}}} \quad (71)$$

If $\theta_r \leq \alpha$ there is no intersection and therefore no shock wave reflection. For $\theta_r > \alpha$ the intersection of the reflected shock wave and the store body axis is determined from Equations (69) and (70).

$$x_{W_r} = \left(\frac{1}{\tan \alpha - \tan \theta_r} \right) \left(z_{W_n} - z_{W_s}^* + x_{W_n} \tan \alpha - x_{W_s}^* \tan \theta_r \right) \quad (72)$$

$$z_{W_r} = z_{W_n} + \tan \alpha (x_{W_n} - x_{W_r}) \quad (73)$$

In the store coordinate system the point at which the reflected shock wave strikes the store x_s axis is

$$x_r = -(x_{W_r} - x_{W_n}) \cos \alpha + (z_{W_r} - z_{W_n}) \sin \alpha \quad (74)$$

To position the first influence of the image store, see Figure 11, at this location requires that the first source and doublets on the image store influence the flow field at x_r on the real store. This is accomplished by assigning the Mach cone angle β_N to the first singularities. As shown in Figure 11, $\beta_N = x_r/z_i$. Thus, the local Mach number which is associated with the nose is $M_N = \sqrt{\beta_N^2 + 1}$. When the store shoulder is reached it is assumed that the free-stream Mach number, M_∞ , characterizes the local flow. The shoulder is taken to be the point along the body where the local surface slope first becomes zero.

The strengths of the sources and doublets on the real store are calculated on the basis of linear theory using the method described in Section A.2 of Appendix A. They are calculated by starting at the nose and marching downstream. The boundary condition includes not only the free-stream component but also all of the parent aircraft induced velocities and, behind the reflected shock wave, those due to the image store. If the store is pitching and yawing, velocities due to this motion are also included. The image store singularity strengths are the same as those on the real store however the value of β used in the velocity calculations changes depending on location on the real store. Referring to Figure 11, β_N is used for the point at which the reflected shock wave strikes the real store axis and β_∞ is used at and aft of the point where the β_∞ Mach cone originating at the image store shoulder strikes the axis. Between these two points, the local Mach number, M_ℓ , is assumed to vary linearly with distance from $M_N = \sqrt{\beta_N^2 + 1}$ to M_∞ and the β used is $\beta_\ell = \sqrt{M_\ell^2 - 1}$. This provides a smooth transition from β_N to β_∞ as the calculation proceeds down the body.

A somewhat similar procedure is used for imaging the store inside the fuselage. A sketch of the imaging method is shown in Figure 12. The shock-wave reflection is calculated in the same way as was done for the wing imaging using the fuselage surface. With x_r determined, two stores are placed inside the fuselage using the method of Reference 15. The image store is placed at r^2/z_B and a center store is placed on the fuselage axis. The image store source strengths are set equal to those of the real store and the doublet strengths are reduced in accordance with Reference 15. That is

$$\left. \begin{aligned} \mu_{s_i} &= \mu_s \\ \mu_{D_i} &= \frac{r^2}{z_B^2} \mu_D \end{aligned} \right\} \quad (75)$$

The center store only has sources whose strengths are the negative of those on the real store.

$$\mu_{s_c} = -\mu_s \quad (76)$$

Since the reflected shock wave strikes the real store at x_r , the first singularities of both the image store and the center store must influence the flow field at this point. Thus, the Mach cone angles for the first singularities are

$$\left. \begin{aligned} \beta_{N_i} &= x_r / \left(z_B - \frac{r^2}{z_B} \right) \\ \beta_{N_c} &= x_r / z_B \end{aligned} \right\} \quad (77)$$

The Mach cone angle variation used on the image store is calculated in the same manner as described previously for wing imaging. The Mach cone angle variation used for the sources on the center store is calculated such that corresponding sources on the image store and center store influence the real store at the same point.

4.4.2 Elliptic Store Imaging

The imaging of an elliptic store, which is modeled by source panels, with respect to either the wing or fuselage is performed in a manner similar to that described in Section 4.4.1 for imaging a circular store with respect to the wing. For the elliptic store, fuselage imaging is also done with respect to a reflection plane. The source panels account for both volume and lift effects so that imaging using the circle theorem approach shown in Figure 12 is not applicable.

The elliptic store shock wave shape is not axisymmetric and is calculated as a function of meridian angle around the

store as described in Section 4.1.2. Since the store can be at arbitrary attitude relative to the wing, interpolation is performed in the calculated shape to define the shape in a plane defined by the store nose and the local streamwise airfoil section immediately above the nose. Once the shock shape in this plane is known the shock wave reflection is calculated in the same manner as described for the circular store wing imaging.

The strengths of the source panels on the real elliptic store are calculated as described in Section 3.2.6 which references Section 3.2.2. The boundary condition is given by Equation (17). The velocity $(W_N/V_\infty)_i$ in that equation is the velocity normal to the panel control point and now includes not only a component of the free stream but also components due to the parent aircraft, the image store, and the store yaw, pitch, and roll angular motions. The latter are damping velocities.

A typical source panel layout on an elliptic body is shown in Figure 3. The panel strengths are solved for by starting at the ring at the nose and marching downstream ring by ring. Velocities induced at a ring of control points by upstream rings of known panel strengths are included in the boundary condition. The determination of the β to use in the image store velocity calculation is identical to that described in the preceeding section for the circular store.

As was mentioned earlier, the elliptic store modeled by source panels is imaged inside the fuselage with respect to a reflection plane. To locate this plane the first step is to determine the shock wave shape to be used in the calculation. This is done in a manner similar to that used for the wing imaging. A plane is constructed which contains the store nose and the fuselage longitudinal axis. Interpolation in the tabulated shock wave shape is performed to determine the shock wave shape in this plane. The intersection of the shock with

the fuselage surface is calculated. This determines the location of the reflection plane relative to the store nose. This reflection plane is treated like the wing chordal plane for wing imaging. At the point where the shock wave strikes the fuselage surface, the shock wave slope and the fuselage surface slope are determined. The location at which the reflected shock wave strikes the real store body is calculated as for wing imaging with the fuselage surface slope replacing the wing thickness envelope slope. The strengths of the source panels are calculated in the manner just described for the wing imaged elliptic store.

5. PARENT AIRCRAFT FLOW-FIELD CALCULATION

This section of the report will describe the procedure used to calculate the parent aircraft induced flow field at a field point such as a point on a separated store during a trajectory calculation. For the present discussion the parent aircraft is defined to be all aircraft components except the store whose trajectory is to be calculated. The linear theory potential flow methods used to model the various aircraft components were described in Section 3. Nonlinear corrections to these methods which are made to position shock waves properly were described in Section 4.

The velocities will be calculated in the fuselage coordinate system shown in Figure 5, the inertial coordinate system used in the trajectory calculation. For each aircraft component the field point is located in the coordinate system associated with the component. The velocities are calculated in that coordinate system and then resolved into the fuselage system.

5.1 Circular Fuselage

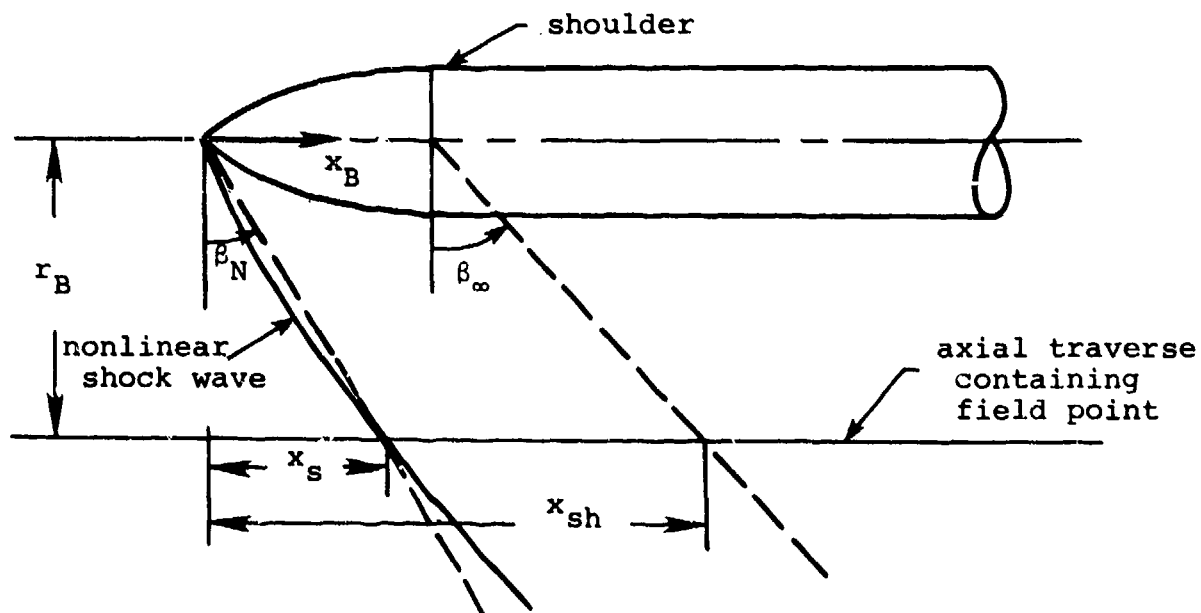
The first step in calculating the velocities at a field point is to calculate the velocities due to the fuselage. If the fuselage is circular and modeled by line singularities, Equation (16) gives the axial, radial, and tangential velocities at point (x_B, r_B, θ) . This coordinate system is shown in the sketch at the end of Section 3.2.1 and is related to the fuselage system by

$$\left. \begin{aligned} x_F &= -x_B \\ y_F &= r_B \sin \theta \\ z_F &= -r_B \cos \theta \end{aligned} \right\} \quad (78)$$

The velocities u_B , v_B , and w_B in Equation (16) are transformed to velocities in the fuselage system by

$$\left. \begin{aligned} u_F &= -u_B \\ v_F &= v_B \sin \theta + w_B \cos \theta \\ w_F &= -v_B \cos \theta + w_B \sin \theta \end{aligned} \right\} \quad (79)$$

The linear theory source and doublet constants, K_n and $K_{d,n}$, are used in Equation (16) but, because of the nonlinear shock-wave shape calculated as described in Section 4.1.1, the Prandtl-Glauert factor β will not always be that associated with the free-stream Mach number. Consider the following sketch



which shows the plane formed by the field point and the fuselage longitudinal axis. The nonlinear shock wave in this plane is also shown and intersects the axial traverse containing the field point at x_s . To cause the first influence of the fuselage to occur at this point, the Mach cone angle for the first singularities must be $\beta_N = x_s/r_B$. If the field point were at

this point, β_N would be used in Equation (16). Downstream of x_s the flow is assumed to return to the free-stream Mach number, M_∞ . The location on the traverse at which this occurs is taken to be the point at which a free-stream Mach cone originating at the shoulder location strikes the traverse, x_{sh} . If the field point is downstream of x_{sh} then $\beta_\infty = \sqrt{M_\infty^2 - 1}$ is used in Equation (16).

For field points between x_s and x_{sh} the β to use in Equation (16) is determined by linear interpolation in the Mach numbers at these two points, $M_N = \sqrt{\beta_N^2 + 1}$ and M_∞ , for M_ℓ where

$$M_\ell = M_N + (M_\infty - M_N) \left(\frac{x_B - x_s}{x_{sh} - x_s} \right) \quad (80)$$

and

$$\beta = \sqrt{M_\ell^2 - 1} \quad (81)$$

5.2 Ejector Rack and Circular Stores

The velocities induced at a field point by an ejector rack or circular stores modeled by line singularities present on the parent aircraft are calculated in the same manner as has just been described for the circular fuselage. The field point is located in the coordinate system of a particular body and the β to be used in Equation (16) is determined. After the axial, radial, and tangential velocities are calculated, they are resolved into axial, lateral, and vertical components in the body coordinate system and then transformed to components in the fuselage system.

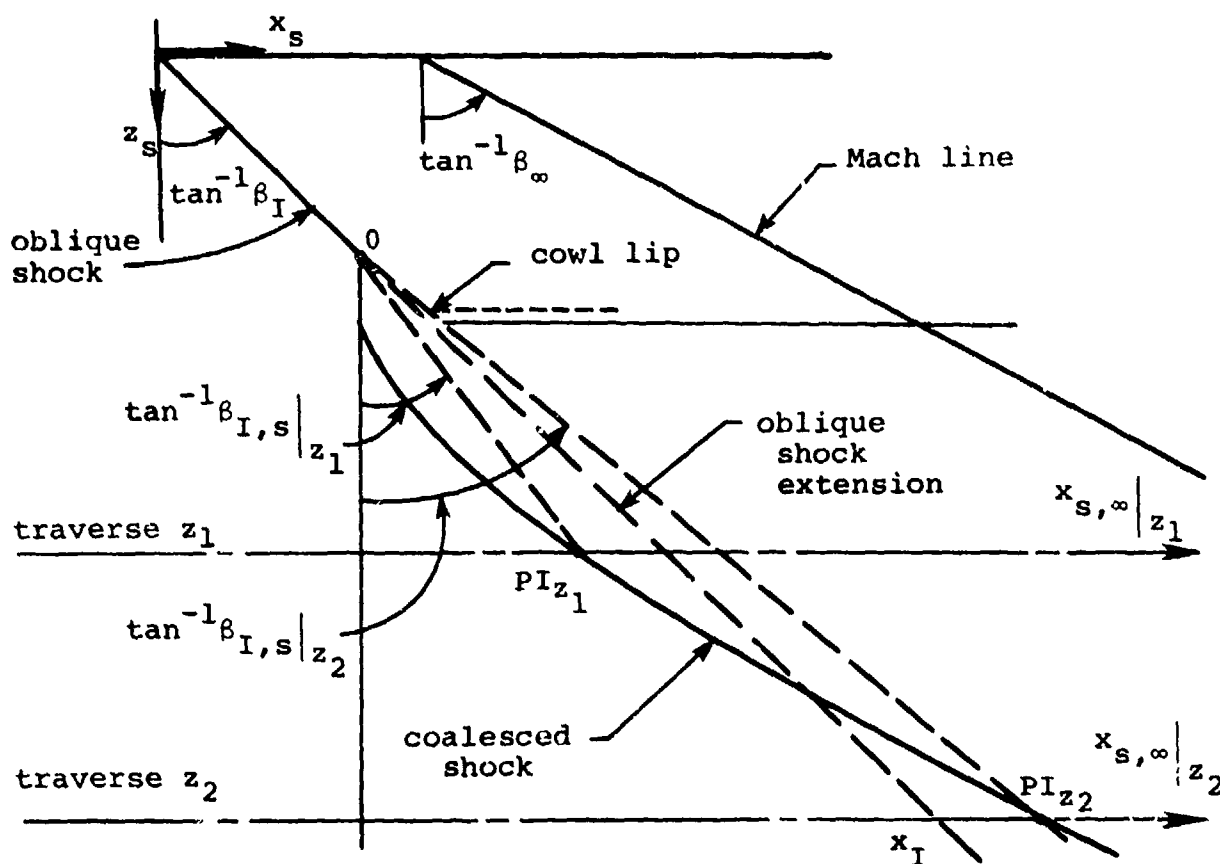
5.3 Noncircular Fuselage

The noncircular fuselage induced velocities are calculated as described in Section 3.5 in the paragraph following Equation (37). The value of β to be used in the calculation is determined in the same way as for the circular fuselage. The source panel strengths calculated on the basis of linear theory are used. The nonlinear shock wave shape in the plane containing the field point and the fuselage longitudinal axis is found by interpolation in the shock wave shapes which were calculated in the manner described in Section 4.1.2.

5.4 Engine Inlets

If the noncircular fuselage has engine inlets, the effect of the inlet shock wave on the flow field must be accounted for. The flow model for the inlets was described in Section 3.2.3 and the calculation of the inlet shock wave system discussed in Section 4.2. At field points ahead of the inlet shock wave the flow field produced by the noncircular fuselage is calculated as described in the preceding paragraph. When the field point lies on or behind the inlet shock the procedure to be described is used.

At points in the region affected by the fuselage mounted inlets, the flow field velocities are determined including effects of the inlet shock. In many ways the procedure resembles the one employed for body-nose shocks described previously in this section. Consider the case shown in the sketch below. A coalesced shock emanates from the inlet opening corresponding to the partially blocked case. The unblocked or full-flow inlet is a degenerate form of the situation shown. These two different conditions can occur within the framework of the shock determination method discussed in Section 4.2. We will consider velocity traverses



in the vertical planes ①, ③, and ⑤ shown in the first sketch in Section 4.2 but the method applies to the other planes as well.

For a given axial traverse, the point of intersection with the inlet shock is determined using the shock surface coordinates calculated by the method described earlier. These points, designated PI_{z_1} and PI_{z_2} in the sketch, can lie ahead or aft of the oblique shock extension. Point 0 is the leading edge, in sideview, of the blocked panels on the inlet opening nearest the cowl lip. For the unblocked or full flow case, point 0 is taken at the ramp leading edge. This point would also be used for the fully blocked case. As such this point is the

origin of the shock system associated with the inlet for both cases. The procedure is to determine a Prandtl-Glauert factor $\beta_{I,s}$ to position the inlet shock influence in the correct location and to return the flow downstream to the free-stream value β_∞ . For points along the traverse between these two points a single value of β_ℓ will be used for all fuselage and inlet panels until β_ℓ becomes equal to β_I , the oblique shock Mach cone angle. Downstream of this point β_I will be used for the inlet panels and β_ℓ for the fuselage panels.

First consider traverse z_1 shown in the sketch. Here the traverse intersects the shock ahead of the oblique shock extension. This intersection point, PI_{z_1} , gives the first or starting value of β_ℓ , $\beta_{I,s}$. It is obtained geometrically by connecting the intersection point PI_{z_1} to shock origin O . At points on the traverse behind the shock, the value of the factor β_ℓ is made to linearly vary from the starting value to β_∞ . The length over which this variation occurs ranges from intersection point PI_{z_1} to an end point fixed as follows. A β_∞ Mach line is drawn from a point on the duct upper surface located axially at the cowl lip location, refer to the previous sketch. This Mach line lies in the same vertical plane as the traverse under consideration, and the point of their intersection with axial coordinate $x_{s,\infty}$ is the point where β_ℓ equals β_∞ . The effects of all source panels distributed on the fuselage and inlet opening are then calculated by this method at points along a traverse such as z_1 .

A slightly different approach is required when the point of intersection PI_z lies aft of the oblique shock extension, as is the case for traverse z_2 shown in the sketch. The Prandtl-Meyer factor is still determined by the method just described. However, since the line connecting PI_{z_2} to O now lies aft of the oblique shock extension (or the β_I line), the source panels on the inlet face will not allow a solution with $\beta_{I,s}|_{z_2}$. To circumvent this problem, the axial coordinates of

points on the traverse on and behind the shock are mapped forward in accordance with

$$x_{s,map} = x_{s,\infty} + \left(\frac{x_I - x_{s,\infty}}{x_{PI} - x_{s,\infty}} \right) (x_s - x_{s,\infty}) \quad (82)$$

where x_I is the axial coordinate of the intersection point of the traverse and the extension of the oblique shock or β_I line. This mapping is done in order that the inlet shock will be present below the point at which the nonlinear shock crosses the β_I line. The velocities calculated at these mapped points are assumed to be those at the unmapped points.

5.5 Elliptic Stores

The velocities induced at a field point by a store modeled by source panels, the elliptic store model, are calculated in the same manner as described in Section 5.3 for the noncircular fuselage. The field point is located in the store coordinate system and then the plane containing this point and the store longitudinal axis is defined. The shock wave shape in this plane is determined by interpolating in the shock wave shapes calculated by the method described in Section 4.1.2. The linear theory panel strengths are used in the velocity calculation. The value of β to use is determined in the same manner as was described for the circular fuselage in Section 5.1. After the velocities are calculated in the store coordinate system they are transformed to the fuselage coordinate system.

5.6 Wing, Pylon, and Fuselage Interference Shell

The method used to calculate the velocities due to the wing, pylon, and fuselage interference shell will now be described. The wing leading edge and trailing-edge shock wave

locations x_{le} and x_{te} , and the Mach numbers, M_{le} and M_{te} , at these locations are determined by the method described in Section 4.3. The velocities due to wing and pylon thickness and the u-velocity panels on the wing, pylon, and fuselage interference shell are calculated as described in Section 3. The linear theory panel strengths are used and, for the pylon, β_{∞} is used for all field points.

For the wing and fuselage interference shell the value of β_l to be used is determined in the following manner. If the field point is downstream of x_{te} , β_{∞} is used. If the field point lies between x_{le} and x_{te} the value of β_l is determined by linear interpolation in the Mach numbers at these two points. Thus, at field point x ,

$$M_l = M_{le} + \left(\frac{x - x_{le}}{x_{te} - x_{le}} \right) (M_{te} - M_{le}) \quad (83)$$

and

$$\beta_l = \sqrt{M_l^2 - 1} \quad (84)$$

6. STORE FORCE AND MOMENT CALCULATION

The calculation of the trajectory of a store separating from an aircraft requires a knowledge of the forces and moments acting on the store at each point in the trajectory. In order to calculate these forces and moments, the nonuniform velocity field in which the store is immersed, as seen by the store, must be determined at each point in time. This field includes the free-stream velocity, the perturbation velocities induced by the parent aircraft, image store velocities, and the angular velocities due to the store's pitch, yaw, and roll motions. The distribution along the body is required in order to calculate the forces and moments acting on the body and, if fins are present, the distribution over the fin surfaces is required for the empennage force and moment calculation.

This section will first describe the calculation of the velocity field utilizing the flow models of Sections 3 and 4. Following this the methods employed to calculate the body and empennage forces and moments from this nonuniform flow field will be presented, first for the circular store and then for the elliptic store.

6.1 Velocity Field as Seen by Store

The x_s, y_s, z_s coordinate system to be used in the force and moment calculations is shown in Figure 13. It is fixed in the store with the origin at the store nose with the velocities $U_s, V_s,$ and W_s positive in the directions shown. These are the total velocities as seen by a point on the store and each is composed of a free-stream component, perturbation components due to the parent aircraft and image store, and a damping component due to the store's rotational motion.

Before writing the expressions for these velocities let us examine Figure 14 which shows the coordinate systems used in the trajectory calculation. The equations of motion will be presented in Section 7. Two coordinate systems are shown

in Figure 14. The ξ, η, ζ system is an inertial system fixed in the aircraft which is in rectilinear flight at uniform velocity. The positive ξ axis is forward along the fuselage longitudinal axis, the η axis is positive laterally to the right, and the ζ axis is positive downward perpendicular to the fuselage longitudinal axis. The origin of this system is fixed in the fuselage nose.

The x, y, z coordinate system is fixed in the store with the origin at the store moment center. Referring back to Figure 13, the x -axis lies along the store longitudinal axis but is positive forward. The y -axis is parallel to the y_s axis and positive in the same direction and the z axis is parallel to the z_s axis but positive downward. The x, y, z system shown in Figure 13 is a right-hand system and the store angular velocity components about the three axes are $p, q,$ and r , respectively.

In Figure 14 the origins of the two coordinate systems have been drawn to coincide in order to show the angles used to determine the orientation of the store with respect to the inertial (ξ, η, ζ) axes. The system of angles chosen consists of three rotations in the yaw, Ψ ; pitch, Θ ; and roll, Φ ; sequence (Reference 16). The two coordinate systems are then related by

$$\begin{bmatrix} \xi \\ \eta \\ \zeta \end{bmatrix} = [A] \begin{bmatrix} x \\ y \\ z \end{bmatrix} \quad (85)$$

where

$$[A] = \begin{bmatrix} \cos \Theta \cos \Psi & \sin \Phi \sin \Theta \cos \Psi & \cos \Phi \sin \Theta \cos \Psi \\ \cos \Theta \sin \Psi & \sin \Phi \sin \Theta \sin \Psi & \cos \Phi \sin \Theta \sin \Psi \\ -\sin \Theta & \sin \Phi \cos \Theta & \cos \Phi \cos \Theta \end{bmatrix} \quad (86)$$

The three velocity components, U_s , V_s , and W_s are

$$\left. \begin{aligned} U_s &= U_{\infty, x_s} + u_{s_p} + u_{s_i} - qz_s - ry_s \\ V_s &= V_{\infty, y_s} + v_{s_p} + v_{s_i} + v_{s_\gamma} + r(x_s - x_{s,m}) - pz_s \\ W_s &= W_{\infty, z_s} + w_{s_p} + w_{s_i} + w_{s_\gamma} + q(x_s - x_{s,m}) + py_s \end{aligned} \right\} \quad (87)$$

The first term on the right side of the equal sign in each of the above expressions is the component of the free-stream velocity vector. If the parent aircraft is moving at velocity, V_∞ , and flying at angle of attack, α_F , then the velocity of the inertial coordinate system relative to a point in space is

$$\vec{V}_\infty = V_\infty \cos \alpha_F \vec{e}_\xi + V_\infty \sin \alpha_F \vec{e}_\zeta \quad (88)$$

The velocity of the store moment center relative to the moving inertial system is

$$\vec{V}_m = \dot{\xi} \vec{e}_\xi + \dot{\eta} \vec{e}_\eta + \dot{\zeta} \vec{e}_\zeta \quad (89)$$

so that the velocity of the store relative to a point in space is

$$\vec{V}_{\infty s} = \vec{V}_\infty + \vec{V}_m = (V_\infty \cos \alpha_F + \dot{\xi}) \vec{e}_\xi + \dot{\eta} \vec{e}_\eta + (V_\infty \sin \alpha_F + \dot{\zeta}) \vec{e}_\zeta \quad (90)$$

Since the velocity components needed in Equation (87) are those seen by a point fixed in the store and moving with the store, Equation (90) becomes

$$\vec{V}_{\infty s} = - (V_\infty \cos \alpha_F + \dot{\xi}) \vec{e}_\xi - \dot{\eta} \vec{e}_\eta - (V_\infty \sin \alpha_F + \dot{\zeta}) \vec{e}_\zeta \quad (91)$$

The components in the x,y,z coordinate system of Figure 13 are then

$$\begin{bmatrix} U_{\infty s,x} \\ V_{\infty s,y} \\ W_{\infty s,z} \end{bmatrix} = [A]' \begin{bmatrix} - (V_{\infty} \cos \alpha_F + \dot{\xi}) \\ - \dot{\eta} \\ - (V_{\infty} \sin \alpha_F + \dot{\zeta}) \end{bmatrix} \quad (92)$$

where $[A]'$ is the transpose, or inverse since $[A]$ is orthogonal, of the matrix given in Equation (86). These velocity components are related to those in the coordinate system of Figure 13 by

$$\left. \begin{aligned} U_{\infty s,x_s} &= -U_{\infty s,x} \\ V_{\infty s,y_s} &= V_{\infty s,y} \\ W_{\infty s,z_s} &= -W_{\infty s,z} \end{aligned} \right\} \quad (93)$$

The second term on the right-hand side in the three expressions of Equation (87) is the parent aircraft perturbation velocity term. This is comprised of the perturbation velocities induced by the fuselage, wing, pylon, rack and other stores and is calculated by the methods presented in Section 5. These velocities are summed up in the fuselage, or inertial, coordinate system. The velocity components in the x, y, and z directions of Figure 13 are

$$\begin{bmatrix} u \\ v \\ w \end{bmatrix} = [A]' \begin{bmatrix} u_{\xi} \\ v_{\eta} \\ w_{\zeta} \end{bmatrix} \quad (94)$$

and, finally, the components in the x_s, y_s, z_s coordinate system of Figure 13 are

$$u_{s_p} = -u, v_{s_p} = v, w_{s_p} = -w \quad (95)$$

The third terms on the right side of Equation (87) are velocities induced at a point on the real store by the image store(s). The calculation of the image store induced velocities was described in Section 4.4. Imaging is done in a different manner depending upon which store modeling option, circular or elliptic, is used. The velocities induced by the image store at control points on the real store body and fins are calculated.

The fourth terms in the last two expressions in Equation (87), v_{s_y} and w_{s_y} , are included only when the elliptic store option is used and, then, only when two sets of fins are present and the option to include trailing-edge vortex effects is selected. These trailing-edge vortices are shed by the forward set of fins. Their paths are calculated back to the leading edge of the rear fins. With the vortices fixed at these positions the velocities induced at the fin control points are calculated. The trailing-edge vortex interference will be described in Section 6.3.3.

The remaining terms in Equation (87) are aerodynamic damping terms due to the rotational motion of the store. The rotational velocities, p , q , and r , are about the x_s , y_s , and z_s axes, respectively, and are positive in the positive sense of the moments shown in Figure 13. The values of p , q , and r at each point in a trajectory are determined by integration of the equations of motion.

The store free-stream velocity will change during its trajectory because of its motion relative to the parent aircraft. The velocities to be used in the force and moment

calculation are made dimensionless by the store free-stream velocity. Thus, Equation (87) becomes

$$\left. \begin{aligned} U_s^* &= \frac{U_s}{V_{\infty s}} \\ V_s^* &= \frac{V_s}{V_{\infty s}} \\ W_s^* &= \frac{W_s}{V_{\infty s}} \end{aligned} \right\} \quad (96)$$

where from Equation (90) or (91)

$$V_{\infty s} = \left[(V_{\infty} \cos \alpha_F + \xi)^2 + \eta^2 + (V_{\infty} \sin \alpha_F + \zeta)^2 \right]^{1/2} \quad (97)$$

6.2 Circular Store Forces and Moments

This section of the report will describe the methods used to calculate the aerodynamic forces and moments acting on the separated store when the circular store option is used. In this option the store body is modeled by line singularities and one set of fins can exist which can be planar or cruciform.

6.2.1 Body Forces and Moments

In the work of Reference 1 slender-body theory was used to calculate the forces and moments acting on the store body. This method was found to be quite inaccurate for a store immersed in a nonuniform flow field at supersonic speed. In the present work the slender body method has been replaced by one in which the store body is modeled by line singularities distributed along the body axis. Supersonic line sources and sinks are distributed along the store centerline to account for volume effects subject to a nonuniform axial velocity distribution. The nonuniform upwash and sidewash fields in which the

store is immersed are accounted for by two distributions of supersonic line doublets on the store longitudinal axis. One doublet distribution cancels the effects of the upwash distribution and the other, the sidewash distribution.

The derivation of the equations used to calculate the singularity strengths, the surface pressure distribution, the axial load distributions, and the overall forces and moments is presented in Appendix A. The nonuniform velocity field in which the store is immersed is calculated as was just described in Section 6.1. As discussed in Appendix A, the velocities are calculated at points on the store axis. Equations (A-13), (A-22), and (A-30) are used to solve for the strengths of the three singularity distributions. The velocity distributions appearing in these three equations are related to the velocities of Equation (96) by

$$\left. \begin{aligned} \frac{U(x_{B_{n+1}})}{U_{\infty s}} &= \left[\frac{U_s(x_s)}{V_{\infty s}} \right] \frac{V_{\infty s}}{U_{\infty s, x_s}} \\ \frac{W(x_{B_{n+1}})}{V_{\infty}} &= \frac{W_s(x_s)}{V_{\infty s}} \\ \frac{V(x_{B_{n+1}})}{V_{\infty}} &= \frac{V_s(x_s)}{V_{\infty s}} \end{aligned} \right\} \quad (98)$$

The singularity strengths modeling the store in the nonuniform flow field have now been determined. The next step in the store force and moment calculation is to calculate the store surface pressure distribution. Sections A-3.1 and A-3.2 of Appendix A describe the surface velocity calculation due to the singularities modeling the store. The surface

pressure coefficient calculation is discussed in Section A-3.3. The Bernoulli equation for compressible, isentropic flow is used and is given by Equation (A-35).

The question arises as to what velocities should be included in the surface pressure distribution calculation. Those due to the singularities modeling the store must be included as must the damping velocities. The velocities in question are those due to the parent aircraft and the image store(s). These latter velocities will be excluded based on comparisons with experimental data.

Figures 15 through 18 show longitudinal pressure distributions on an ogive-cylinder store under the left wing of a wing-fuselage combination in a position at which the store nose shock wave reflects off the wing and strikes the store. The data are from Reference 6. Two theoretical curves are shown in the figures. The solid curve has the velocities due to the store singularities as well as those due to the wing, fuselage, and image store included in the surface velocity calculation. These velocities determine the pressures. The dashed curve omits the image store velocities which start where these curves begin. As can be seen, the agreement between experiment and theory is quite good when the image store velocities are excluded.

Reference 17 gives some insight into why the calculated pressures with the image store included are too large. According to the conclusions drawn in this reference, the following phenomena can occur: (1) when an oblique shock impinges on an elongated, cylindrical body, the main feature is a strong boundary-layer crossflow and separation on the lee side accompanied by a rapid relieving of pressures on the incident side, (2) details of the pressure distributions depend on the nature and thickness of the boundary layer and the shock strength, and (3) on the incident side, the presence of the boundary layer also allows for upstream

propagation of the pressure rise associated with the impinging shock. Thus, the pressure distribution on a body in the region enveloped by an oblique shock is very much subject to viscous effects. Prediction methods based on nonviscous theories tend to overpredict the magnitude of the peak pressures, and therefore, such methods require suitable corrections. One improvement may be to neglect the presence of the shock wave in the pressure distribution calculation in the region enveloped by the shock wave.

This has been done in the calculations shown by the dashed curves in Figures 15 through 18. In these calculations the image store contribution to the velocity field has been eliminated everywhere. As can be seen the agreement between the calculation and the experimental data is now quite good. A similar improvement has been observed for other flight conditions and store positions relative to the parent aircraft. It has also been found that a similar situation occurs when the wing shock wave strikes the store in the cylindrical region. In the example shown in the figures, the wing shock strikes the store near the tip of the nose and the effect is not as apparent. In calculating the surface velocities to be used in the pressure distribution calculation only the velocities due to the singularities modeling the separated store and rotational velocities are included in the present method.

The axial distributions of forces and moments are calculated from the pressure distribution using Equations (A-39) and (A-40) of Appendix A and the overall forces and moments are given by Equation (A-41).

6.2.2 Empennage Forces and Moments

The circular store option allows one set of planar or cruciform fins to be placed on the store body. The method used to calculate the empennage forces and moments is that presented in Section 5.3 and Appendix I of Reference 18. The method used there is based on a combination of reverse flow theorems

and slender-body theory scaled for the effects of aspect ratio as done in wing-body interference theory, Reference 19. The effects of interference between the body and the fins are accounted for.

The method requires that the velocity field across the span of each fin be known. The velocities are calculated as described in Section 6.1. With this velocity distribution known, the method of Reference 18 yields the normal and side forces and the pitching, yawing, and rolling moments due to the empennage. The total aerodynamic forces and moments acting on the circular store are obtained by adding the store body forces and moments to those for the empennage.

6.3 Elliptic Store Forces and Moments

This section will describe the methods used to calculate the aerodynamic forces and moments acting on the separated store when the elliptic store option is used. The methods used are modifications to those described in Reference 7. The store body is modeled by source panels. Up to two sets of fins can be positioned on the body and each set can have from one to four fins. The fins and the interference shell placed on the body to account for fin-body interference are modeled by constant u-velocity panels like those used for the wing and fuselage interference shell described in Section 3.3. If two sets of fins are present, interference of the forward set on the aft set can be accounted for. Positions and strengths of vortices are calculated at the trailing edge of the forward set. Their positions at the leading edge of the aft set are determined by integration of their paths.

6.3.1 Body Forces and Moments

The first step in determining the forces and moments acting on the elliptic store is to determine the strengths of the source panels modeling the body. The method used is the same

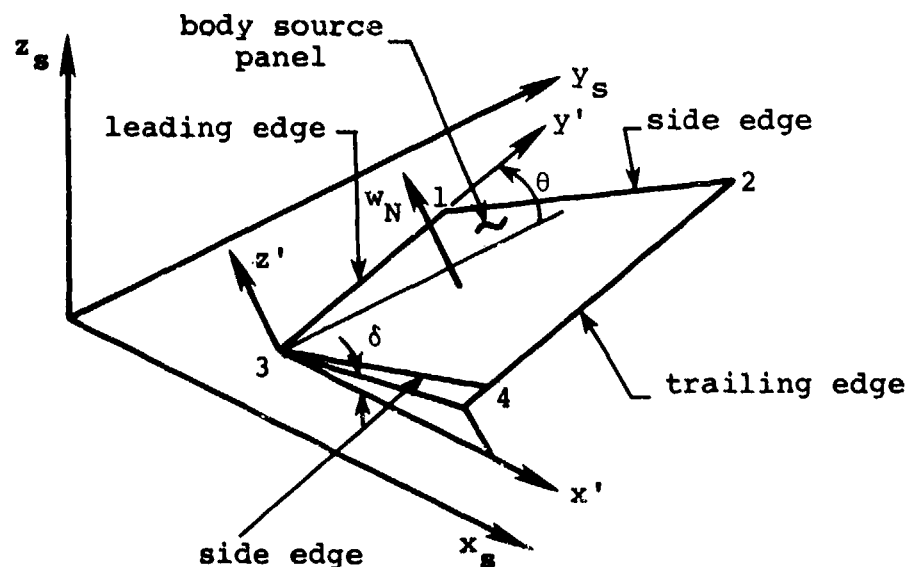
as that described in Section 3.3.2 for the noncircular fuselage and in Section 3.2.6 for the elliptic store. In those two sections the boundary condition only included the free-stream flow. In calculating the panel strengths for use in the force and moment calculation, the boundary condition reflects the velocities calculated as described in Section 6.1. Thus, Equation (17) is replaced by

$$\sum_{j=1}^N A_{ij} \gamma_j = \left(\frac{W_N}{V_{\infty s}} \right)_i \quad i = 1, 2, \dots, N \quad (99)$$

where, using the velocities of Equation (96),

$$\left(\frac{W_N}{V_{\infty s}} \right)_i = W_{s_i}^* \cos \theta_i \cos \delta_i - V_{s_i}^* \sin \theta_i \cos \delta_i = U_{s_i}^* \sin \delta_i \quad (100)$$

The angles θ_i and δ_i are the panel orientation angles measured in the store body x_s, y_s, z_s coordinate system. They are measured as shown in the following sketch. The positive senses are shown.



The panel strengths are determined by using a marching procedure over the length of the store body. This procedure solves for the strengths ring by ring beginning at the store nose. This is done in order that the image store induced velocities $u_{s_i}, v_{s_i}, w_{s_i}$ in Equation (87) can be calculated. These velocities are determined in the manner described in Section 4.4.2.

The next step in the force and moment calculation is to calculate the pressure coefficient at the control points of all of the panels. This calculation is identical to that describe in Section 6.2.1 for the circular store and presented in Section A-3.3 of Appendix A. The Bernoulli relationship given by Equation (A-35) is used with the velocity given by Equation (A-37). As for the circular store, only the velocities due to the source panels and store rotational motion are included in the pressure calculation for the same reasons discussed in Section 6.2.1. In Equation (A-37)

$$\left. \begin{aligned} \frac{u_{x_B}}{V_\infty} &= \frac{u_s}{V_{\infty s}} - \frac{qz_s}{V_{\infty s}} - \frac{ry_s}{V_{\infty s}} \\ \frac{v_{y_B}}{V_\infty} &= \frac{v_s}{V_{\infty s}} + \frac{r(x_s - x_{s,m})}{V_{\infty s}} - \frac{pz_s}{V_{\infty s}} \\ \frac{w_{z_B}}{V_\infty} &= \frac{w_s}{V_{\infty s}} + \frac{q(x_s - x_{s,m})}{V_{\infty s}} + \frac{py_s}{V_{\infty s}} \end{aligned} \right\} \quad (101)$$

where u_s, v_s, w_s are the source panel induced velocities at a control point in the store body coordinate system shown in Figure 13. The remaining terms are the velocities at the control points due to the store rotational motion, see Equation (87).

The forces and moments acting on a panel are calculated by first determining the total force acting at the control point in a direction normal to the panel surface, C_{F_i} . This force is

$$C_{F_i} = -C_{P_i} A_i / S_R \quad (102)$$

where C_{P_i} is the pressure coefficient at the i^{th} panel control point and A_i is the area of the i^{th} panel. This force is resolved into normal-force and side-force components using the angles θ and δ shown in the preceeding sketch by

$$\left. \begin{aligned} C_{N_i} &= C_{F_i} \cos \theta \cos \delta \\ C_{Y_i} &= -C_{F_i} \sin \theta \cos \delta \end{aligned} \right\} \quad (103)$$

The axial-force component is not used in the present method as an axial force but is used as a contribution to the pitching and yawing moments. This component is

$$C_{A_i} = -C_{F_i} \sin \delta \quad (104)$$

The moment contributions due to a panel, positive in the directions shown in Figure 13, are

$$\left. \begin{aligned} C_{m_i} &= -C_{N_i} \frac{(x_{cp} - x_{s,m})}{l_R} + C_{A_i} \frac{z_{cp}}{l_R} \\ C_{n_i} &= -C_{Y_i} \frac{(x_{cp} - x_{s,m})}{l_R} + C_{A_i} \frac{y_{cp}}{l_R} \\ C_{l_i} &= -C_{N_i} \frac{y_{cp}}{l_R} + C_{Y_i} \frac{z_{cp}}{l_R} \end{aligned} \right\} \quad (105)$$

where x_{cp} , y_{cp} , and z_{cp} are the control point location in the x_s, y_s, z_s coordinate system.

The total forces and moments acting on the store body are determined by summing Equations (103) and (105) over all of the source panels modeling the store.

6.3.2 Empennage Forces and Moments

The elliptic store option allows one or two sets of fins to be present on the store body. In addition, if there are two sets of fins interference of the forward set on the rear set can be accounted for by including the velocities induced by the trailing edge vorticity associated with the forward set in the nonuniform flow field. The methods used model the fins and fin-body interference, determine the trailing-edge vortex strengths and positions, and calculate the vortex paths along the body. They are modifications of those presented in Reference 7. Some features included in the work of that reference have been deleted and others added. This section will describe the fin-body model and the calculation of the forces and moments. The trailing-edge vortex method will be discussed in the next section.

The methods used to model the fins and the fin-body interference were extracted from program DEMON2 described in Reference 7. Certain features were eliminated such as nose vorticity in the boundary condition, leading-edge and side-edge suction calculations, and the option of modeling a circular store by line singularities. In the present program the store can only be modeled by line singularities by using the circular store option. Fin thickness effects are also not included.

Other features have been added to the present program. Each set of fins can be comprised of 1, 2, 3, or 4 fins. They can be located circumferentially anywhere on the body and may be at any angle relative to the tangent to the body surface

in the crossflow plane. The program was modified to include parent aircraft and image store velocities in the boundary condition. Velocities at the control points due to store angular motion are also included.

The fins are modeled in the same manner as described in Section 3.3 for the wing and fuselage interference shell. The fins and the interference shell placed on the store body for fin-body interference are represented by constant u-velocity panels. A typical panel layout is shown in Figure 19. The interference shell shown in the figure extends over the length of the root chord of the fins and the panel layout is the same as that used for the source panels modeling the store body. The interference shell should extend beyond the fin trailing edge to include all of the lift carryover if the body extends beyond the trailing edge. Use of the u-velocity panel method has shown that if this is done difficulties are encountered in the solution for the panel strengths. To avoid this problem, the shell is terminated at the trailing edge. Most of the lift carryover is still accounted for.

The flow tangency condition at a fin control point is

$$\sum_{n=1}^{NWBP} \frac{v_{N,n}}{V_{\infty s}} = - \frac{W_{sv}}{V_{\infty s}} \cos \phi_f + \frac{V_{sv}}{V_{\infty s}} \sin \phi_f - \sin \delta_f \quad (106)$$

$$v = 1, 2, \dots, NPANLS$$

In the above notation there are NPANLS on the fins and NWBP panels on the fins and the interference shell. The summation on the left side of Equation (106) is the perturbation velocity normal to the v^{th} panel induced by all of the u-velocity panels on the fins and interference shell. The velocities V_{sv} and W_{sv} are the sums of the velocities given by

Equation (87) and those induced at the v^{th} control point by the source panels modeling the store body. The angle ϕ_f is measured as shown in Figure 20 which is taken from Reference 3. The last term on the right-hand side of Equation (106) is the sine of the fin deflection angle. Positive fin deflection is such that the fin produces a force in the direction of C_F shown in Figure 20.

The flow tangency condition at an interference shell control point is

$$\sum_{n=1}^{\text{NWBP}} \frac{V_{N_{v,n}}}{V_{\infty s}} = 0 \quad (107)$$

$$v = \text{NPANLS}+1, \text{NPANLS}+2, \dots, \text{NWBP}$$

These panels only account for mutual interference between the fins and the body. Hence, the right-hand side is zero. Solution of the set of equations given by Equations (106) and (107) following the procedure described in Section 3.3 yields the strengths of the constant u-velocity panels modeling the fins and the associated interference shell.

The next step in the empennage force and moment calculation is to calculate the pressure coefficient at the control points of all of the u-velocity panels on the fins and the interference shell. The Bernoulli relationship given by Equation (A-35) of Appendix A is used to calculate the pressures, as before, with the velocity used in the relationship given by Equation (A-37). The velocity components in this equation are given by Equation (101). The velocities u_s , v_s , and w_s in Equation (101) are the sums of those induced at the control points by the constant u-velocity panels, the body source panels, and external vortices if they are present.

The total force acting on a panel in a direction normal to the panel surface is given by Equation (102).

$$C_{F_i} = -C_{P_i} A_i / S_R \quad (108)$$

The positive sense of this force on fins in the four quadrants is shown in Figure 20. The positive sense on a body interference panel is outward from the body. This force is resolved into normal and side force components using the angle ϕ_f for the fins and $\theta_{2,BIP}$ for the body interference panels. It should be noted that ϕ_f for the fin arrangement shown in Figure 20 is positive in the upper right and lower left quadrants, $\phi_f = \phi_F$, and negative in the other two quadrants, $\phi_f = -\phi_F$. The normal-force and side-force components in the four quadrants are

$$\begin{aligned} C_{N_i} &= C_{F_i} \cos \phi_f \\ C_{Y_i} &= -C_{F_i} \sin \phi_f \end{aligned} \quad (109)$$

For panels on the interference shell

$$\begin{aligned} C_{N_i} &= C_{F_i} \cos \theta_{2,BIP} \\ C_{Y_i} &= C_{F_i} \sin \theta_{2,BIP} \end{aligned} \quad (110)$$

The angle $\theta_{2,BIP}$ is defined in Figure 20.

The moment contributions due to a panel are calculated using Equation (105) with C_{A_i} set equal to zero. The total forces and moments acting on the fins and the length of body covered by the interference shell are calculated by summing the individual panel forces and moments over all of the panels.

The forces and moments calculated in the manner just described are made up of five components

- (a) Fin alone
- (b) Body alone

- (c) Those due to body interference on fins
- (d) Those due to fin interference on body
- (e) Those due to fin-fin interference

The empennage forces and moments are the increments due to adding the fins to the body. To determine these forces and moments, the body alone (b) contribution must be subtracted. These forces and moments were calculated as described in Section 6.3.1 and are the sums of those acting on the body source panels which coincide axially with the interference shell.

6.3.3 Trailing Edge Vortex Interference

For elliptic stores with two sets of fins, the effects of trailing edge vorticity from the forward set of fins can be included in the calculation of the forces and moments acting on the rear set of fins. Methods for doing this are included in program VPATHL of Reference 7 and they have been incorporated into the present computer program. Only certain fin arrangements can be handled. These cases are where each fin in the forward set lies in either the $y_f = 0$ or $z_f = 0$ plane shown in Figure 19. For other fin arrangements interference of the forward set of fins on the rear set cannot be accounted for because of program limitation.

The steps in determining the interference effects on the forward set of fins on the rear set are

- (a) Calculate vortex positions and strengths at trailing edge of forward set of fins.
- (b) Calculate the vortex paths from the trailing edge of the forward set of fins to the root-chord leading edge of the aft set.
- (c) Calculate the vortex induced velocities at the control points on the rear fins and interference shell.

The vortex strengths and positions at the trailing edge of the forward set of fins are calculated using the method described in Appendix B of Reference 7. This method requires the spanwise load distribution on each fin. They can be calculated from the individual panel forces C_{F_i} determined by the method described in the preceeding section. The forces on the panels in a chordwise row are summed and divided by the panel width to determine the force per unit span. The vortex strengths and positions are calculated from the spanwise load distribution as described in Appendix B of Reference 7.

The second step, (b) above, is to integrate the vortex paths from these initial positions to the root-chord leading edge of the rear set of fins. The vortex strengths remain constant over this region. The body shape is elliptical and may be expanding or contracting. Also, the ratio of horizontal semi-axis length to vertical semi-axis length, a/b , need not be constant.

The method used for the vortex tracking is that described for program VPATHL in Appendix L of Reference 7. It makes use of crossflow plane solutions obtained from slender-body theory. Because of the linear nature of the problem it is possible to superimpose different solutions.

Fundamentally, at given axial stations, velocity components are computed in the crossflow plane at the points occupied by a finite set of external vortices in the presence of the elliptic body. In this calculation, mutual interaction between the vortices, the interaction between the vortices and the body, the effects of local angles of attack and sidewash, and changes in body shape are included. Once the lateral velocity components are known, the vortex locations at the next axial station downstream can be determined by means of an integration scheme. The vortices move from one axial station to the next in accordance with the flow angle calculated from the lateral velocity components.

The crossflow plane solution used to account for the local angles of attack and sidewash is given in Section 6 of Appendix I, Equations (I130) and (I132). The angles α and β appearing in the equations are calculated in the present work from the velocities given by Equation (87) of this report with $v_{s\gamma}$ and $w_{s\gamma}$ set to zero.

Changing body shape, that is expansion, contraction, and/or changing a/b ratio, is accounted for by using the method of Section 8 of Appendix I of Reference 7, Equation (I136). One change has been made to allow for the varying a/b ratio. In Reference 7, the axial rate of change of body cross-sectional area, S' , is written assuming a constant a/b ratio. In the present work the following expression is used.

$$S' = \pi \left[a \frac{db}{dx_s} + b \frac{da}{dx_s} \right] \quad (111)$$

It is obtained by differentiation of the following expression for the cross-sectional area of an ellipse.

$$S = \pi ab \quad (112)$$

Finally, the velocities induced at an external vortex by all the other external vortices and all of the image vortices inside the body are calculated using the method of Section 5 of Appendix I of Reference 7, Equation (I124).

The velocities described in the preceeding three paragraphs are calculated and summed up at each external vortex location. The vortices are then moved to the next axial station using flow angles calculated from the velocities. This process is repeated until the vortices have been tracked to the root-chord leading edge of the aft set of fins.

The velocities at the control points on the aft set of fins and the interference shell can now be calculated. For all control points the vortices are assumed to be at the

same y_s, z_s locations as they were at the root-chord leading edge. The velocities v_{s_γ} and w_{s_γ} in Equation (87) due to N vortices are given by

$$v_{s_\gamma} - iw_{s_\gamma} = -\frac{i}{2\pi} \sum_{j=1}^N \Gamma_j \left(\frac{1}{\zeta - \zeta_j} - \frac{\bar{\zeta}_j}{\zeta \bar{\zeta}_j - R^2} \right) \frac{d\zeta}{dz} \quad (113)$$

The notation used above is that used in Section 5 of Appendix I of Reference 7.

7. TRAJECTORY CALCULATION

The complete derivation of the equations of motion of a rigid body with mass and inertia asymmetries was presented in Appendix II of Reference 18. Since the publication of that report an error in the derivation has been found which affects all of the equations of motion. The equations in the appendix changed by correcting the error are Equations (II-15) through (II-18), (II-32), and (II-40) through (II-43). The corrected derivation is presented in Appendix B of the present report. The following paragraphs describe the derivation and the equations.

Generally, the body, a store in the present application, will have axes of geometrical asymmetry about which the store forces and moments are determined. By mass asymmetry it is meant that the store center of mass does not have to lie at the origin of this coordinate system. By inertia asymmetry it is meant that the principal axes of inertia of the store do not coincide with the geometric axes of symmetry so that the tensor of inertia possesses off-diagonal terms, the products of inertia.

In the derivation of Appendix B the two coordinate systems discussed earlier in conjunction with the velocity field calculation, Section 6.1, are used. They are shown in Figure 14. The x, y, z coordinate system is fixed in the store and rotates with the store. The x -axis lies along the store longitudinal axis and is positive forward, the y -axis is positive to the right, and the z -axis is positive downward. These axes coincide with the geometric axes of symmetry with the origin at the point about which the moments and products of inertia and the aerodynamic moments are calculated. The equations of motion are derived in this coordinate system since, by allowing the coordinate system to rotate with the store, the time derivatives of the moments and products of inertia do not appear in the rotational equations of motion. The equations of motion

in this coordinate system are given by Equation (B-15) and (B-40) of Appendix B.

Since the store coordinate system in which these equations of motion are written does not allow the store position and orientation to be determined relative to the parent aircraft, a coordinate system is introduced which is fixed in the fuselage nose, the ξ, η, ζ system of Figure 14. In the present work it is assumed that the parent aircraft is flying at constant velocity, constant angle of attack, and constant flight path angle relative to the horizontal so that this system is a non-rotating system. As such, it can be regarded as an inertial system and the store motion relative to this moving system calculated.

The ξ, η, ζ system is fixed in the fuselage nose, and coincides with the x_F, y_F, z_F system of Figure 5, with ξ forward along the fuselage longitudinal axis, η laterally to the right, and ζ vertically downward. In order to determine the orientation of the store with respect to these axes, a system of angles must be introduced. These angles are also shown in Figure 14 and consist of three rotations in the yaw, ψ ; pitch, θ ; roll, ϕ ; sequence. In order to determine the time histories of these angles, differential equations expressing them as a function of the store rotational velocities, p , q , and r , are required. These are given by Equation (B-1) of Appendix B. The rotational velocities, p , q , and r , are shown in Figure 14. The velocity about the x-axis is p and is positive right-wing down. Those about the y- and z-axes are q and r , respectively and are positive nose up and nose to the right.

The final differential equations which are to be integrated to determine the store position and orientation relative to the inertial system fixed in the fuselage are Equations (B-1), (B-16) through (B-18), and (B-41) through (B-43). The latter

six equations are obtained from Equations (B-15) and (B-40) by using the direction cosines relating the two coordinate systems, Equation (B-2). In the equations, $\ddot{\xi}$, $\ddot{\eta}$, and $\ddot{\zeta}$ are the accelerations of the store moment center, the point about which the moments and products of inertia are taken, in the inertial coordinate system. The velocities in this system are $\dot{\xi}$, $\dot{\eta}$, and $\dot{\zeta}$ and the quantities \dot{x}_O , \dot{y}_O , and \dot{z}_O are these velocities resolved into the store body coordinate system. That is

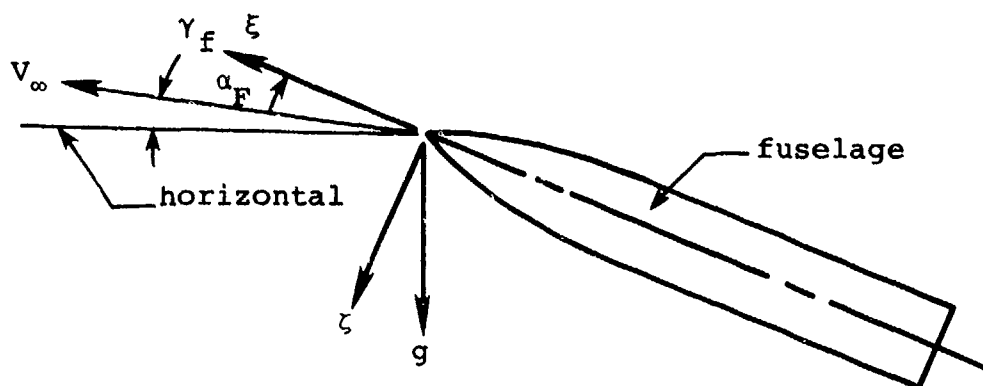
$$\begin{bmatrix} \dot{x}_O \\ \dot{y}_O \\ \dot{z}_O \end{bmatrix} = [A]' \begin{bmatrix} \dot{\xi} \\ \dot{\eta} \\ \dot{\zeta} \end{bmatrix} \quad (114)$$

where $[A]'$ is the transpose of the matrix given by Equation (B-2). The location of the store center of mass relative to the store moment center in store body coordinates is $\bar{x}, \bar{y}, \bar{z}$. The three rotational velocities in the store body coordinate system are p , q , and r and the corresponding accelerations are \dot{p} , \dot{q} , and \dot{r} . The quantities I_{xx} , I_{yy} , and I_{zz} are the moments of inertia and I_{yz} , I_{xz} , and I_{xy} are the products of inertia. They are defined by Equation (B-36).

The remaining parameters in the equations of motion are the store mass, m , and the forces, F_x , F_y , and F_z , and moments, M_x , M_y , and M_z , acting on the store which are positive in the positive x , y , z , p , q , and r directions, respectively. The three forces are

$$\left. \begin{aligned} F_x &= mg_x - q_{\infty} S_R C_A + F_t + F_{e_x} \\ F_y &= mg_y + q_{\infty} S_R C_Y + F_{e_y} \\ F_z &= mg_z - q_{\infty} S_R C_N + F_{e_z} \end{aligned} \right\} \quad (115)$$

In these equations g_x , g_y , and g_z are the component of the gravitational acceleration vector \vec{g} in the store body coordinate system. Consider the following sketch which shows the



fuselage flying at velocity V_∞ , angle of attack α_F , and flight path angle γ_f . The gravitational force acts normal to the local horizontal so that in the inertial coordinate system

$$\vec{g} = -g \sin (\alpha_F + \gamma_f) \vec{e}_\xi + g \cos (\alpha_F + \gamma_f) \vec{e}_\zeta \quad (116)$$

Then

$$\begin{bmatrix} g_x \\ g_y \\ g_z \end{bmatrix} = [A]' \begin{bmatrix} -g \sin (\alpha_F + \gamma_f) \\ 0 \\ g \cos (\alpha_F + \gamma_f) \end{bmatrix} \quad (117)$$

The second terms in Equation (115) are the aerodynamic forces acting on the store. The axial-force coefficient, C_A , is specified and is positive in the negative x direction. The side-force and normal-force coefficients, C_Y and C_N , are calculated by the methods described in Section 6 and are the

total forces acting on the store and empennage(s). If the circular store option is used, the forces are calculated using the methods of Section 6.2. For the elliptic store, the methods of Section 6.3 are used.

The third term in the F_x equation is a thrust force, F_t , positive in the positive x direction. This force acts along the store longitudinal axis and, in the computer program, is specified as a function of time from the beginning of separation.

The last terms in Equation (115) are ejector force terms. The ejector model in the computer program allows the pylon or rack to have one or two ejector feet. The force produced by each foot is specified, in the program, as a function of time or stroke length. The ejector model in the computer program allows the store to move relative to the ejector feet during separation so that forces in all three directions and moments about all three axes can be produced.

The parameters $q_{\infty s}$ and S_R are the dynamic pressure and reference area used in nondimensionalizing the aerodynamic forces. In the present work they are taken as the store free-stream dynamic pressure and the store maximum cross-sectional area

$$q_{\infty s} = \frac{1}{2} \rho_{\infty} V_{\infty s}^2 \quad (118)$$

$$S_R = \pi r_{\max}^2 \text{ or } \pi ab \quad (119)$$

where r_{\max} is the maximum radius of a circular store and a and b are the semi-axes of an elliptic store. The density ρ_{∞} is assumed constant at the value for the aircraft flight altitude at time $t = 0$ and the store free-stream velocity is given by Equation (97).

The three moments about the store moment center are

$$\left. \begin{aligned} M_x &= q_{\infty} S_R \ell_R C_{\ell} + m(g_z \bar{y} - g_y \bar{z}) + M_{e_x} \\ M_y &= q_{\infty} S_R \ell_R C_m + m(g_x \bar{z} - g_z \bar{x}) + M_{e_y} \\ M_z &= q_{\infty} S_R \ell_R C_n + m(g_y \bar{x} - g_x \bar{y}) + M_{e_z} \end{aligned} \right\} \quad (120)$$

The first term on the right-hand side of each of the above expressions is the aerodynamic moment. The moment coefficients, C_{ℓ} , C_m , and C_n are calculated by the methods of Section 6. The reference length, ℓ_R , is taken as the maximum store diameter for a circular store and the diameter of a circle with the same area as the frontal area of an elliptical store. The second terms are moments produced by the gravitational force when the location of the store center of mass does not coincide with the center of moments. The third terms are the moments produced by the force exerted by the ejector feet.

In order to integrate the equations of motion given by Equations (B-16) through (B-18) and (B-41) through (B-43) and the equations determining the angular orientation, Equation (B-1), initial conditions of the variables must be specified. These are the position of the store center of moments (ξ, η, ζ) , the translational velocity of this point $(\dot{\xi}, \dot{\eta}, \dot{\zeta})$, the angular velocities about the three store axes (p, q, r) , and the initial orientation angles (ψ, θ, ϕ) . With these specified the equations can be integrated with the aerodynamic forces and moments being recalculated at each point in the trajectory.

8. COMPARISONS WITH EXPERIMENTAL DATA

This section of the report will present comparisons between the results predicted using the present computer program and experimental data. The comparisons will serve to assess the accuracy of the methods described in the preceding sections for predicting flow fields, store loading distributions, store forces and moments, and store trajectories. The data used for the comparisons were obtained during wind-tunnel tests conducted during the present investigation and during the investigation documented in Reference 1. These test programs and the data obtained are described in detail in Reference 6. Before presenting the comparisons, the wind-tunnel models will be described.

8.1 Wind-Tunnel Model Description

The basic wing-fuselage combination used in the test program is shown in Figure 21. It is made up of nose N_1 , body B_2 , and wing, W . This configuration is designated N_1B_2W . To obtain data in the vicinity of a circular body alone, nose N_1 was used in conjunction with body B_1 shown in Figure 22 to form configuration N_1B_1 . A noncircular body alone configuration, $N_3B_1A_3$, was also tested. This was formed using nose N_3 shown in Figure 23 with the noncircular fuselage adapter A_3 shown in Figure 24 attached to body B_1 . Data comparisons will be presented for all of these basic configurations.

Comparisons will also be presented for two noncircular wing-fuselage combinations. These are designated $N_3B_2WA_3$ and $N_3B_2WA_4$. The first configuration is built up from components described in the preceding paragraph. The second configuration has A_3 replaced by duct assembly A_4 shown in Figure 25.

The parent aircraft model has provisions for mounting pylons on the fuselage centerline and left wing 1/3 semispan or 2/3 semispan positions. Figure 26 shows these positions.

The centerline of the wing pylons is located at the 40 percent chord. The centerline of the fuselage pylon is located at fuselage station (FS) 19.42.

Two different pylon configurations were tested. The double-wedge pylon (P_2) shown in Figure 27 was tested at the three pylon positions. The model component designations are $(P_2)_C$, $(P_2)_{1/3}$, and $(P_2)_{2/3}$. These pylons are located as shown in Figure 26. The swept pylon (P_3) was tested only at the 1/3 semispan position, $(P_3)_{1/3}$. This pylon is shown in Figure 28.

Some tests were conducted with the triple ejector rack, T, shown in Figure 4 attached to $(P_2)_{1/3}$. When attached, the rack centerline shown in Figure 4 is aligned with the pylon centerline shown in Figure 27.

Dummy ogive-cylinder stores were used in conjunction with pylon $(P_2)_{1/3}$ and rack, T. The store is shown in Figure 29. When attached to $(P_2)_{1/3}$, the store midpoint is aligned with the pylon centerline shown in Figure 27. When used with the rack T, the stores, S_{DOC2} and S_{DOC3} , were attached at the two shoulder locations with the midpoints aligned with the rack centerline shown in Figure 4.

8.2 Flow Fields

Comparison will now be presented between flow fields predicted using the present methods and data from Reference 6. A number of comparisons will be shown for parent aircraft configurations built up from the circular fuselage, wing combination, N_1B_2W . A few will be presented for the noncircular fuselage configurations. The comparisons to be presented will start with the simplest parent aircraft configuration and increase in complexity.

Figure 30 presents a comparison of the calculated radial velocity, v_B/V_∞ , about configuration N_1B_1 with experimental

data. Three theoretical curves are shown; the linear theory solution using source panels, the modified linear theory solution using source panels, and the modified linear theory solution using line sources. The modified linear theory solutions account for the nonlinear shock wave shape as described in Section 4.1. The modified linear theory results predict the location at which the body first influences the flow field quite accurately but do not show the sharp jump in velocity as shown by the experimental data. The theory shows a gradual build up. This is the nature of both solutions. The velocity induced at the Mach cone location is zero and increases with distance. The source panel method produces a saw-toothed curve compared to the line source method. This behavior is due to the axial density of the source panels as is shown in Figure 31.

In this figure results are shown for two different axial spacings of source panels. The solid curve is the result of panels 0.5 inch long in the axial direction and the dashed curve is for panels 2.0 inches long. As can be seen, increasing the axial density of the panels smooths the calculated radial velocity distribution. Thus, to obtain smooth velocity fields the axial length of the source panels modeling the body must be as small as possible.

Figure 32 presents another comparison for the radial velocity induced by configuration N_1B_1 . The radial distance to the traverse location is 5.86 inches. Results for both linear theory and modified linear theory are shown. The nonlinear method predicts the shock location much better than linear theory. The agreement between experiment and theory is as good as that shown in Figure 30 for $r_B = 2.87$ inches.

Figure 33 presents a comparison of the upwash velocity, positive in the negative z_F direction of Figure 5, 5.86 inches below the centerline of N_1B_1 at an angle of attack of 5° .

The agreement between experiment and modified lineary theory is about the same as it was at 0° angle of attack.

The next two figures present comparisons between experiment and the modified source panel linear theory for the flow field about a noncircular body, in this case $N_3B_1A_3$. In Figure 34 the upwash velocity is shown for two axial traverses below the body centerline. A sketch of the cross section is shown in the figure. The traverses are below the flat bottom of the body. The agreement for the noncircular body is as good as was obtained for the circular body. The roughness seen in the calculated results can be reduced by increasing the density of the source panels in the axial direction.

Figure 35 presents comparisons for both upwash and side-wash for an axial traverse at $y_F = -2.49$ in. and $z_F = 4.36$ in. Again the comparisons are quite good except immediately behind the nose shock wave influence, $x_F \approx -5$ inches. Negative side-sh velocity, V_s , is in the negative y_F direction.

The next nine figures will present comparisons of flow field calculations with experimental data for the circular fuselage, wing combination N_1B_2W . In the calculations the line singularity method, Section 3.2.1, is used to model the fuselage. The wing shock wave system is located in the manner described in Section 4.3.

Figure 36 presents results at the wing one-third semi-span position for $M_\infty = 1.5$ and $\alpha_F = 0^\circ$. The vertical location relative to the local wing chord is $z_F = 1.37$ inches. This position corresponds to the centerline of the store shown in Figure 26. The x_F, y_F, z_F coordinate system is shown in Figure 5. The velocities U_s, V_s , and W_s are positive in the $-x_F, +y_F$, and $-z_F$ directions. As can be seen in Figure 36, all three velocity components are well predicted by the theory. The wing leading-edge influence, $x_F \approx -17.75$ inches, and the trailing-edge influence, $x_F \approx -26.75$ inches are positioned

properly. In the work of Reference 1, the wing-fuselage velocity field calculated between the wing leading-edge and trailing-edge influences was smoothed. This is no longer being done so that the theoretical curves shown are the actual calculated results.

Figures 37 and 38 present similar results for two other z_F locations, 2.12 and 4.37 inches. Only V_s and W_s velocities are shown. The agreement between data and theory for U_s is similar. For both z_F locations the comparisons between experiment and theory are quite good. As z_F increases, the predicted location of the wing leading-edge effect moves slowly aft of that shown by the data.

In Figure 39 results are presented for $z_F = 1.37$ inches at the wing two-thirds semispan location, $y_F = -8.0$ inches. Again, the comparisons are quite good.

Similar results are shown in Figure 40 for the flow field under the fuselage centerline. The z_F location, 2.87 inches, is 1.2 inches below the bottom of the fuselage. The comparisons between data and theory are good. Some unexplained scatter occurs in the data. The wing effect which occurs at $x_F \approx -19$ inches is well predicted.

Figures 41 and 42 present comparisons between experiment and theory for $M_\infty = 2.0$ and 2.5 . The location is at the wing one-third semispan, $y_F = -4$ inches, and $z_F = 1.37$ inches. At both Mach numbers, the predicted wing leading-edge influence is downstream of that shown in the data. At $M_\infty = 2.5$ the magnitude of the jump is overpredicted. Except in the vicinity of the wing leading-edge influence, the velocities are well predicted.

Figures 43 and 44 present results for $M_\infty = 1.5$ with the wing-fuselage combination at 5° angle of attack, $\alpha_F = 5^\circ$. At $z_F = 1.37$ inches, Figure 43, the wing leading-edge influence is predicted downstream of that shown by the data. The sidewash

velocity is overpredicted in this region. Otherwise, the velocities are well predicted. The same holds true at $z_F = 4.37$ inches, Figure 44, except that the sidewash velocity magnitude is well predicted in the wing leading-edge influence region.

The next three figures will present comparisons of flow field predictions with experimental data for the circular fuselage, wing combination N_1B_2W with the double wedge pylon, P_2 , shown in Figure 27 mounted at the wing one-third semispan location, $y_W = -4$ inches.

Figure 45 presents results for $M_\infty = 1.5$ and $\alpha_F = 0^\circ$. The vertical location relative to the local wing chord is $z_F = 1.37$ inches. Both pylon-on and pylon-off data are shown in the figure to illustrate the large effect the pylon has on the flow field. Theoretical curves are also shown for both cases. For all three velocity components, the theory predicts the pylon effect quite well. Downstream of $x_F = -22$ inches, the pylon-on calculation becomes quite rough. This is caused by wing-pylon mutual interference. If more constant u-velocity panels than the present program is capable of handling could be used on the wing and pylon, this roughness could be minimized. These panels account for the wing-pylon interference.

Figure 46 presents similar pylon-on results at $z_F = 2.87$ inches. Two sets of data are shown and give some indication of the data repeatability. They were taken during two different test programs. The theory again predicts the data quite well. The pylon influence begins at $x_F = -21.5$ inches.

In Figure 47 results are presented for $M_\infty = 1.5$ and $\alpha_F = 5^\circ$ for $z_F = 1.37$ inches. In general the agreement is not quite as good as in Figure 45 for $\alpha_F = 0^\circ$ but the trends are predicted. The experimental data are not nearly as smooth as at $\alpha_F = 0^\circ$. The roughness in the calculation downstream of $x_F = -23$ inches is again due to wing-pylon interference.

Figures 48 and 49 present comparisons between experiment and theory for the case of the TER shown in Figure 4 added to the pylon at the wing one-third semispan location. The Mach number is 1.5 and the angle of attack is 0° . In the theoretical calculations, the small rack pylon was modeled by extending the wing pylon through the rack body as shown in the sketch at the top of Figure 48(a). The thickness distribution for the portion inside the rack body, the cross-hatched area, was set to zero. Constant u-velocity panels are laid out on this portion, however, to cancel the sidewash velocity on this portion of the rack body. Note that the velocity scale in Figures 48 and 49 has been changed from that used in the previous figures.

An examination of the two figures for the two z_F positions, 2.12 and 3.62 inches, shows that the general trends shown by the data are predicted quite well by the theory. The theoretical curves are quite rough because of the mutual interference being accounted for by the u-velocity panels. A finer panel layout should smooth this out. The experimental data also exhibit roughness. As the complexity of the aircraft configuration increases, many more shock-wave interactions and reflections occur producing a very complicated flow field.

Figure 50 presents a comparison between experiment and theory for an aircraft configuration with inlets and fuselage centerline pylon. The Mach number is 1.5 and the angle of attack is 5° . The agreement between experiment and theory is quite poor. The data show the inlet shock wave at $x_F \approx -15$ inches while the theory predicts it at $x_F \approx -17$ inches. It is apparent considerably more work has to be done to provide a theory which will predict the flow field for as complex an aircraft configuration as this. There is also experimental evidence that viscous effects are influencing the flow field. This will be shown in the next figure.

Figure 51 shows four sets of experimental data taken at the same y_F, z_F location as the data shown in Figure 50 but at $\alpha_F = 0^\circ$ and with the pylon removed. The circles are data for the circular fuselage, wing combination and the squares are for the noncircular fuselage, wing combination. As can be seen the fuselage shape has little effect on the data. The remaining two sets of data have the inlets present on the configuration and are for two different inlet velocity ratios V_I/V_∞ . This ratio was determined during the tests of Reference 6 by measuring pressures in the duct. The method of determining and varying the ratio is discussed in Section 3.3 of Reference 6.

Figure 51 shows that by reducing the velocity ratio from 0.8 to 0.4 the inlet shock-wave location is moved forward from $x_F \approx -16$ inches to $x_F \approx -15$ inches. The other significant fact to be pointed out about the two sets of inlet-on data is that at $x_F = -24$ inches there are large differences in the velocities. This location is 8 inches downstream of the inlet cowl lip (see the sketch at the top of Figure 50) where, except for viscous effects, the two flows should be nearly equal. Viscosity appears to have a large effect. Vortices from the cowl lip or inlet corner are probably present.

8.3 Store Load Distributions

This section will present comparisons of store longitudinal load distributions predicted using the present theory and measured during the test programs described in Reference 6. The data to be compared with were obtained using the ogive-cylinder pressure distribution model shown in Figure 52. Complete pressure distributions were obtained by rolling the model through 360° in 10° increments. The forces per unit length were obtained by a circumferential integration of the pressures. The theoretical calculations were made using the circular-store option, that is, the body is modeled by line

sources, sinks, and doublets. The method is described in Section 6.2.1. The store coordinate system (x_s, y_s, z_s) is shown in Figure 13 along with the positive directions of the normal-force, C_N , and side-force, C_Y , coefficients. The reference area used in forming the coefficients is the store frontal area.

Figures 53 through 57 present comparisons of calculated load distributions with experimental data for the circular fuselage, wing combination N₁B₂W. Plotted in the figures are the force distributions per inch against distance from the store nose divided the store length, 6.375 inches. At the top of each figure is a sketch showing the store position relative to the wing, wing-pylon, fuselage, or fuselage-pylon immediately above the store. The store positions in the carriage position on the pylons are shown in Figure 26. At the one-third semispan location, $y_F = -4$ inches, the store longitudinal axis is at $z_F = 1.37$ inches. Below the fuselage centerline, it is at $z_F = 2.83$ inches. Data could not be obtained in these positions since the store had to be rolled. The minimum z_F positions where data were taken are 1.47 and 2.94 inches.

Figure 53 presents results at the wing one-third semispan position, $y_F = -4$ inches, for $M_\infty = 1.5$ and $\alpha_F = 0^\circ$ at $z_F = 1.47$ inches. In all comparisons the store is at the same angle of attack relative to the free stream as the parent aircraft. Figure 53(a) shows the normal force distribution. Two sets of data are shown. They were taken during two different test programs and indicate the repeatability of the data. From $x_s/l_s = 0$ to about 0.25 the down load is due to the flow field produced by the wing-fuselage combination. The down load is underpredicted by the theory. As was seen in the flow-field comparisons, the wing shock wave location given by the theory is slightly downstream of that shown by the data. This causes the underprediction.

Beginning at $x_s/l_s = 0.25$ the effect of the store nose shock wave reflecting off the wing is seen. As can be seen, the theory predicts the effect quite well. Without the wing image store used in the theory to account for the reflection, the predicted result would be approximately that shown by the dashed curve. The theory predicts a down load from $x_s/l_s = 0.7$ to 0.75 not shown by the data.

Figure 53(b) shows the comparison for the side-force distribution. The agreement between data and theory is quite good. The store shock wave reflection off the wing does not effect the side force to any extent. The reflection off the fuselage shows a small effect. The effect is seen in the theory beginning at $x_s/l_s \approx 0.6$.

Figure 54 presents comparisons for the same conditions except the store is at $z_F = 2.87$ inches, two store diameters below the position shown in Figure 26. The agreement is not so good as that shown in the preceeding figure. The data show the wing-fuselage effect to begin at $x_s/l_s \approx 0.15$ while the theory predicts it at $x_s/l_s \approx 0.25$. The location of the shock wave reflection off the wing is well predicted at $x_s/l_s \approx 0.7$.

A comparison for the store under the fuselage centerline is presented in Figure 55. The theory predicts the wing and reflected shock effects at about the same location, $x_s/l_s \approx 0.3$ for $z_F = 2.94$ inches and $x_s/l_s \approx 0.5$ for $z_F = 3.59$ inches. This is downstream of that shown by the data. The positive load downstream of the down load is not predicted by the theory.

Figures 56 and 57 present results for the store at the one-third semispan position for $M_\infty = 1.5$ and $\alpha_F = 5^\circ$. For both z_F locations, 1.47 and 2.87 inches, the trends shown by the data are well predicted. There are some regions where the theory does not predict details shown by the data.

The next four figures present comparisons of load distributions on the store for parent aircraft configurations which include a double wedge pylon, P_2 shown in Figure 27, mounted at either the wing one-third semispan location or under the fuselage centerline. Figure 58 shows results at the one-third semispan location for $M_\infty = 1.5$, $\alpha_F = 0^\circ$, and $z_F = 1.47$ inches. There is a 0.1 inch gap between the top of the store and the bottom of the pylon. Data and theoretical results for configurations with and without a pylon are shown in order that the large effect of the pylon on the store load distributions can be seen. The pylon-off data and theory were previously shown in Figure 53. A large effect of the pylon is seen on the normal-force distribution, Figure 58(a), while little effect is seen on the side-force distribution, Figure 58(b). In general, the pylon effects are fairly well predicted by the theory.

Figure 59 presents results for the store one diameter below the carriage position on the pylon, $z_F = 2.12$ inches. The agreement between data and theory is quite good.

The effect of adding a pylon below the fuselage centerline is shown in Figure 60. Again both pylon-on and pylon-off data and theory are shown to illustrate the large effect of the pylon on the normal-force distribution. The theory predicts the trends shown by the data quite well while missing the magnitudes of the peaks.

Figure 61 shows comparisons for the store below the pylon at the wing one-third semispan location for $M_\infty = 1.5$ and $\alpha_F = 5^\circ$. The store is at $z_F = 1.47$ inches. This location is shown in the sketch in Figure 58. The agreement is not as good as that shown in Figure 58 for $\alpha_F = 0^\circ$.

The results shown in Figures 53 through 61 are typical of those obtained for other flight conditions for similar parent aircraft configurations. It was shown in Section 8.2

that as the aircraft configuration became more complex, the flow field predictions were not as accurate. This is reflected in a loss of accuracy in the load distribution calculations.

All of the comparisons presented have used the line-singularity method to model the store. During the test program described in Reference 6 pressure data were taken on an elliptic store. Only eight pressures were measured around the circumference of the store. This was insufficient to determine accurately the load distributions in a complicated nonuniform flow field but yielded quite accurate results for the store in a uniform flow. Some comparisons will now be presented in order that the accuracy of the force and moment calculation method used for the elliptic-store option can be examined for the store in a uniform flow field. This method is described in Section 6.3.1. The store is modeled by source panels on the body surface rather than by line singularities on the body axis.

The elliptic store model on which the pressures were measured is the body of the store shown in Figure 62. The wing and tail fins were not present. The comparisons to be shown are for $M_\infty = 1.5$ with the store at a combined angle of attack of 10° and at various roll angles. The combined angle of attack is the angle between the store longitudinal axis and the free-stream velocity vector. Positive roll is right wing down.

Figure 63 shows the ratio of local static pressure, p , to free-stream static pressure, p_∞ , plotted against distance from the store nose divided by store length. For this store $l_s = 6.0$ inches. Data and theory are shown for the leeward, top, and windward, bottom, sides of the store. Except near the nose, the theory predicts the pressures very well.

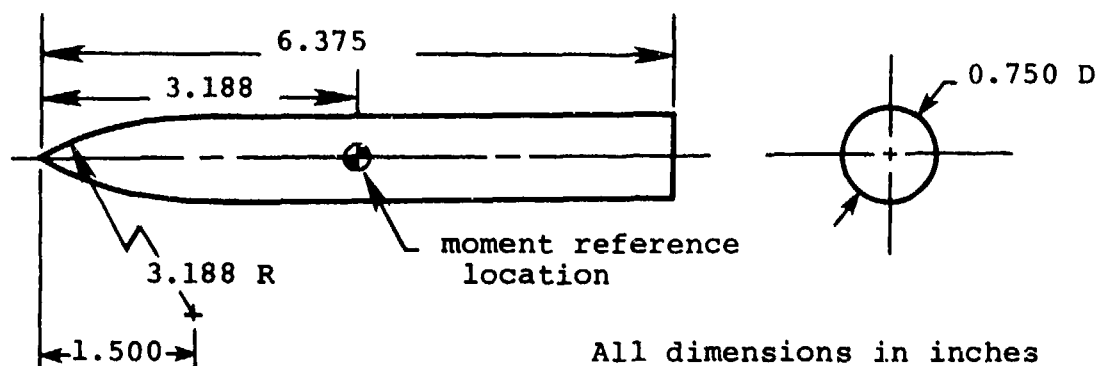
Figures 64 through 66 present comparisons of load distributions on the elliptic store at three roll angles, $\phi_s = 0^\circ$, 45° , and 90° . As the store rolls the coordinate system shown in Figure 13 and, therefore, the direction of positive forces rolls with the store. At $\phi_s = 0^\circ$ the major axis of the ellipse is horizontal. At all three roll angles the theory predicts the load distributions very well except near the base where flow separation may be occurring.

8.4 Store Forces and Moments

Comparisons between experiment and theory of the overall forces and moments acting on a store will be presented in this section of the report. The first comparisons to be shown are for a finless ogive-cylinder store in the presence of the circular fuselage, wing combination with and without a pylon. The wing-fuselage combination, N_1B_2W , is shown in Figure 21 and the pylon is shown in Figure 27. The pylon locations when attached to the aircraft are shown in Figure 26. The calculated forces and moments were obtained using the circular store option described in Section 6.2.1. Following this, results will be presented for two different stores in uniform flow; that is, no parent aircraft is present. These stores have fins and the forces and moments were calculated using the elliptic store option described in Section 6.3.

The store coordinate system (x_s, y_s, z_s) is shown in Figure 13. The positive directions of the forces and moments measured and calculated in that system are also shown in the figure. As the store pitches, yaws, and rolls, the coordinate system moves with the store.

The next seven figures, Figures 67 through 73, present results for the store shown in the following sketch. It has an ogive nose and a cylindrical afterbody. The figures



present the forces and moments as a function of Δz_F . The $\Delta z_F = 0$ positions at the three pylon locations are shown in Figure 26 and correspond to the carriage positions on the pylons. The store coordinate system (x_s, y_s, z_s) is kept parallel to the fuselage system (x_F, y_F, z_F) shown in Figure 5. The reference area used in forming the coefficients is the store frontal area, 0.4418 in^2 , and the reference length in the moment coefficients is the maximum diameter, 0.75 in. The point about which the moments are taken is shown in the sketch.

Figures 67 through 69 present results for the store in the presence of the wing-fuselage combination without a pylon. The Mach number is 1.5 and the angle of attack is 0° . Figure 67 presents results at the wing one-third semispan location, $y_F = -4$ inches. Results under the fuselage centerline, $y_F = 0$ inches, are shown in Figure 68, and results at the wing two-thirds semispan location, $y_F = -8$ inches, are shown in Figure 69. In general, the trends shown by the data are predicted fairly well. The poorest agreement between data and theory occurs at the two-thirds semispan location, Figure 69. At both wing stations, the normal force is not well predicted as the carriage position is approached, $\Delta z_F \rightarrow 0$.

Figure 70 presents results at the one-third semispan for $\alpha_F = 5^\circ$. The store is also at this angle of attack relative to the free stream. Comparing these results with those in Figure 67 for $\alpha_F = 0^\circ$ shows poorer agreement for $\alpha_F = 5^\circ$.

Comparisons with a pylon present either at the wing one-third semispan location or under the fuselage centerline are presented in Figures 71 through 73. The results shown in Figure 71 are for $M_\infty = 1.5$ and $\alpha_F = 0^\circ$ at the one-third semispan location. The trends shown by the data are predicted quite well by the theory except for C_N and C_m as $\Delta z_F \rightarrow 0$.

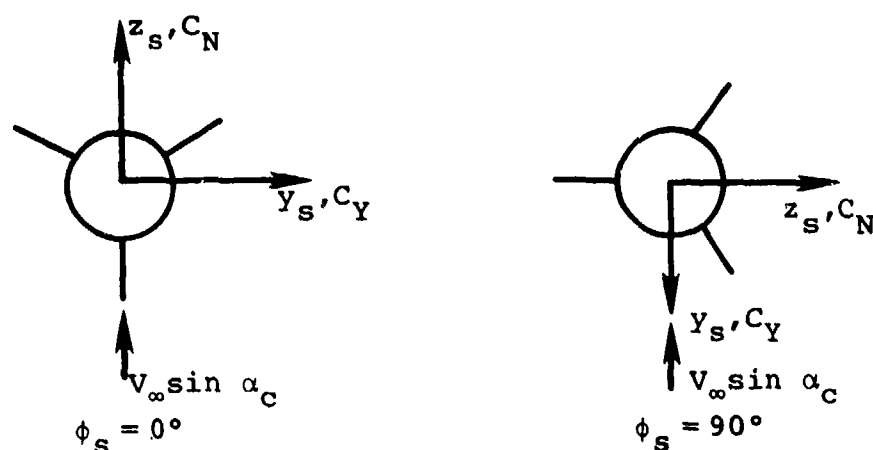
Figure 72 presents comparisons for the fuselage centerline location at $M_\infty = 1.5$ and $\alpha_F = 0^\circ$. The trends shown by the data are well predicted by the theory. At large Δz_F the theory predicts a return to the free-stream values of $C_N = C_m = 0$ sooner than seen in the data.

Comparisons are present in Figure 73 for $M_\infty = 1.5$ and $\alpha_F = 5^\circ$ for the store under the pylon at the wing one-third semispan location. The agreement between experiment and theory is not as good as that shown in Figure 71 for $\alpha_F = 0^\circ$.

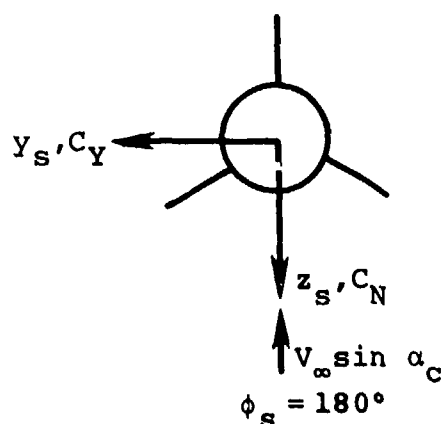
The comparisons presented in Figures 67 through 73 used the circular store option to calculate the body forces and moments, Section 6.2.1. It is of interest to see how the elliptic store option predicts the store forces and moments. This will be done by comparing with data obtained on two different store models. These data were taken without a parent aircraft present; that is, the store is in the free stream. The methods used to calculate the forces and moments are described in Section 6.3.

The first comparisons are for the store shown in Figure 74. It has an ogive nose, cylindrical body, and tri-form fins. The forces and moments measured on this store at $M_\infty = 1.5$ are shown in Figure 75 along with those predicted by the theory. Data are shown for two store roll angles, $\phi_s = 0^\circ$

and 90° . The fin orientations at these two angles and the orientations of the store coordinate system are shown in the following sketch. Positive directions of C_N and C_Y are also



shown in the sketch. Also presented in Figure 75 are results for $\phi_s = 0^\circ$ at negative α_c . This corresponds to $\phi_s = 180^\circ$ at positive α_c . This fin orientation is as shown below.



The agreement between experiment and theory shown in Figure 75 is quite good. Comparisons of C_Y , C_N , and C_ℓ are presented only for $\phi_s = 90^\circ$. These coefficients are zero for the $\phi_s = 0^\circ$ and 180° roll orientations.

Figure 76 presents comparisons between experiment and theory for the elliptic store shown in Figure 62. This store has an elliptic body with a monoplane wing and an interdigitated tail. Comparisons are shown in Figure 76 for three roll angles, $\phi_s = 0^\circ, 50^\circ, \text{ and } 90^\circ$. It should be remembered that as the store rolls the coordinate system in which the forces and moments are measured rolls with the store as shown in the preceding sketches. Thus, C_N and C_m are zero for $\phi_s = 90^\circ$, C_Y and C_n are zero for $\phi_s = 0^\circ$, and C_l is equal to zero for $\phi_s = 0^\circ$ and 90° . It can be seen the method of Section 6.3 predicts the forces and moments quite well. Because of the close coupling of the wing and tail fins, the trailing-edge vortex interference described in Section 6.3.3 has not been included in the calculations. In this short of a distance, the vortices are not fully developed.

8.5 Store Trajectories

Comparison between theory and data will now be presented for two store separation trajectories. The data are from Reference 6. The trajectory calculation method was described in Section 7 of this report. One trajectory uses a circular fuselage, wing, and pylon combination for the parent aircraft. The second configuration is made up of a noncircular fuselage, engine inlets, wing, and pylon. In order to simulate full-scale flight conditions the wind-tunnel model components shown in Figures 21 through 28 have been scaled up by a factor of twenty.

For both trajectories the simulated altitude is 40,000 feet, the Mach number is 1.5, and the aircraft angle of attack is 5° . The store angle of attack at time, t , equal zero is the same as the aircraft. In both cases the aircraft flight path angle, γ_f , is zero degrees. That is, the aircraft is in horizontal flight, not climbing or diving. At $t = 0$ seconds the store is

in the carriage position on the pylon and is not moving relative to the parent aircraft. For both trajectories aerodynamic damping was set to zero. The store thrust is zero.

In both trajectories the following ejector force, time history is used for $0 \leq t \leq 0.075$ seconds.

$$F_e = 1.41448 \times 10^5 t + 2.68614 \times 10^6 t^2 - 2.2209 \times 10^8 t^3 \\ + 3.52968 \times 10^9 t^4 - 1.70086 \times 10^{10} t^5, \text{ lbs}$$

At $t = 0$ seconds $F_e = 0$ pounds. The force reaches a maximum of $F_e \approx 3,000$ pounds at $t \approx 0.03$ seconds and then decreases to $F_e \approx 2,000$ pounds at $t = 0.075$ seconds. This force is shown graphically in Figure 24 of Reference 6. When $t > 0.075$ seconds, $F_e = 0$ pounds. One ejector foot is used in both trajectories, however, the location is different.

The store center of mass in both cases is taken to coincide with the moment centers so that in the equations of motion

$$\bar{x} = \bar{y} = \bar{z} = 0$$

and, therefore,

$$I_{xy} = I_{yz} = I_{xz} = 0$$

The parent aircraft configuration used for the first trajectory is shown in Figure 77. The dimensions shown are full scale in feet. The configuration consists of the circular fuselage, wing combination $N_1 B_2 W$ shown in Figure 21 with pylon P_3 shown in Figure 28 attached at the wing one-third semispan position. An ogive-cylinder store with cruciform tail fins is located as shown. The tail fins are oriented 45° from the vertical and horizontal. Details of the store in model scale

are shown in Figure 78. For this trajectory, the one ejector foot strikes the store 1.5 feet full scale behind the moment reference location shown in Figure 78. In both experiment and theory the store rolling moment is set to zero. The store mass and inertia characteristics are

$$\begin{aligned} m &= 40 \text{ slugs} \\ I_{xx} &= 20 \text{ slug-ft}^2 \\ I_{yy} &= I_{zz} = 700 \text{ slug-ft}^2 \end{aligned}$$

The trajectory results for this case are shown in Figure 79. Figures 79(a), (b), and (c) show the location of the store center of gravity (moment reference location) relative to its location in the carriage position on the pylon. The ξ, η, ζ coordinate system coincides with the x_F, y_F, z_F system shown in Figure 5. The store moves aft, outboard, and down relative to the aircraft. The axial and vertical motion are well predicted by the theory while the small outboard lateral motion is underpredicted. Figures 79(d) and (e) show the pitch and yaw motions of the store relative to the carriage attitude, $\theta = 5^\circ$, $\psi = 0^\circ$. The theory underpredicts both motions.

The parent aircraft used for the second trajectory comparison is shown in Figure 80. It is configuration $N_3B_2WA_4(P_2)_C$. These model components are shown in Figures 21, 23, 25, and 27. The dimensions shown in Figure 80 are full scale. The elliptic store in model scale is shown in Figure 62. When the store is mounted on the pylon, the reference mark shown in Figure 62 is at the pylon 50 percent chord location. For this trajectory, the one ejector foot strikes the store 1.0 foot behind the store moment center, the assumed center of gravity. The store mass and inertia characteristics are

$$\begin{aligned}
 m &= 20 \text{ slugs} \\
 I_{xx} &= 20 \text{ slug-ft}^2 \\
 I_{yy} &= I_{zz} = 250 \text{ slug-ft}^2
 \end{aligned}$$

The trajectory results for this case are shown in Figure 81. The axial motion is well predicted and there is no lateral motion since the store is under the fuselage centerline and the configuration is symmetric. For the first 0.2 second the vertical motion is well predicted by the theory but for $t > 0.2$ second the agreement is poor. This can be explained in the following way. The initial vertical motion is due to the ejector stroke, $0 \leq t \leq 0.75$ second. At the end of this time the aerodynamic forces are the only forces other than the gravitational force acting on the store. If the pitch motion shown in Figure 81(d) is examined, it is seen the theory predicts the store to pitch nose up while the data show the store pitching nose down. The store angle of attack relative to the free stream is the sum of α_F and $\Delta\theta$ where, in this case, $\alpha_F = 5^\circ$. The theory predicts the store to always be at positive angle of attack, $\Delta\theta > -5^\circ$, which causes it to want to lift toward the aircraft. The data show the store pitching nose down to negative angle of attack, $\Delta\theta < -5^\circ$, which would fly the store away from the aircraft. The poor prediction of the initial pitch motion is not surprising in view of the poor velocity field prediction shown in Figure 50. Those are the velocities along the store centerline at $t = 0$ seconds.

9. CONCLUDING REMARKS

This report presents the results of an investigation which has been conducted with the objective of extending and improving the supersonic store separation prediction method of References 1 and 2. In this earlier work the fuselage and single store were limited to bodies of revolution. The store could have one set of planar or cruciform fins. Wing dihedral and incidence relative to the fuselage were not accounted for. An ejector rack could not be modeled. The forces and moments acting on the separating store in the nonuniform flow field were calculated using slender-body theory and wing-fuselage-store interference effects were not accurately modeled. All of these shortcomings have been eliminated in the present work.

In the present work linear, potential flow methods are used to model the various aircraft components. Nonlinear corrections are made to these models to position shock waves more accurately. Two fuselage models are available. A circular fuselage can still be modeled by a distribution of line sources, sinks, and doublets on the fuselage axis. A noncircular fuselage, including engine inlets, is modeled by a distribution of source panels on the body surface which account for both volume and angle of attack effects.

A layout of constant u-velocity panels on the wing and pylon (if present) model the lifting surfaces. The wing may have dihedral which can vary across the span. Wing incidence relative to the fuselage is included in the wing boundary condition. Wing and pylon thickness effects are modeled by an additional layout of source panels. Wing and pylon mutual interference is fully accounted for. Mutual interference between the wing and pylon and the fuselage is handled by constant u-velocity panels placed on an interference shell which extends over part of the fuselage.

An ejector rack model is included. The rack body is modeled as a body of revolution by a distribution of line sources, sinks, and doublets on the body axis.

Up to seven stores may be included. They may be modeled as bodies of revolution by line sources, sinks, and doublets on the body axis or as an elliptical body by a distribution of source panels on the body surface to account for both volume and lift effects.

In conjunction with the analytical work, an extensive and systematic wind-tunnel test program was carried out to provide flow-field data for checking and improving the accuracy of the flow models and the flow-field calculation methods. In addition, store axial load distributions, store forces and moments, and store separation trajectories were measured to provide data to be used in evaluating the methods used in calculating the store forces and moments and trajectories. The wind-tunnel test program is described in detail in Reference 6.

Flow-field comparisons presented in this report show that the flow fields produced by a circular fuselage, a non-circular fuselage, a circular fuselage with wing, and a circular fuselage with wing and pylon are quite accurately predicted by the theory. The agreement deteriorates with increasing Mach number and configuration complexity. Comparisons are also presented for a configuration which has a triple ejector rack attached to a wing mounted pylon. The flow-field prediction is fair. Improved predictions could be obtained if more singularities could be used in modeling the aircraft. A comparison presented for a complex aircraft configuration including engine inlets shows poor agreement between data and theory. Additional work is required to improve the inlet shock wave model. The wind-tunnel data also show significant viscous effects.

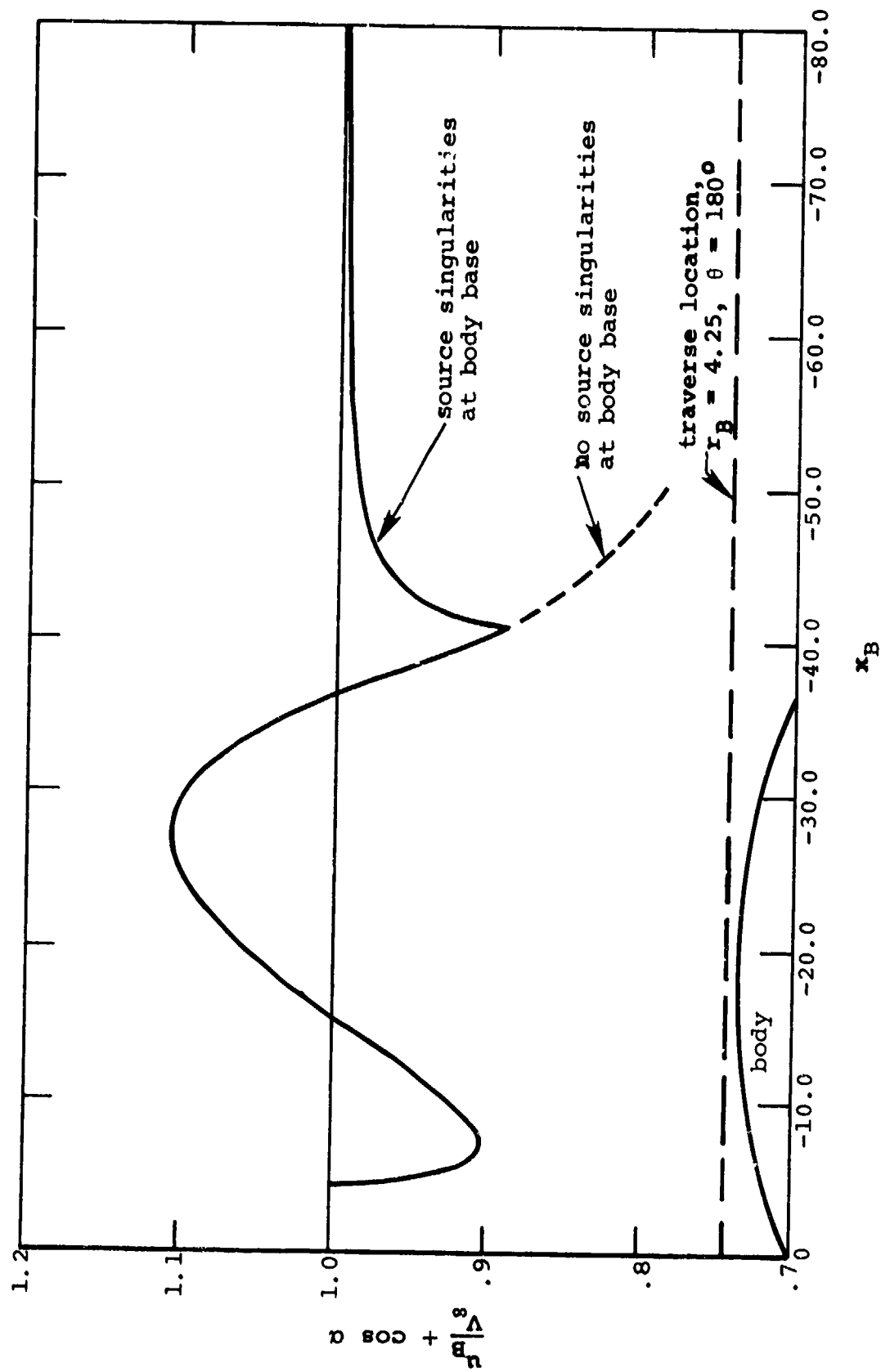
In the present work, mutual interference between the separating store and the wing-fuselage combination is accounted for by an imaging scheme. Image stores are placed above the wing and inside the fuselage to account for reflections of the store nose shock wave off of these surfaces. Comparisons with experimental load distributions show this imaging scheme to work quite well.

Two options exist in the computer program for calculating the store forces and moments. The circular store option uses line sources and sinks and two sets of line doublets placed on the store axis to model the store body in the nonuniform flow field. This method replaces the slender-body theory method used in Reference 1. The method used to calculate empennage forces is unchanged. It is based on slender-body theory with a correction for aspect ratio and includes an application of reverse-flow theorems. Comparisons with data for store-body load distributions and total forces and moments show that the line-singularity method gives quite accurate results for parent aircraft configurations consisting of a circular fuselage with wing or wing and pylon.

The second option, the elliptic store option, models the store body in the nonuniform flow field by a distribution of source panels placed on the body surface. The store can have two sets of fins. They are modeled by distributions of constant u -velocity panels placed on the fins and on interference shells on the body to account for fin-body interference. Comparisons between data and theory are presented for two stores in a uniform stream, an ogive-cylinder store with triform fins and an elliptic store with monoplane wing and interdigitated tails. The theory predicts the forces and moments for both configurations quite well.

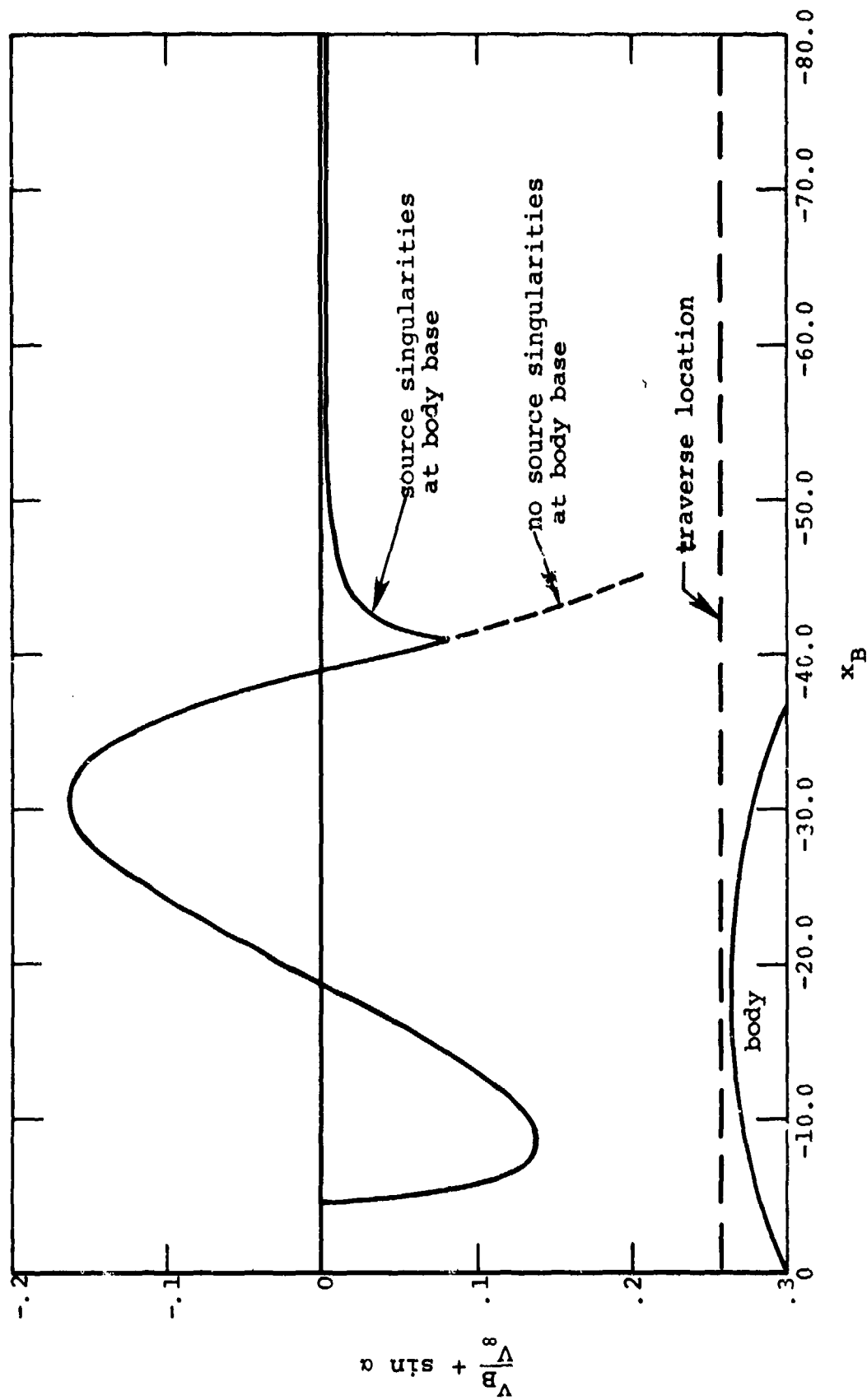
Comparisons between theory and experiment are presented for two store separation trajectories. The first is for an ogive-cylinder store separating from a pylon on the wing of

a circular fuselage, wing combination. The theory predicts the separation trajectory well enough that it could be used for preliminary design purposes. The parent aircraft used in the second comparison is comprised of a noncircular fuselage with engine inlets, wing, and fuselage centerline pylon. An elliptic store with monoplane wing and interdigitated tail is separated from the pylon. The agreement between theory and experiment is poor. The reason for this is thought to be that the flow field induced by the inlets is not modeled accurately. Additional work must be done to improve the inlet model. Additional comparisons should also be made to validate the method further.



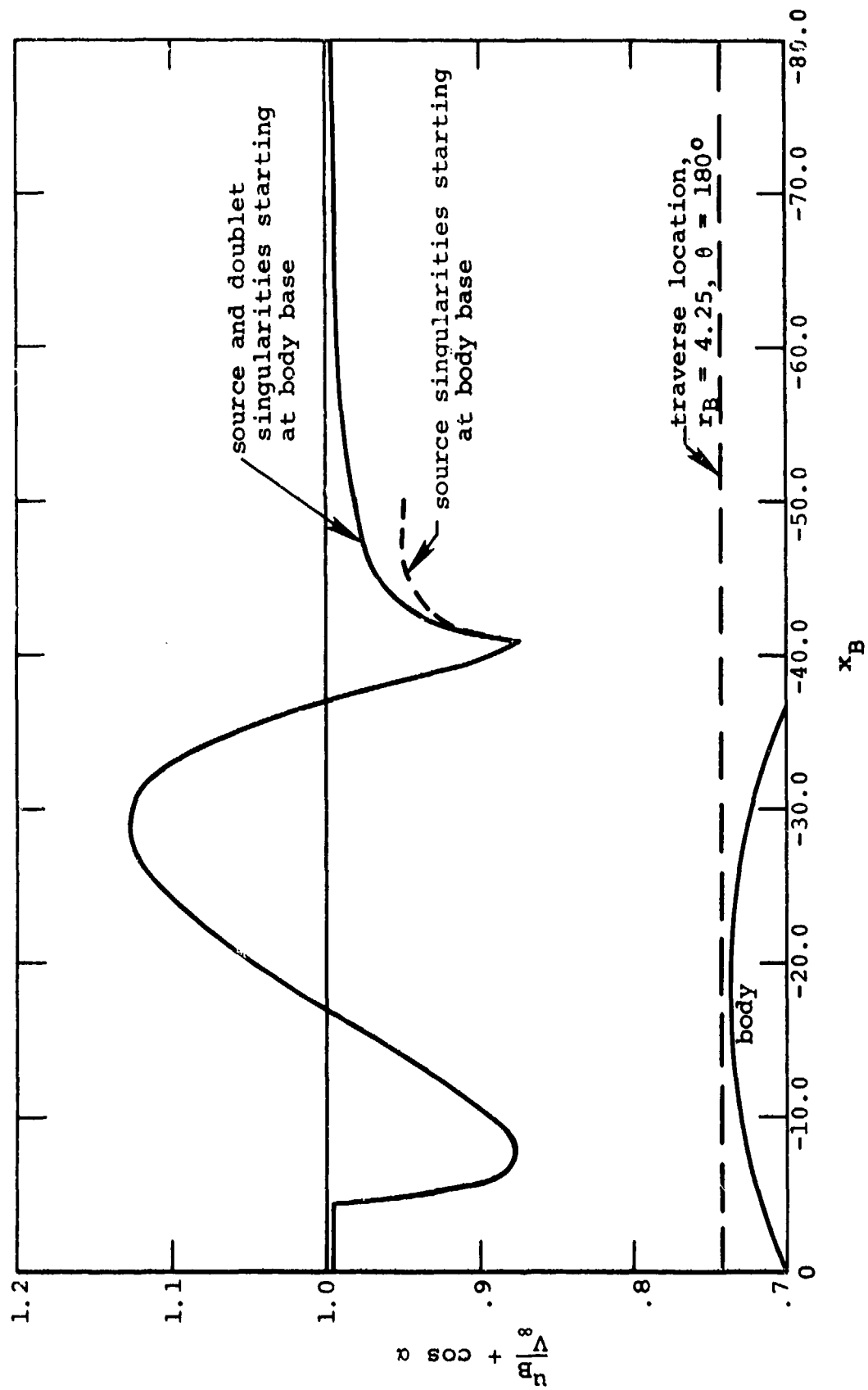
(a) Axial velocity.

Figure 1.- Flow field below a circular arc body ($L/D=5$), $M_\infty 1.5$, $\alpha = 0^\circ$.



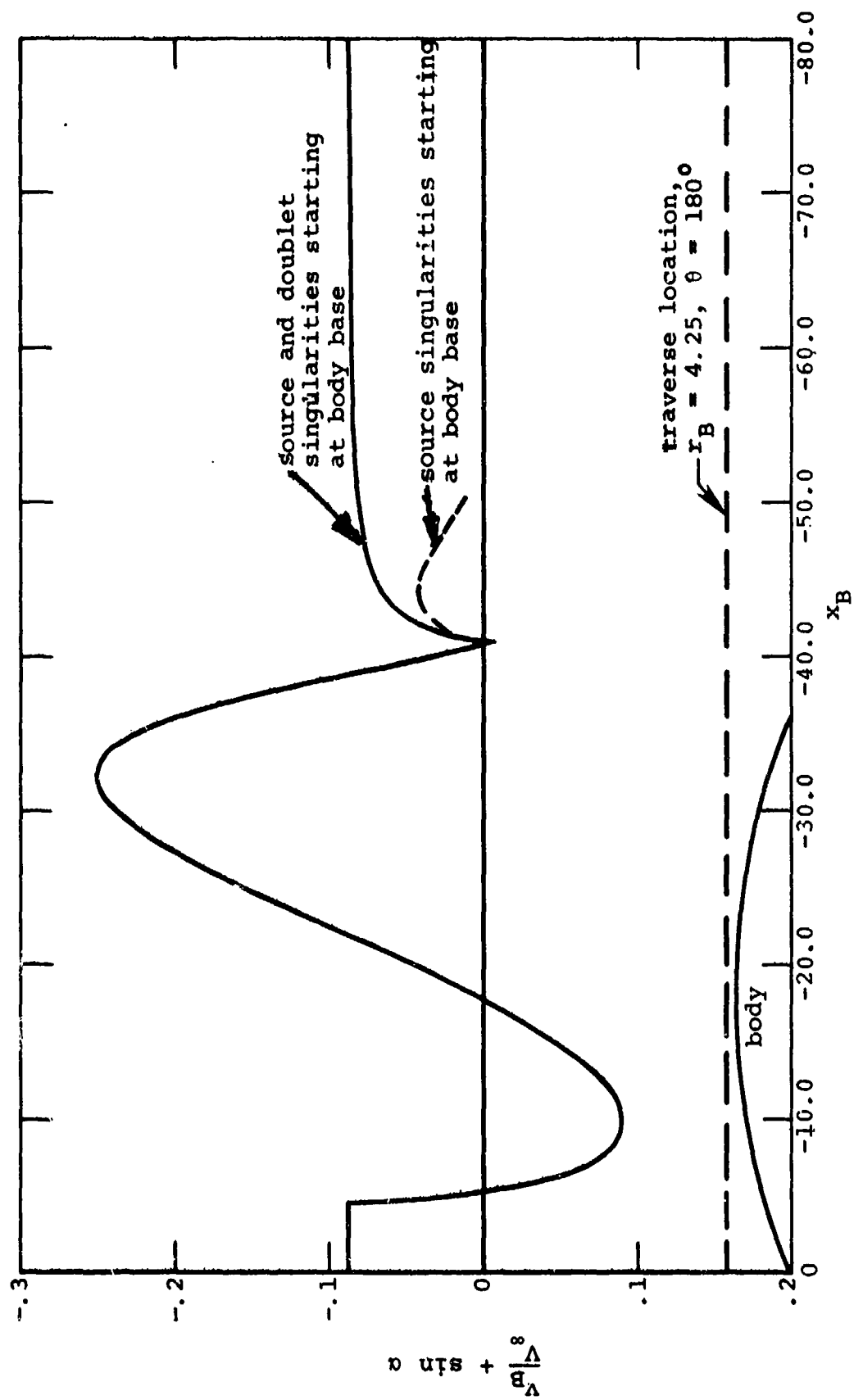
(b) Radial velocity.

Figure 1.- Concluded.



(a) Axial velocity.

Figure 2.- Flow field below a circular arc body ($L/D=5$), $M_\infty = 1.5$, $\alpha = 5^\circ$.



(b). Radial velocity.

Figure 2.- Concluded.

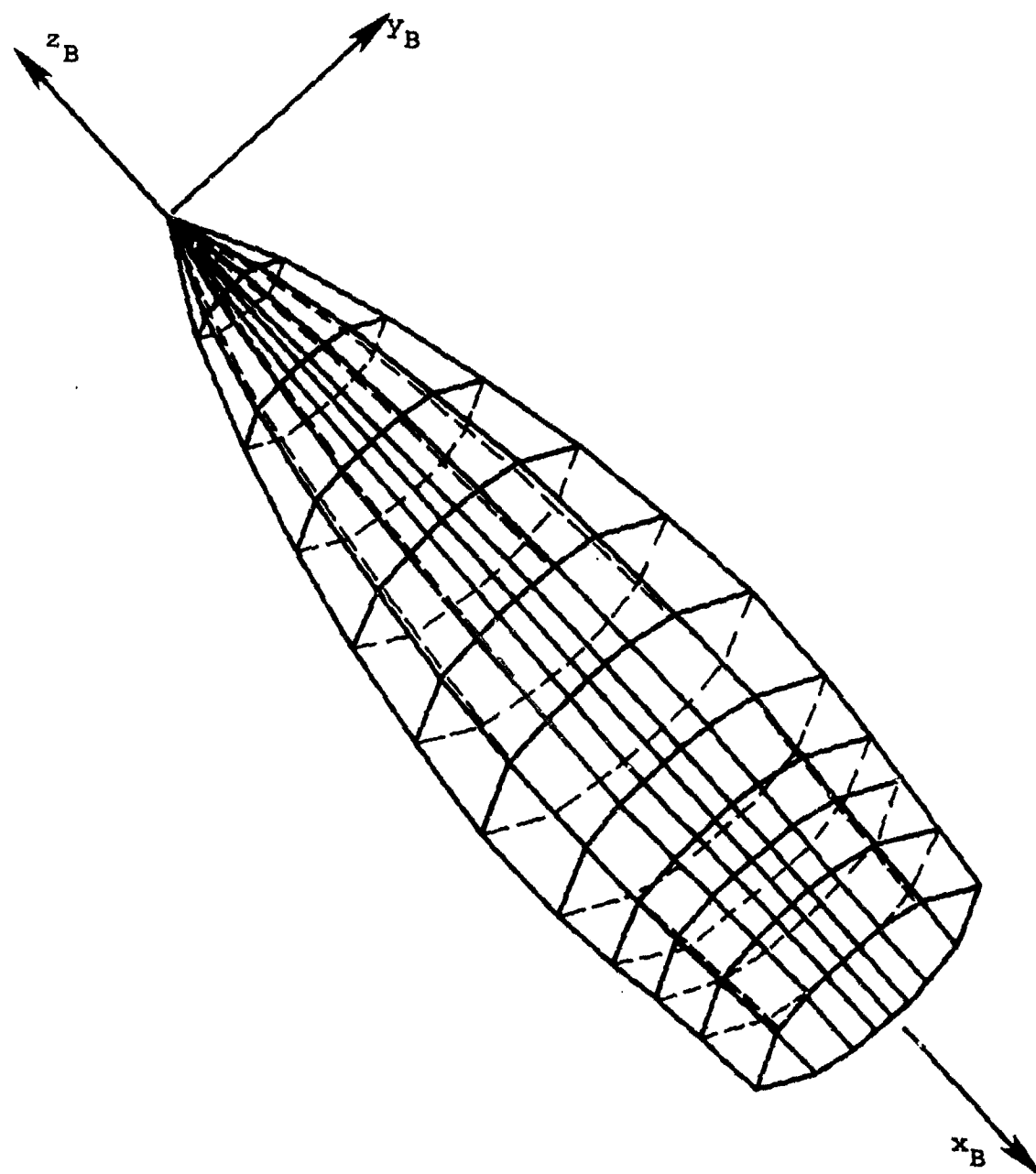


Figure 3.- Isometric view of typical layout of body source panels on the surface of a body with elliptical cross section, 11 rings with 16 panels each.

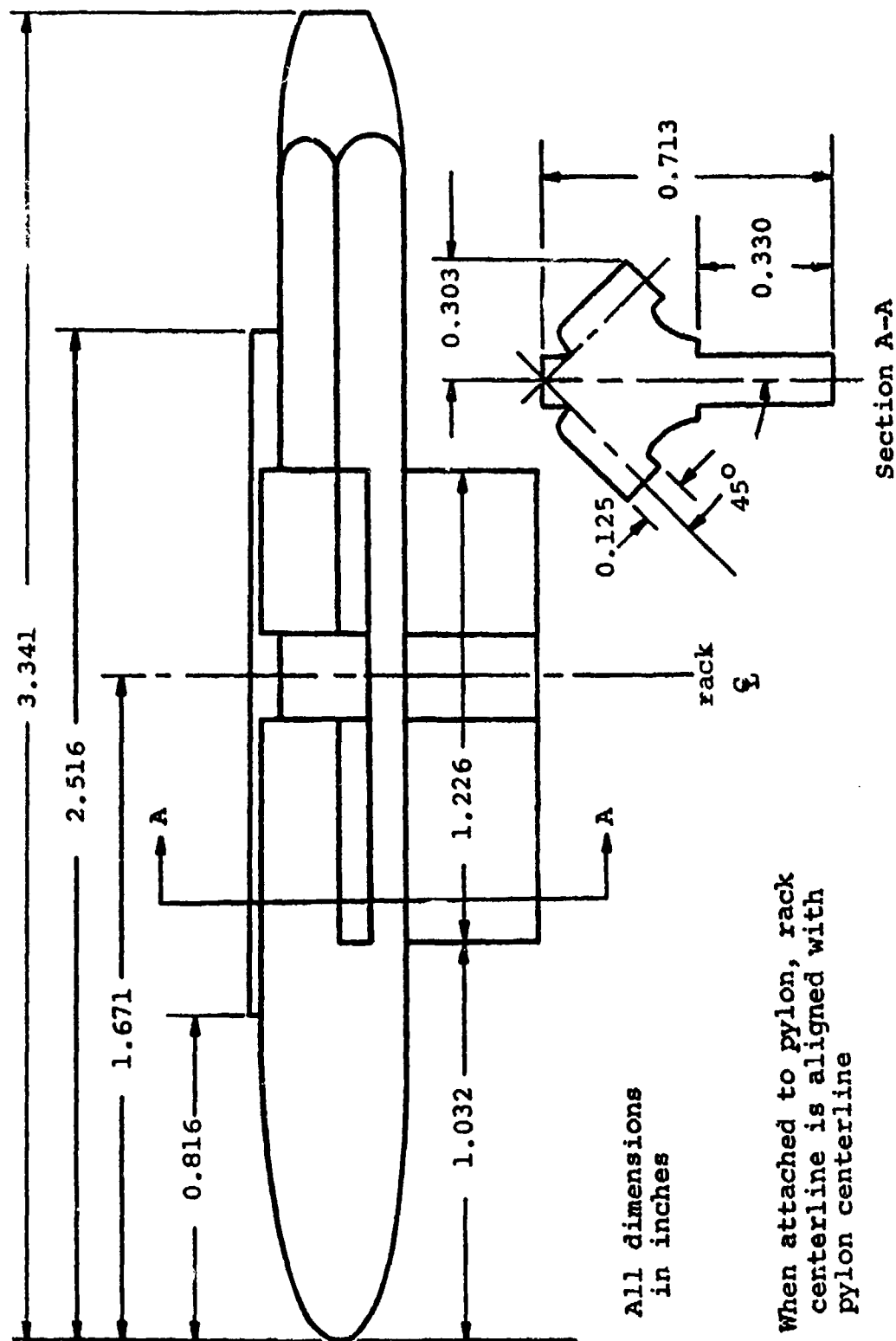


Figure 4.- Triple ejection rack, TER.

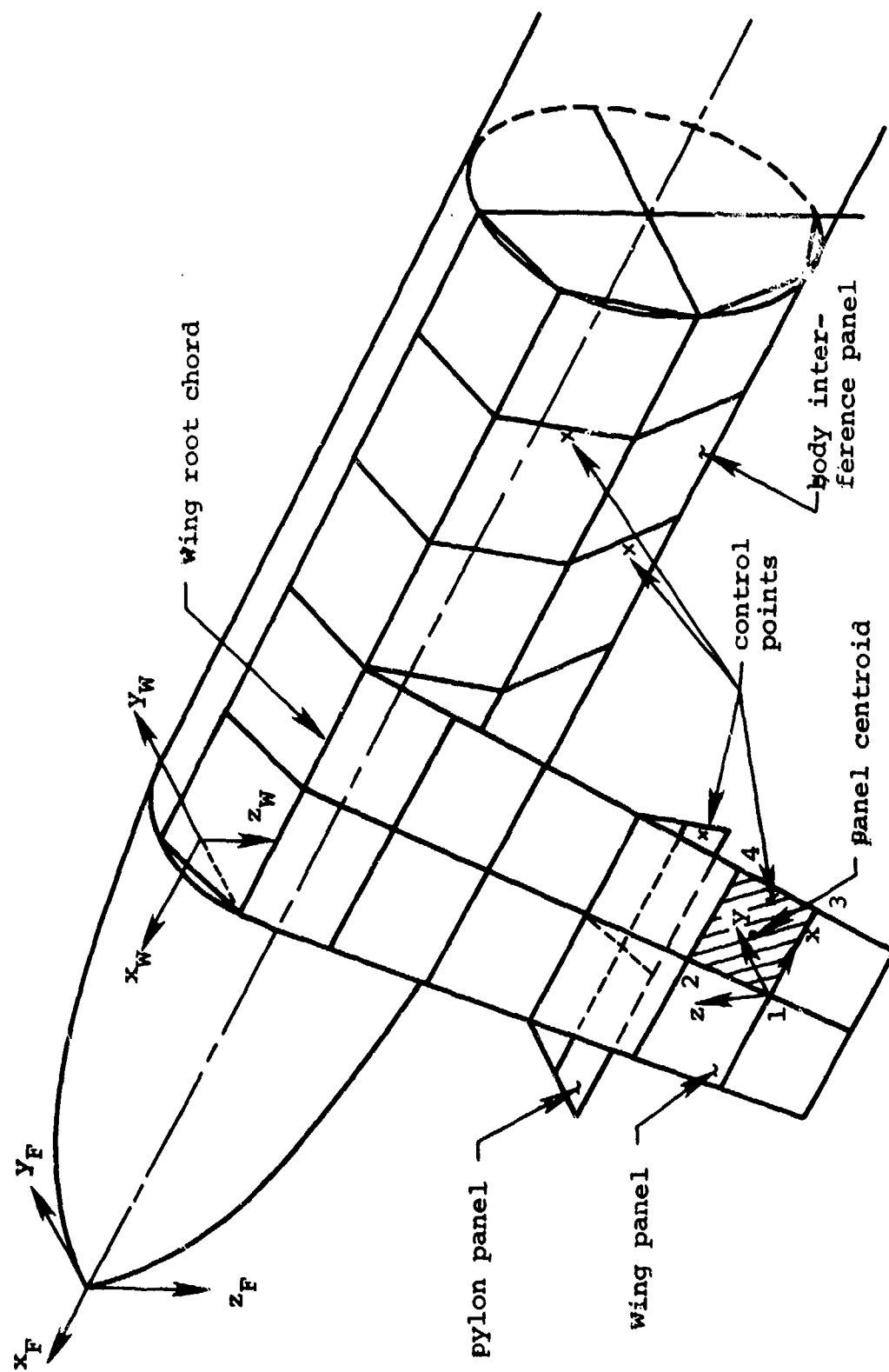


Figure 5.- Simplified layout of panels for wing-pylon-fuselage combination.

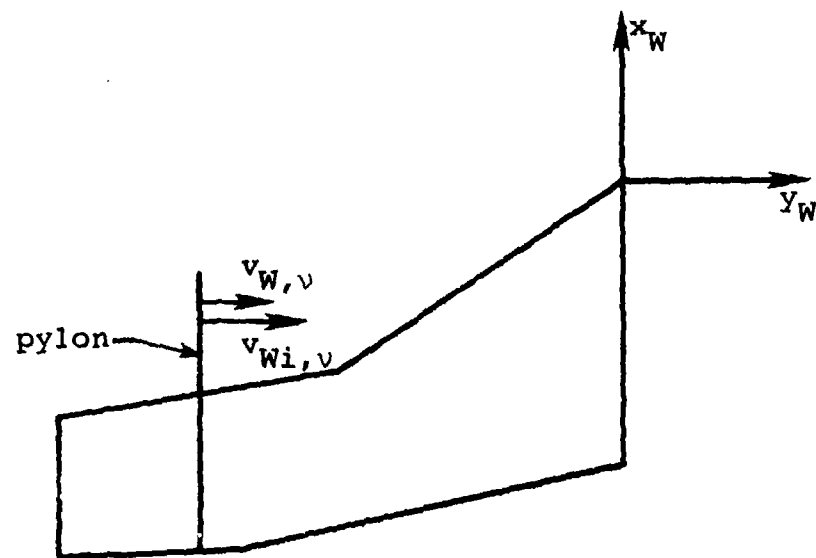
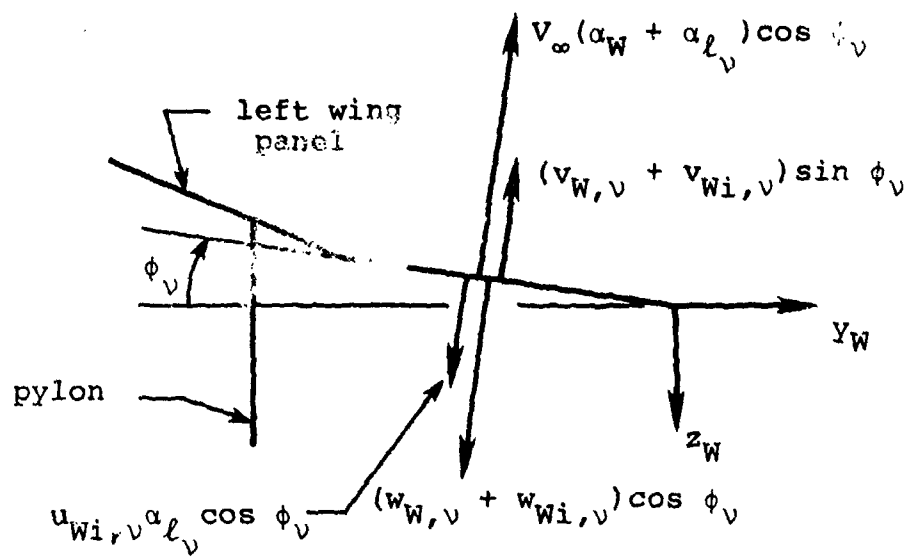


Figure 6.- Flow tangency boundary conditions for the wing and pylon.

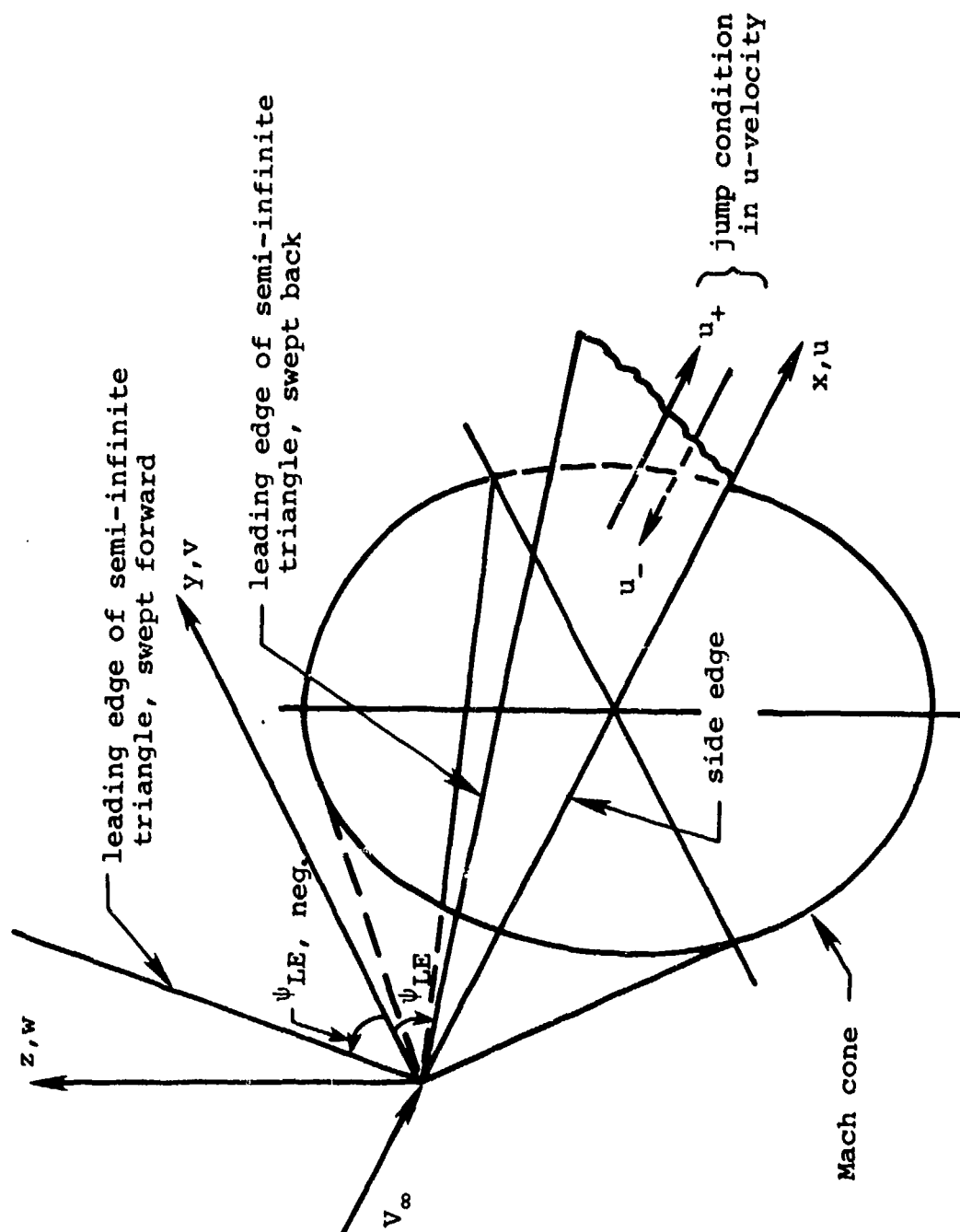


Figure 7.- Layout of semi-infinite triangular shape and associated coordinate system.

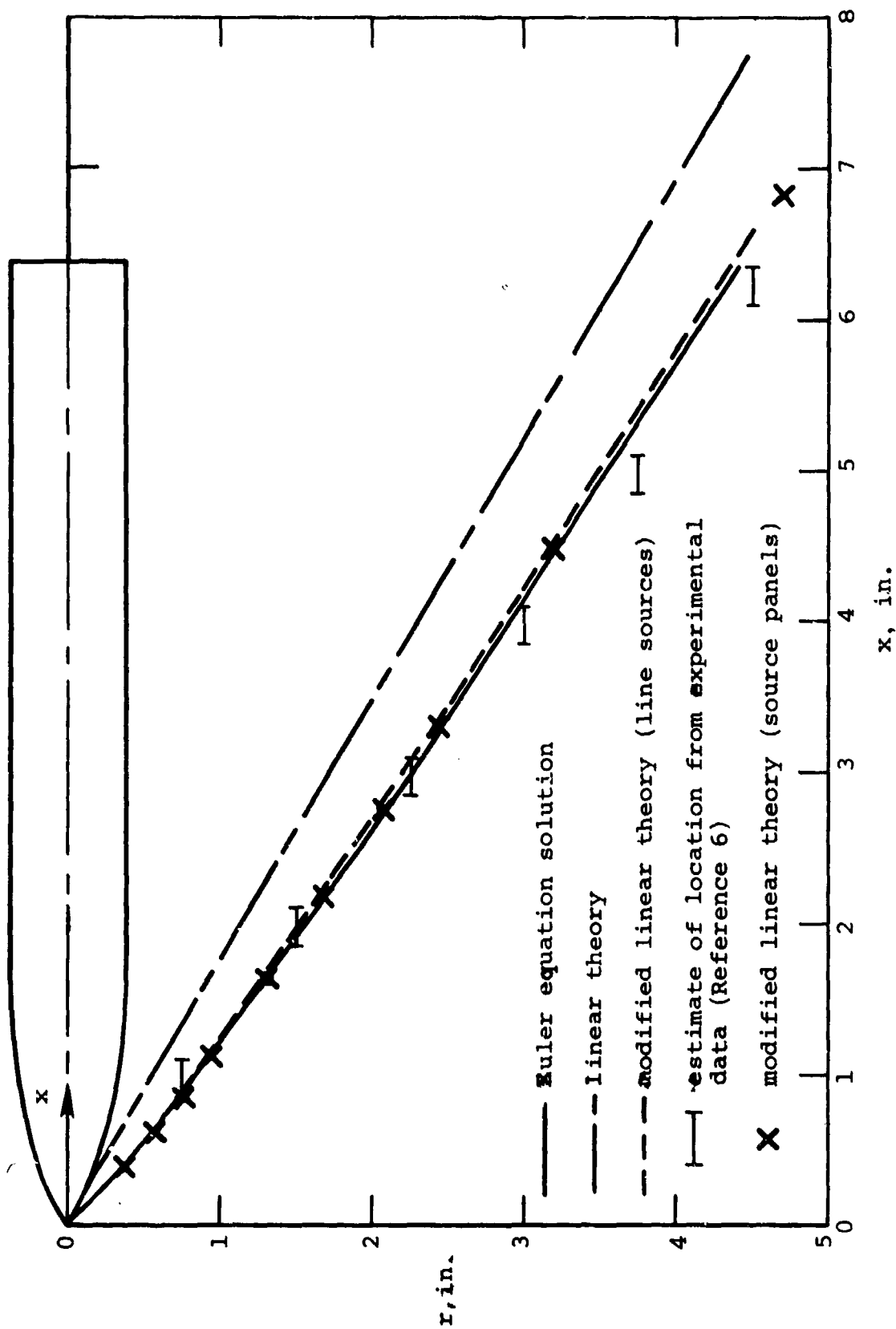


Figure 8.- Predictions of shock wave shape; $M_\infty = 2.0$, $\alpha = 0^\circ$.

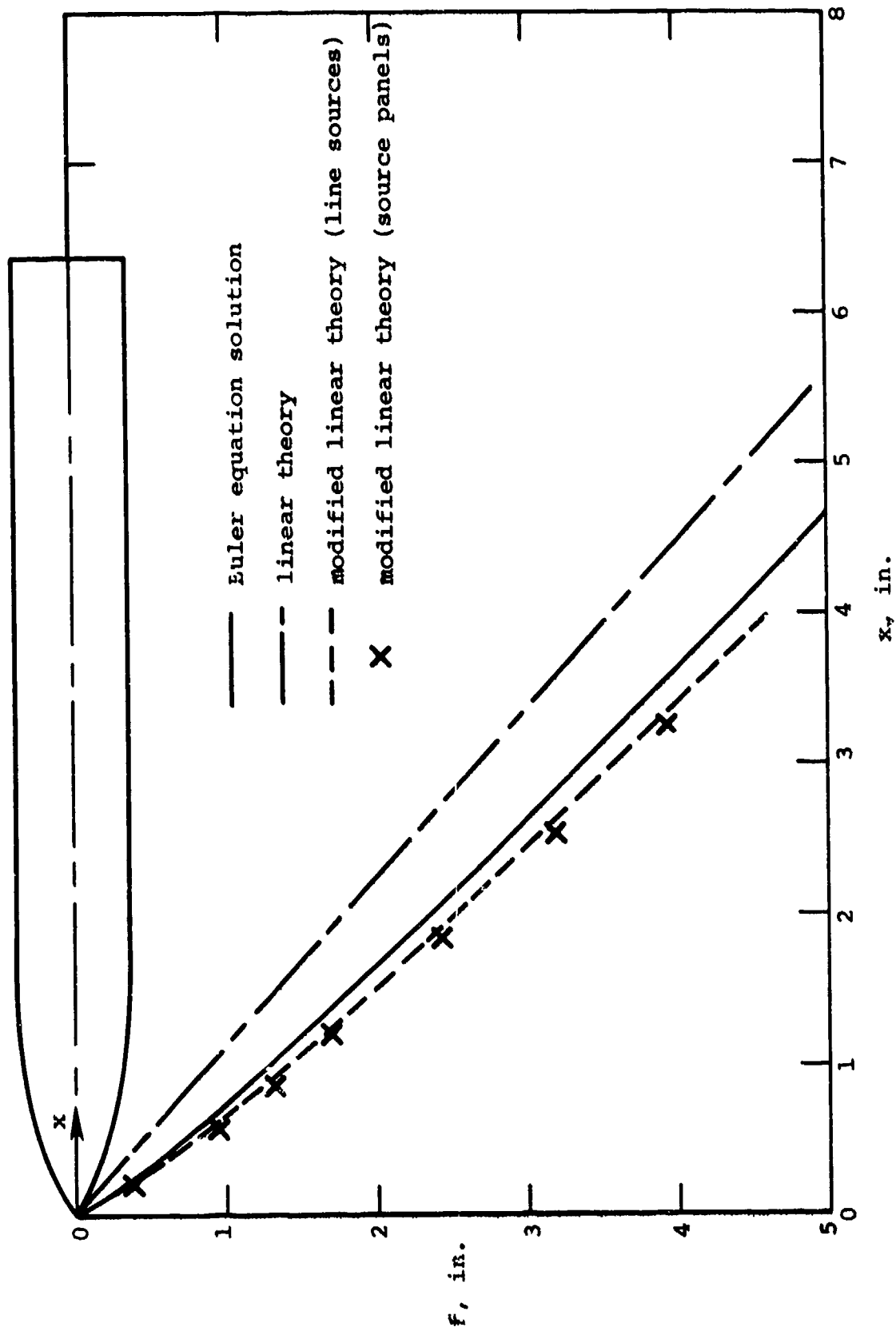


Figure 9.- Prediction of shock wave shape; $M_\infty = 1.5$, $\alpha = 0^\circ$.

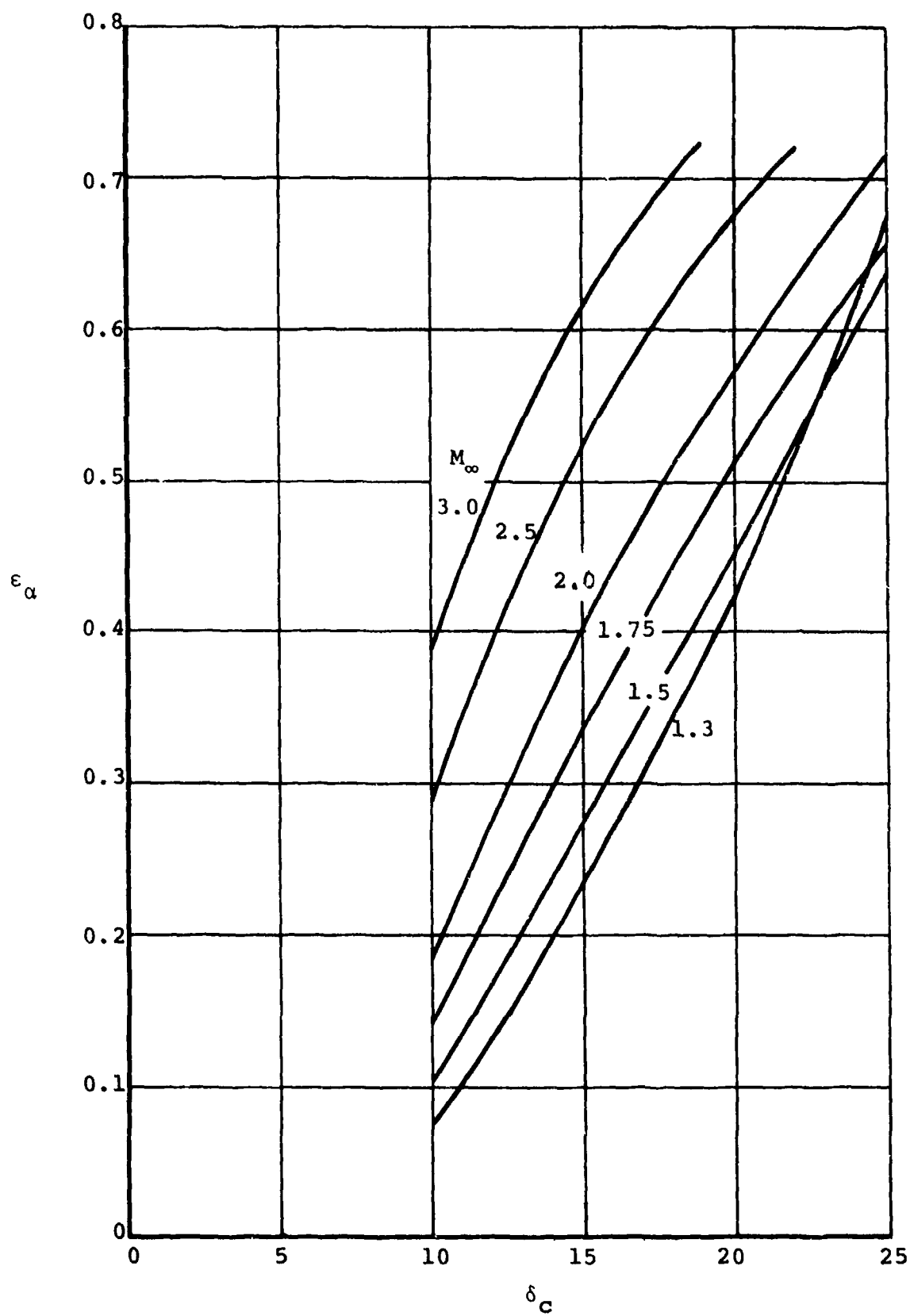


Figure 10.- Shock angle of attack correction factor, ϵ_α .

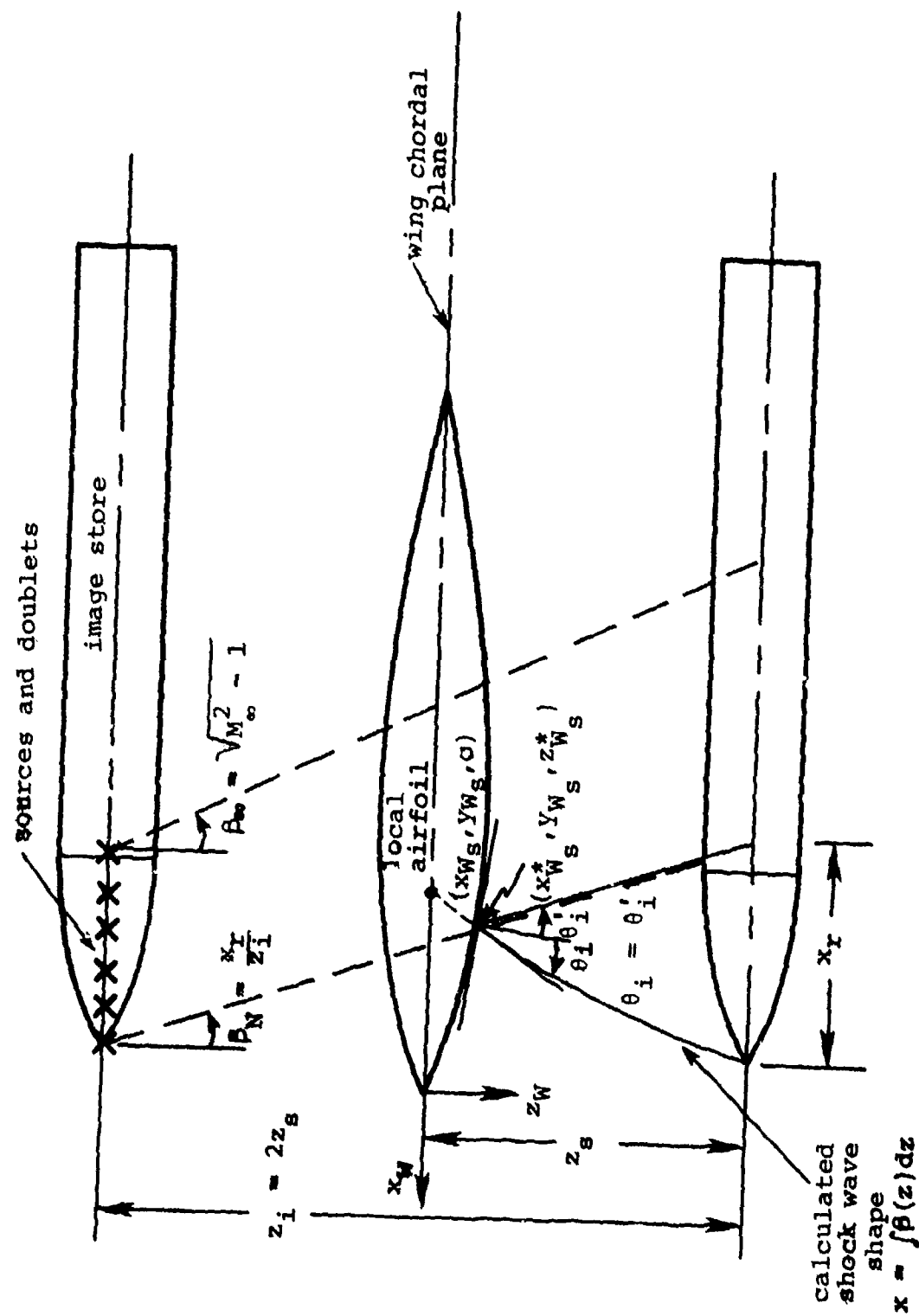


Figure 11.- Circular store wing imaging.

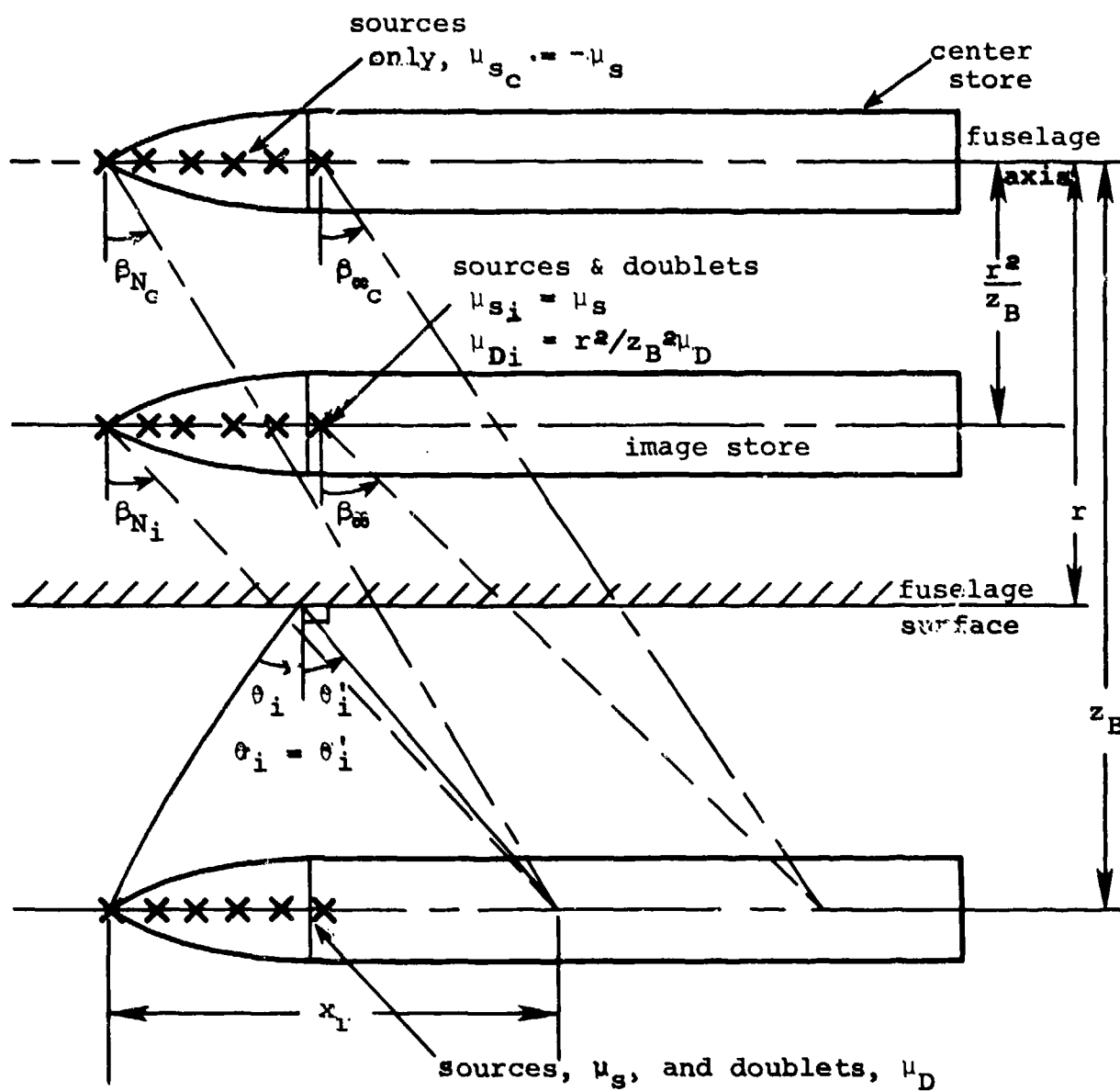


Figure 12.- Circular store fuselage imaging.

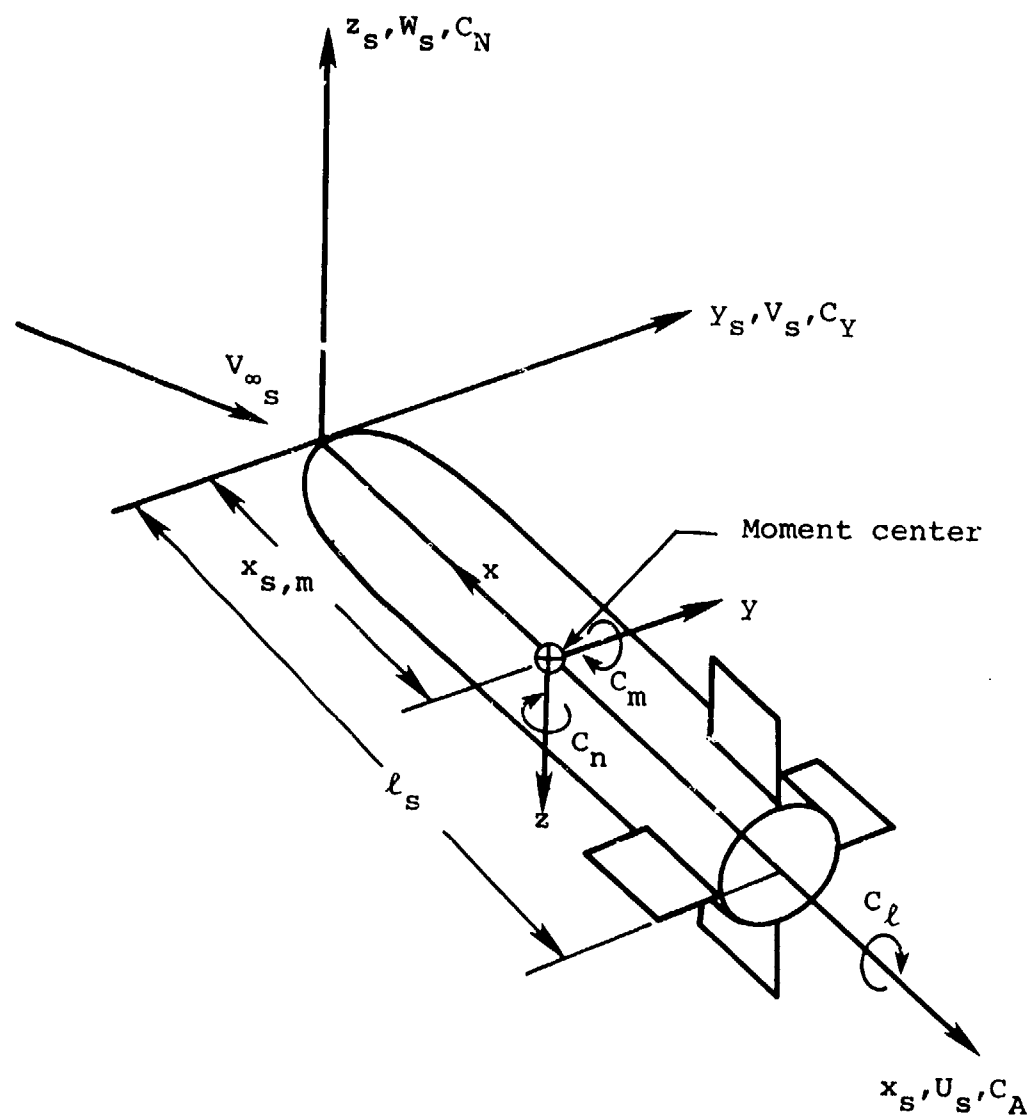


Figure 13.- Coordinate systems fixed in separated store and used in force and moment calculation.

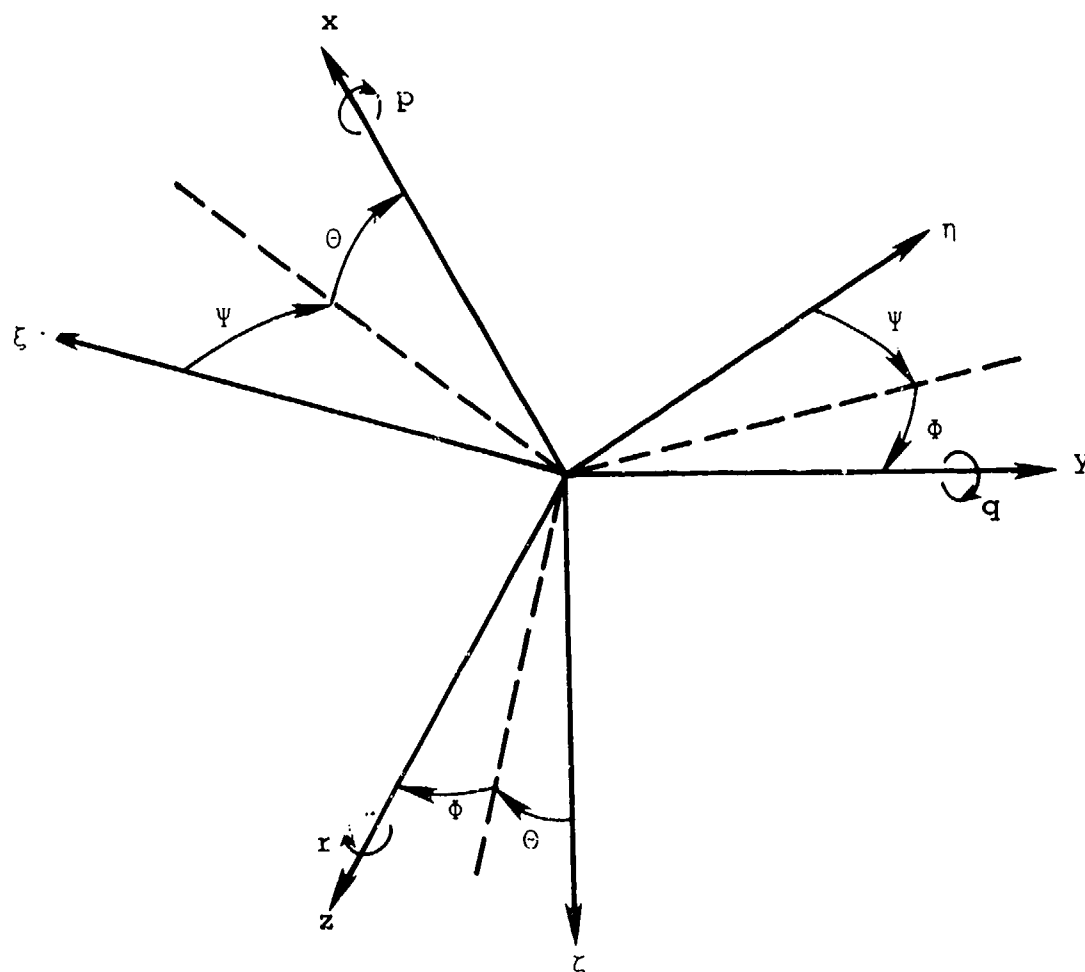


Figure 14.- Coordinate system used in trajectory calculation.

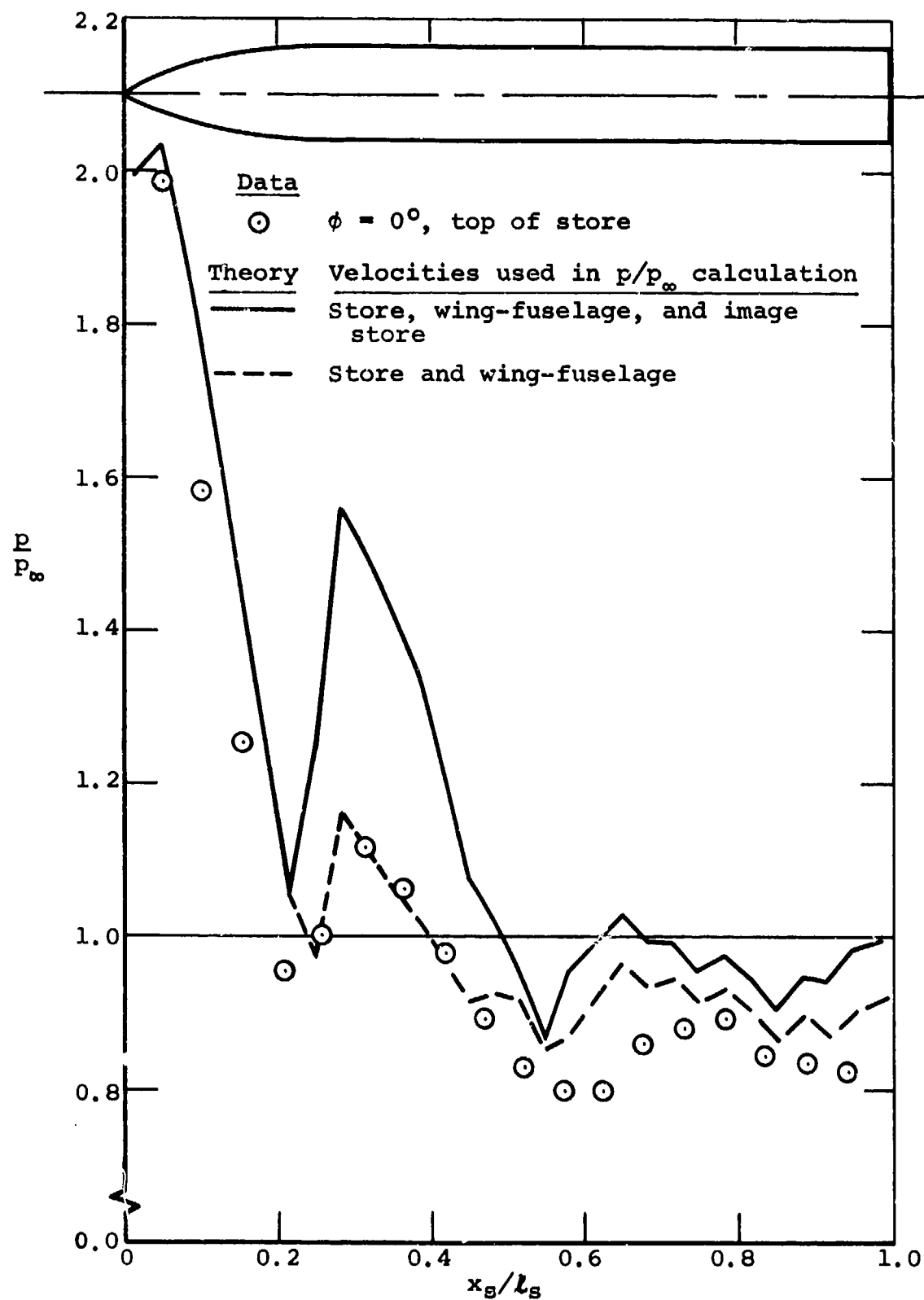


Figure 15.- Pressure distribution on top of store in presence of wing-fuselage; $M_\infty = 1.5$, $\alpha = 0^\circ$, $y_F = -4$ in., $z_F = 1.47$ in.

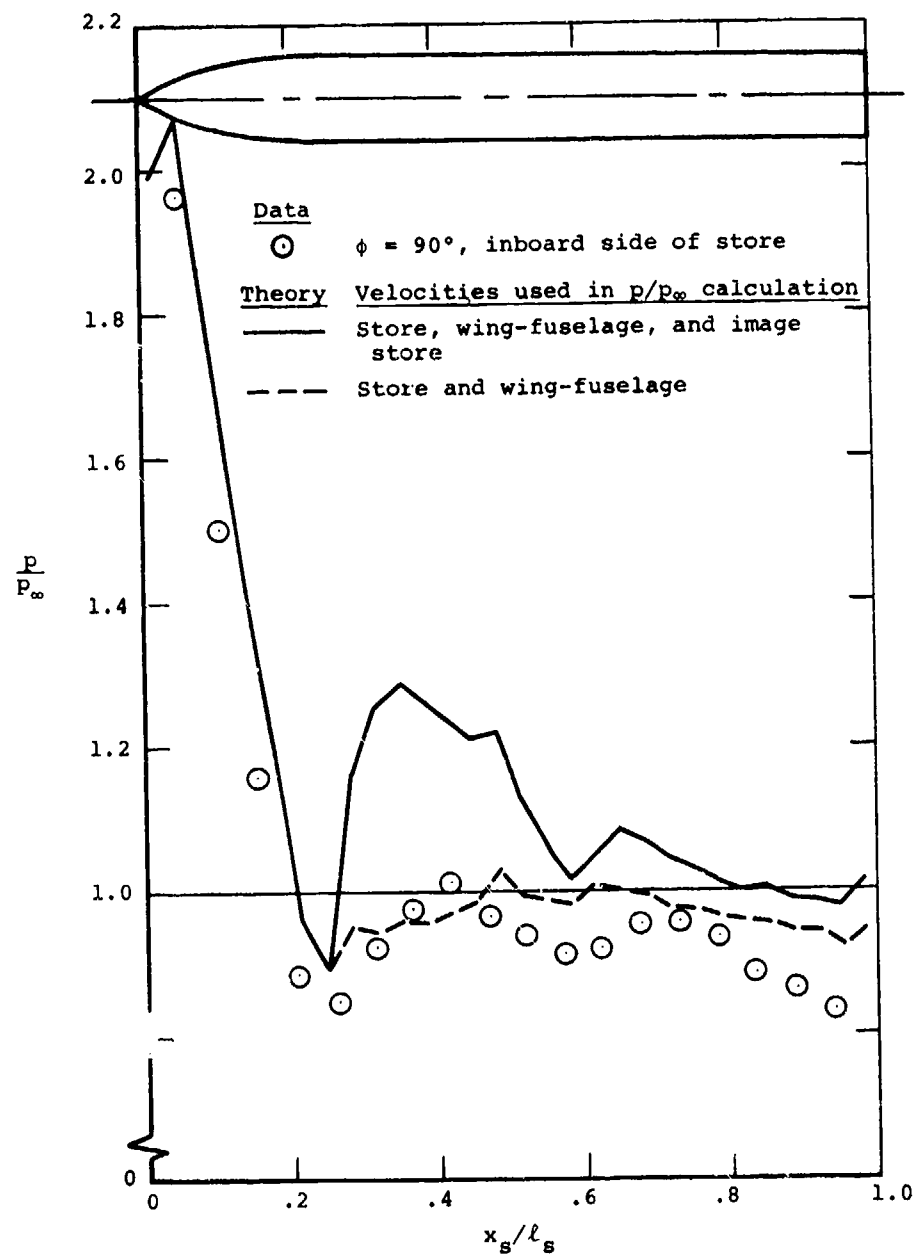


Figure 16.- Pressure distribution on inboard side of store in presence of wing-fuselage; $M_\infty = 1.5$, $\alpha = 0^\circ$, $y_F = -4$ in., $z_F = 1.47$ in.

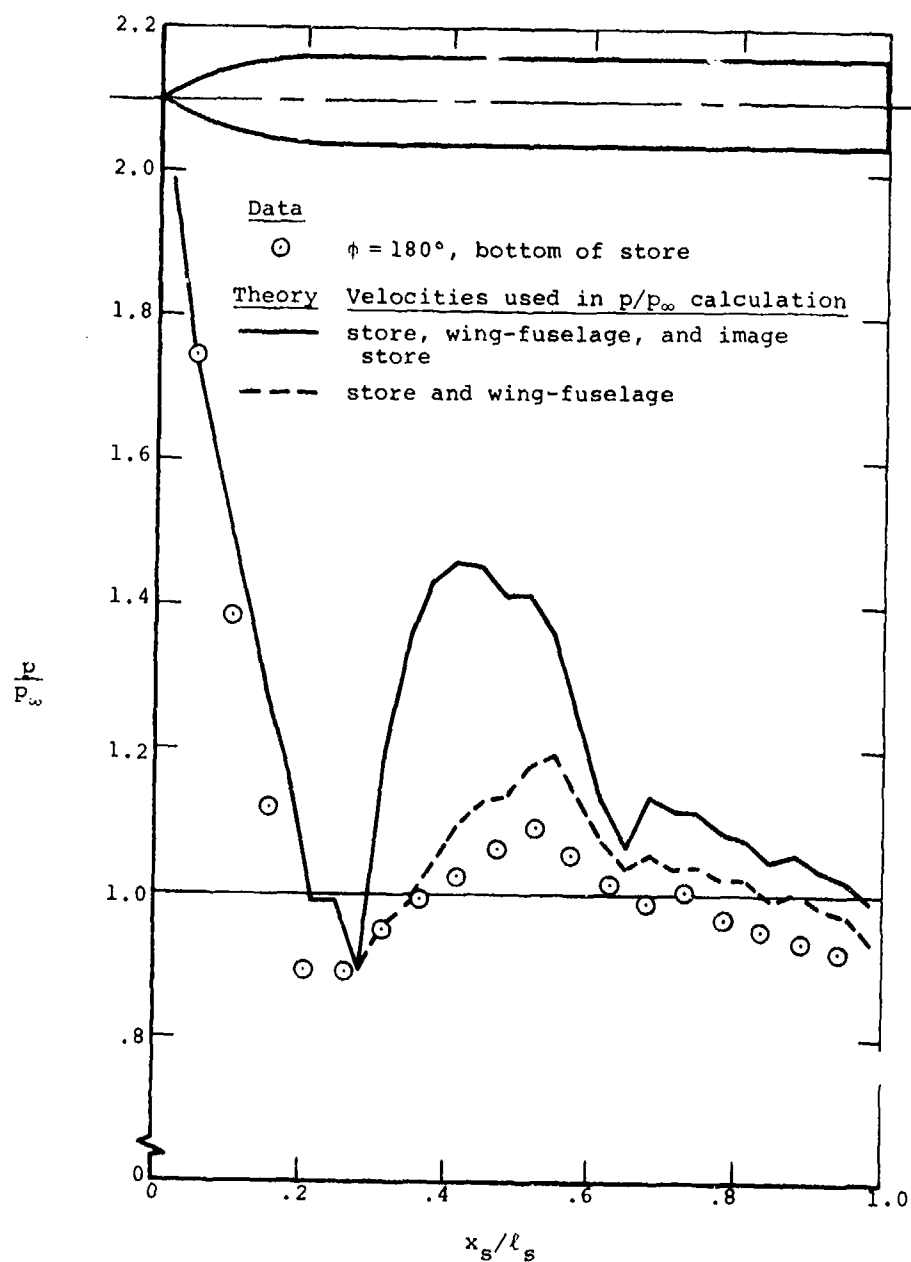


Figure 17.- Pressure distribution on bottom of store in presence of wing-fuselage; $M_\infty = 1.5$, $\alpha = 0^\circ$, $y_F = -4$ in., $z_F = 1.47$ in.

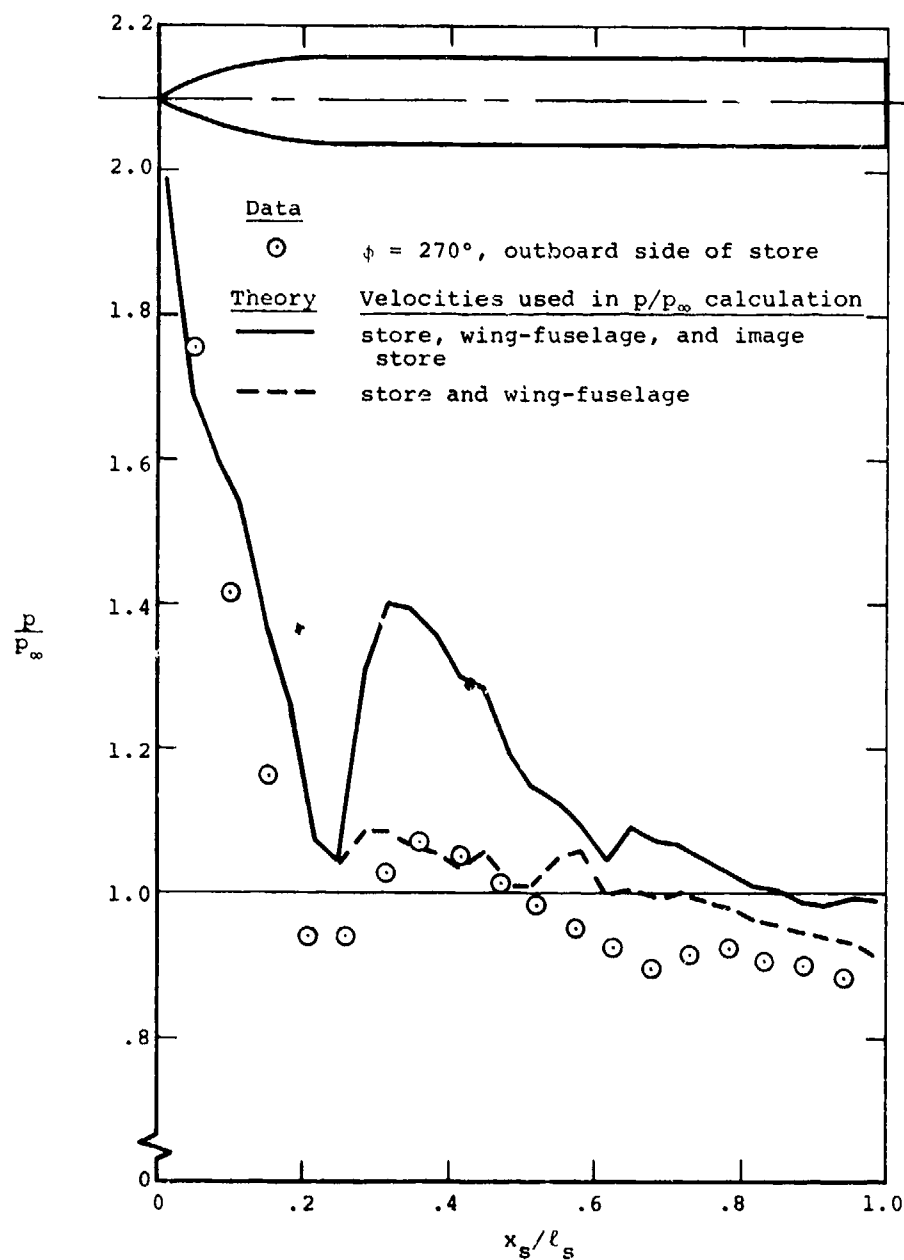


Figure 18.- Pressure distribution on outboard side of store in presence of wing-fuselage; $M_\infty = 1.5$, $\alpha = 0^\circ$, $y_F = -4$ in., $z_F = 1.47$ in.

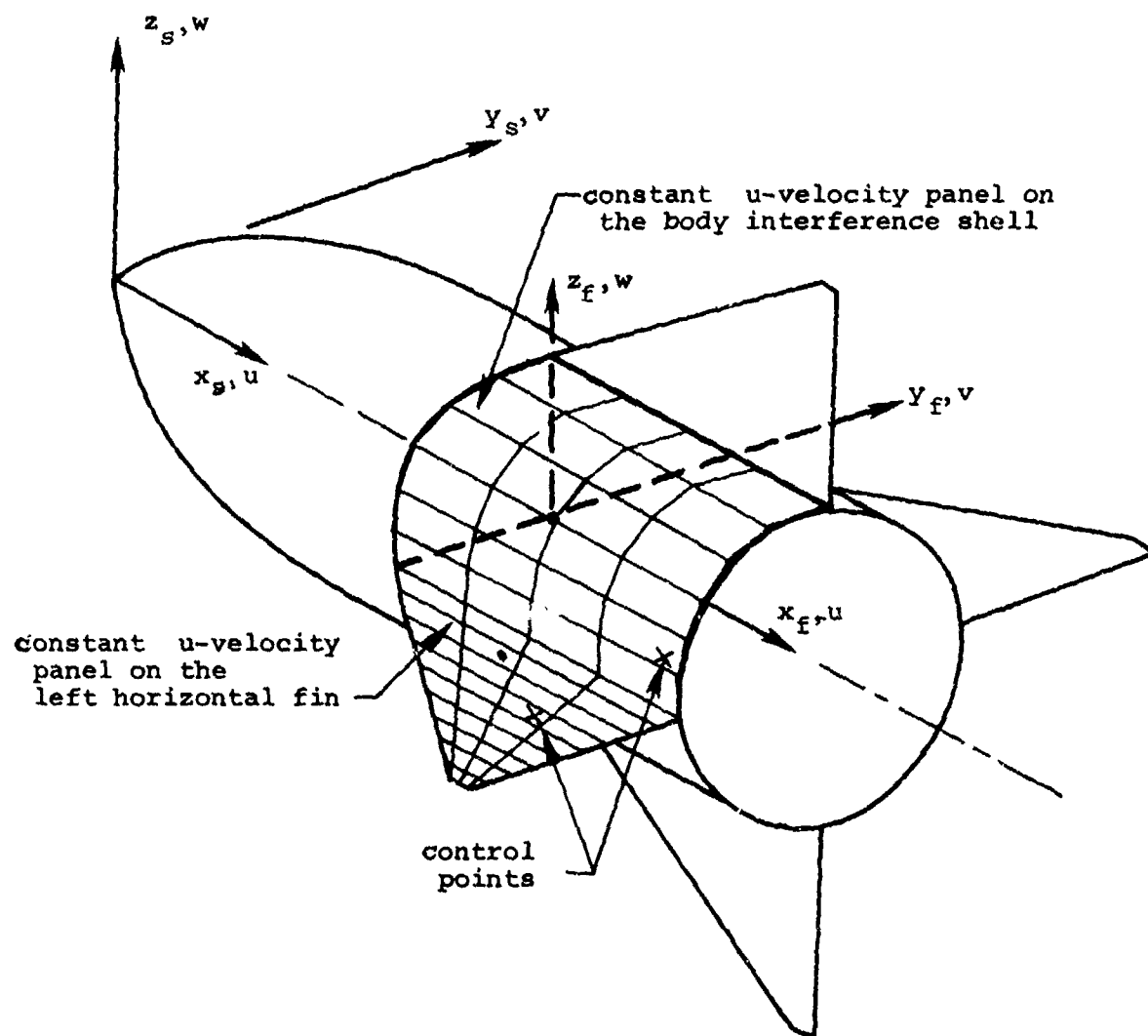
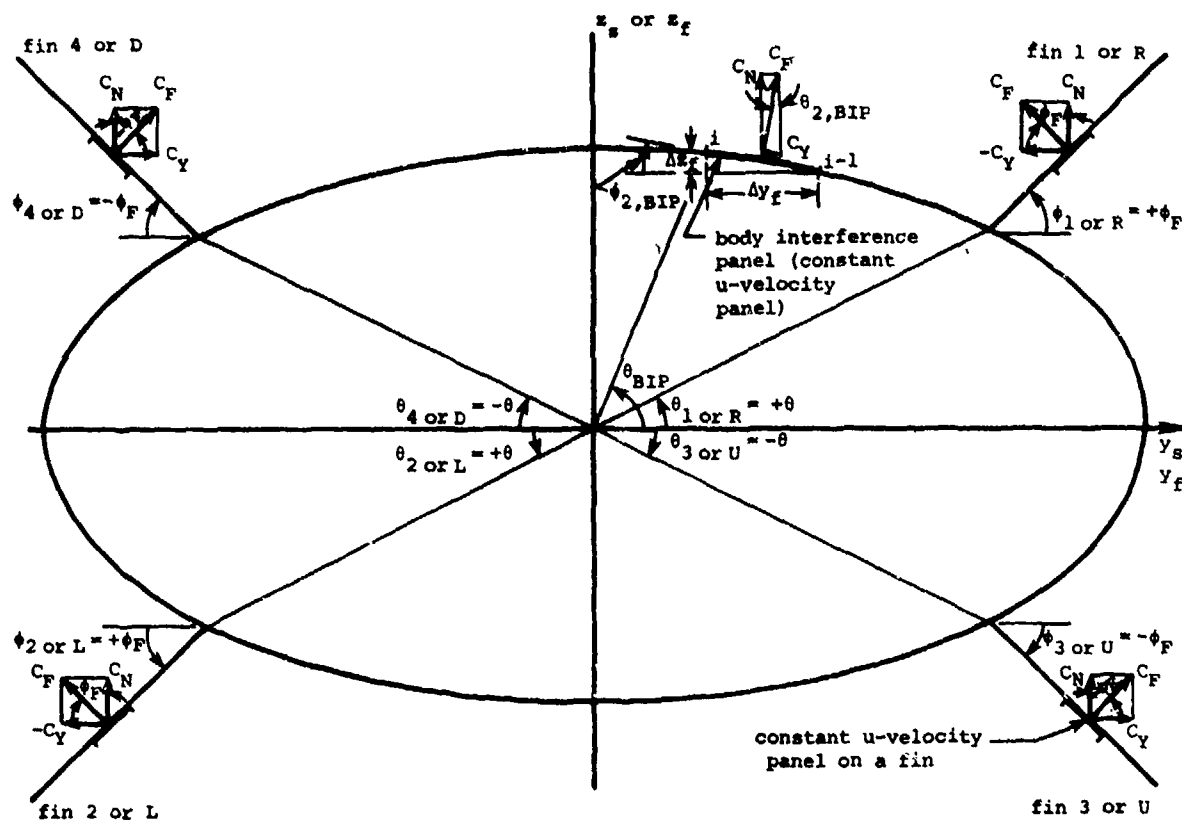


Figure 19.- Coordinate systems and typical panel layout shown for one fin and quarter of the interference shell.



- ϕ_F = fin dihedral angle, PHIDIH
 ϕ_1 or R = dihedral angle of right upper fin, PHIPR=PHIDIH
 ϕ_2 or L = dihedral angle of left lower fin, PHIFL=PHIDIH
 ϕ_3 or U = dihedral angle of right lower fin, PHIFU=-PHIDIH
 ϕ_4 or D = dihedral angle of left upper fin, PHIFD=-PHIDIH
 θ = fin location polar angle, THETIT
 θ_1 or R = polar angle of right upper fin, THETR=THETIT
 θ_2 or L = polar angle of left lower fin, THETL=THETIT
 θ_3 or U = polar angle of right lower fin, THETI=-THETIT
 θ_4 or D = polar angle of left upper fin, THETD=-THETIT

Body interference panels:

$$\theta_{BIP,j} = \text{THTI}(j),$$

$$\Delta x_f = z_{f,i} - z_{f,i-1}$$

$$\Delta y_f = y_{f,i} - y_{f,i-1}$$

$$\sin \theta_{2,BIP} = \frac{\Delta x_f}{\sqrt{\Delta x_f^2 + \Delta y_f^2}}$$

$$\cos \theta_{2,BIP} = \frac{-\Delta y_f}{\sqrt{\Delta x_f^2 + \Delta y_f^2}}$$

these functions are used in the transformation (rotation) of the body interference panel to the reference (x_s, y_s, z_s) or (x_f, y_f, z_f) system

Figure 20.- Geometrical angles associated with case involving fins on body with elliptical cross section and force coefficients associated with fins and body interference panel.

NACA 65A006

AIRFOIL COORDINATES		
X, % CHORD	Y, % CHORD	SEE SEC
0.00	0.000	
0.50	0.464	
0.75	0.563	
1.25	0.718	
2.50	0.991	
5.00	1.313	
7.50	1.591	
10.00	1.824	
15.00	2.194	
20.00	2.474	
25.00	2.687	
30.00	2.842	
35.00	2.945	
40.00	2.996	
45.00	2.992	
50.00	2.923	
55.00	2.793	
60.00	2.602	
65.00	2.364	
70.00	2.087	
75.00	1.775	
80.00	1.437	
85.00	1.083	
90.00	0.727	
95.00	0.370	
100.00	0.013	
LE RADIUS 0.229 % CHD		
TE RADIUS 0.014 % CHD		

BODY COORDINATES		
STATION	RADIUS	PERCENT LENGTH
0.00	0.00	
3.28	0.91	
6.57	1.71	
9.86	2.41	
13.15	3.00	
16.43	3.50	
19.72	3.90	
23.01	4.21	
26.29	4.43	
29.58	4.53	
32.80	4.57	
36.00	4.57	
39.28	4.54	
42.56	4.48	
45.84	4.38	
49.13	4.26	
52.41	4.18	
55.69	4.05	
58.98	3.95	
62.26	3.72	
65.55	3.49	
68.84	3.26	
72.12	3.02	
75.41		
78.69		
81.98		
85.26		
88.55		
91.84		
95.12		
98.41		
101.70		

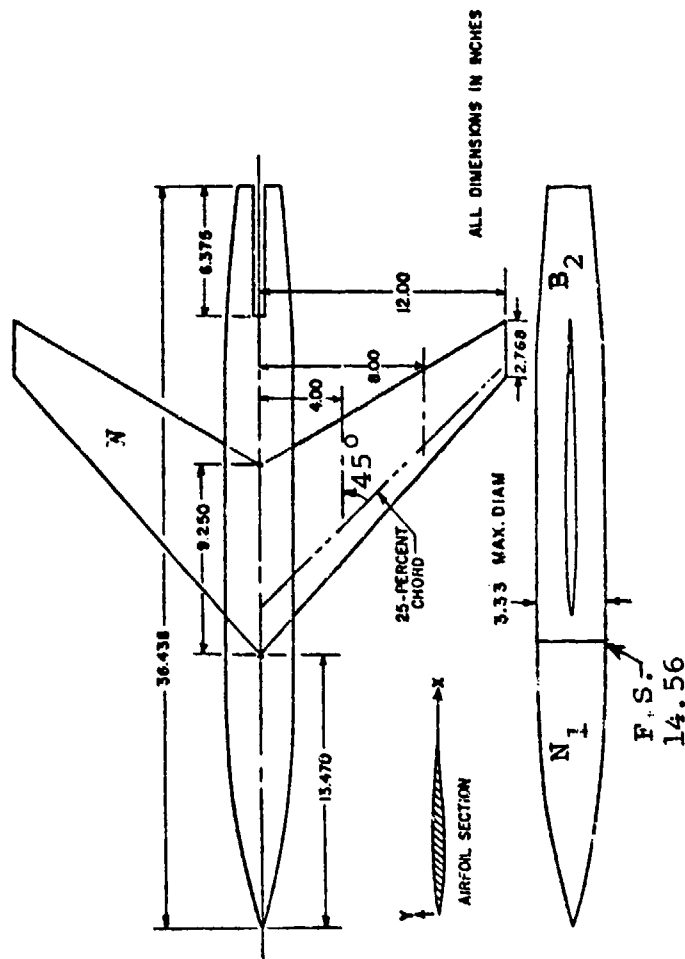


Figure 21.- Configuration N₁B₂W.

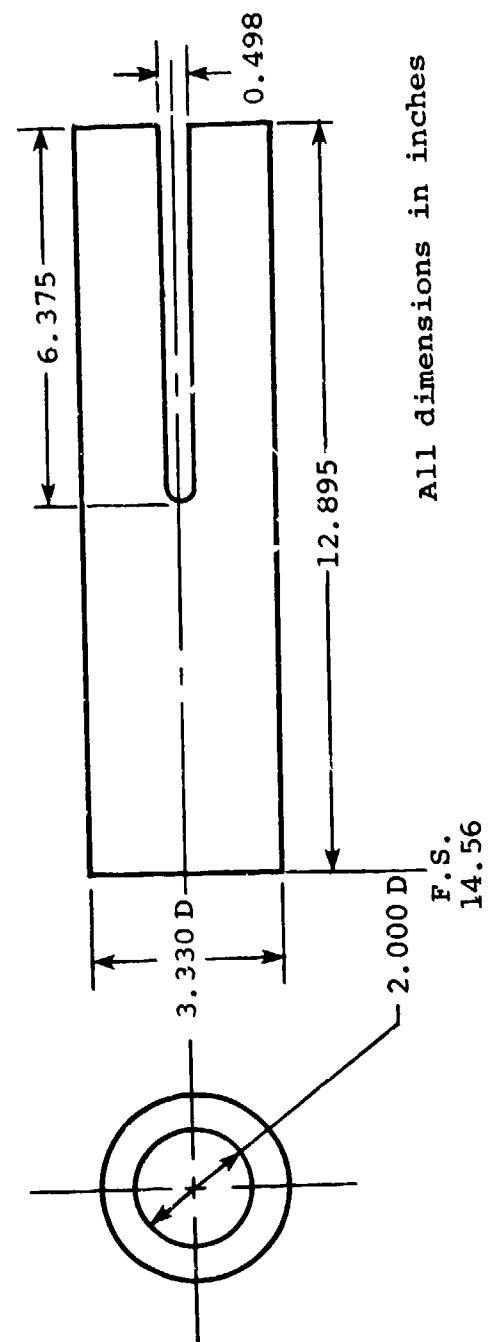
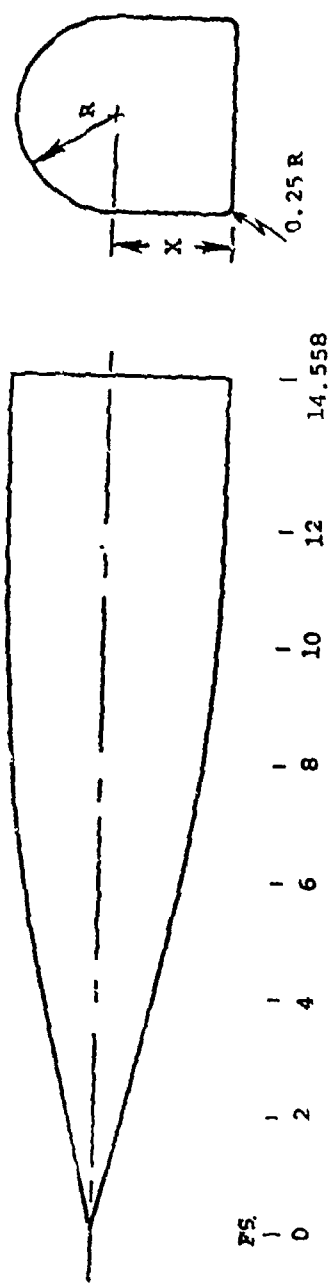
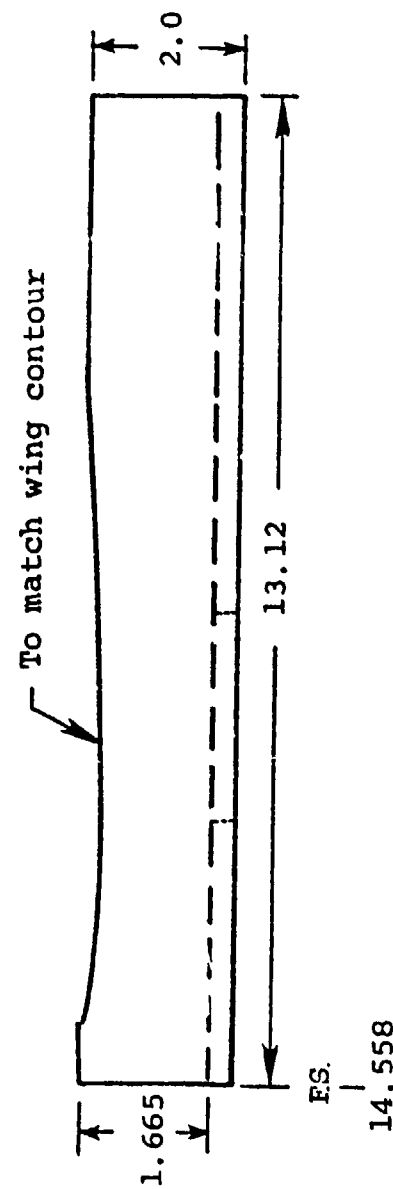


Figure 22.- Short fuselage, B₁.

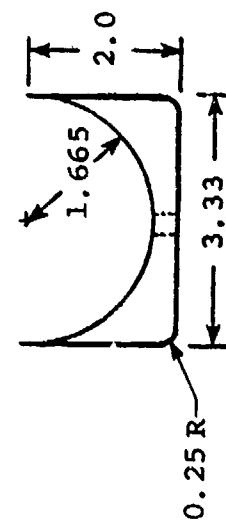


All dimensions in inches

Figure 23.- Noncircular nose, N_3 .



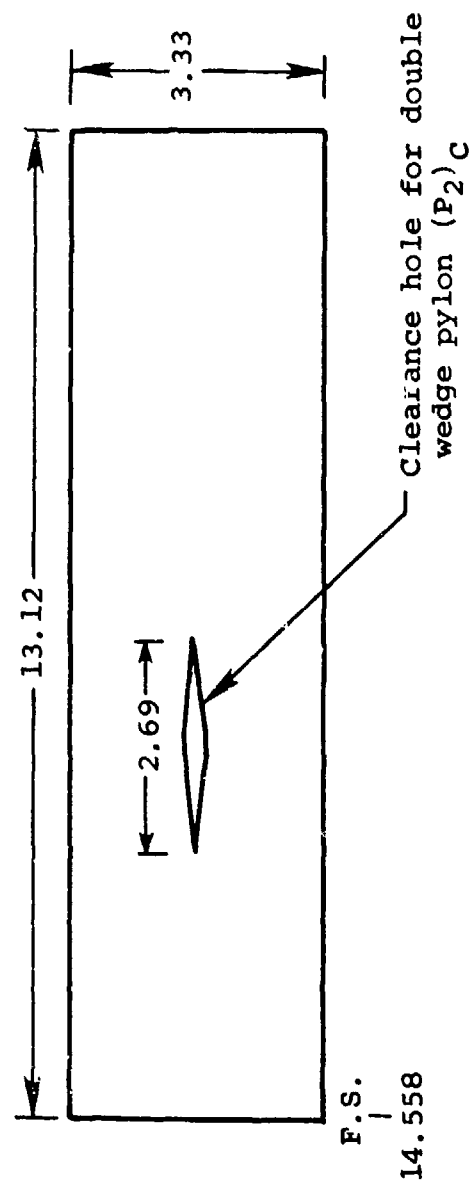
(a) Side view.



(b) Front view.

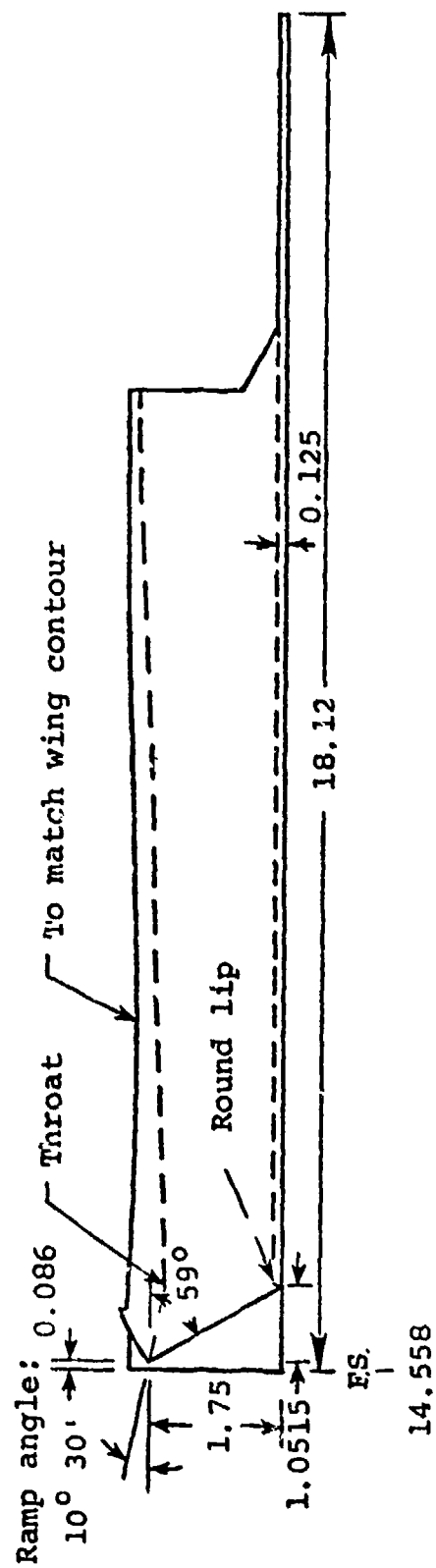
All dimensions in inches

Figure 24.- Noncircular fuselage adapter, A₃.

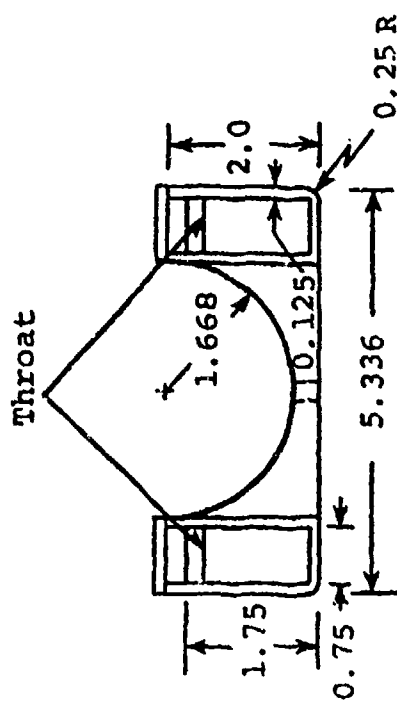


(c) Top view.

Figure 24.- Concluded.



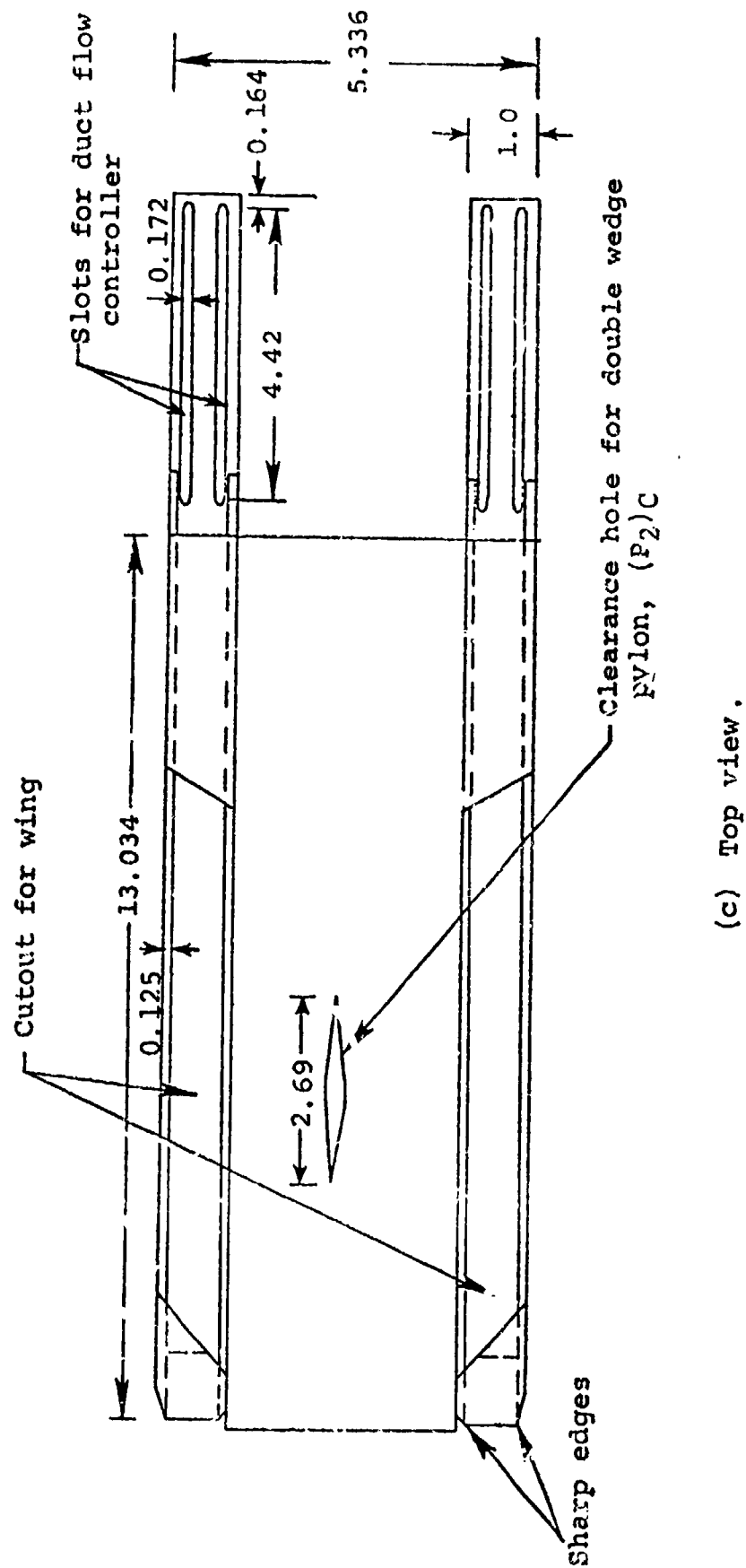
(a) Side view.



(b) Front view.

All dimensions in inches

Figure 25.- Duct assembly for $M_\infty = 1.5$, A_4 .



(c) Top view.

Figure 25.- Concluded.

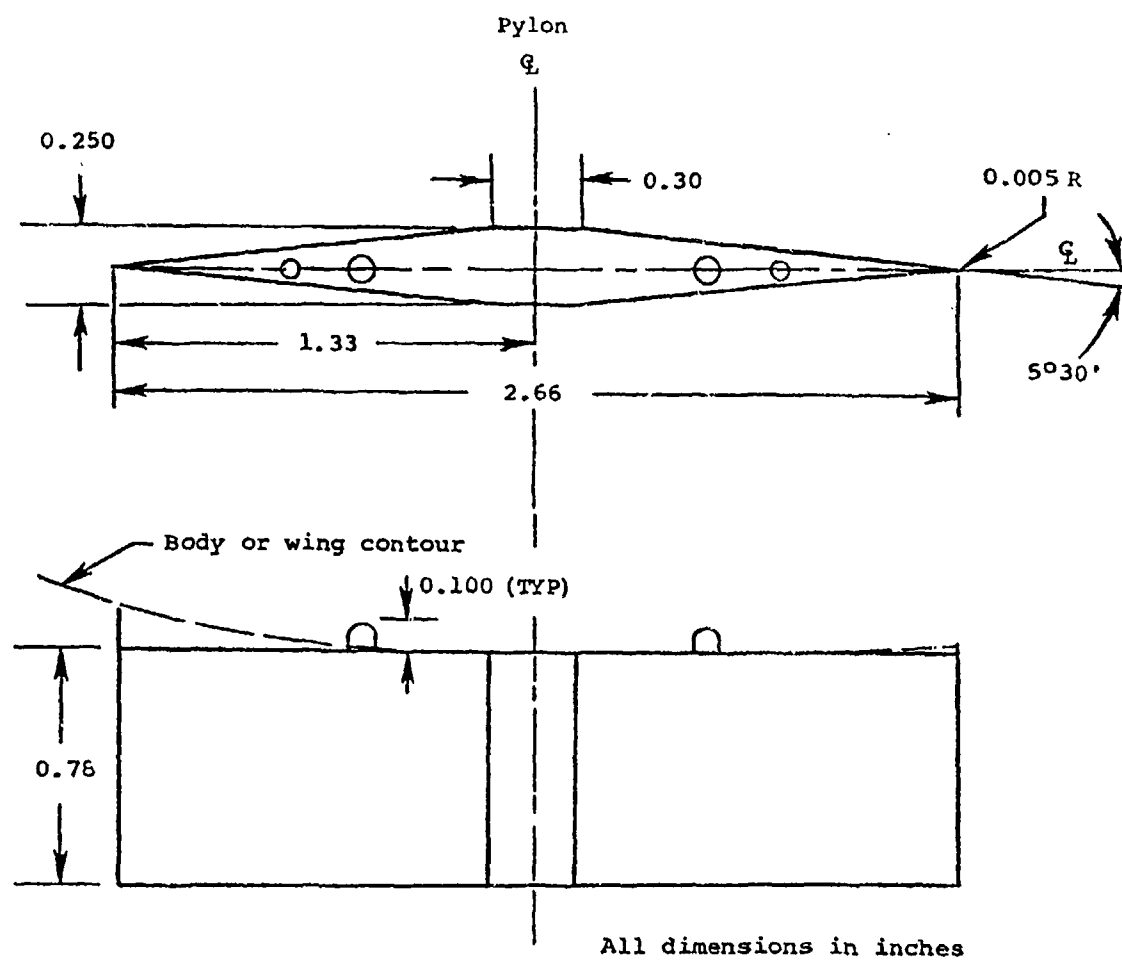


Figure 27.- Double-wedge pylon, P_2 .

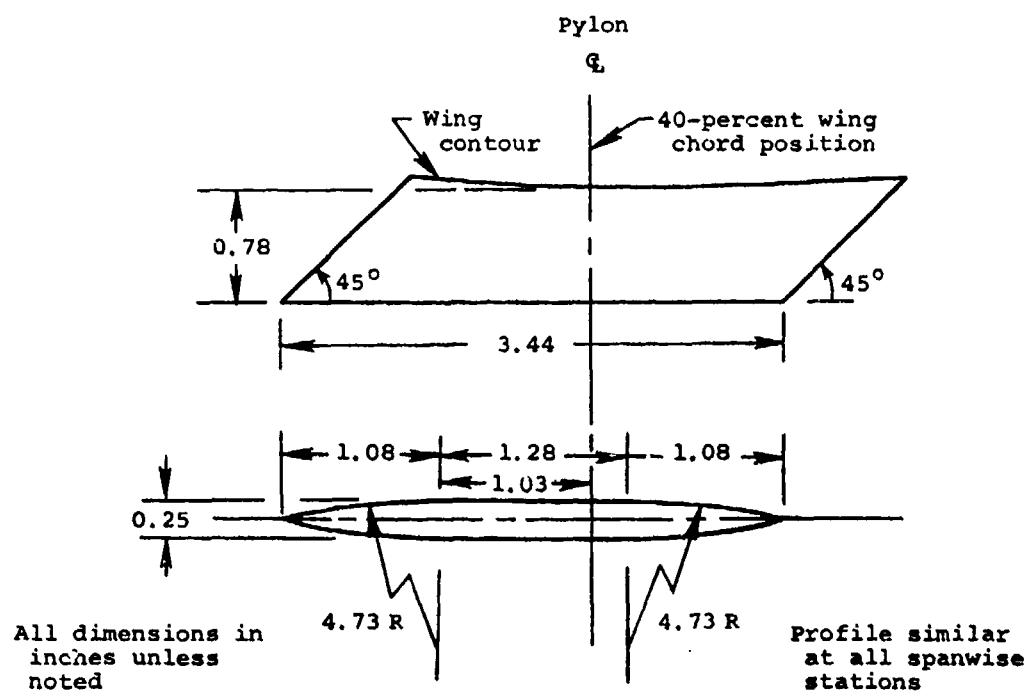
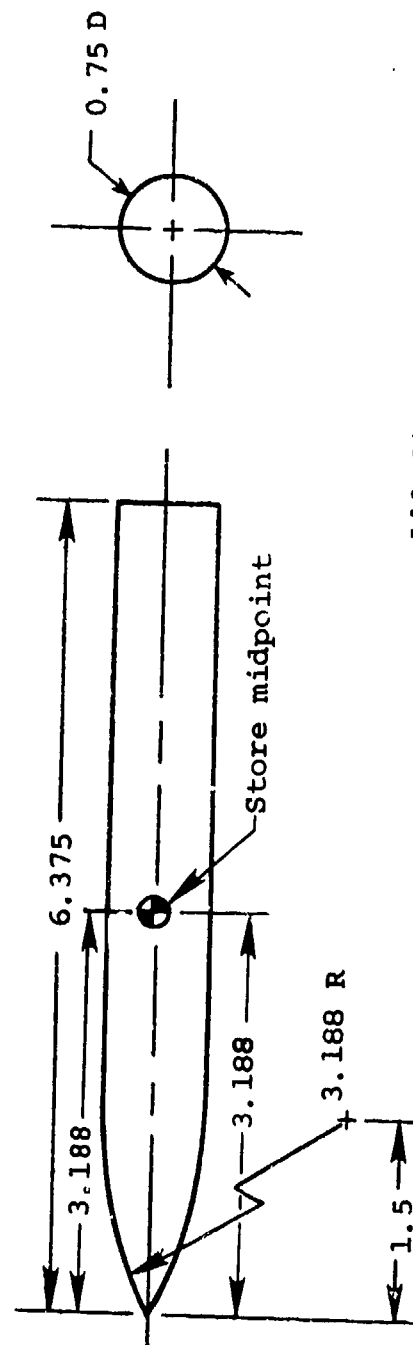


Figure 28.- Swept pylon, P_3 .



All dimensions in inches

Figure 29.- Dummy ogive-cylinder store, S_{DOC} , S_{DOC2} , or S_{DOC3} .

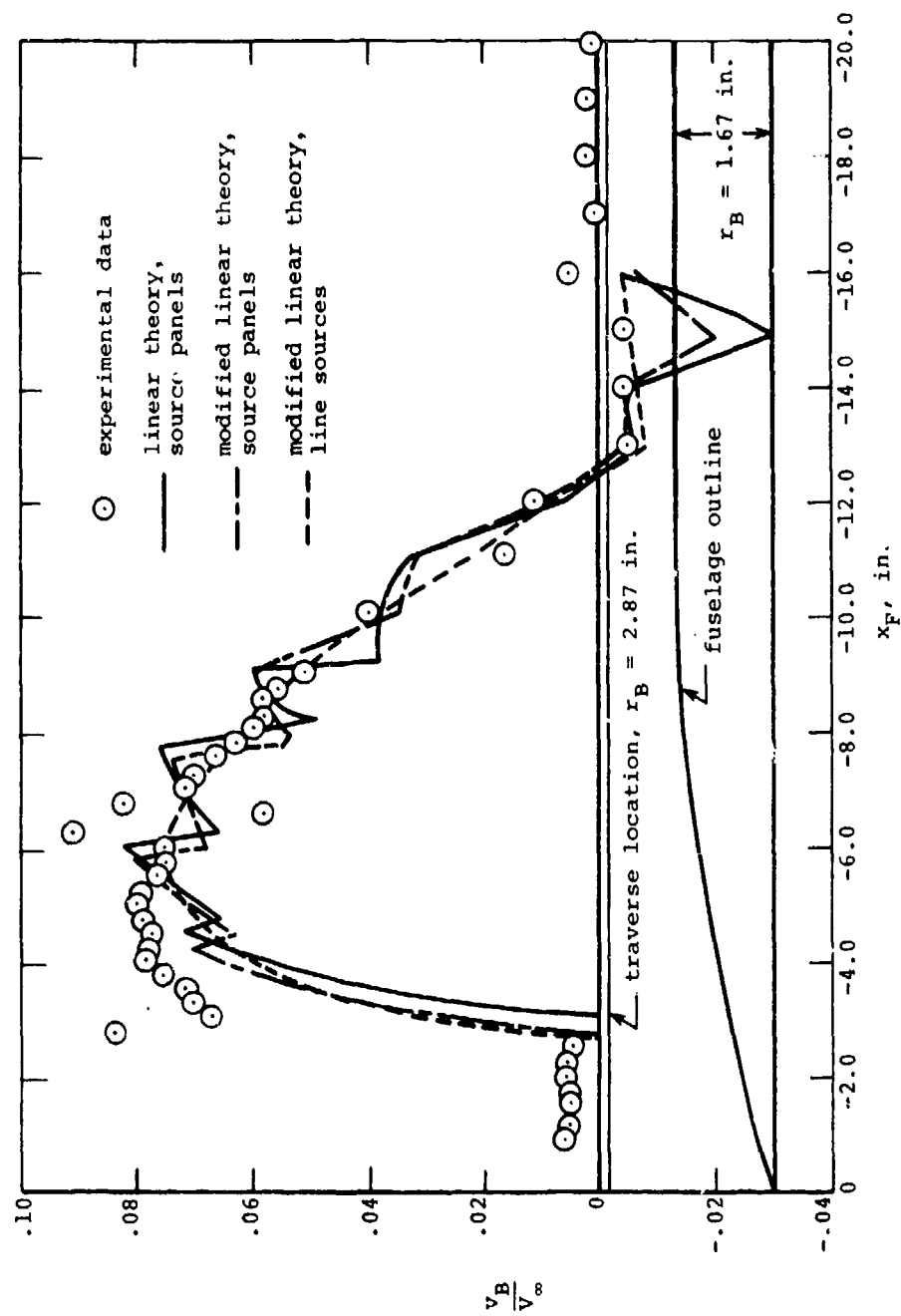


Figure 30.- Comparison of calculated radial velocity with experimental data
for configuration N1B1; $M_\infty = 1.5$,
 $\alpha_F = 0^\circ$, $r_B = 2.87$ in.

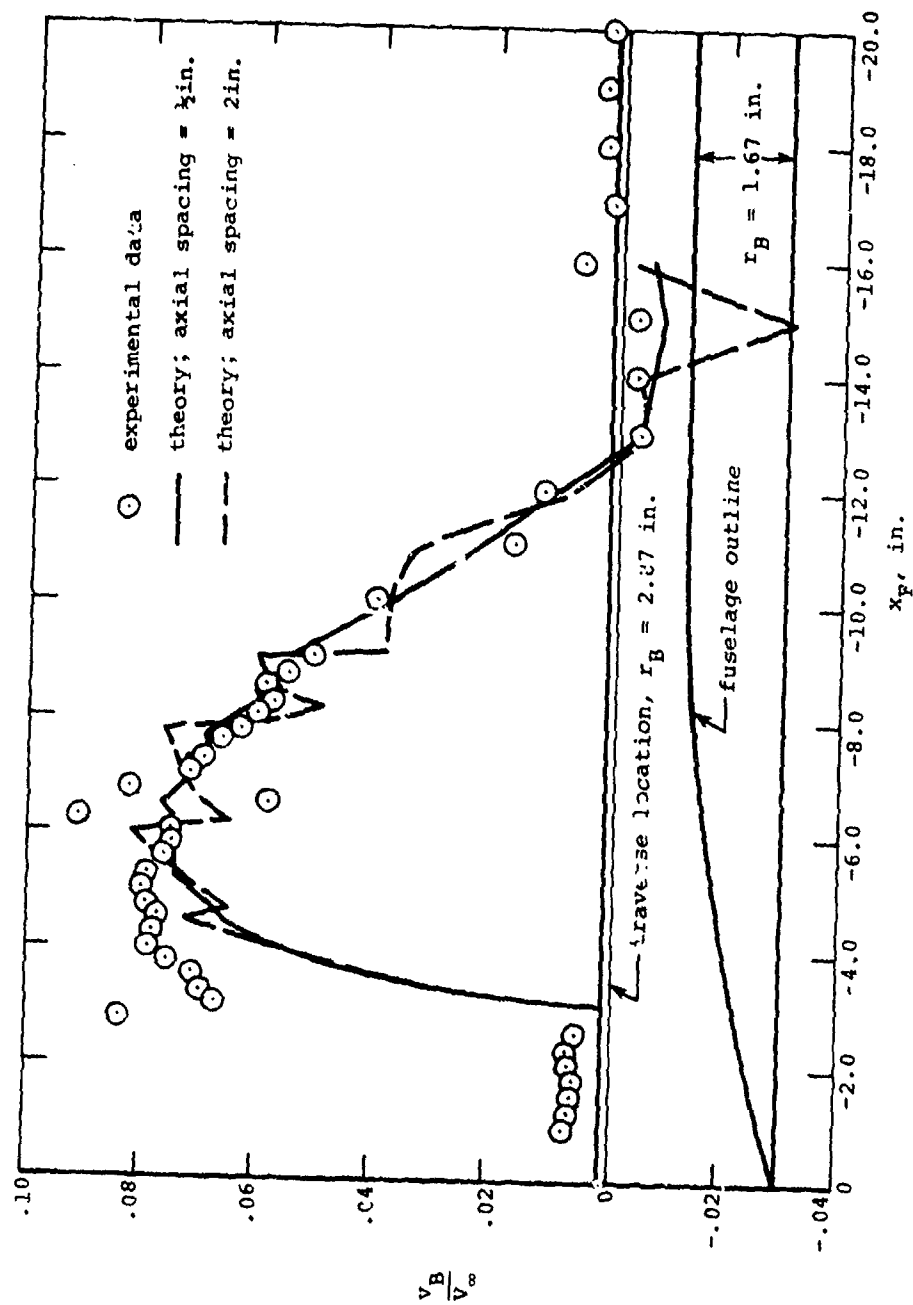


Figure 31.- Effect of axial density of source panels on flow field of configuration $N_1 B_1$; $M_\infty = 1.5$, $\alpha_F \approx 0^\circ$.

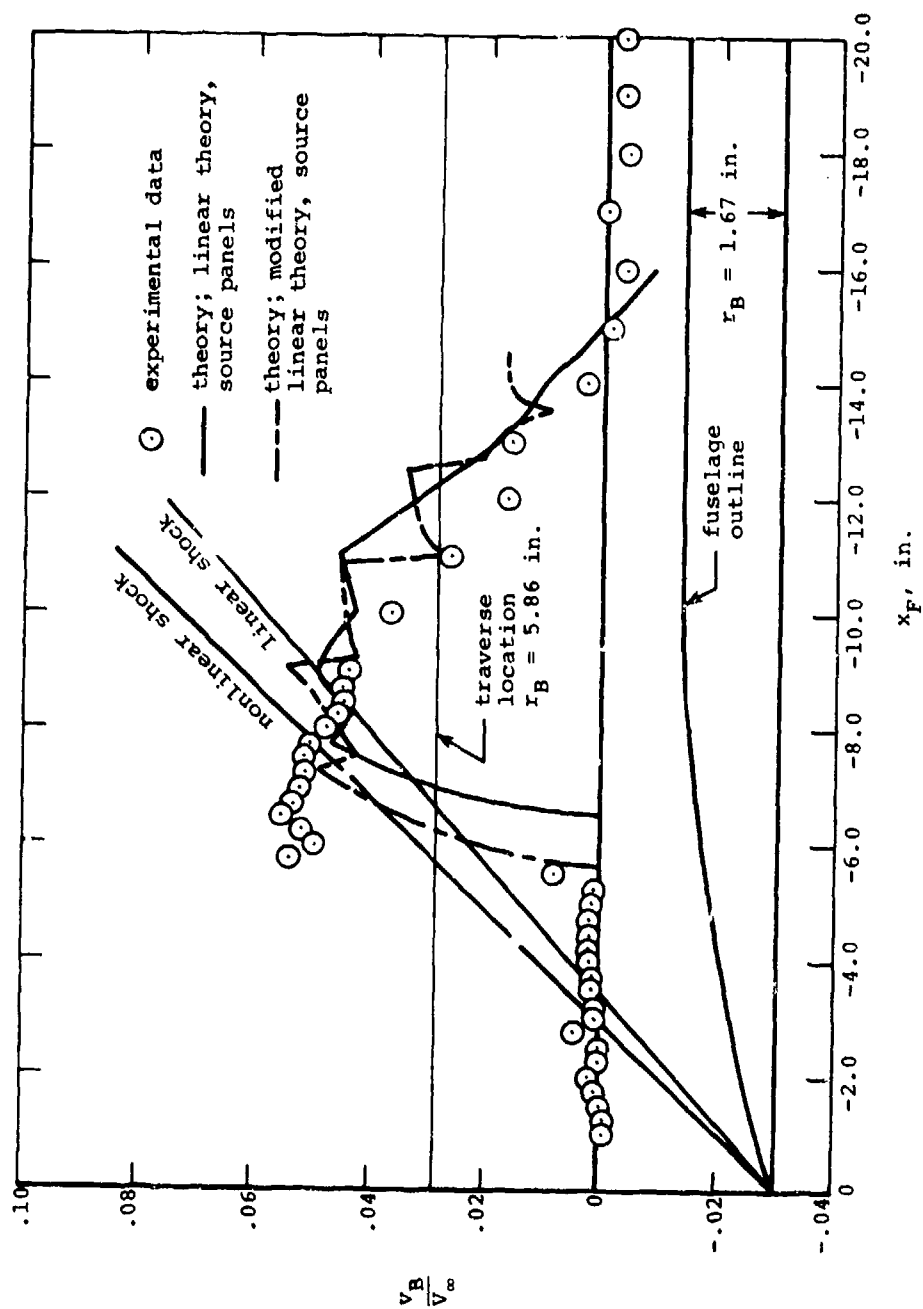


Figure 32.- Comparison of calculated radial velocity with experimental data for configuration N1B1; $M_\infty = 1.5$, $\alpha_F = 0^\circ$, $r_B = 5.86$ in.

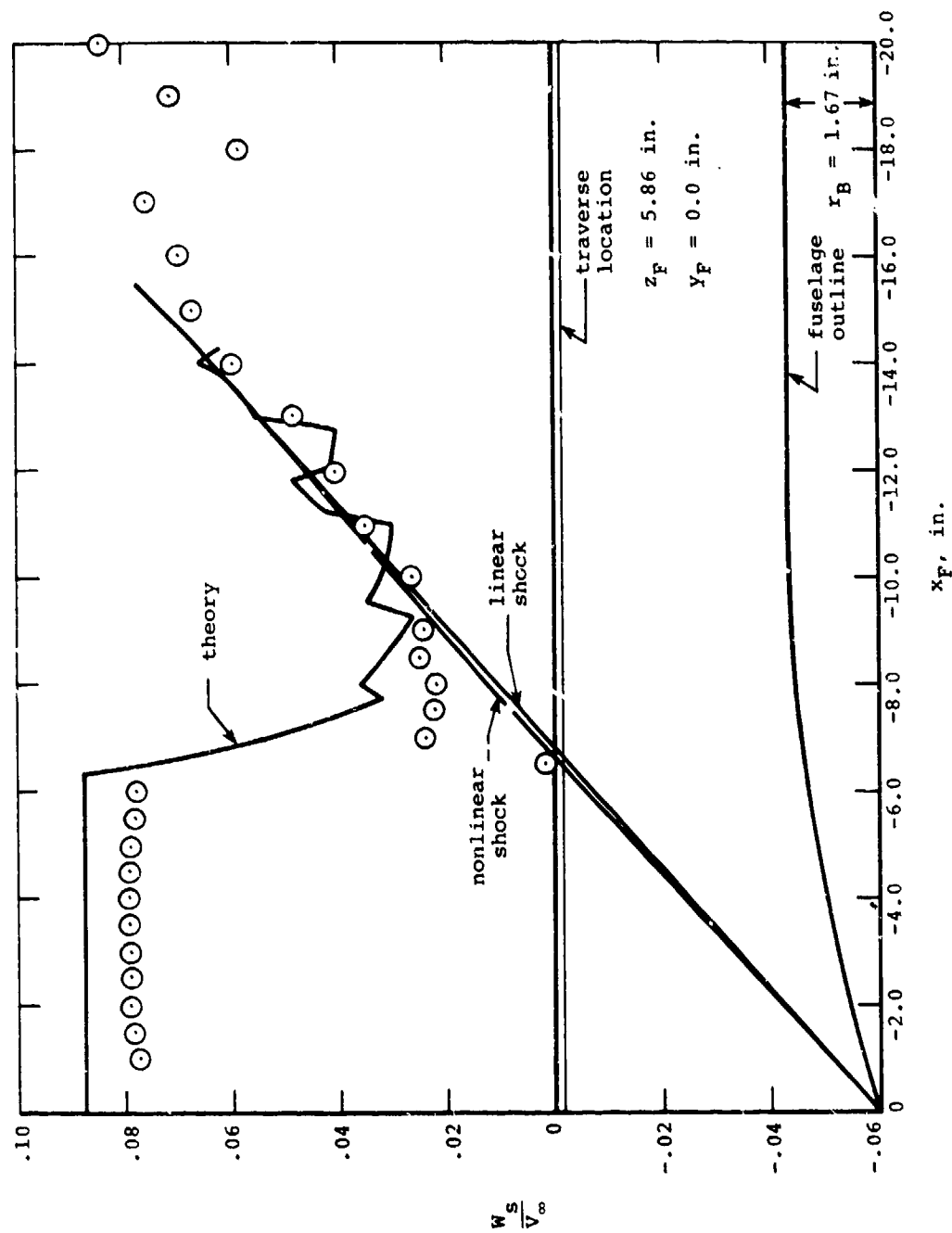


Figure 33.- Comparison of calculated upwash velocity with experimental data
5.86 inches below the centerline of configuration N1B1;
 $M_\infty = 1.5$, $\alpha_F = 5^\circ$.

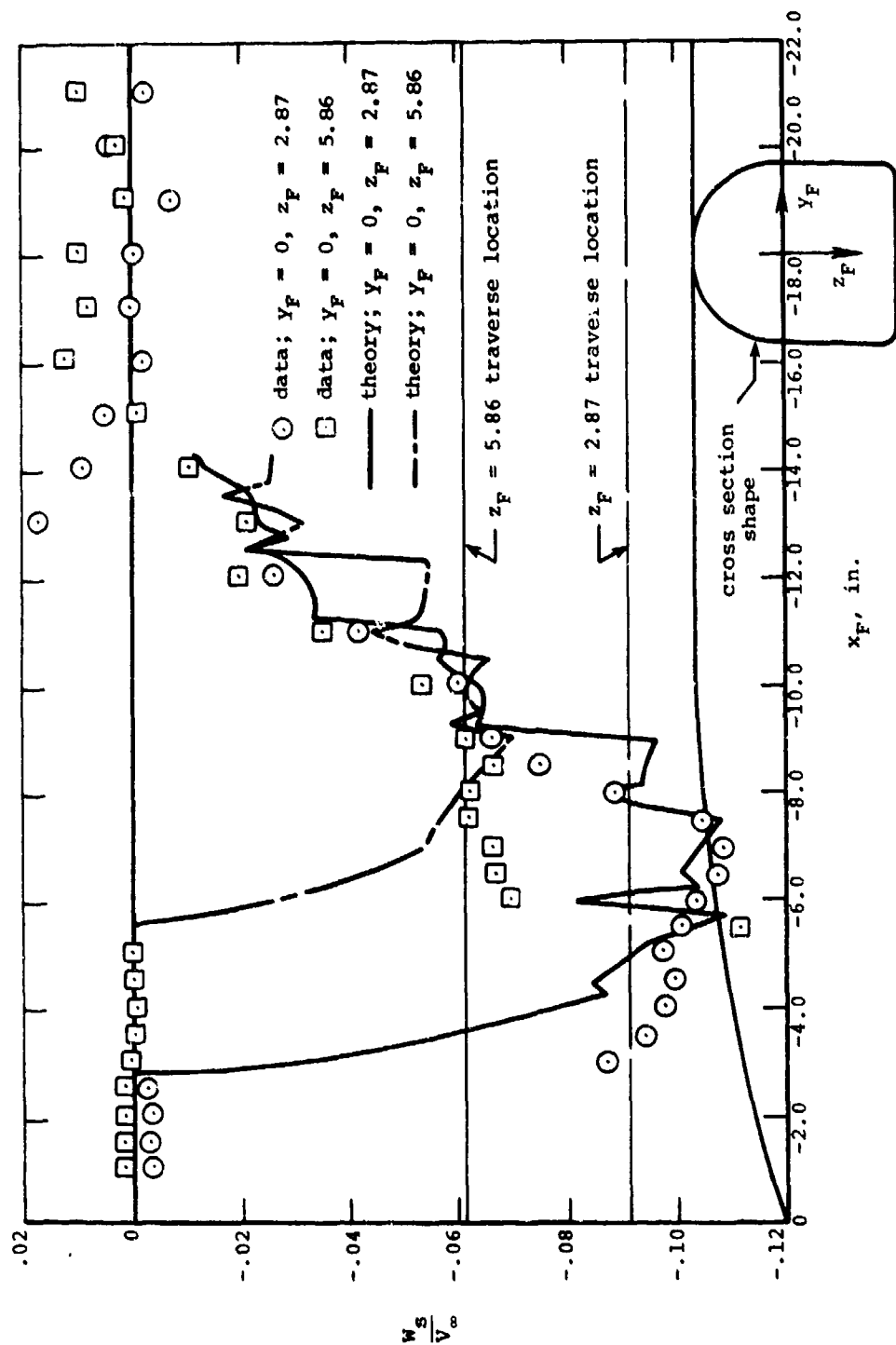


Figure 34.- Upwash velocity below the centerline of configuration N3B1A3;
 $M_\infty = 1.5, \alpha_F = 0^\circ$.

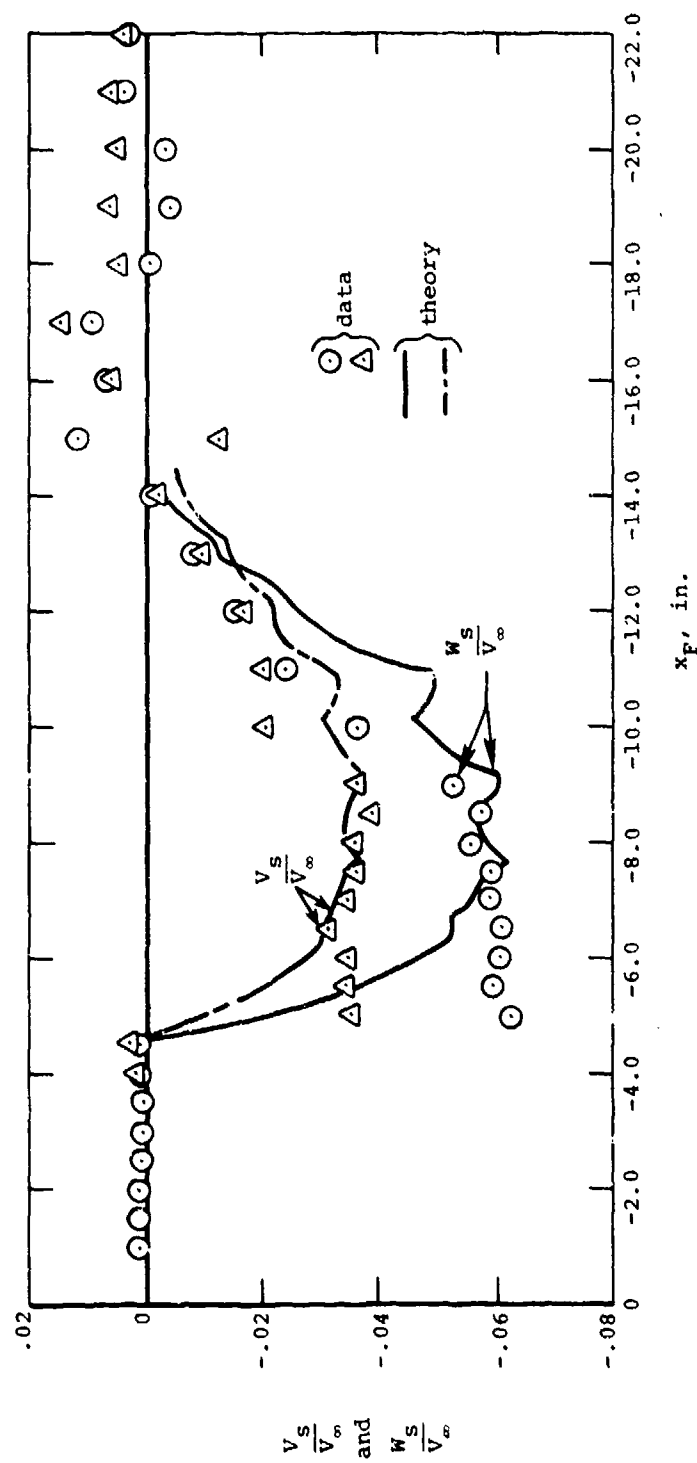
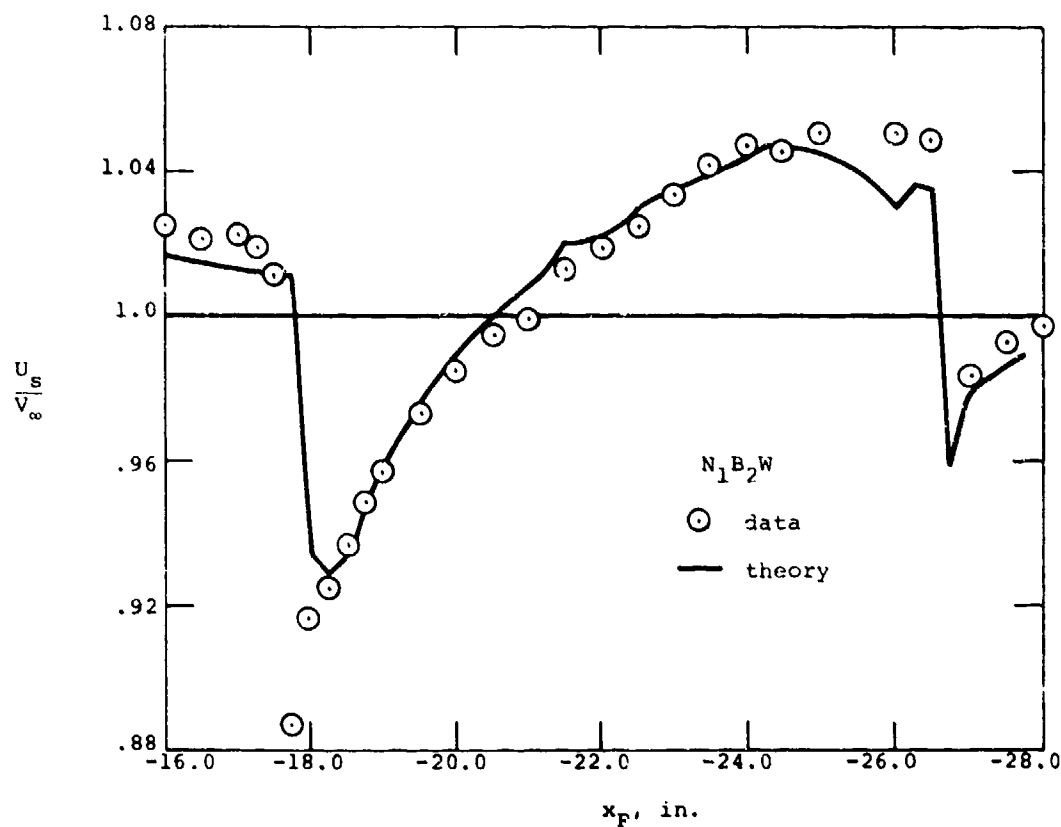
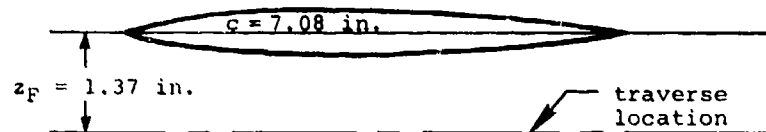
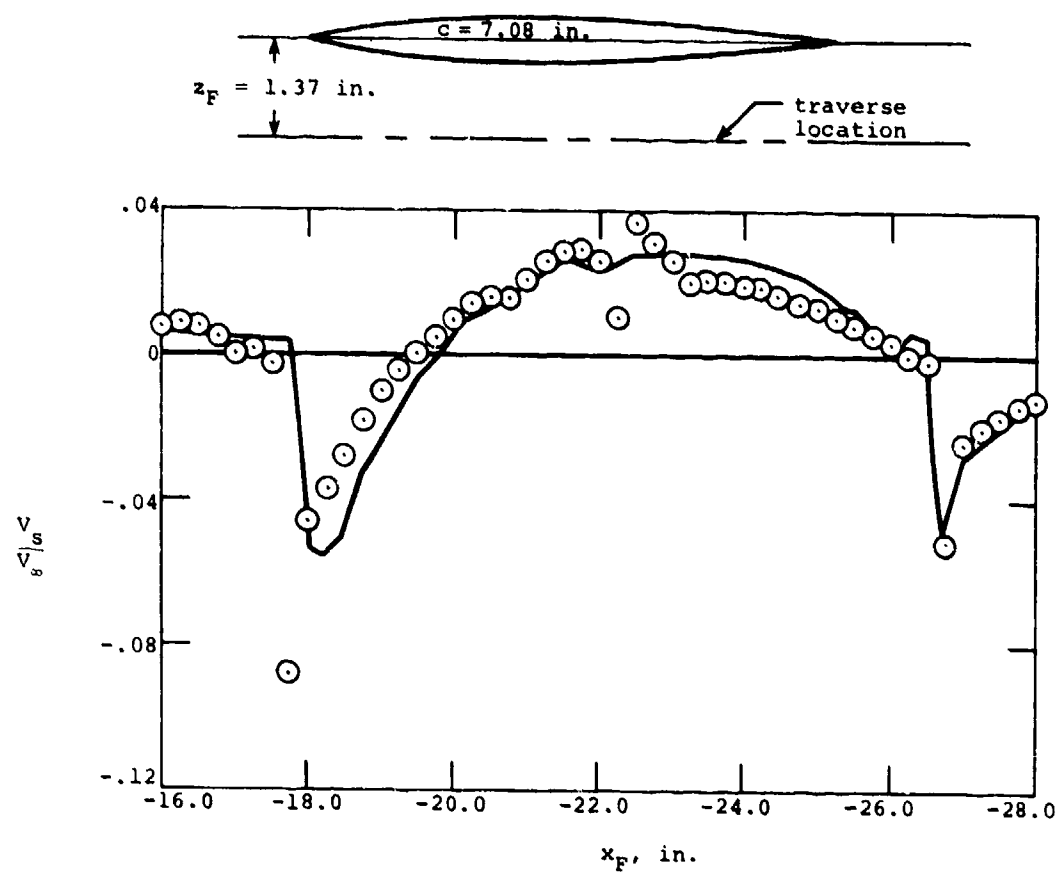


Figure 35.- Upwash and sidewash velocities at $y_F = -2.49$ in. and $z_F = 4.36$ in. for configuration $N_3B_1A_3$; $M_\infty = 1.5$, $\alpha_F = 0^\circ$.



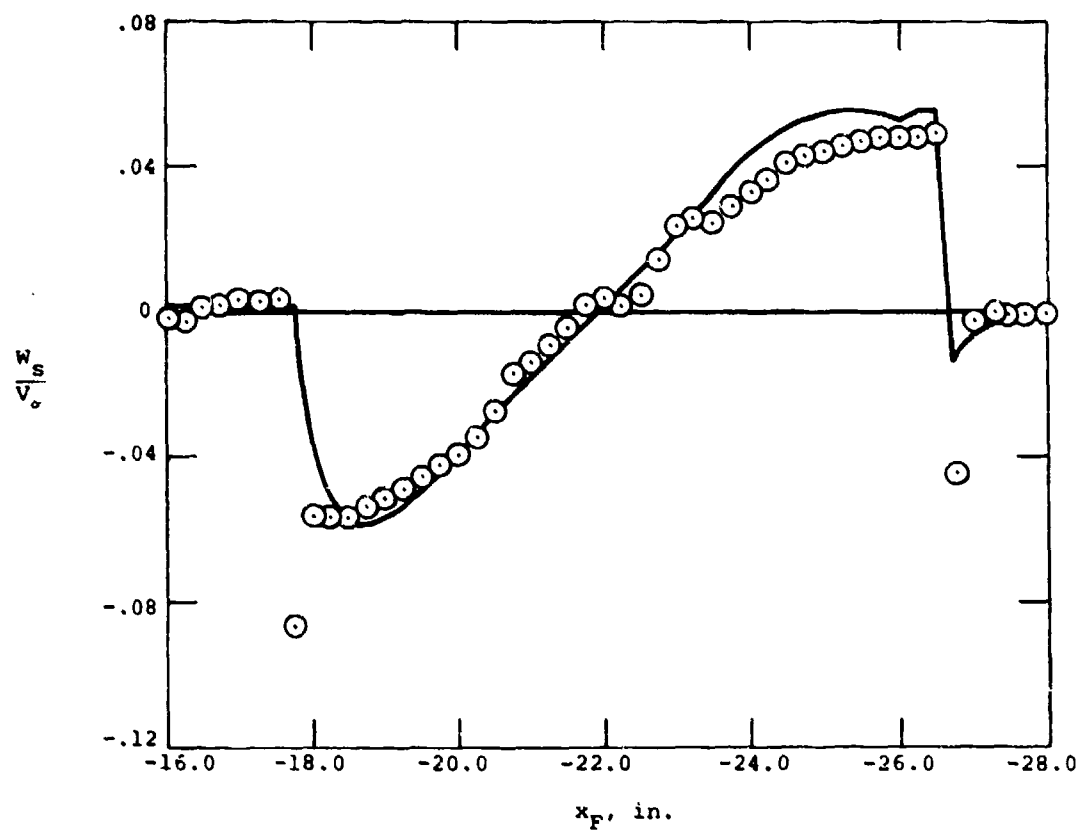
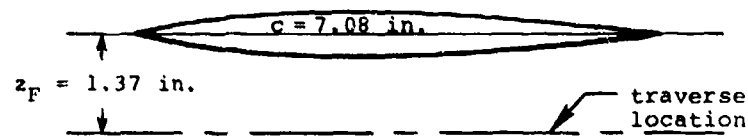
(a) Axial velocity.

Figure 36.- Flow field under the wing at the one-third semispan location; $M_\infty = 1.5$, $\alpha_F = 0^\circ$, $z_F = 1.37 \text{ in.}$



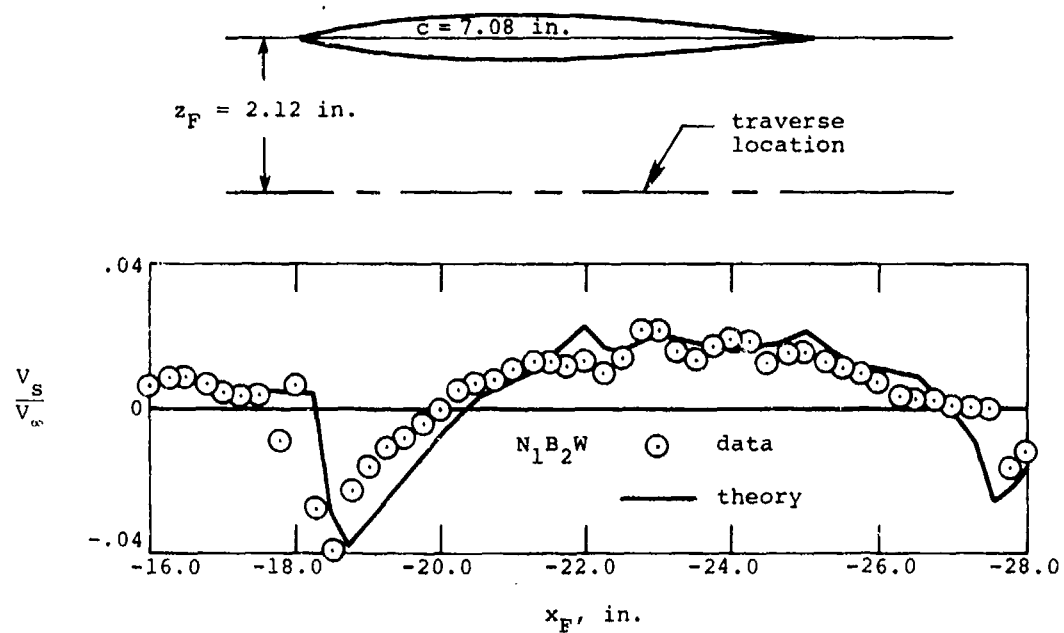
(b) Sidewash velocity.

Figure 36.- Continued.



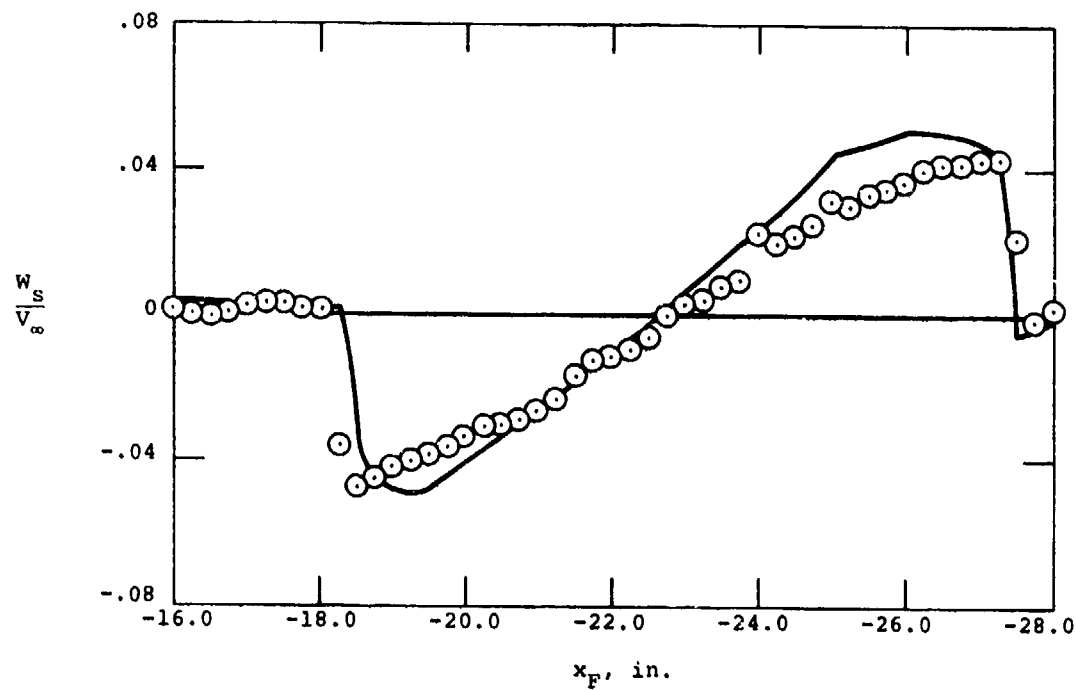
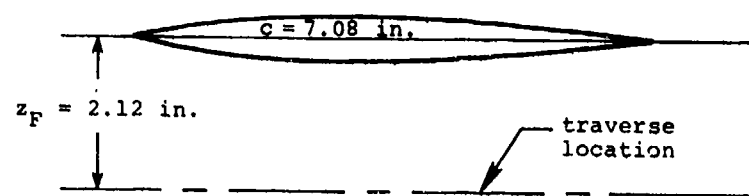
(c) Upwash velocity.

Figure 36.- Concluded.



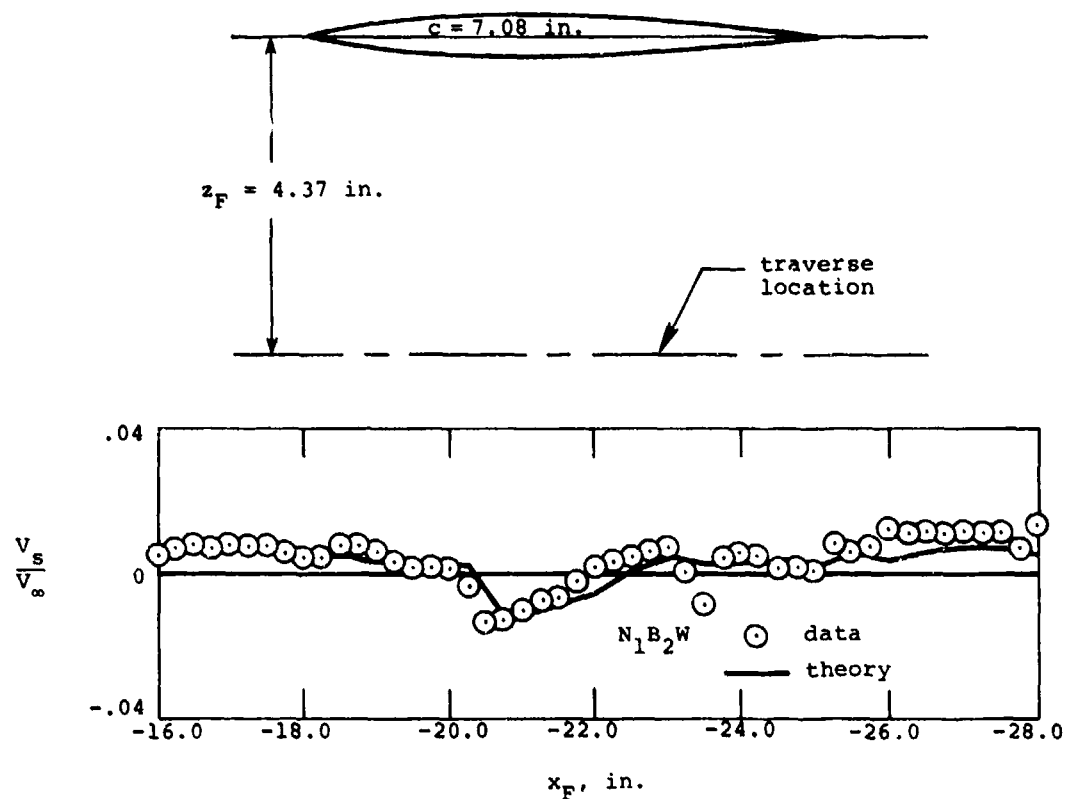
(a) Sidewash velocity.

Figure 37.- Flow field under the wing at the one-third semispan location, $M_\infty = 1.5$, $\alpha_F = 0^\circ$, $z_F = 2.12$ in.



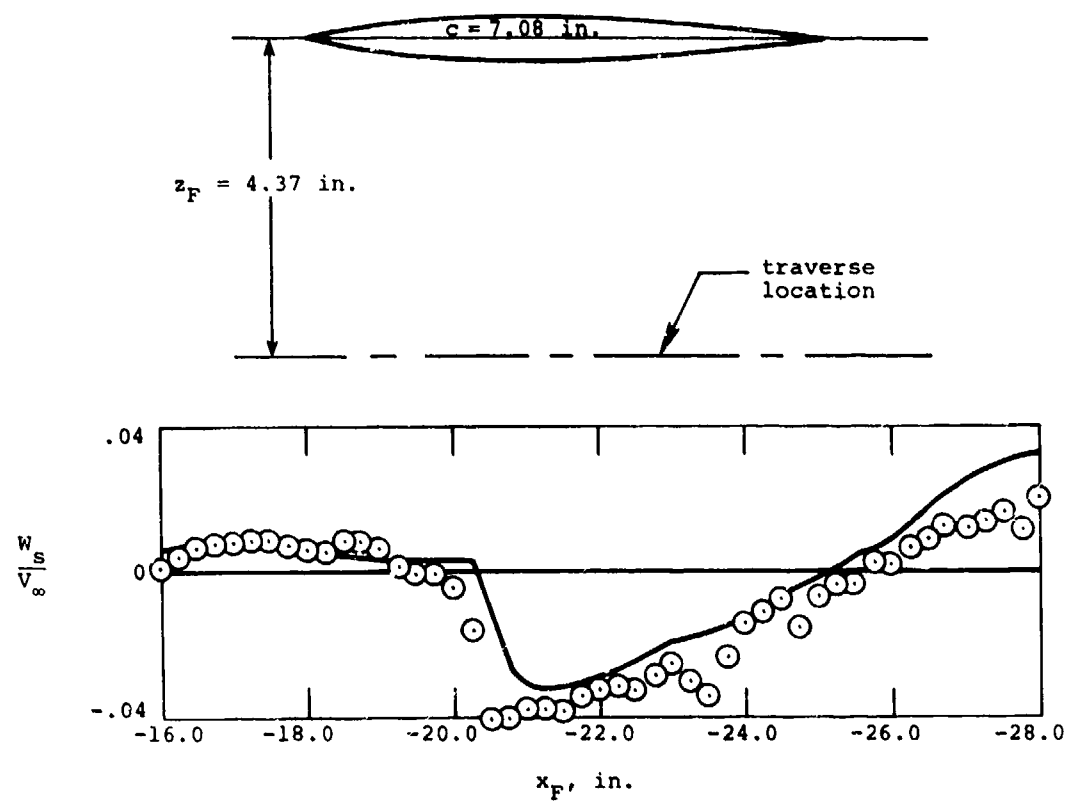
(b) Upwash velocity.

Figure 37.- Concluded.



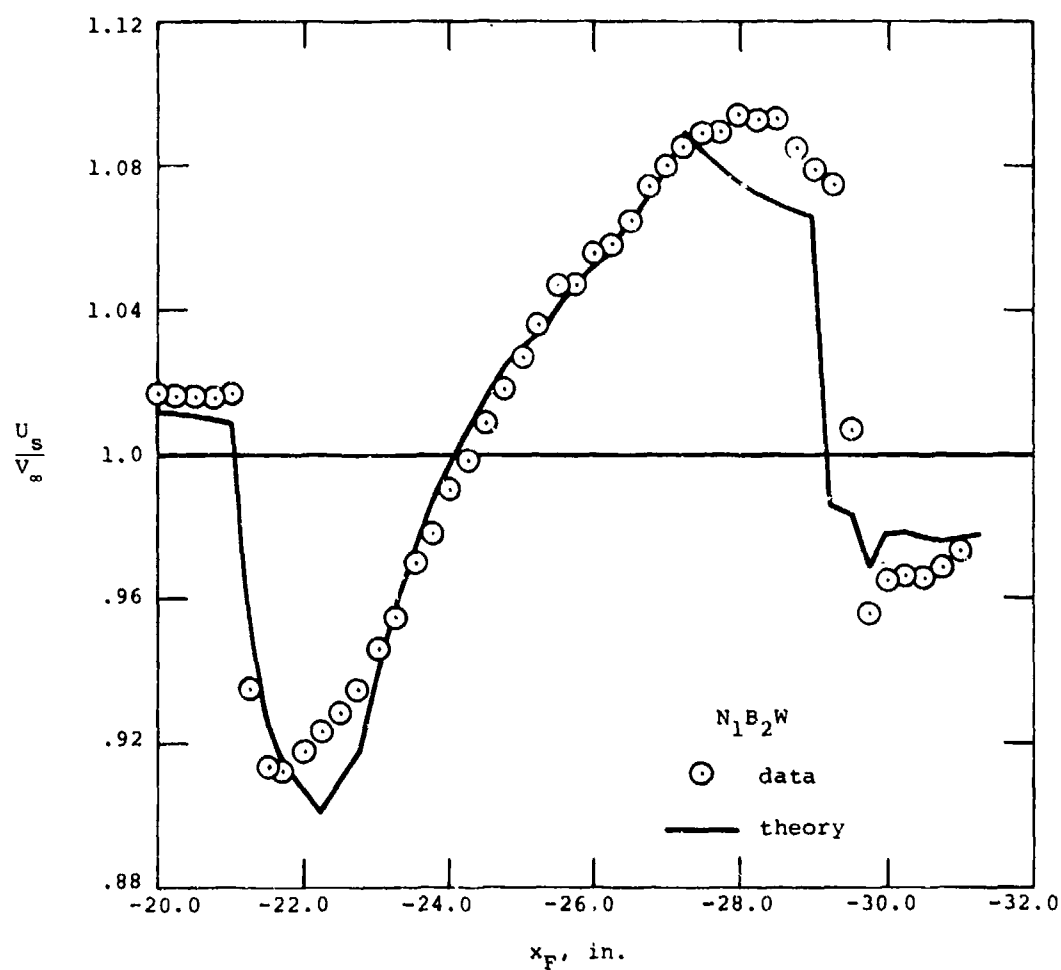
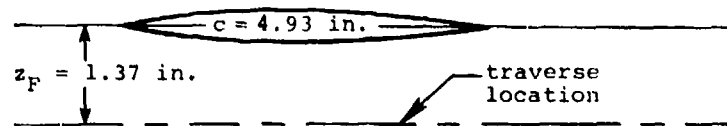
(a) Sidewash velocity.

Figure 3E.- Flow field under the wing at the one-third semispan location; $M_\infty = 1.5$, $\alpha_F = 0^\circ$, $z_F = 4.37$ in.



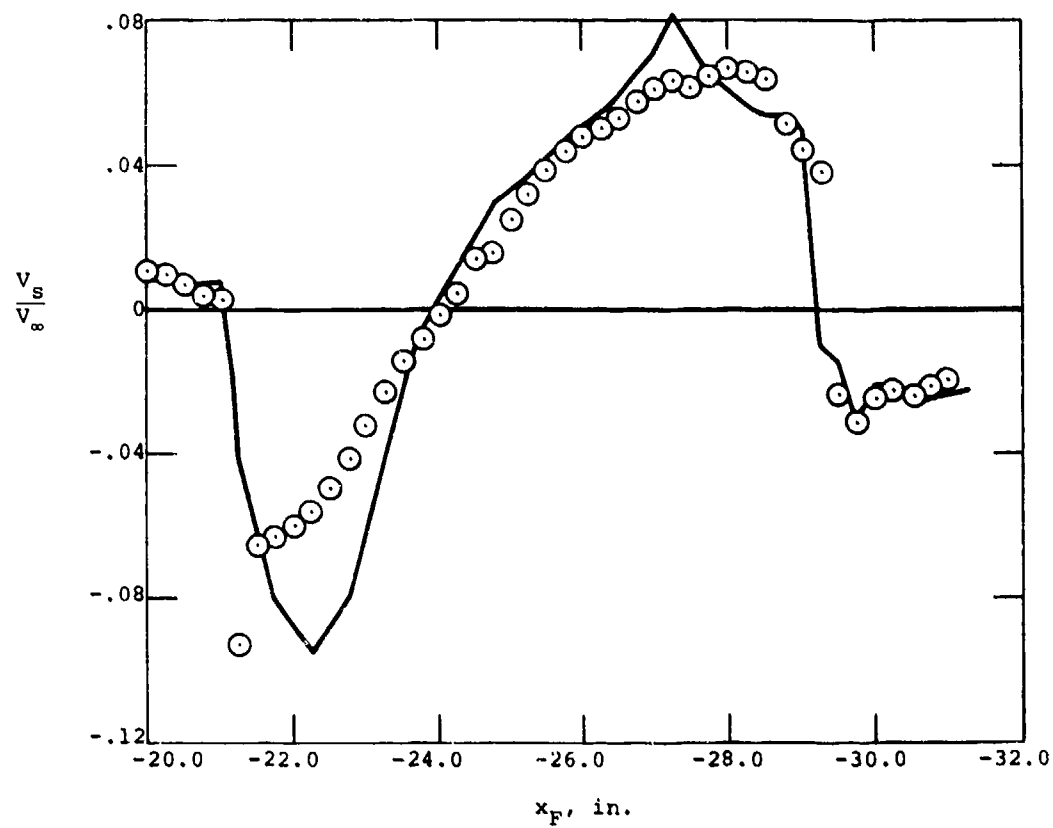
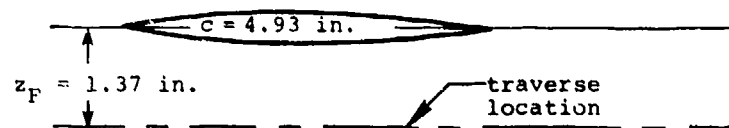
(b) Upwash velocity.

Figure 38.- Concluded.



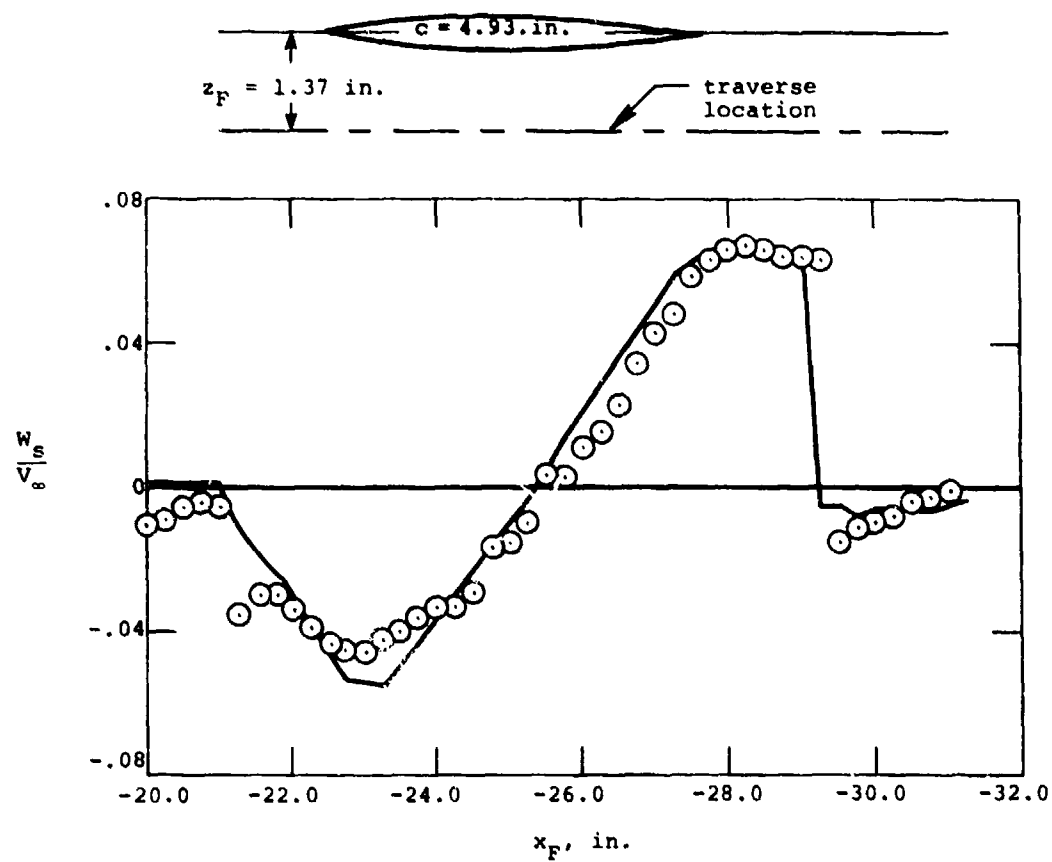
(a) Axial velocity.

Figure 39.- Flow field under the wing at the two-third semispan location; $M_\infty = 1.5$, $\alpha_F = 0^\circ$, $z_F = 1.37 \text{ in.}$



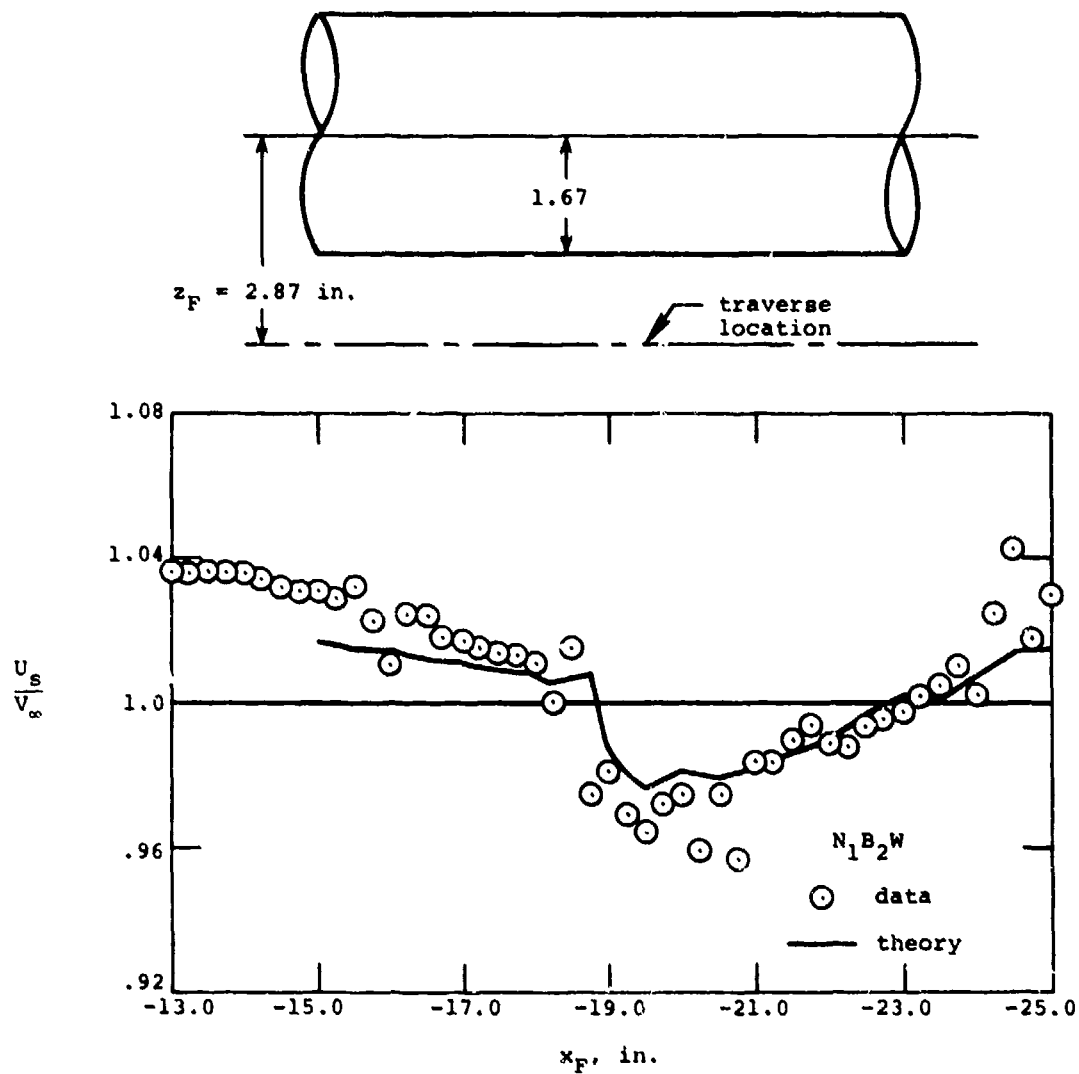
(b) Sidewash velocity.

Figure 39.- Continued.



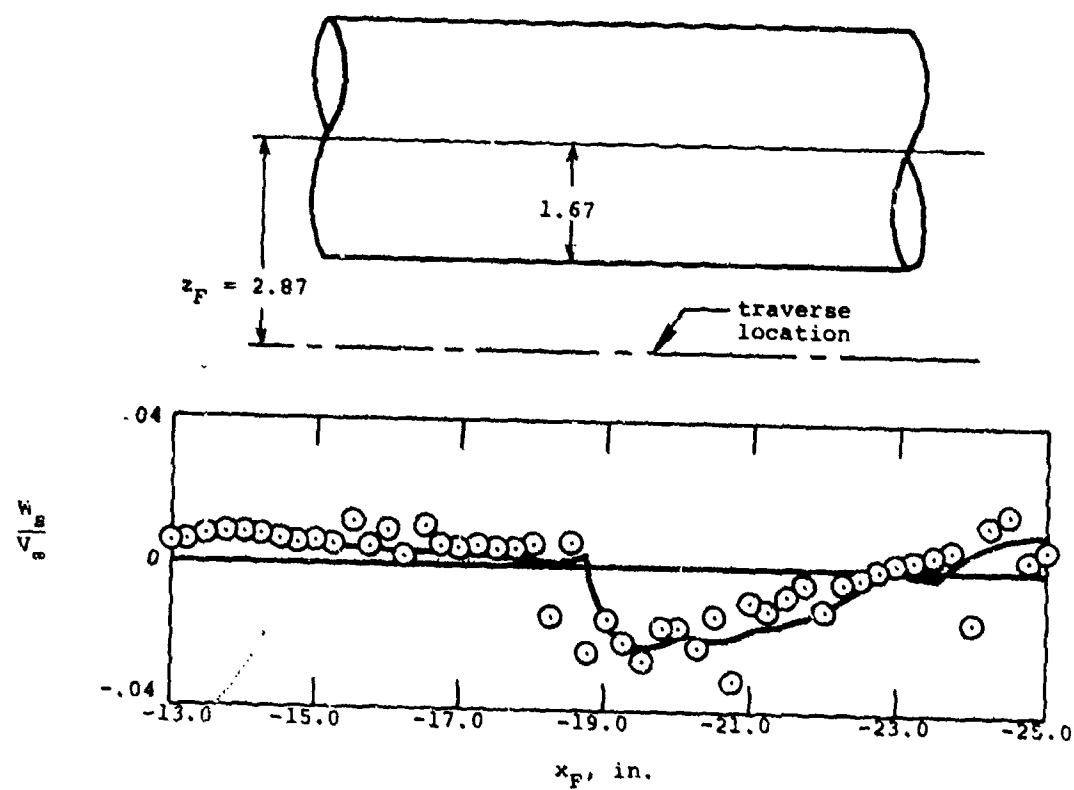
(c) Upwash velocity.

Figure 39.- Concluded.



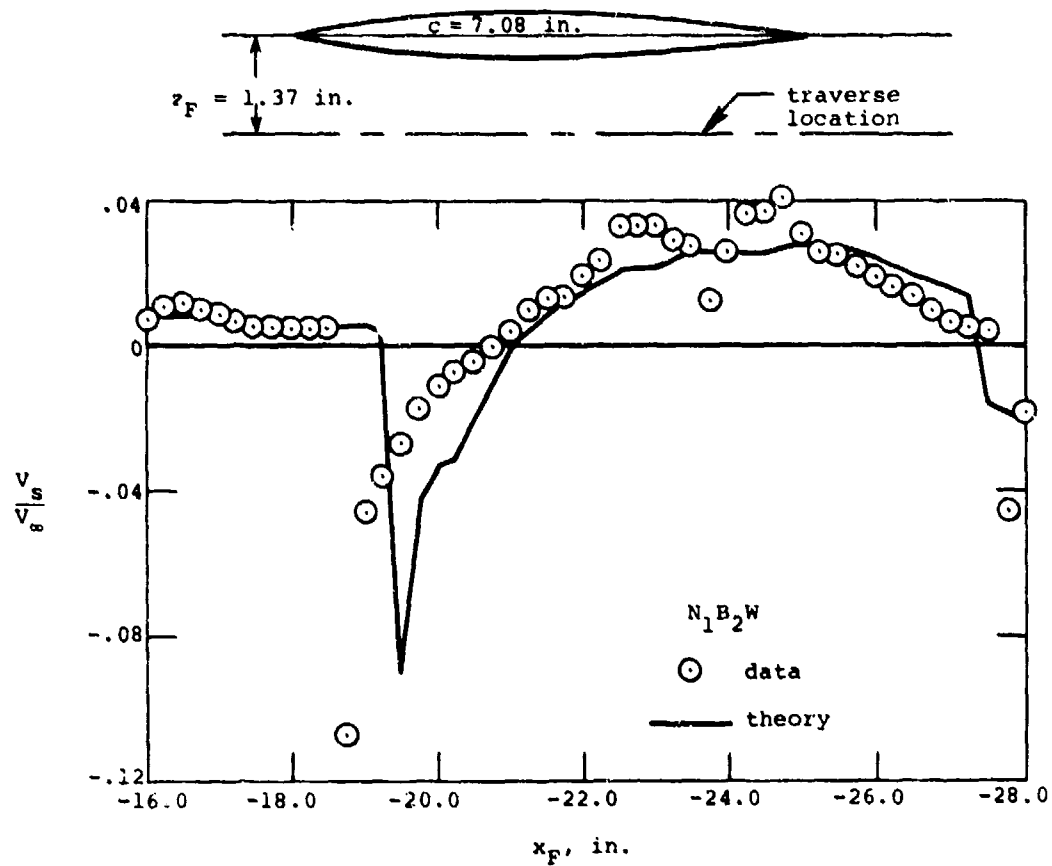
(a) Axial velocity.

Figure 40.- Flow field under the fuselage centerline;
 $M_\infty = 1.5$, $\alpha_F = 0^\circ$, $z_F = 2.87$ in.



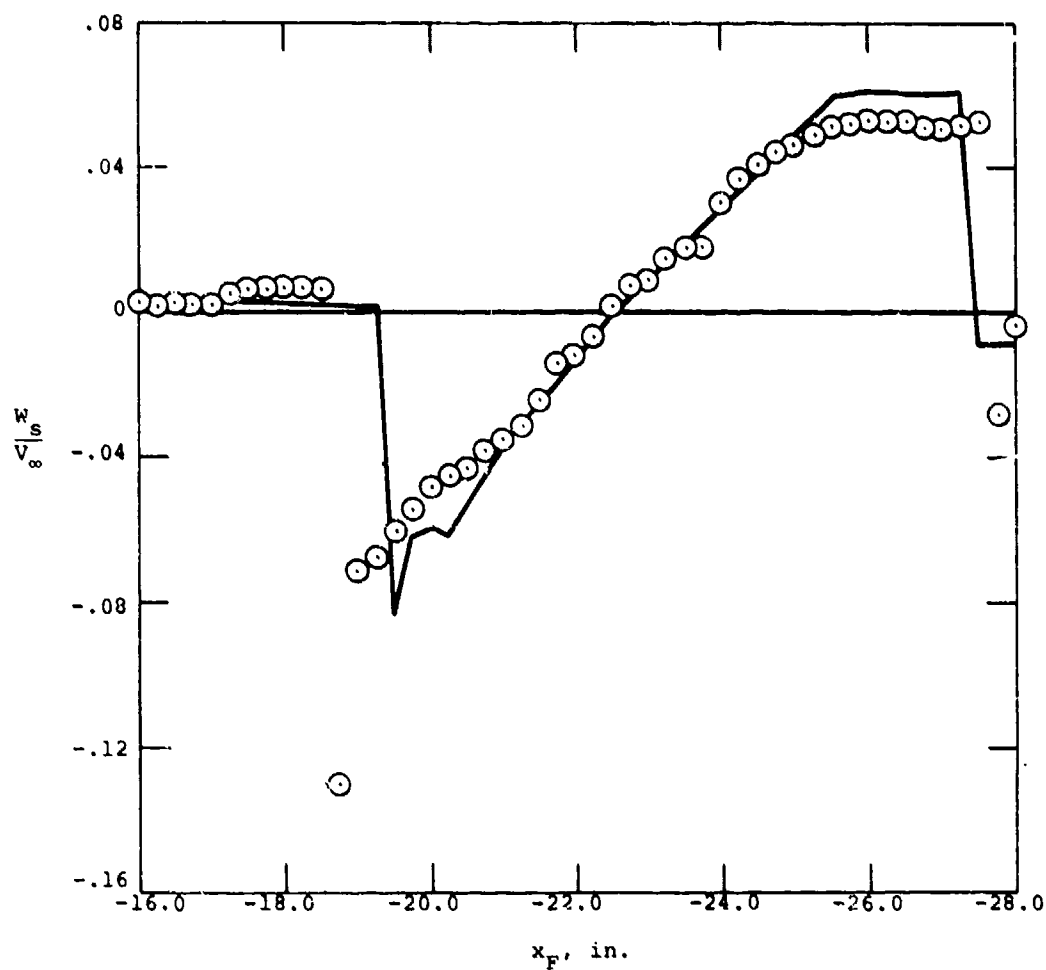
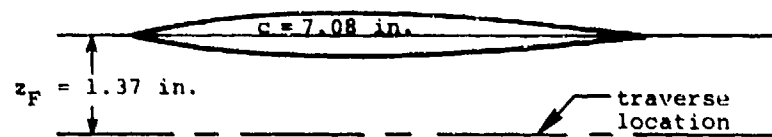
(b) Upwash velocity.

Figure 40.- Concluded.



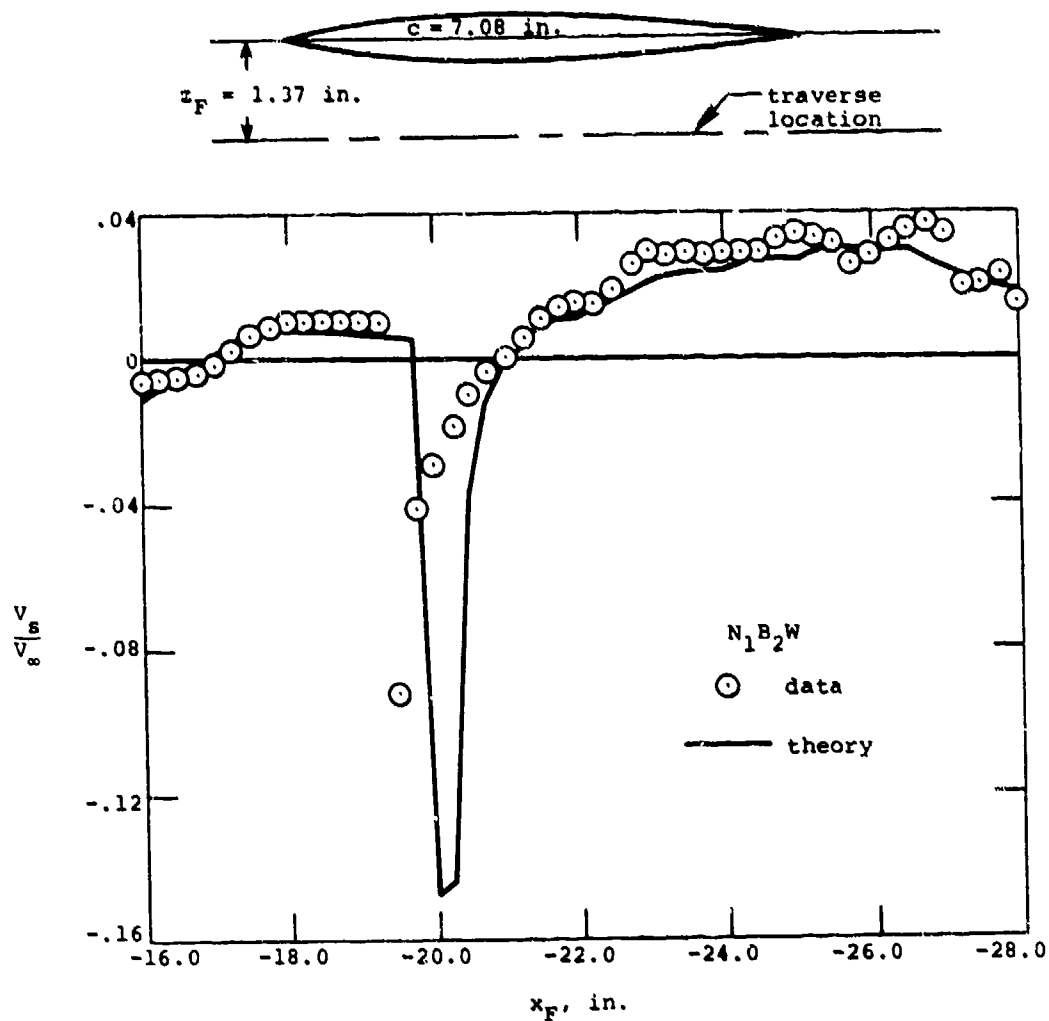
(a) Sidewash velocity.

Figure 41.- Flow field under the wing at the one-third semispan location; $M_\infty = 2.0$, $\alpha_F = 0^\circ$, $z_F = 1.37$ in.



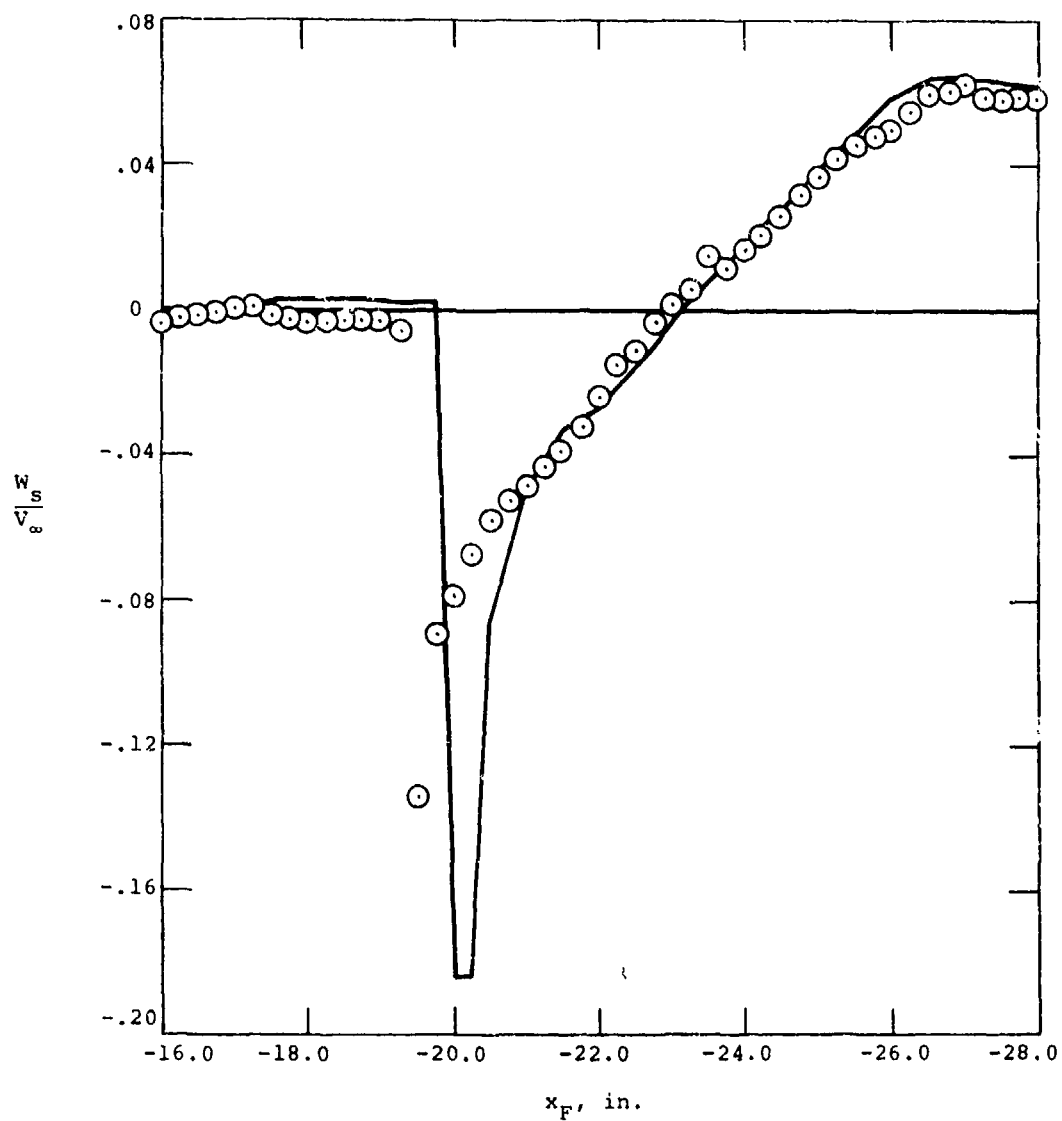
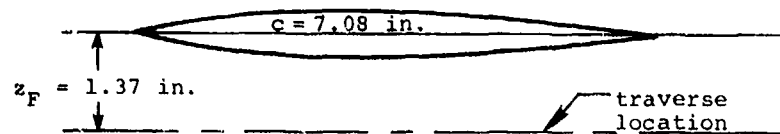
(b) Upwash velocity.

Figure 41.- Concluded.



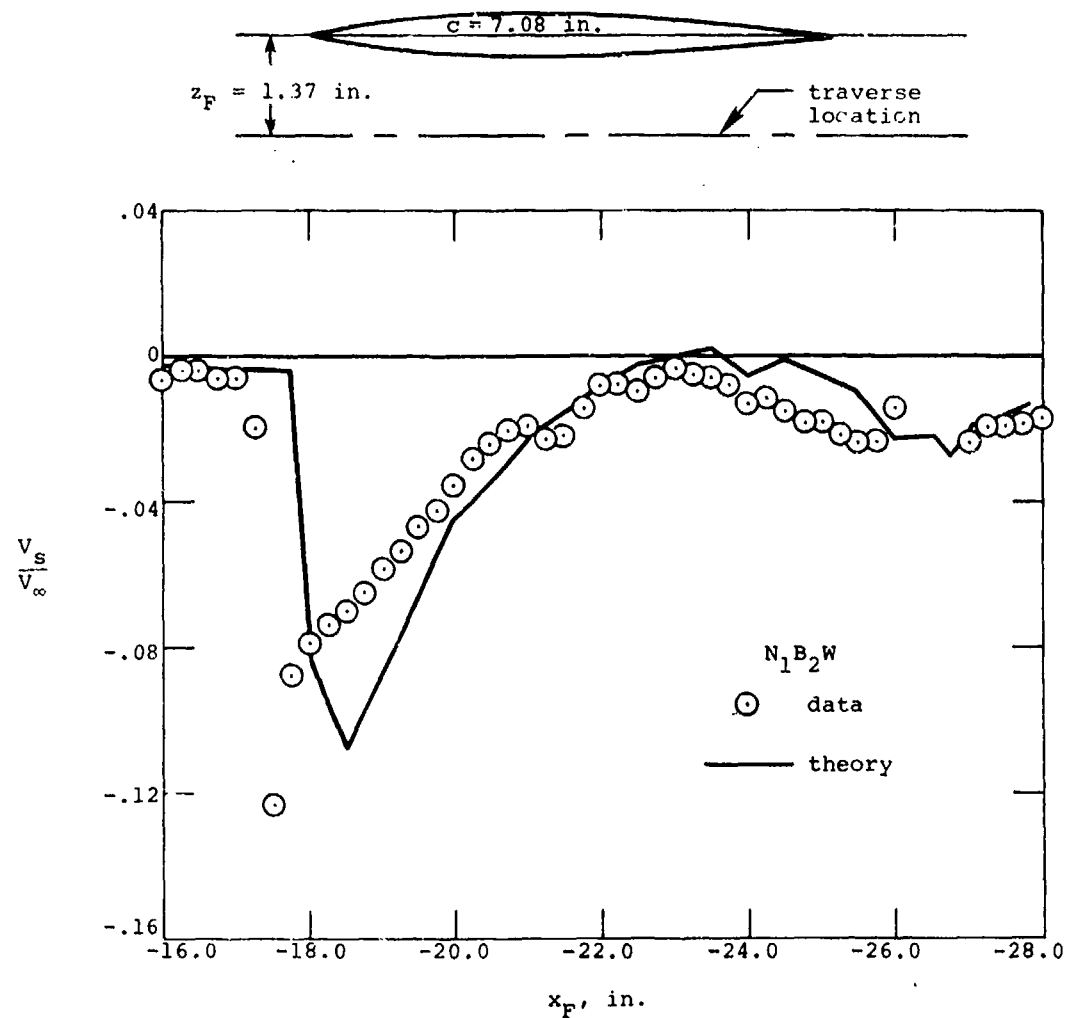
(a) Sidewash velocity.

Figure 42.- Flow field under the wing at the one-third semispan location; $M_\infty = 2.5$, $\alpha = 0^\circ$, $z_F = 1.37$ in.



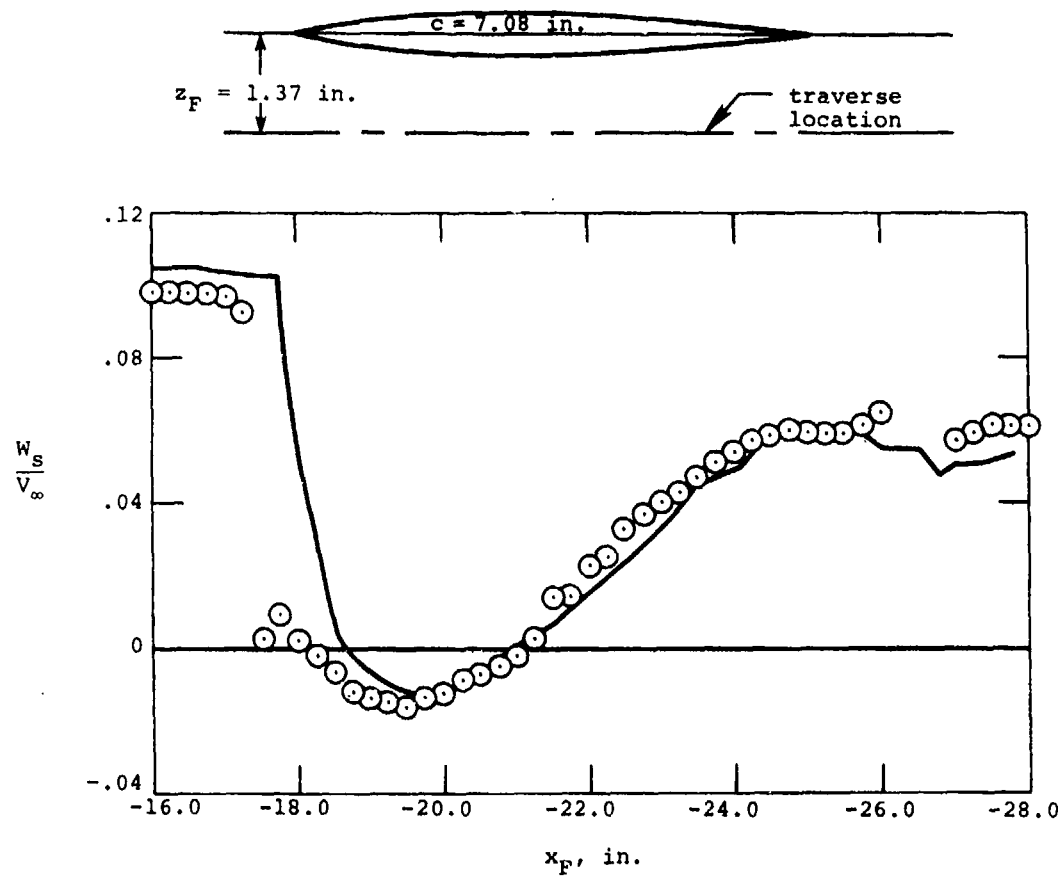
(b) Upwash velocity.

Figure 42.- Concluded.



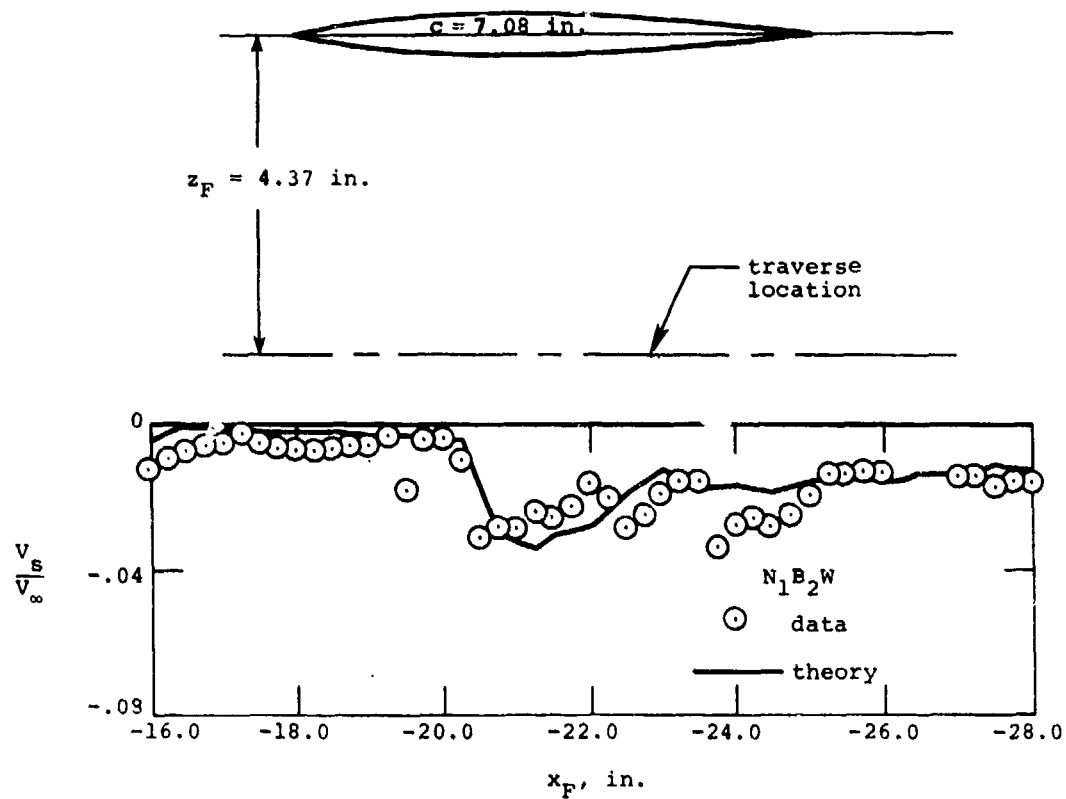
(a) Sidewash velocity.

Figure 43.- Flow field under the wing at the one-third semispan location; $M_\infty = 1.5$, $\alpha_F = 5^\circ$, $z_F = 1.37$ in.



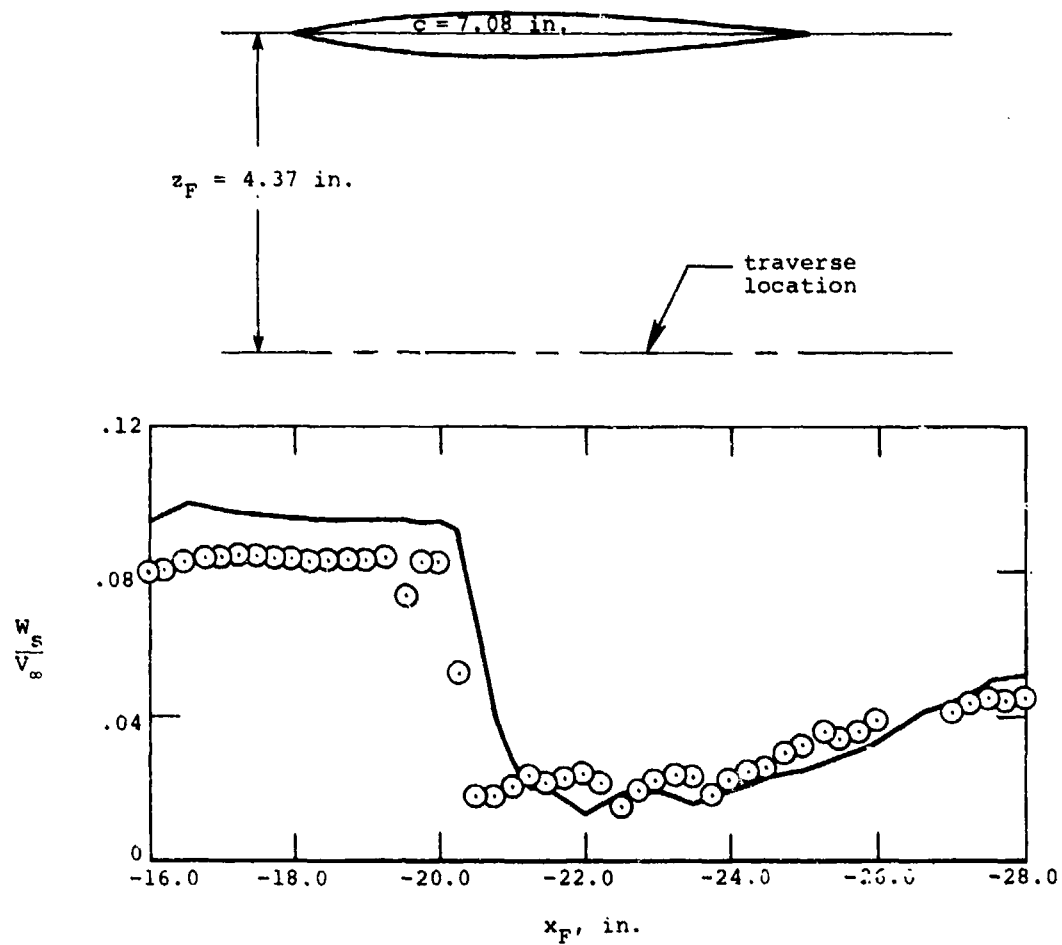
(b) Upwash velocity.

Figure 43.- Concluded.



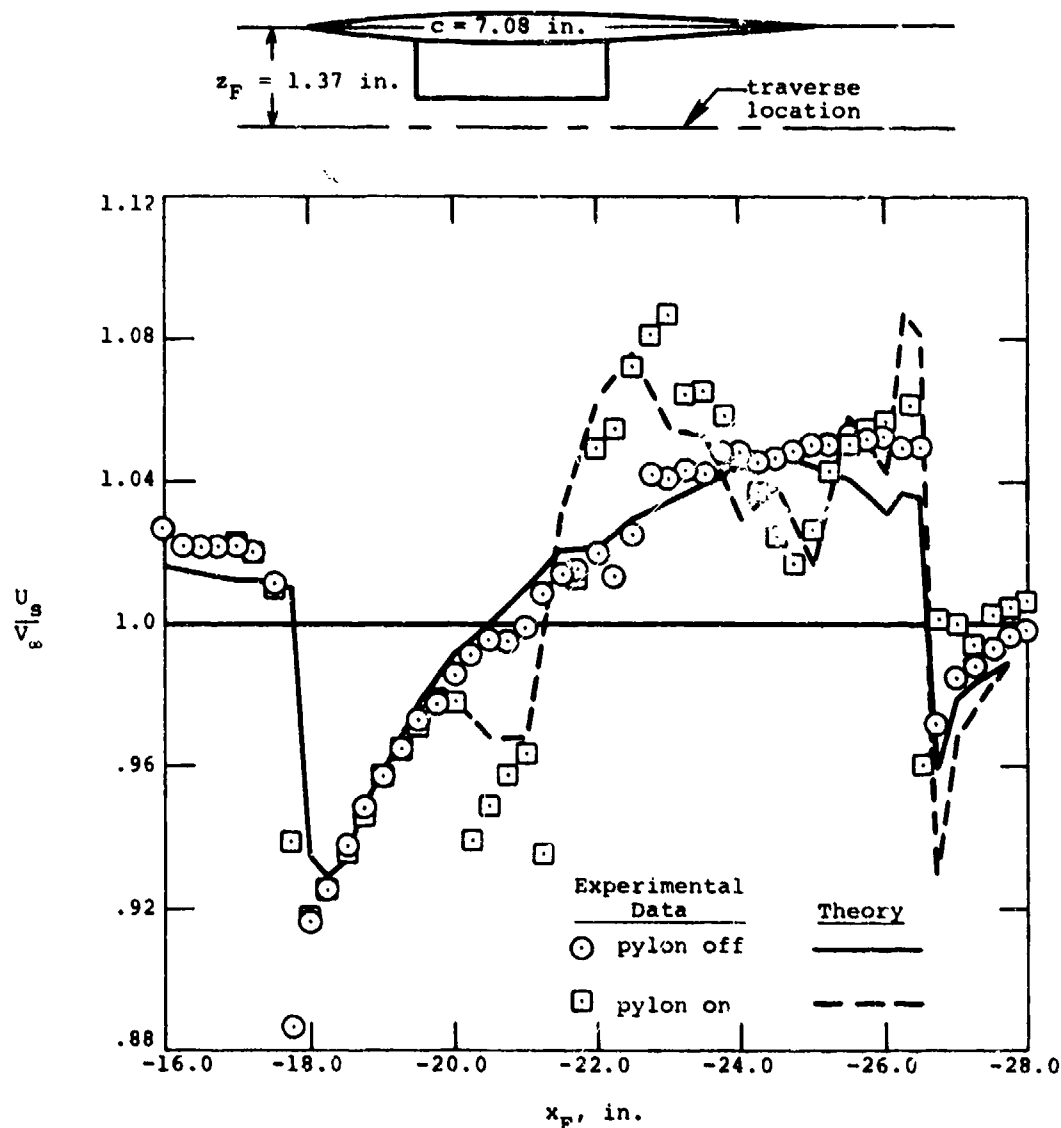
(a) Sidewash velocity.

Figure 44.- Flow field under the wing at the one-third semispan location; $M_\infty = 1.5$, $\alpha_F = 5^\circ$, $z_F = 4.37$ in.



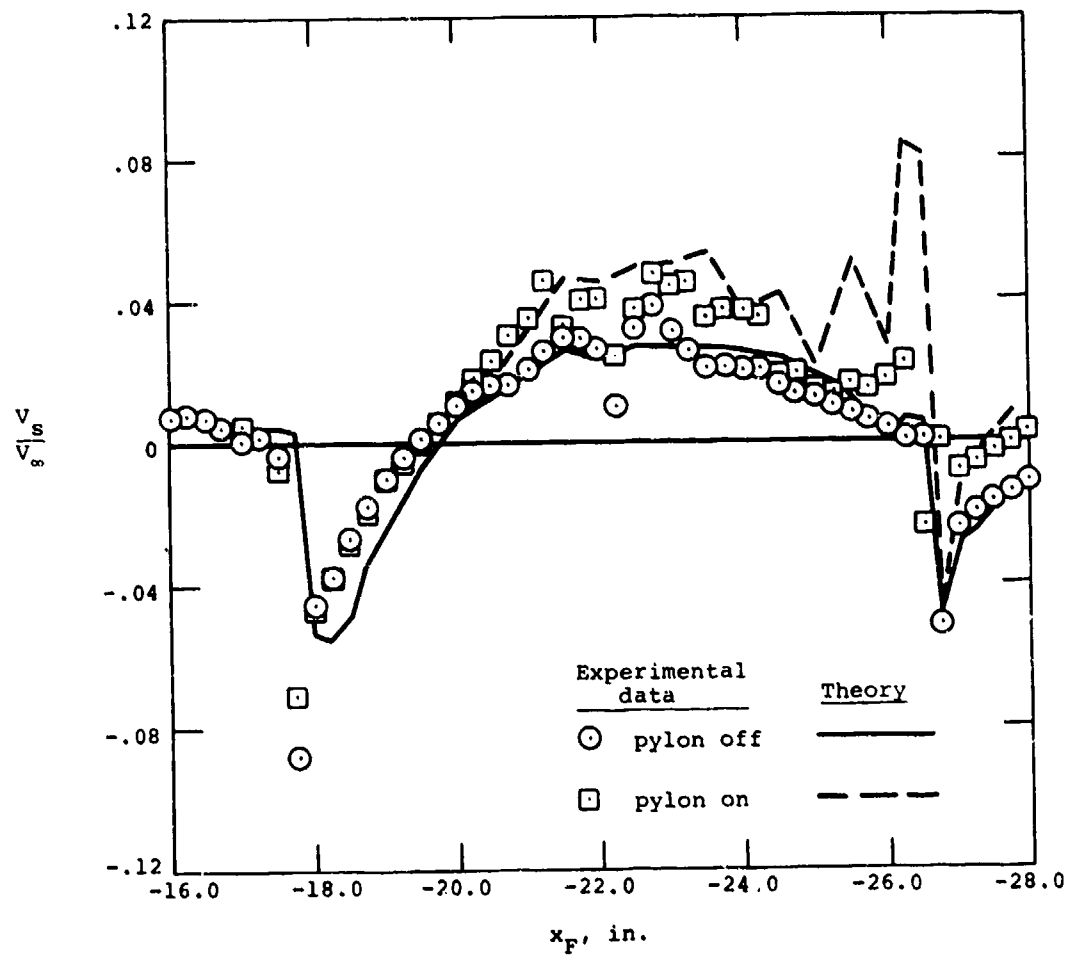
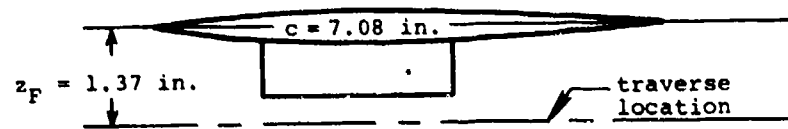
(b) Upwash velocity.

Figure 44.- Concluded.



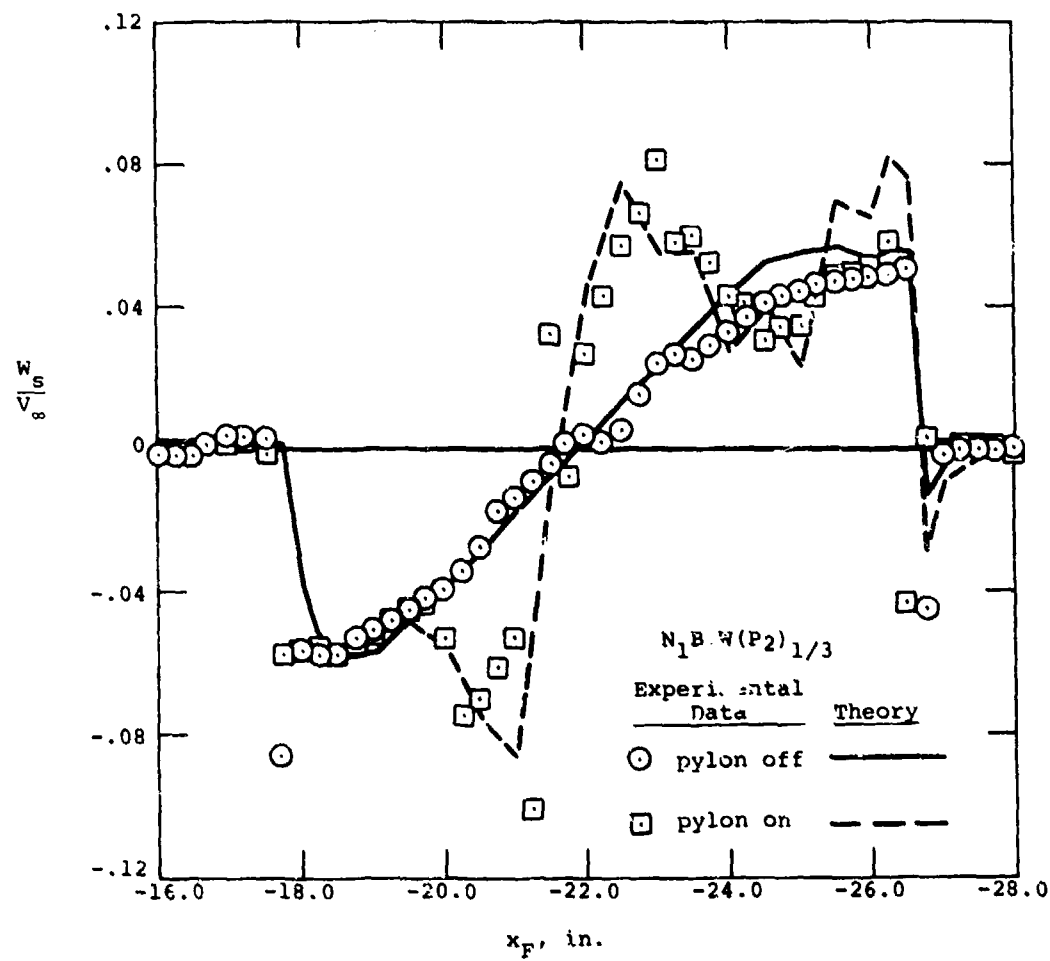
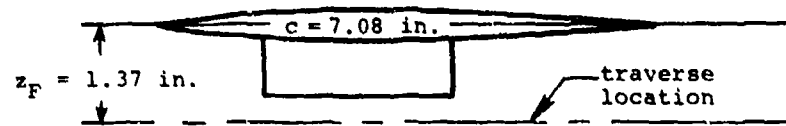
(a) Axial velocity.

Figure 45.- Effect of the pylon on the flow field under the left wing panel at the one-third semispan location;
 $M_\infty = 1.5$, $\alpha_F = 0^\circ$, $z_F = 1.37$ in.



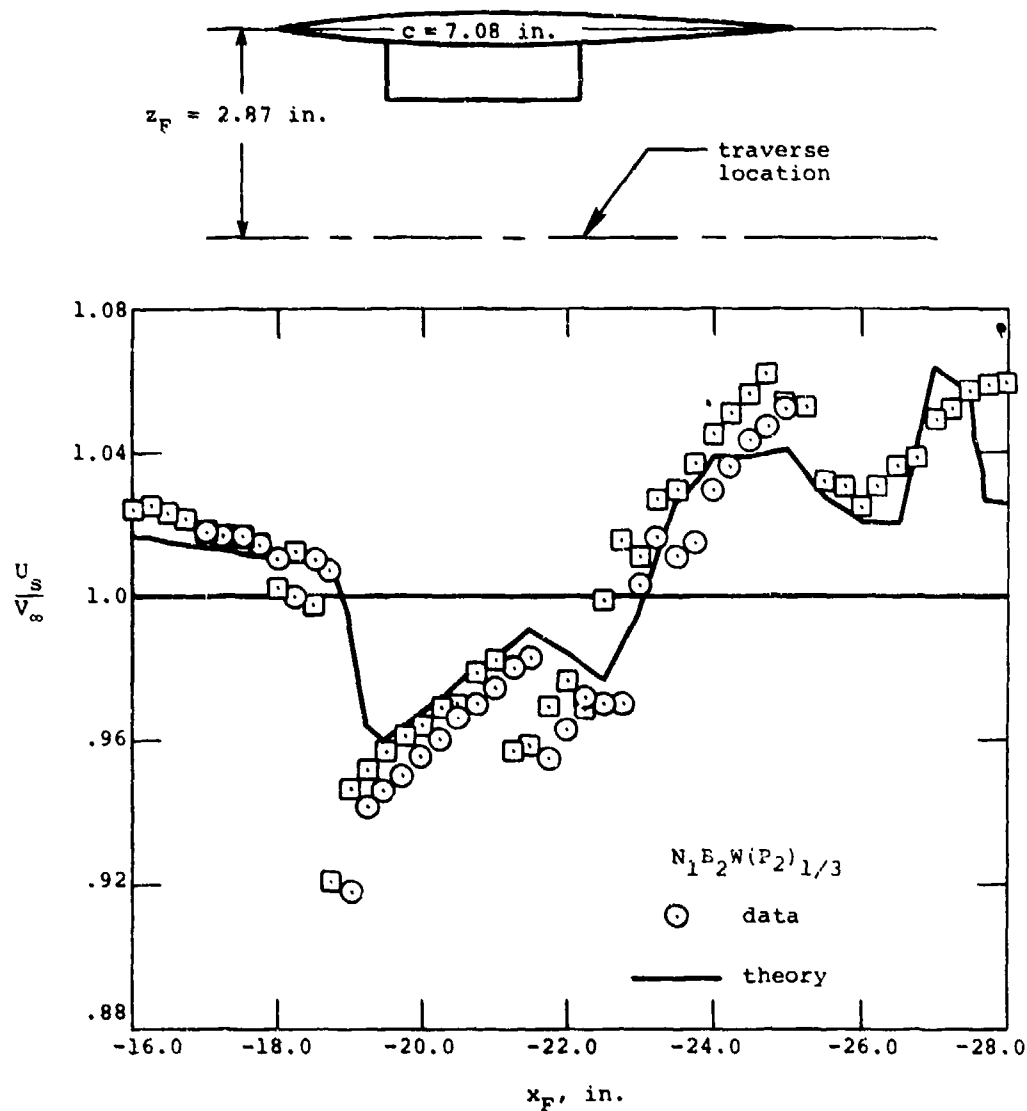
(b) Sidewash velocity.

Figure 45.- Continued.



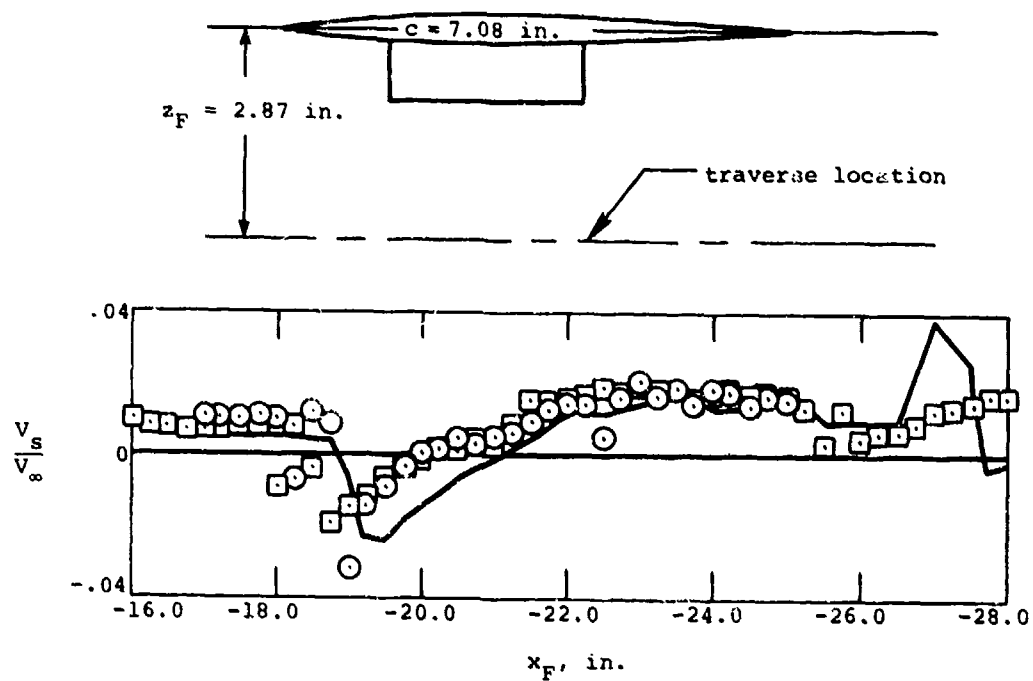
(c) Upwash velocity.

Figure 45.- Concluded.



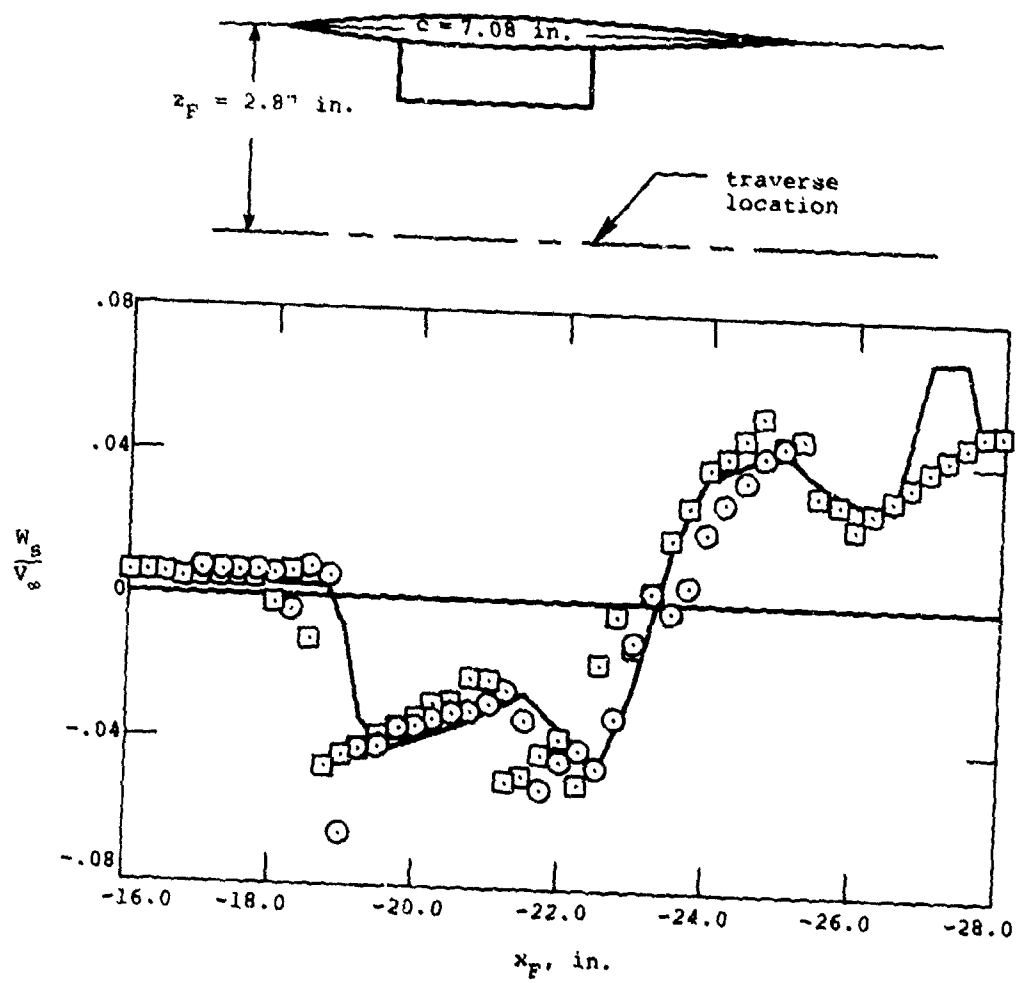
(a) Axial velocity.

Figure 46.- Flow field under the pylon at the one-third semispan location; $M_\infty = 1.5$, $\alpha_F = 0^\circ$, $z_F = 2.87$ in.



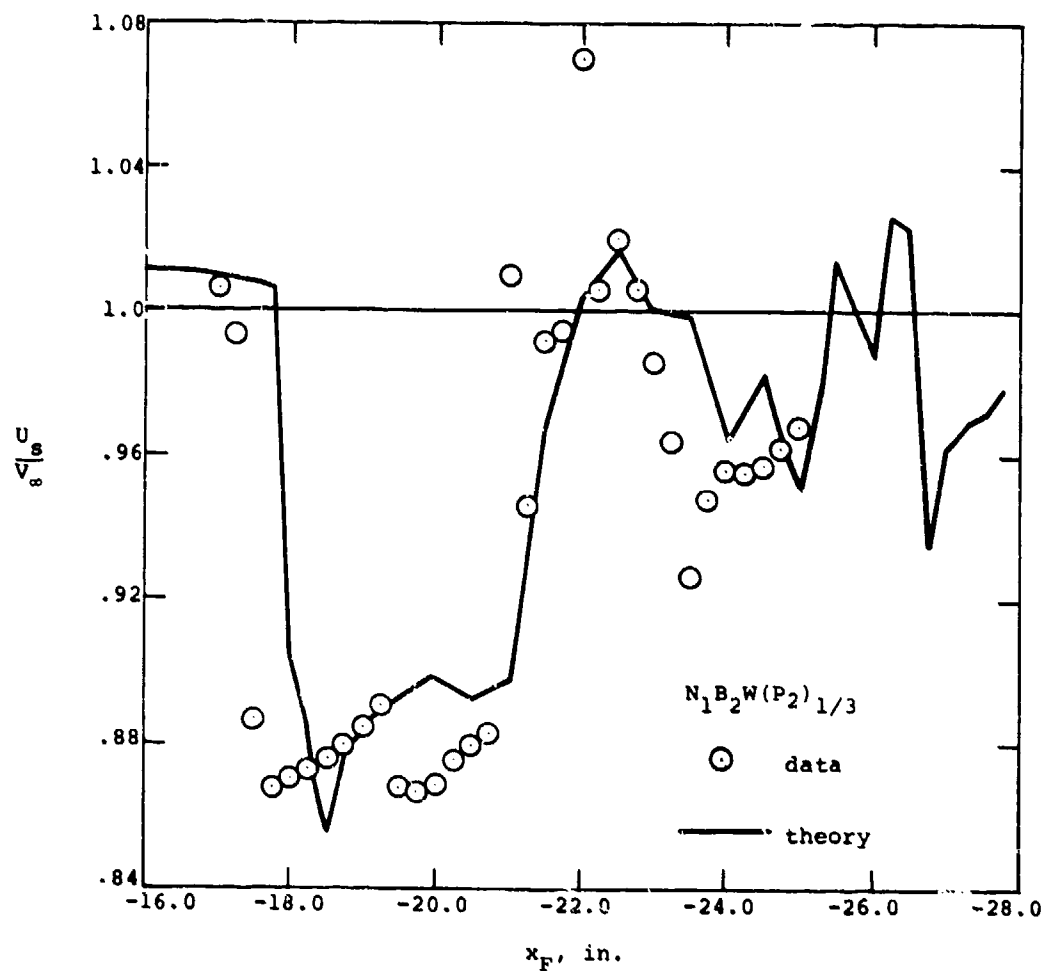
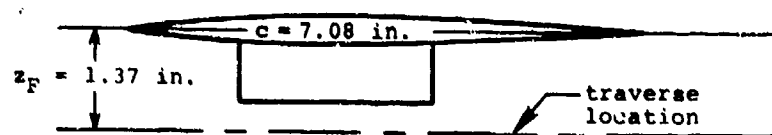
(b) Sidewash velocity.

Figure 46.- Continued.



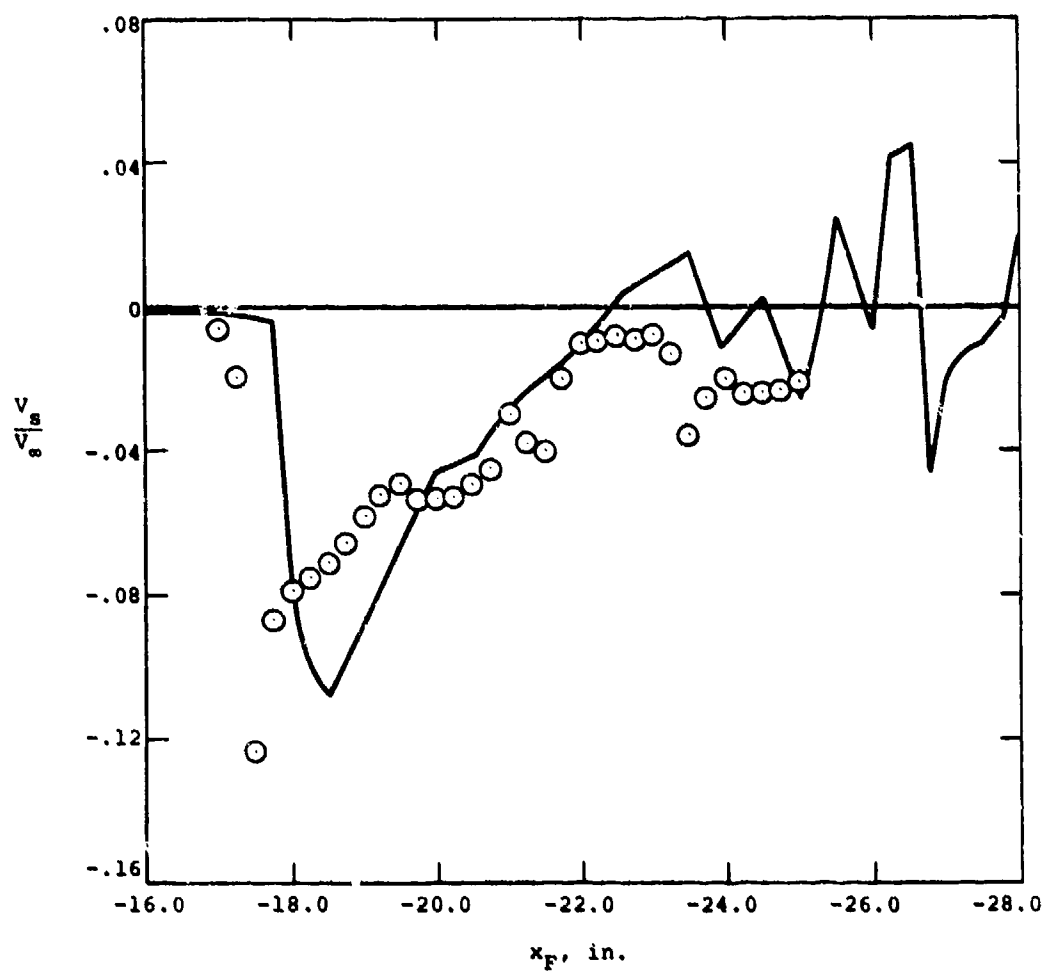
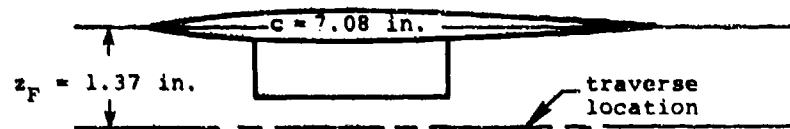
(c) Upwash velocity.

Figure 46.- Concluded.



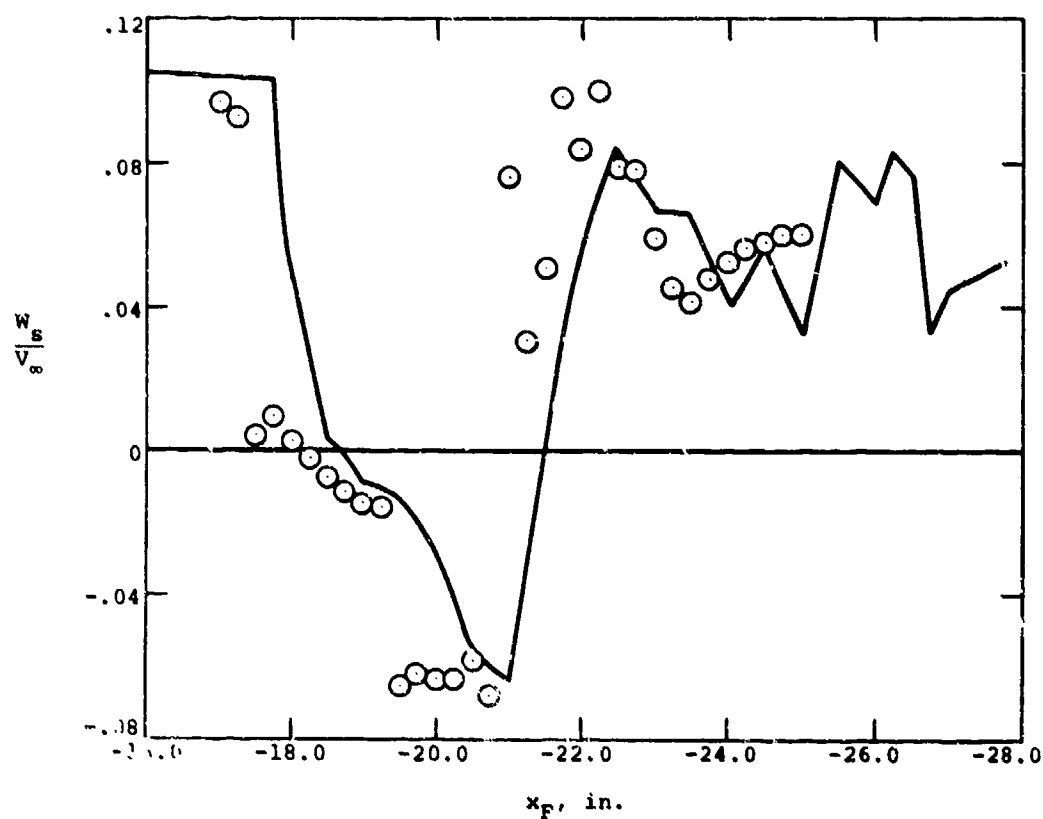
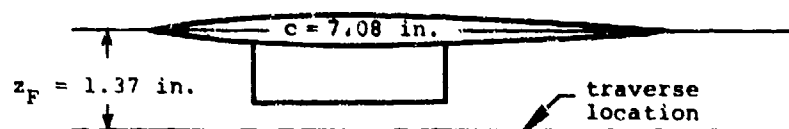
(a) Axial velocity.

Figure 47.- Flow field under the pylon at the one-third semispan location; $M_\infty = 1.5$, $\alpha_F = 5^\circ$, $z_F = 1.37$ in.



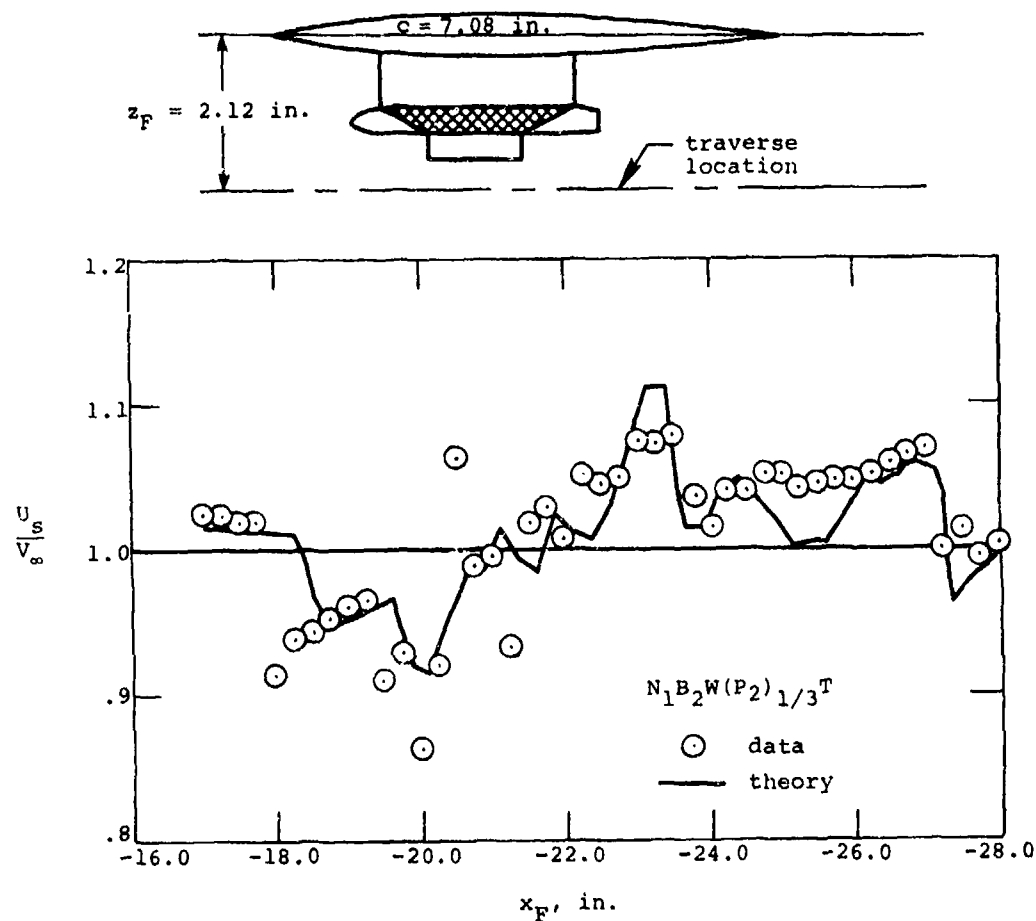
(b) Sidewash velocity.

Figure 47.- Continued.



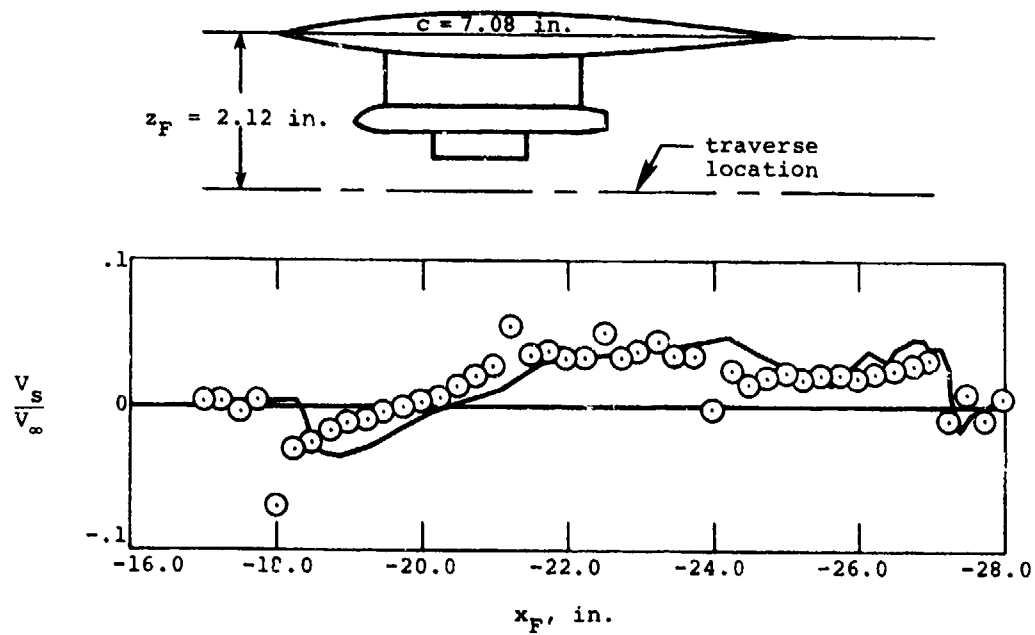
(c) Upwash velocity.

Figure 47.- Concluded.



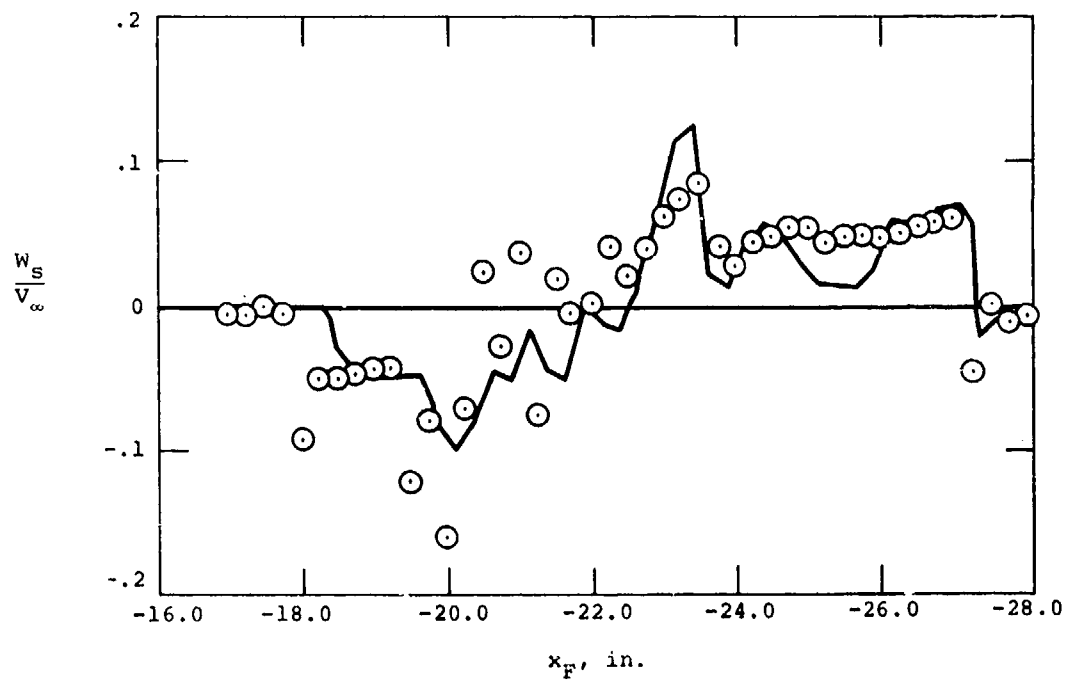
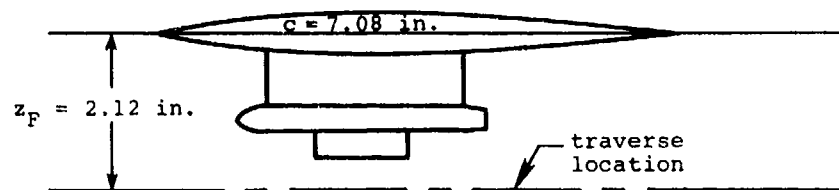
(a) Axial velocity.

Figure 48.- Flow field under the TER at the one-third semispan location; $M_\infty = 1.5$, $\alpha_F = 0^\circ$, $z_F = 2.12$ in.



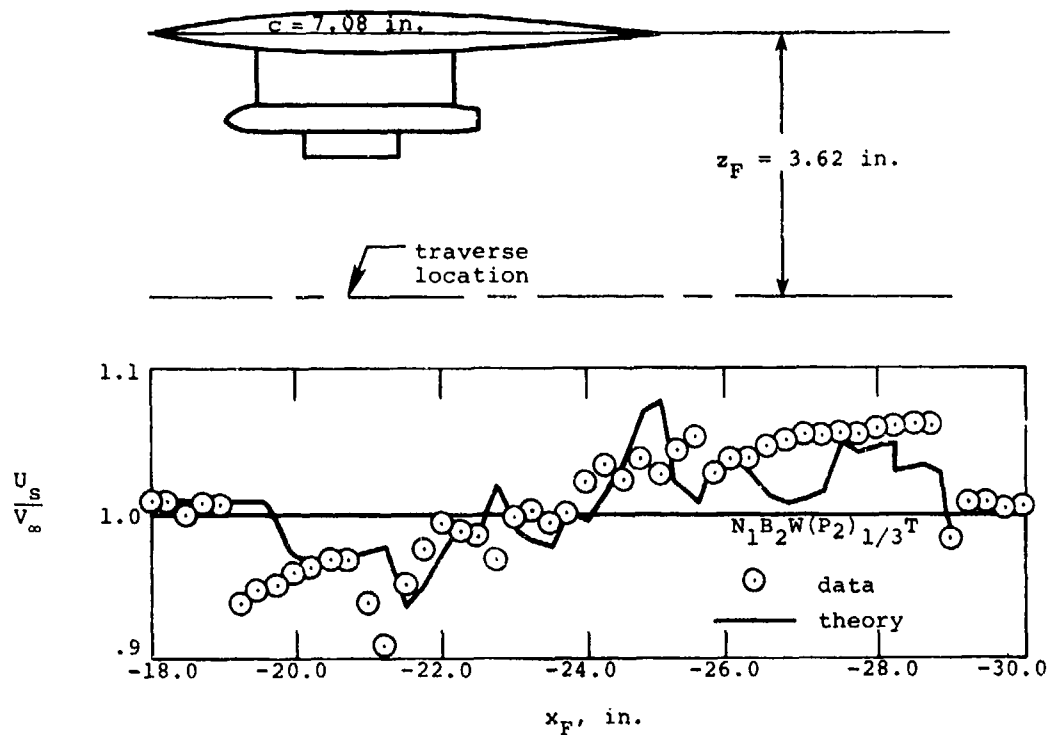
(b) Sidewash velocity.

Figure 48.- Continued.



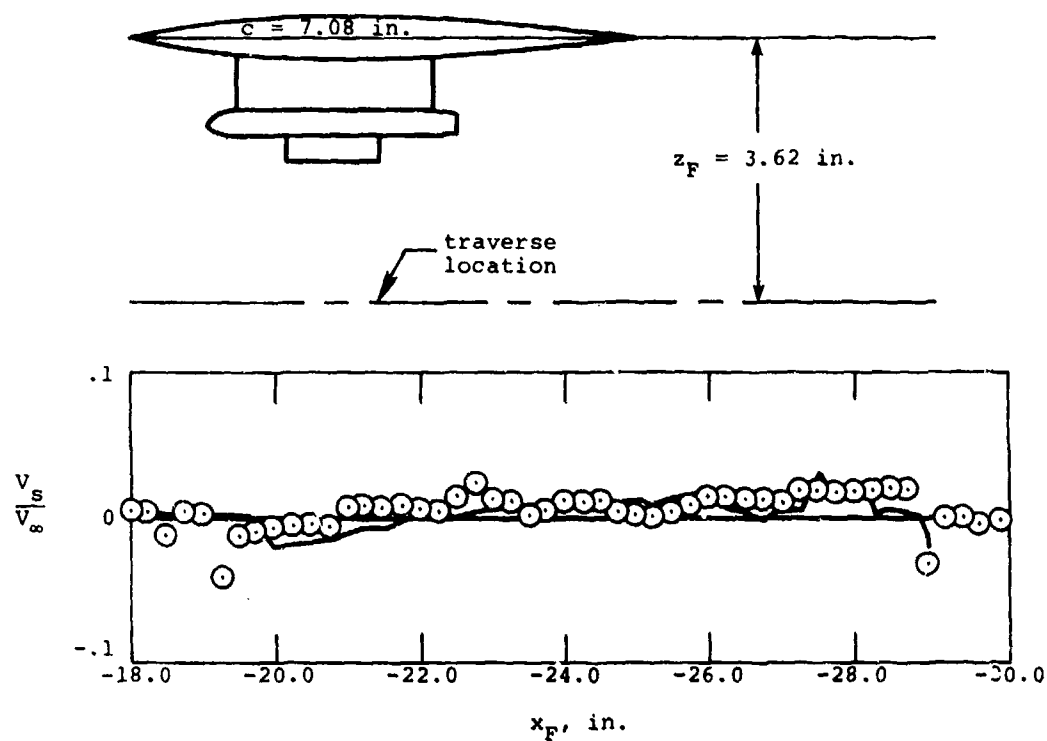
(c) Upwash velocity.

Figure 48.- Concluded.



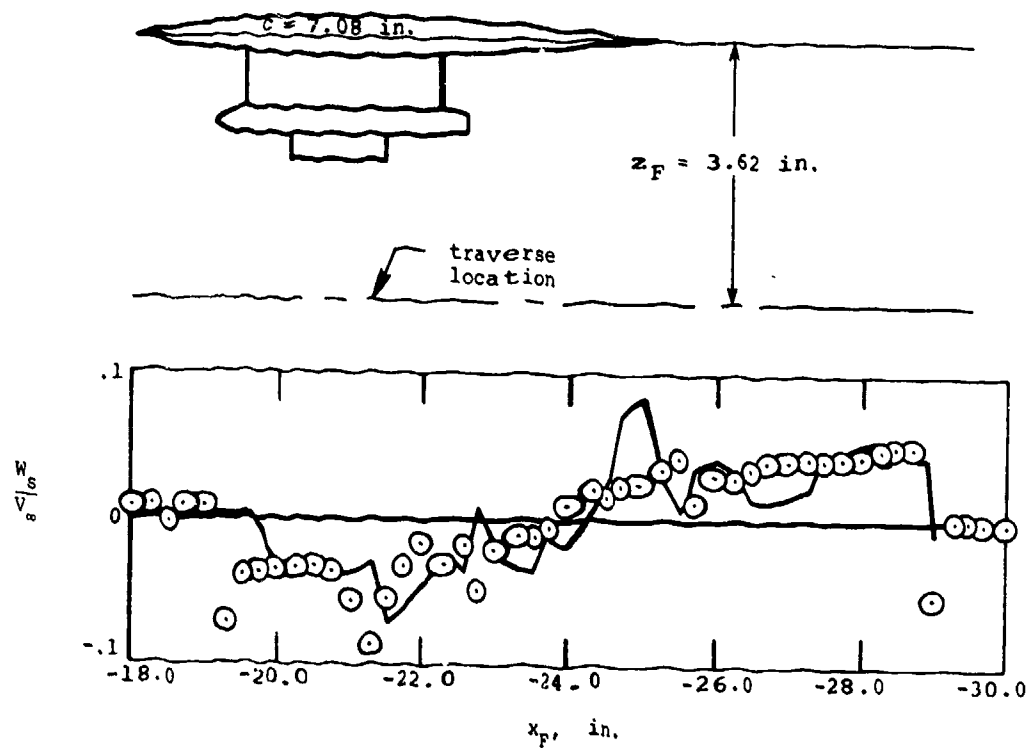
(a) Axial velocity.

Figure 49.- Flow field under the TER at the one-third semispan location; $M_\infty = 1.5$, $\alpha_F = 0^\circ$, $z_F = 3.62$ in.



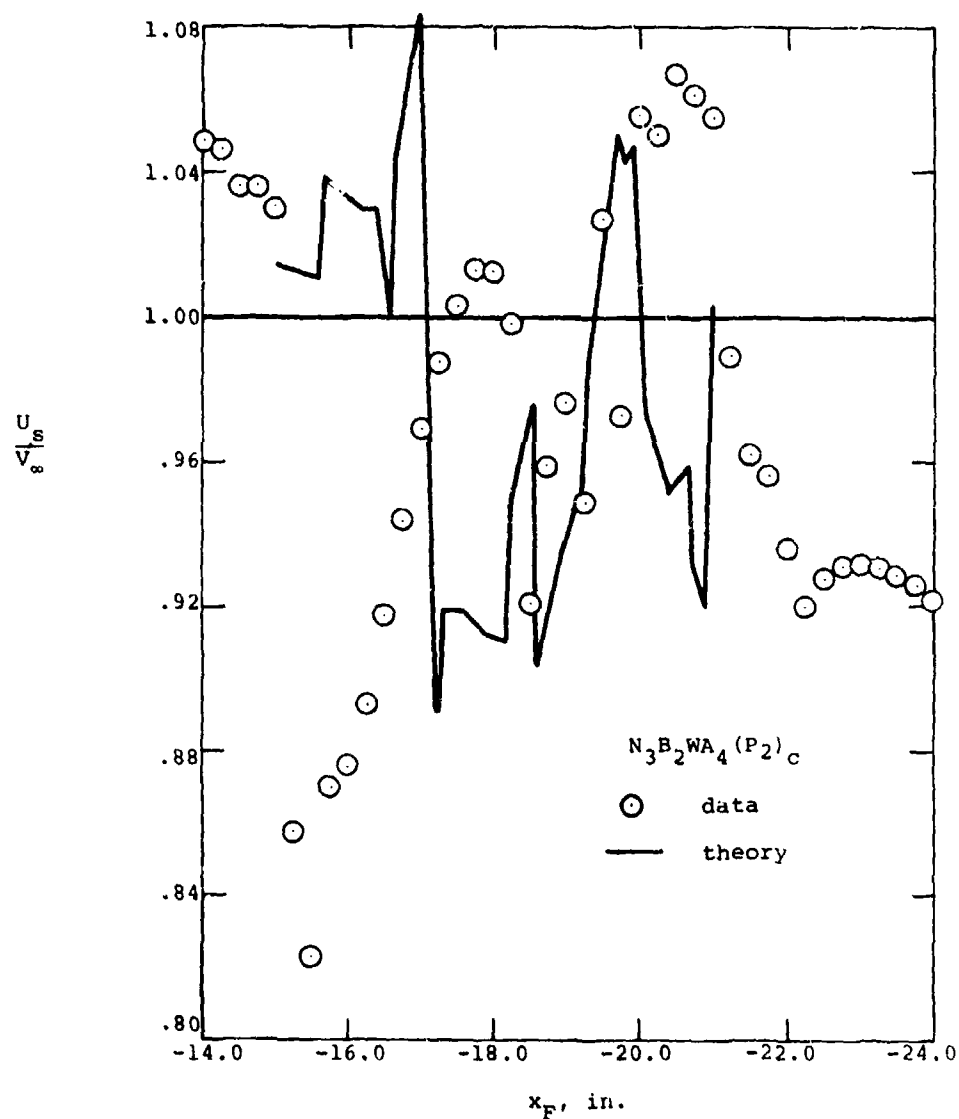
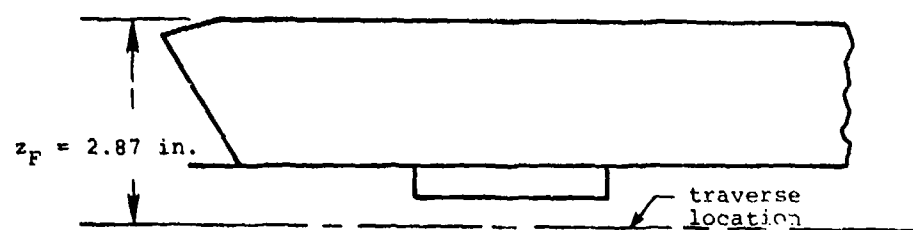
(b) Sidewash velocity.

Figure 49.- Continued.



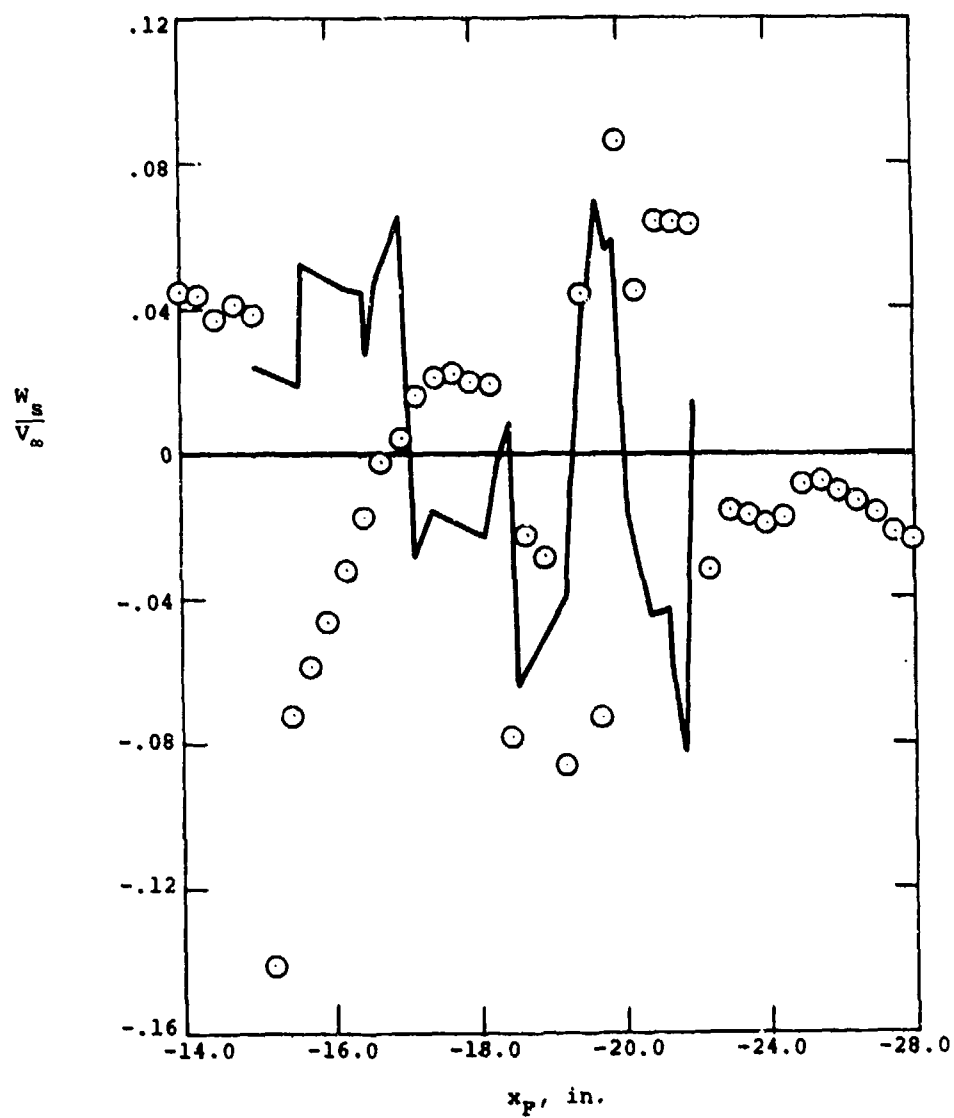
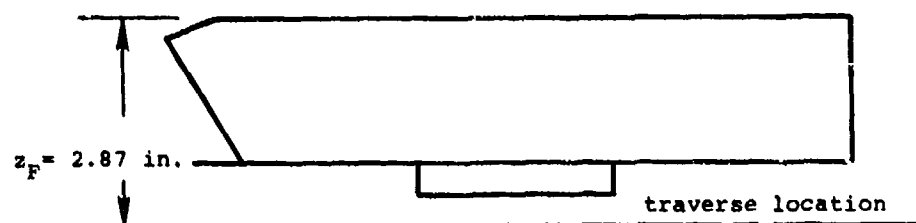
(c) Upwash velocity.

Figure 49.- Concluded.



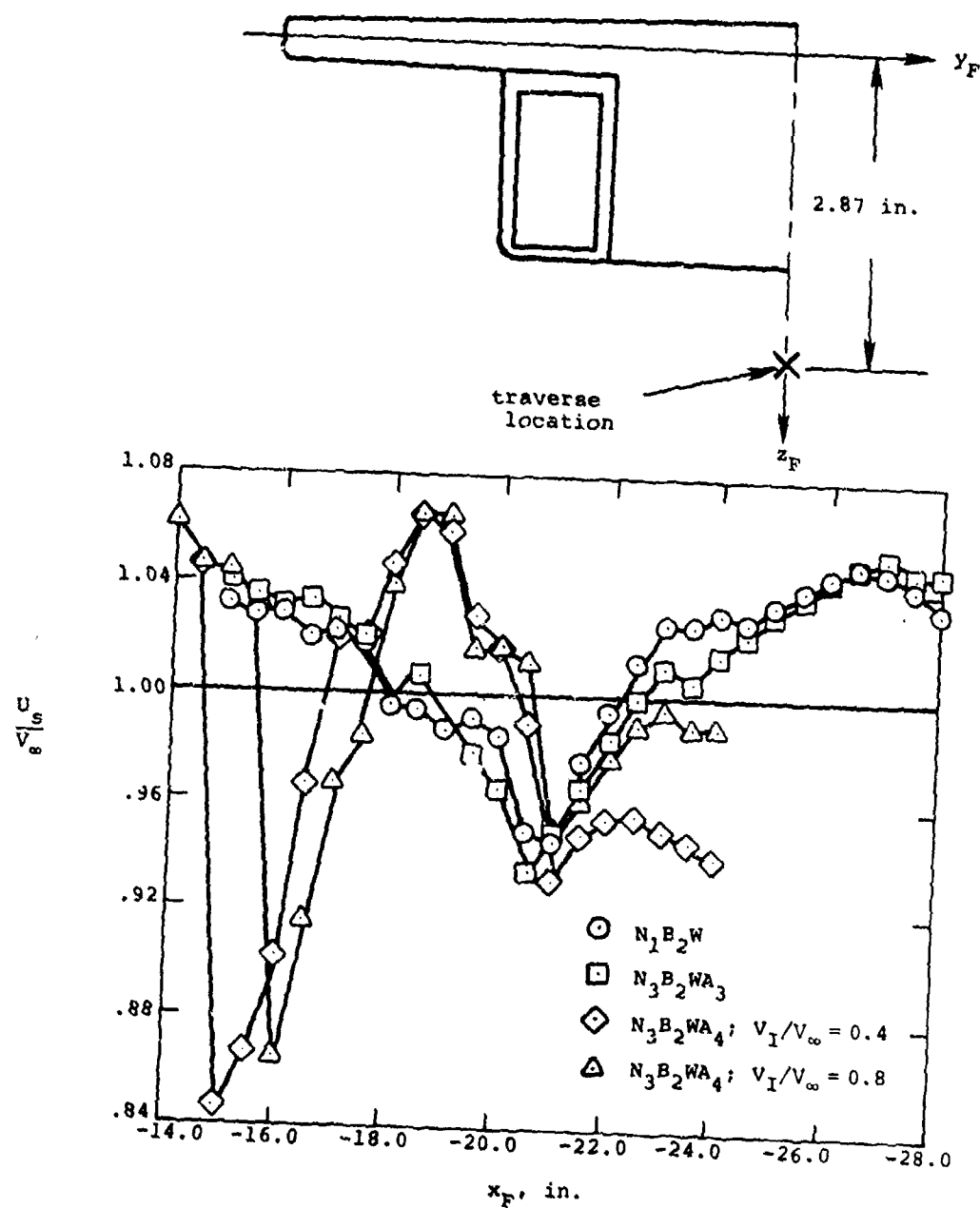
(a) Axial velocity.

Figure 50.- Flow field under the fuselage centerline of the configuration with inlets; $M_\infty = 1.5$, $\alpha_F = 5^\circ$, $z_F = 2.87$ in.



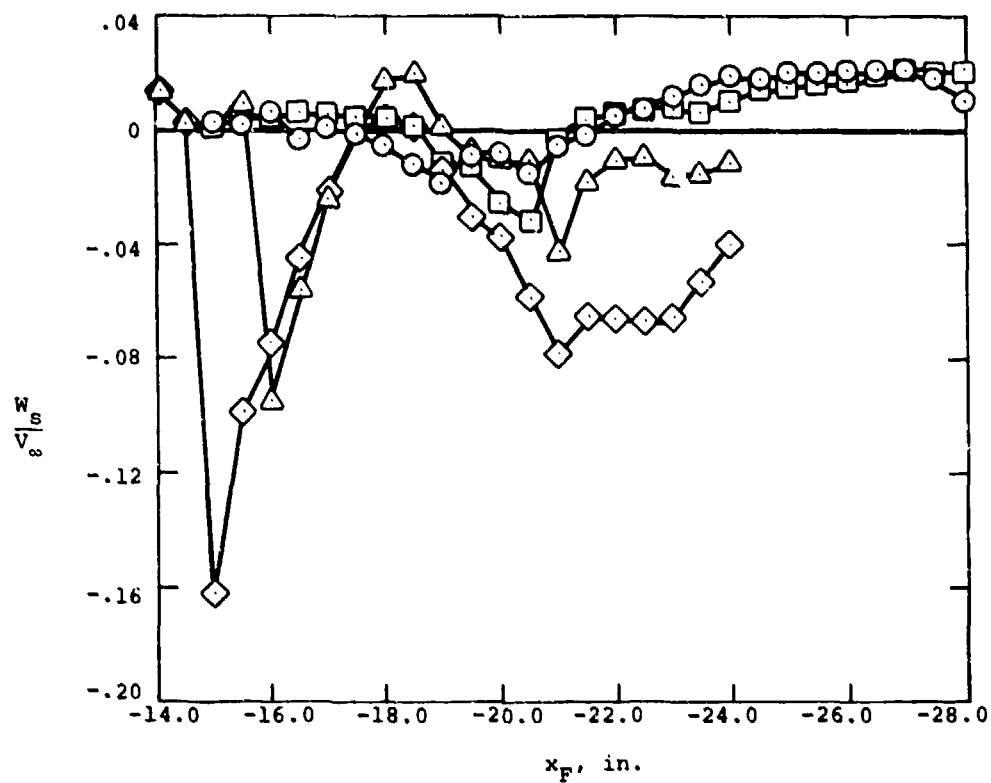
(b) Upwash velocity.

Figure 50.- Concluded.



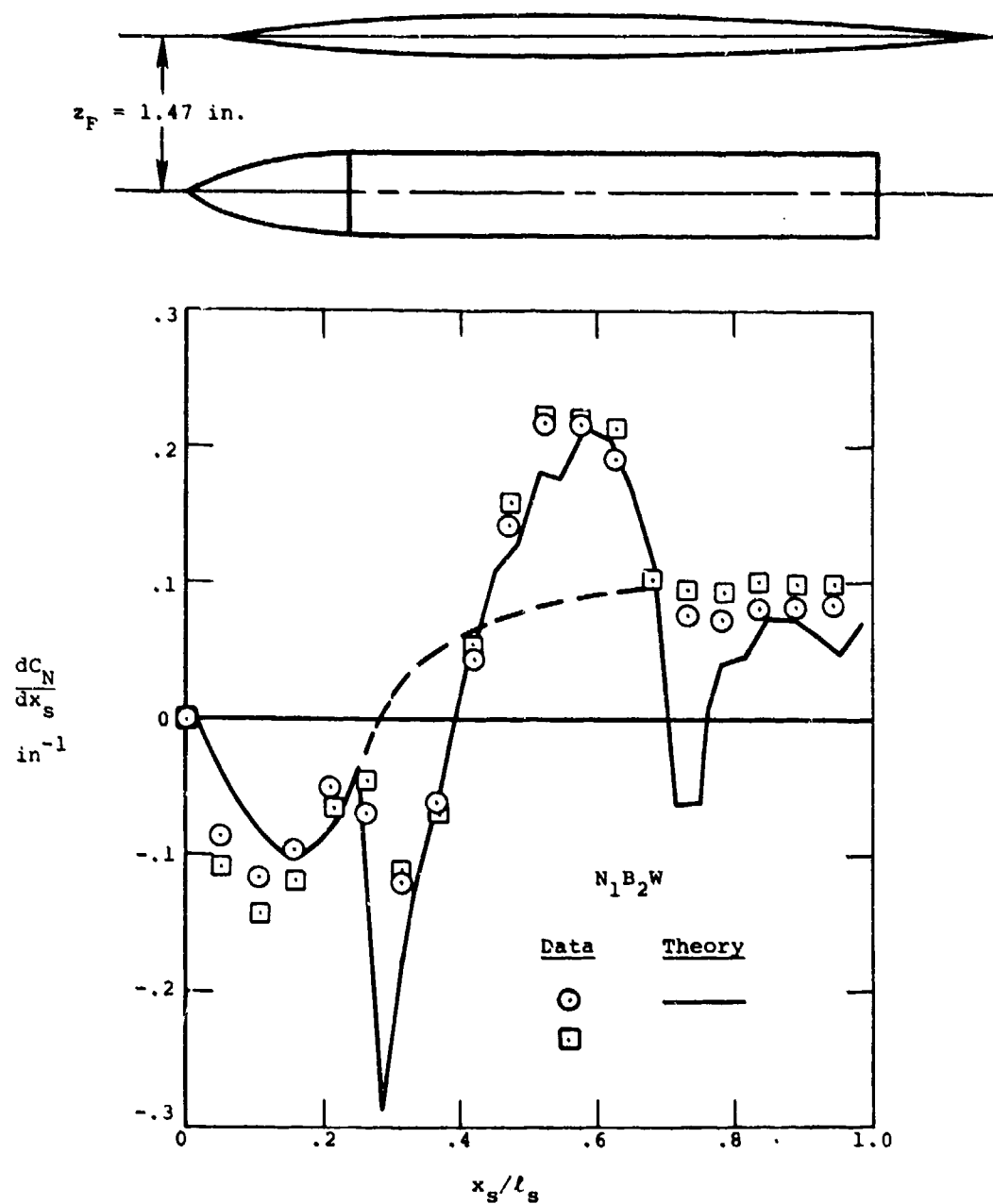
(a) Axial velocity.

Figure 51.- Experimental flow fields below the fuselage centerline for various configurations; $M_\infty = 1.5$, $\alpha_F = 0^\circ$, $z_F \approx 2.87$ in.



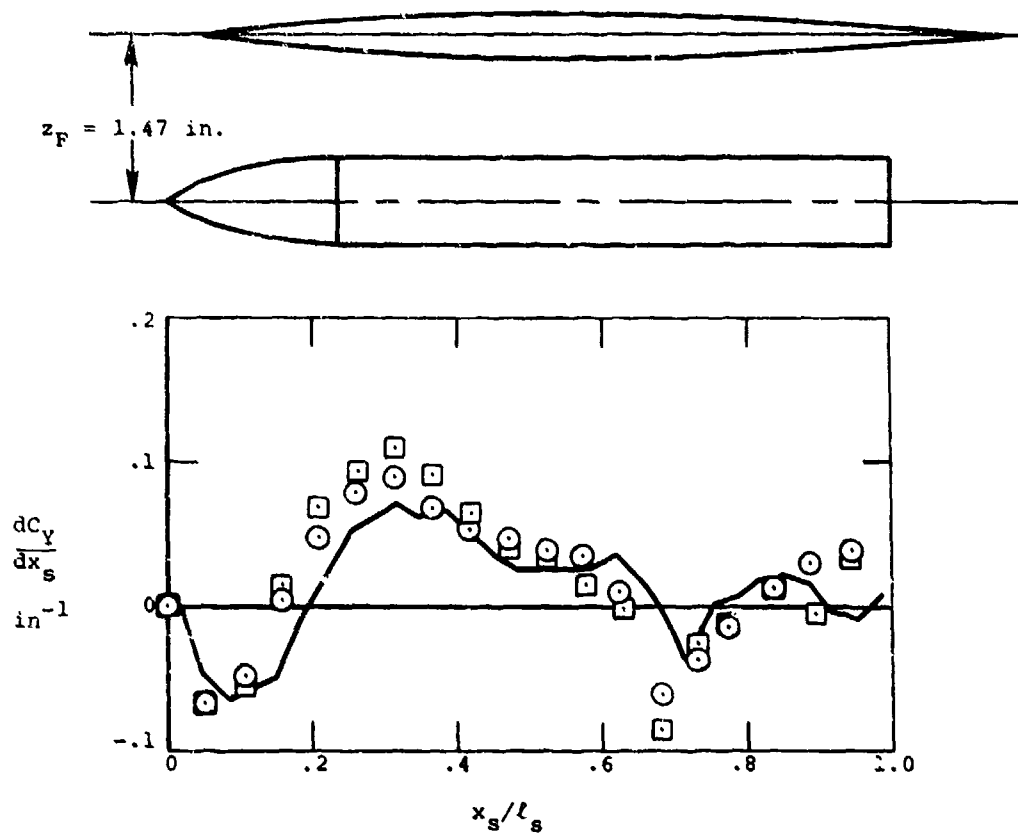
(b) Upwash velocity.

Figure 51.- Concluded.



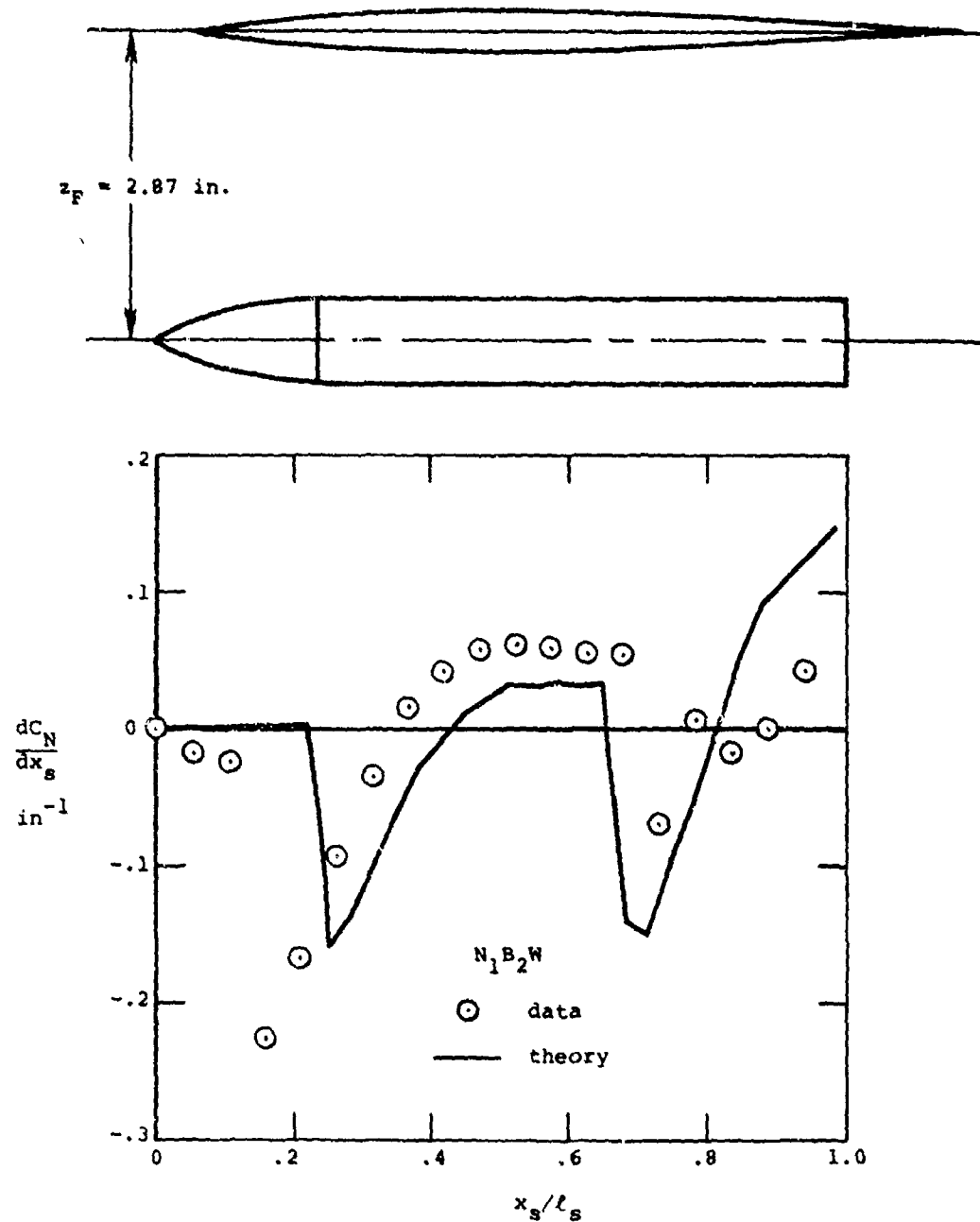
(a) Normal-force distribution.

Figure 53.- Store load distributions under the wing at the one-third semispan location; $M_\infty = 1.5$, $\alpha_F = 0^\circ$, $z_F = 1.47 \text{ in.}$



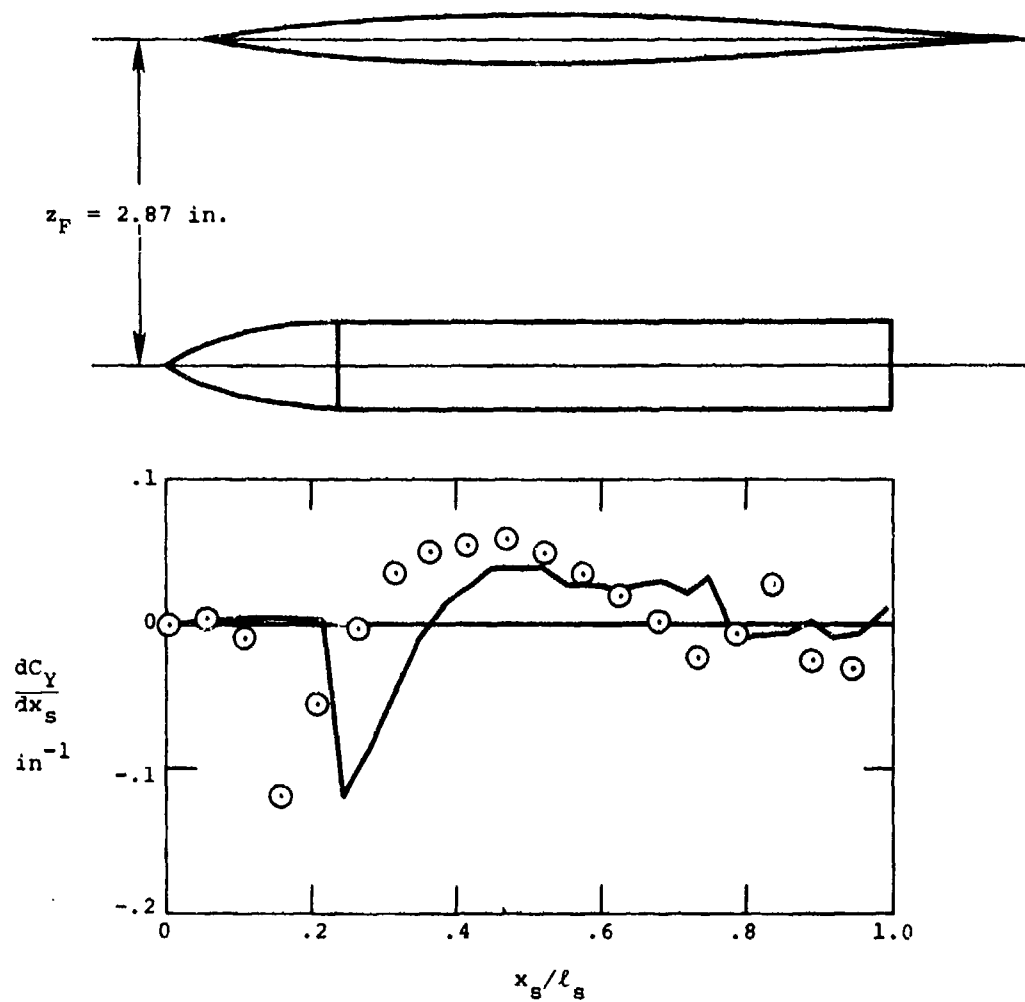
(b) Side-force distribution.

Figure 53.- Concluded.



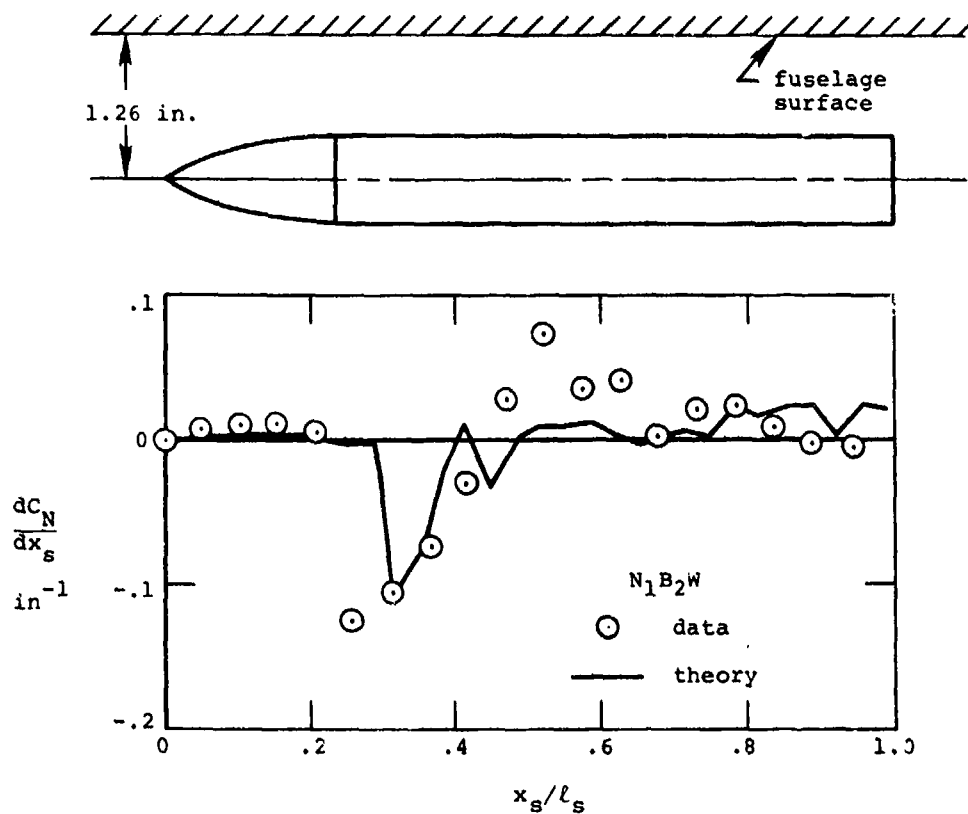
(a) Normal-force distribution.

Figure 54.- Store load distributions under the wing at the one-third semispan location; $M_\infty = 1.5$, $\alpha_F = 0^\circ$, $z_F = 2.87 \text{ in.}$



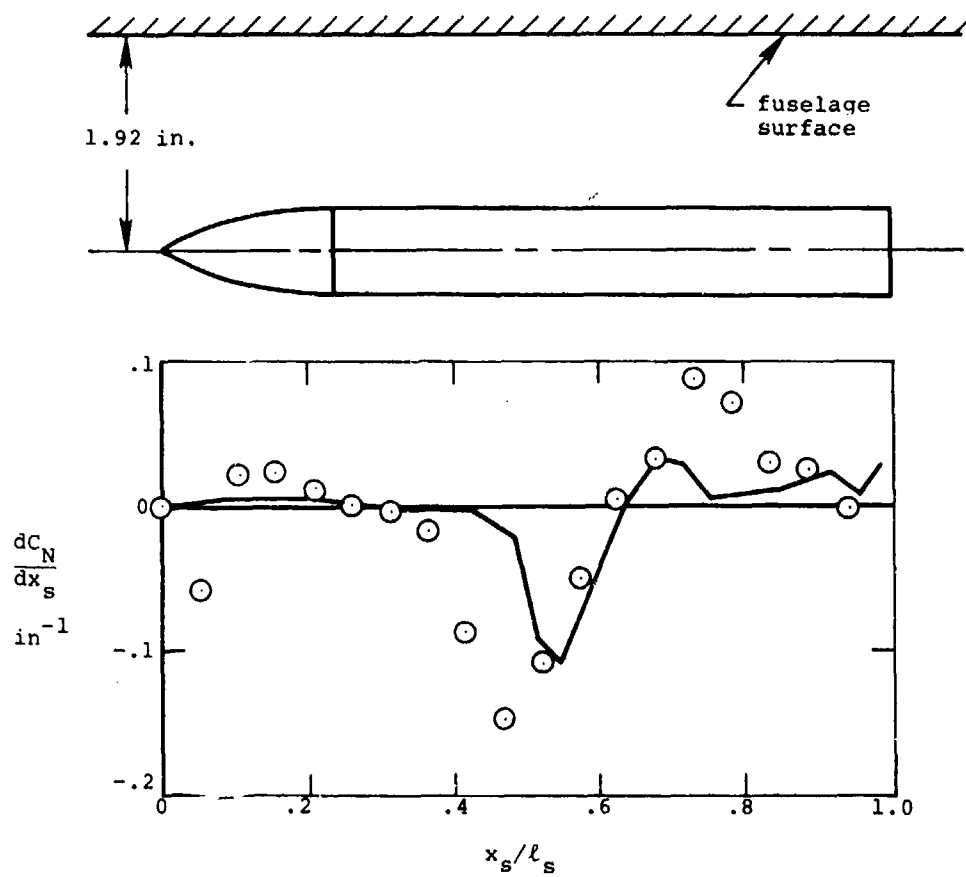
(b) Side-force distribution.

Figure 54.- Concluded.



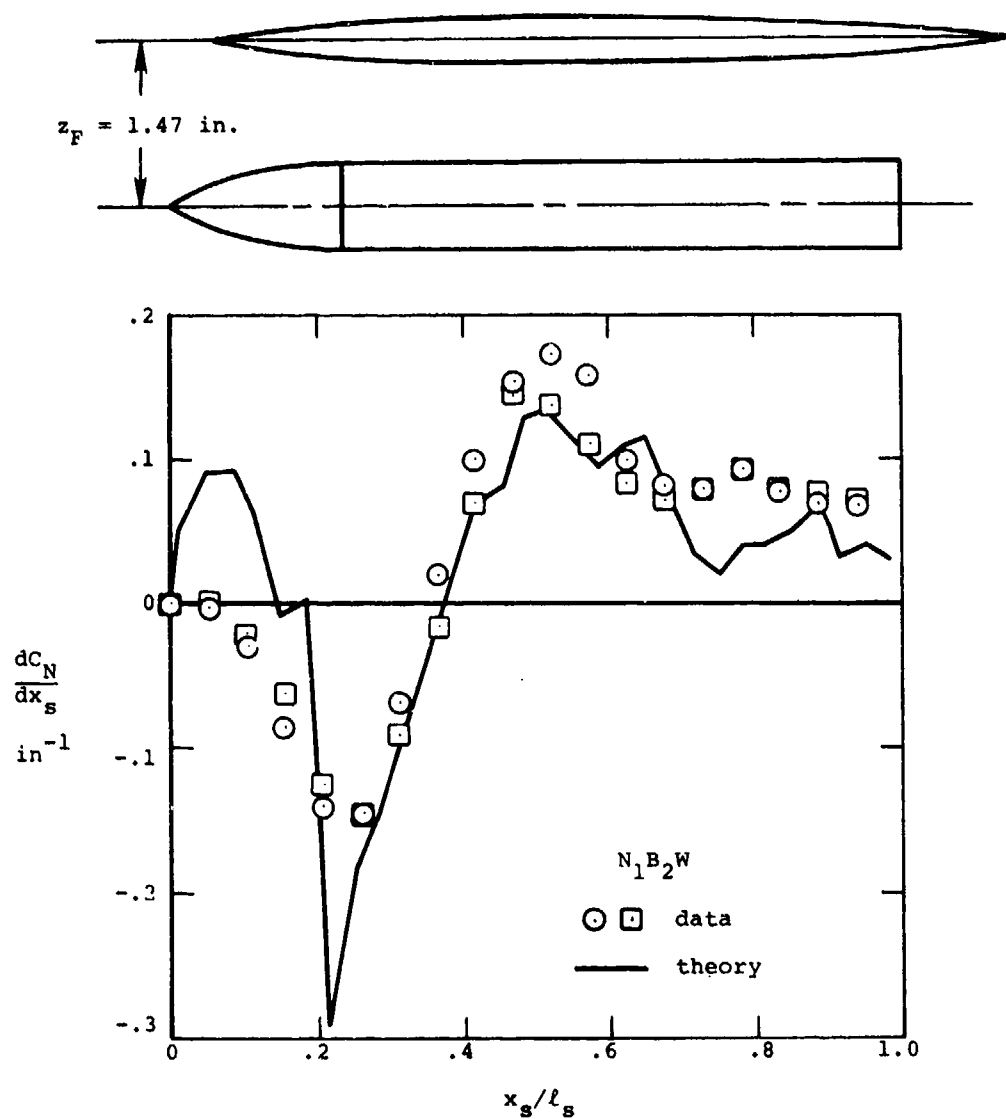
(a) $z_F = 2.94$ in.

Figure 55.- Store normal-force distribution under the fuselage centerline; $M_\infty = 1.5$, $\alpha_F = 0^\circ$.



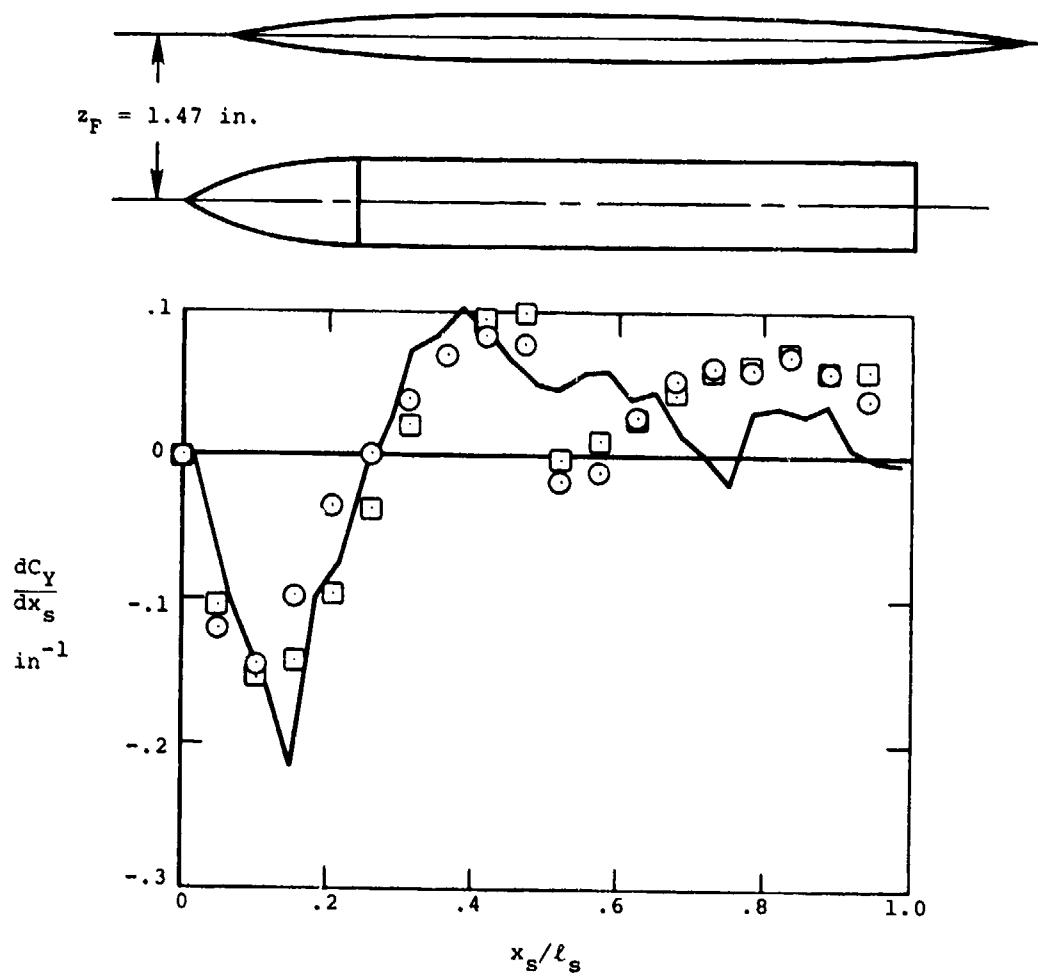
(b) $z_F = 3.59$ in.

Figure 55.- Concluded.



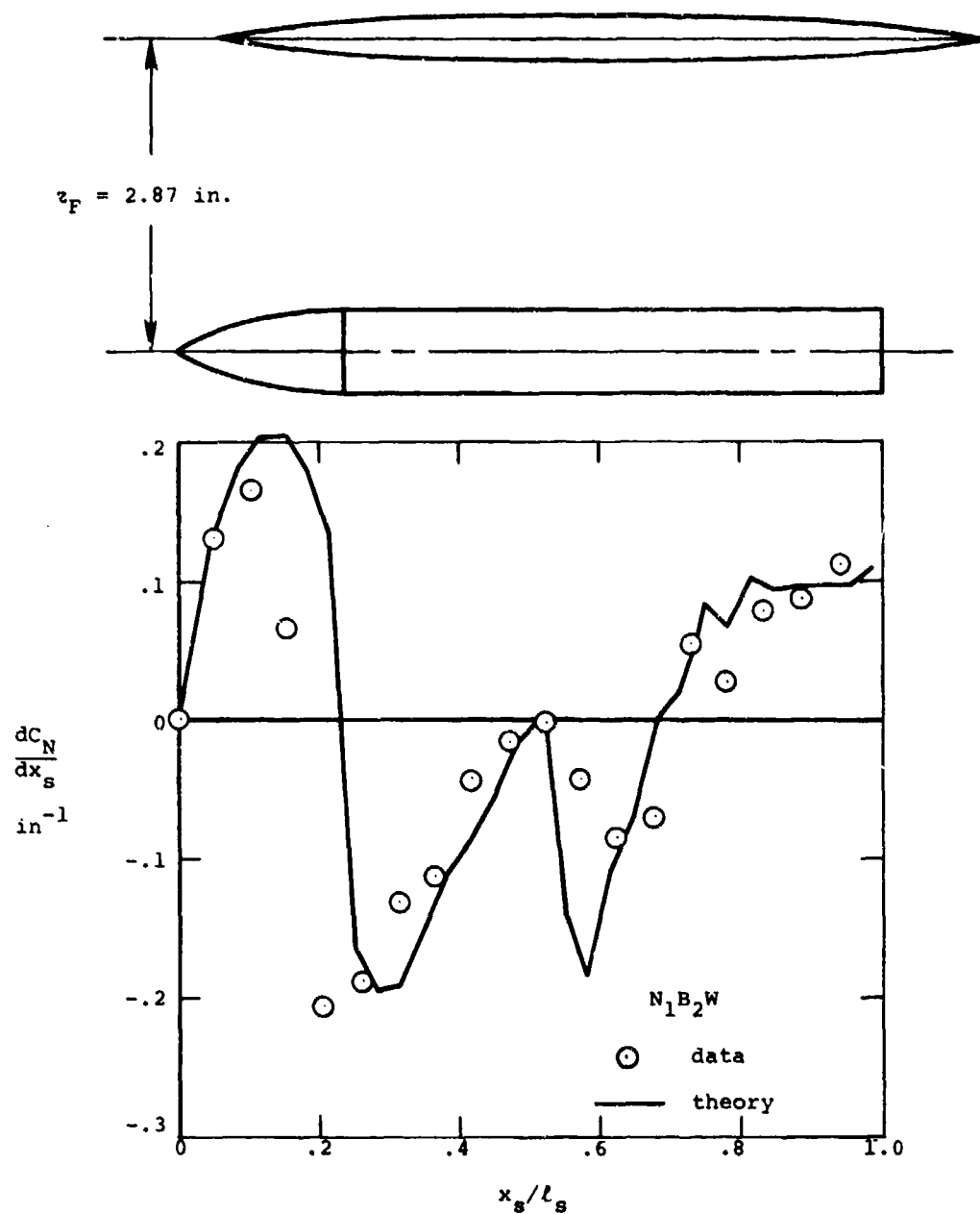
(a) Normal-force distribution.

Figure 56.- Store load-distribution under the wing at the one-third semispan location; $M_\infty = 1.5$, $\alpha_F = 5^\circ$, $z_F = 1.47 \text{ in.}$



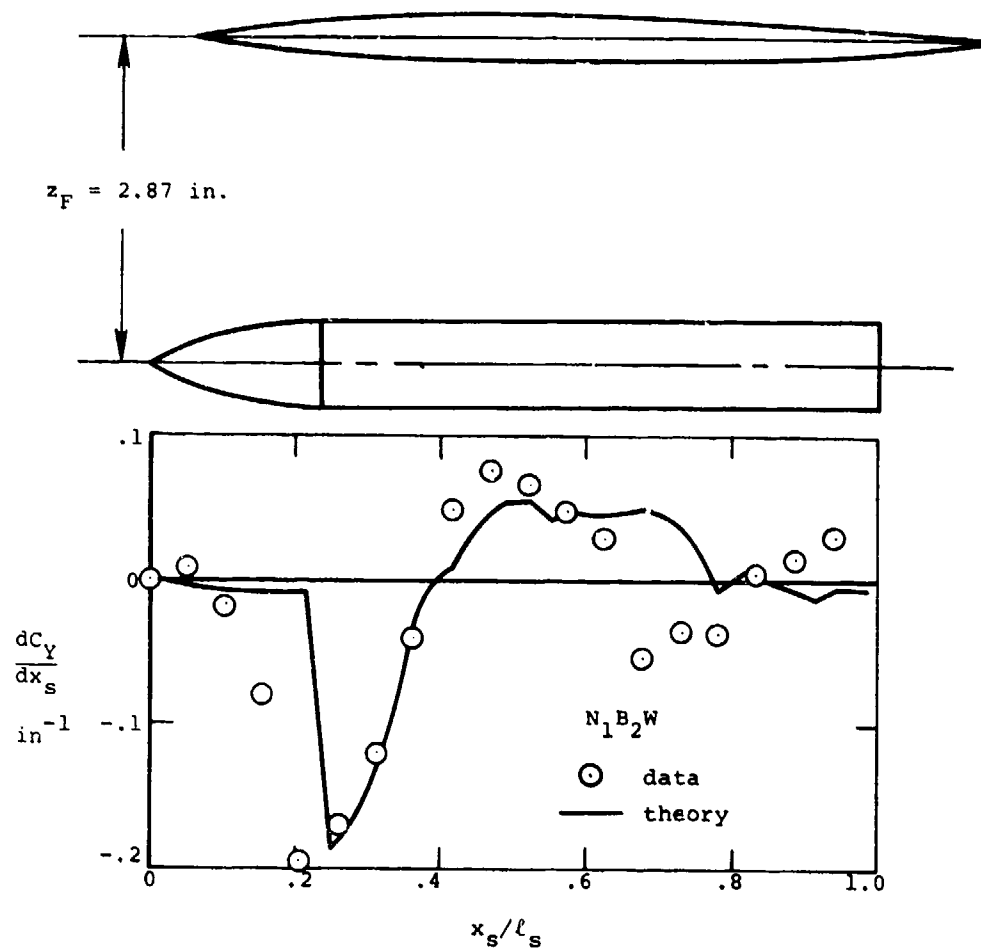
(b) Side force distribution.

Figure 56.- Concluded.



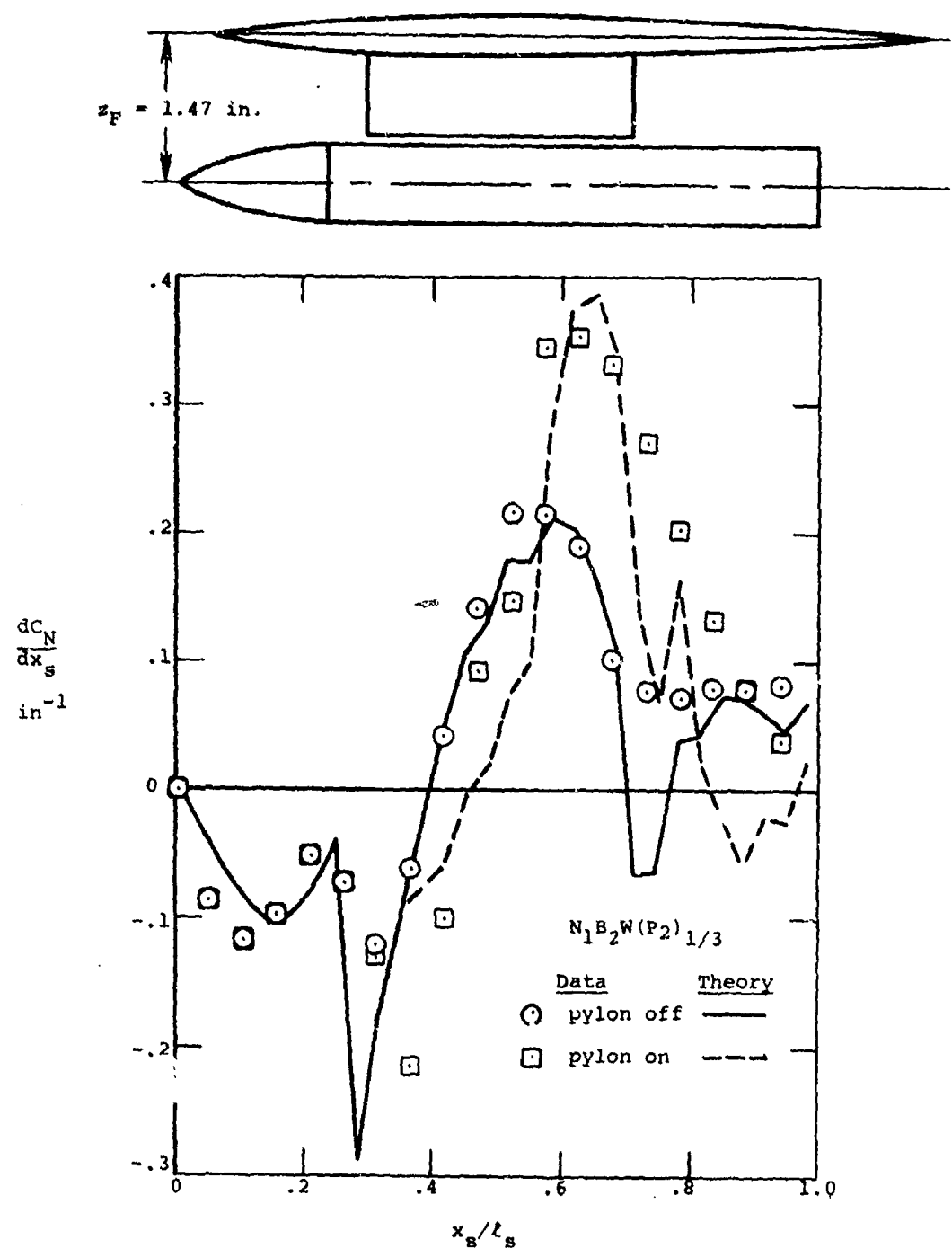
(a) Normal-force distribution.

Figure 57.- Store load distributions under the wing at the one-third semispan location; $M_\infty = 1.5$, $\alpha_F = 5^\circ$, $z_F = 2.87$ in.



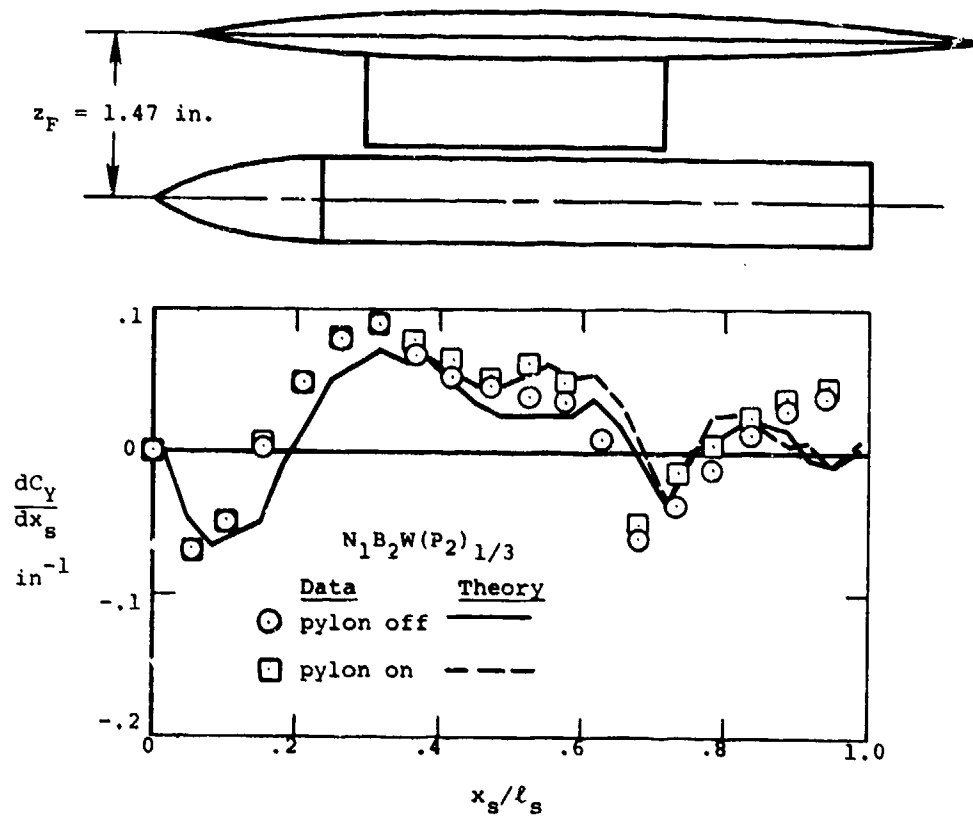
(b) Side-force distribution.

Figure 57.- Concluded.



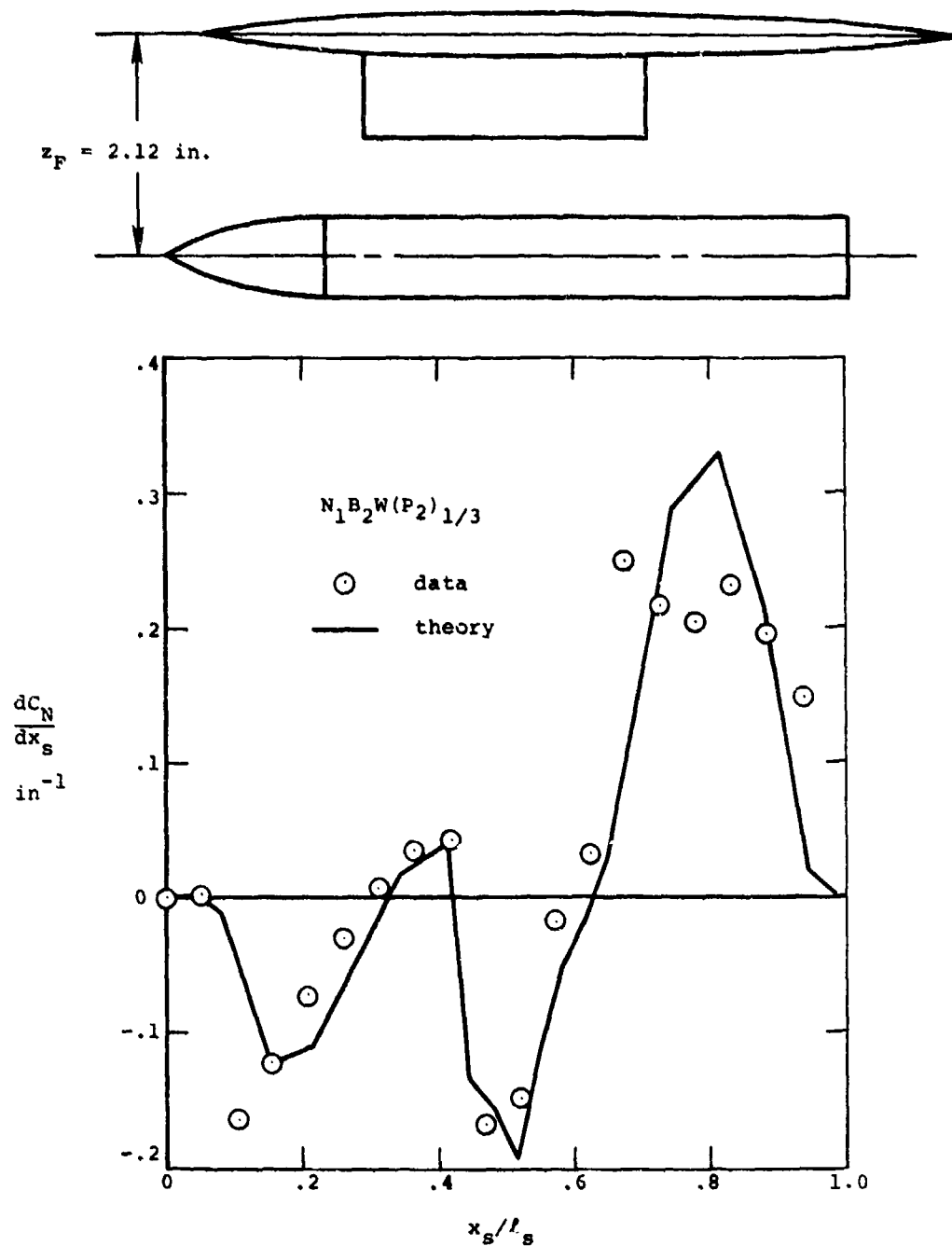
(a) Normal-force distribution.

Figure 58.- Effect of pylon on load distributions on store at one-third semispan location; $M_\infty = 1.5$, $\alpha_F = 0^\circ$, $z_F = 1.47$ in.



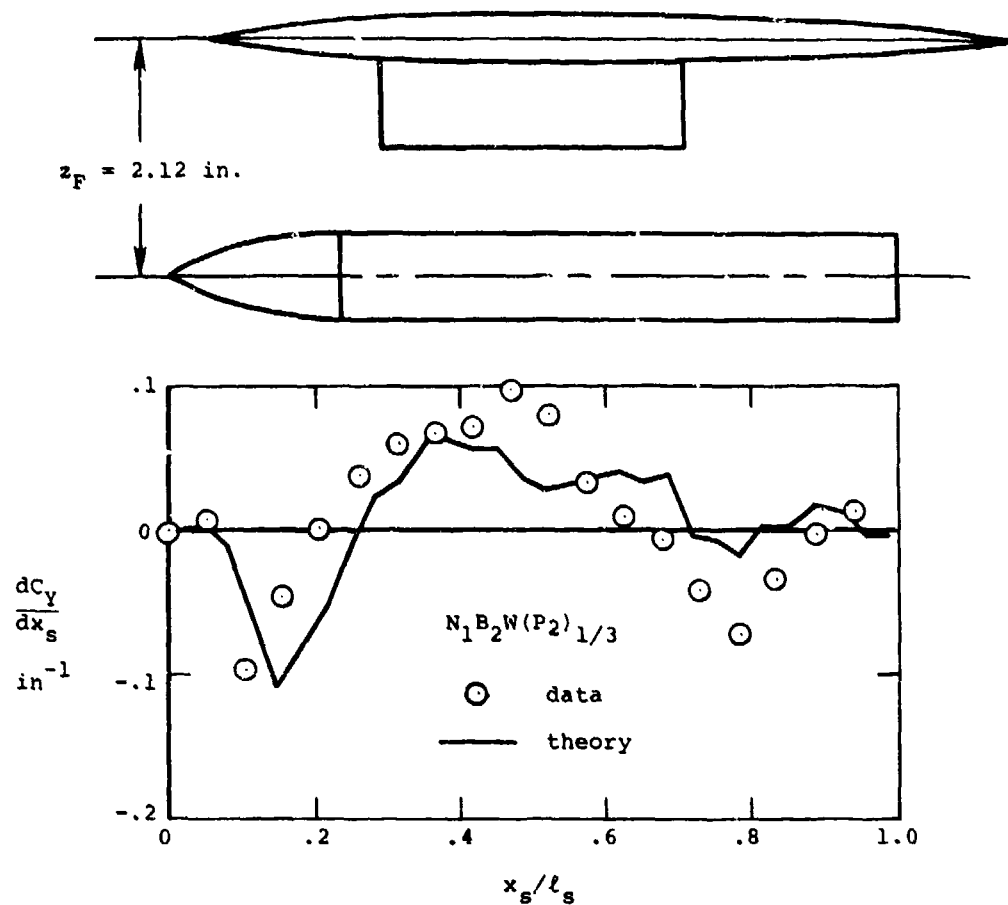
(b) Side-force distribution.

Figure 58.- Concluded.



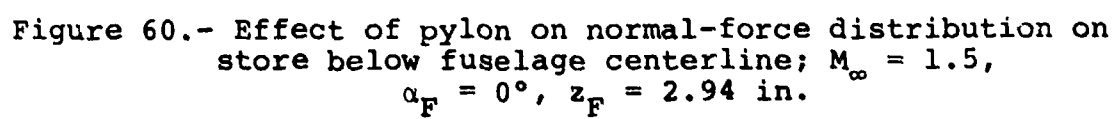
(a) Normal-force distribution.

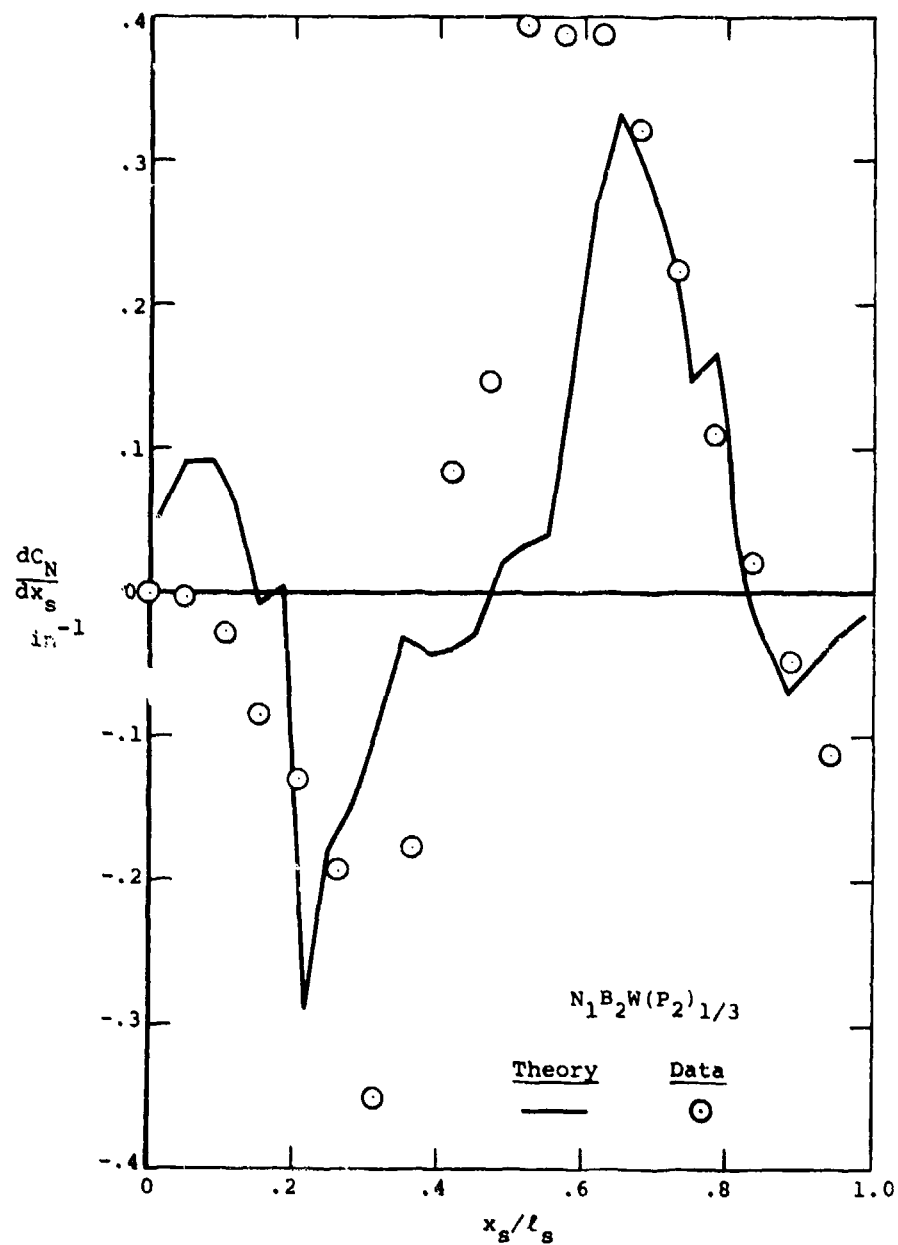
Figure 59.- Effect of pylon on load distributions on store at one-third semispan location; $M_\infty = 1.5$, $\alpha_F = 0^\circ$, $z_F = 2.12$ in.



(b) Side-force distribution.

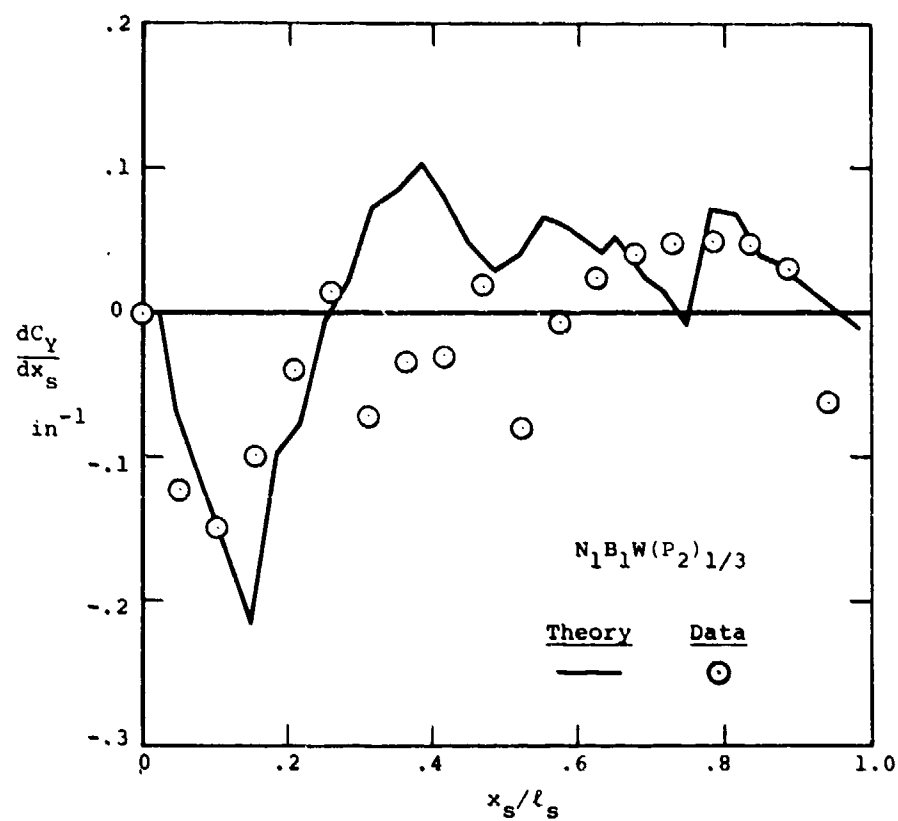
Figure 59.- Concluded.





(a) Normal-force distribution.

Figure 61.- Effect of pylon on load distribution on store
at one-third semispan location
 $M_\infty = 1.5$, $\alpha_F = 5^\circ$, $z_F = 1.47$ in.



(b) Side-force distribution.

Figure 61.- Concluded.

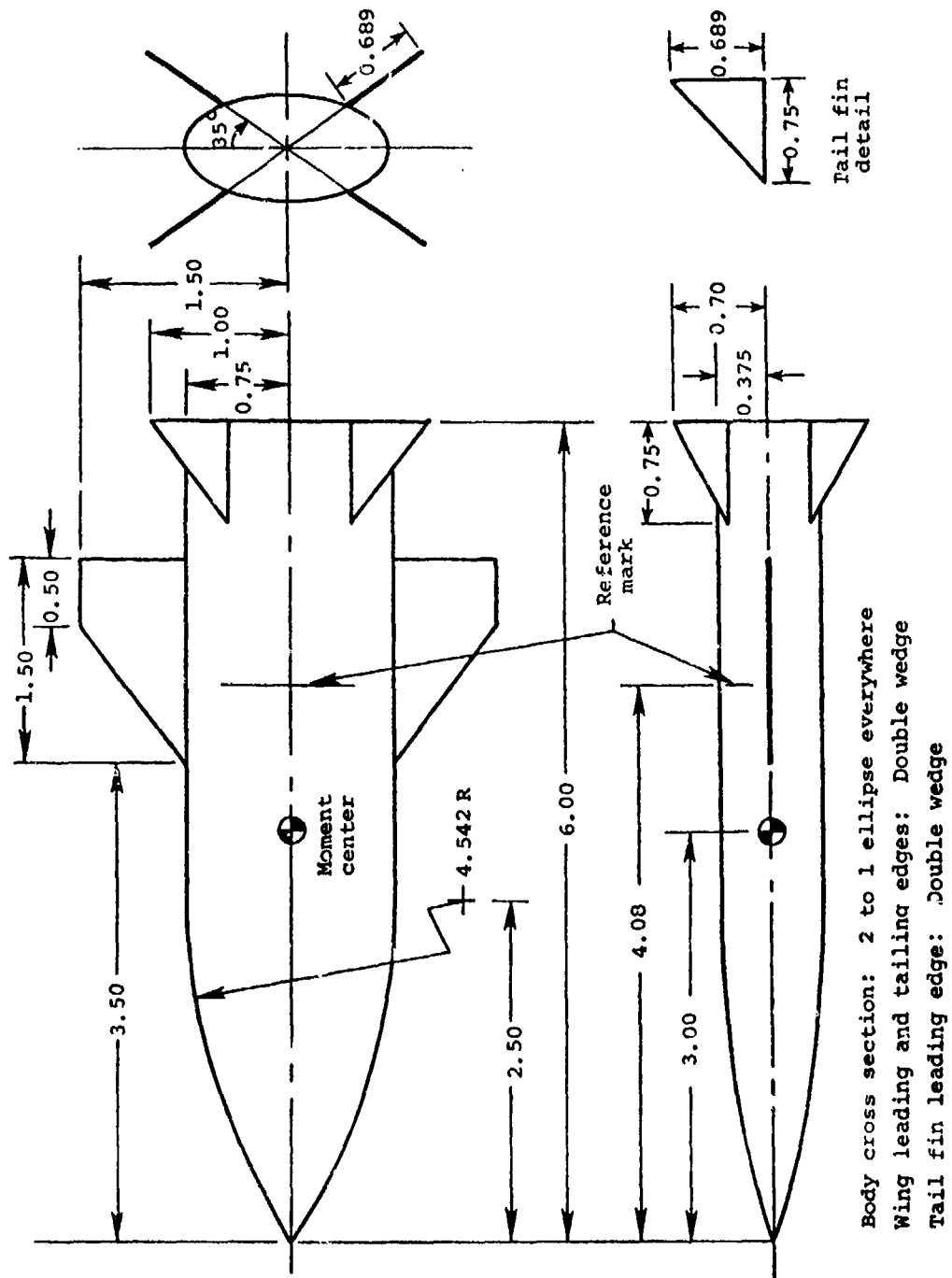


Figure 62.- Elliptic force and moment model.

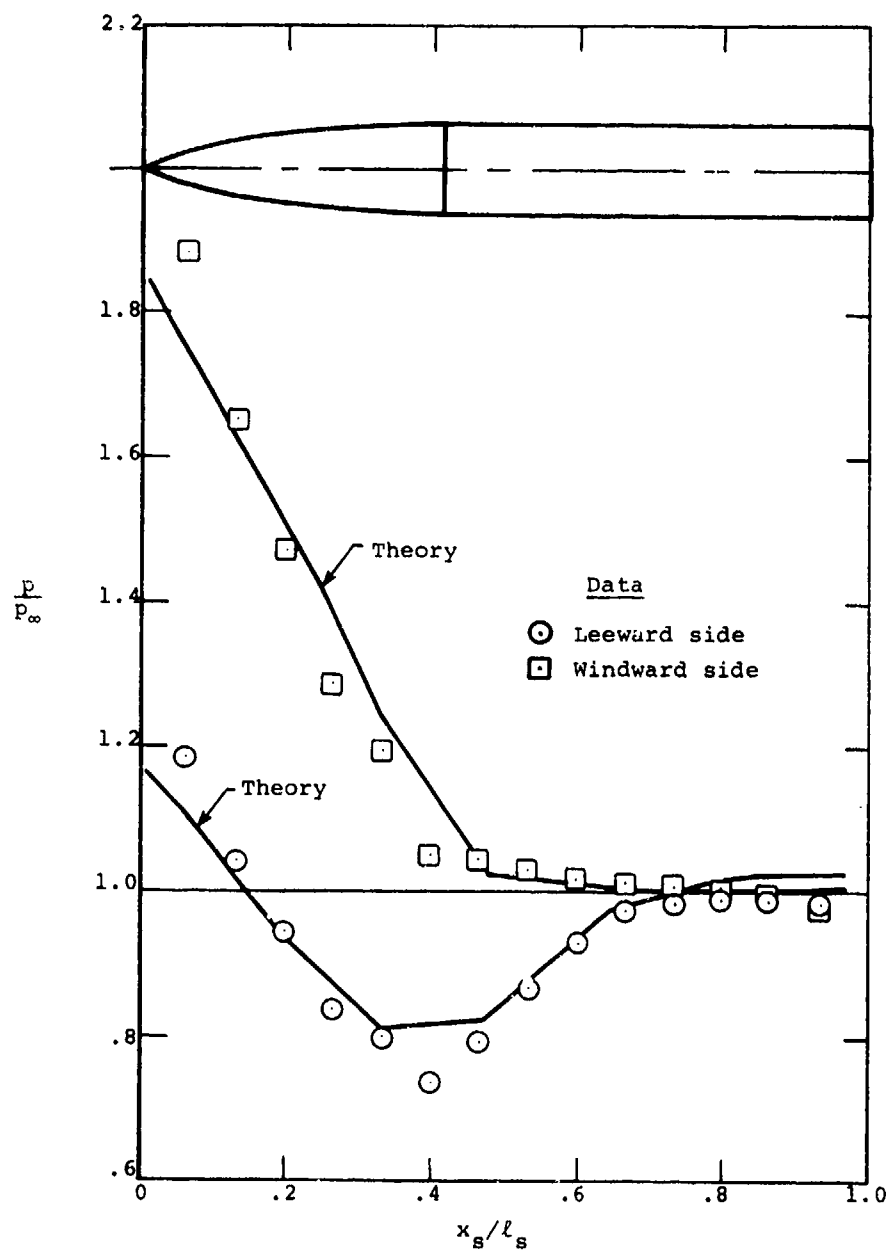


Figure 63.- Pressure distributions on the top and bottom of the elliptic store; $M_\infty = 1.5$, $\alpha_c = 10^\circ$, $\phi_s = 0^\circ$.

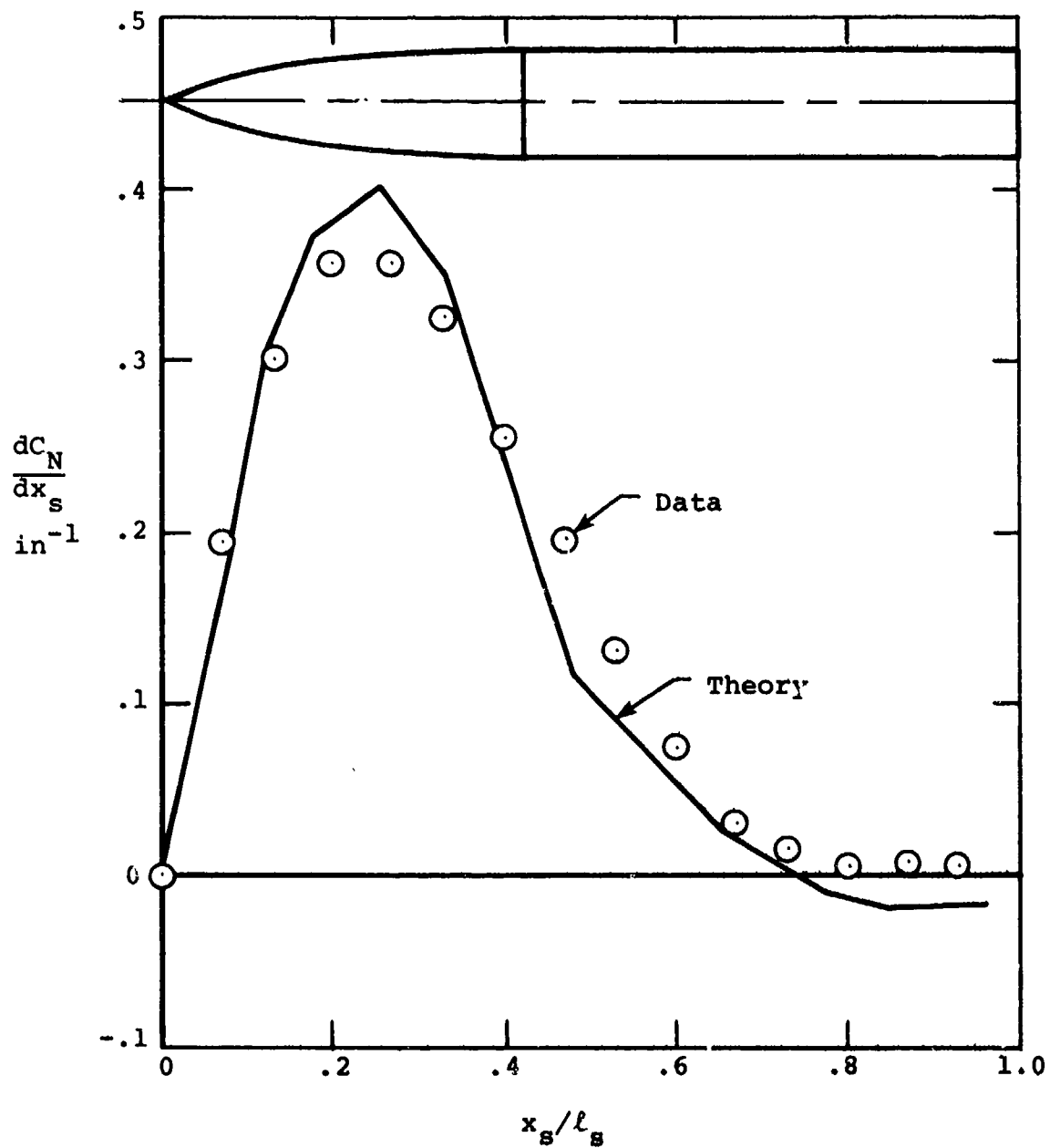
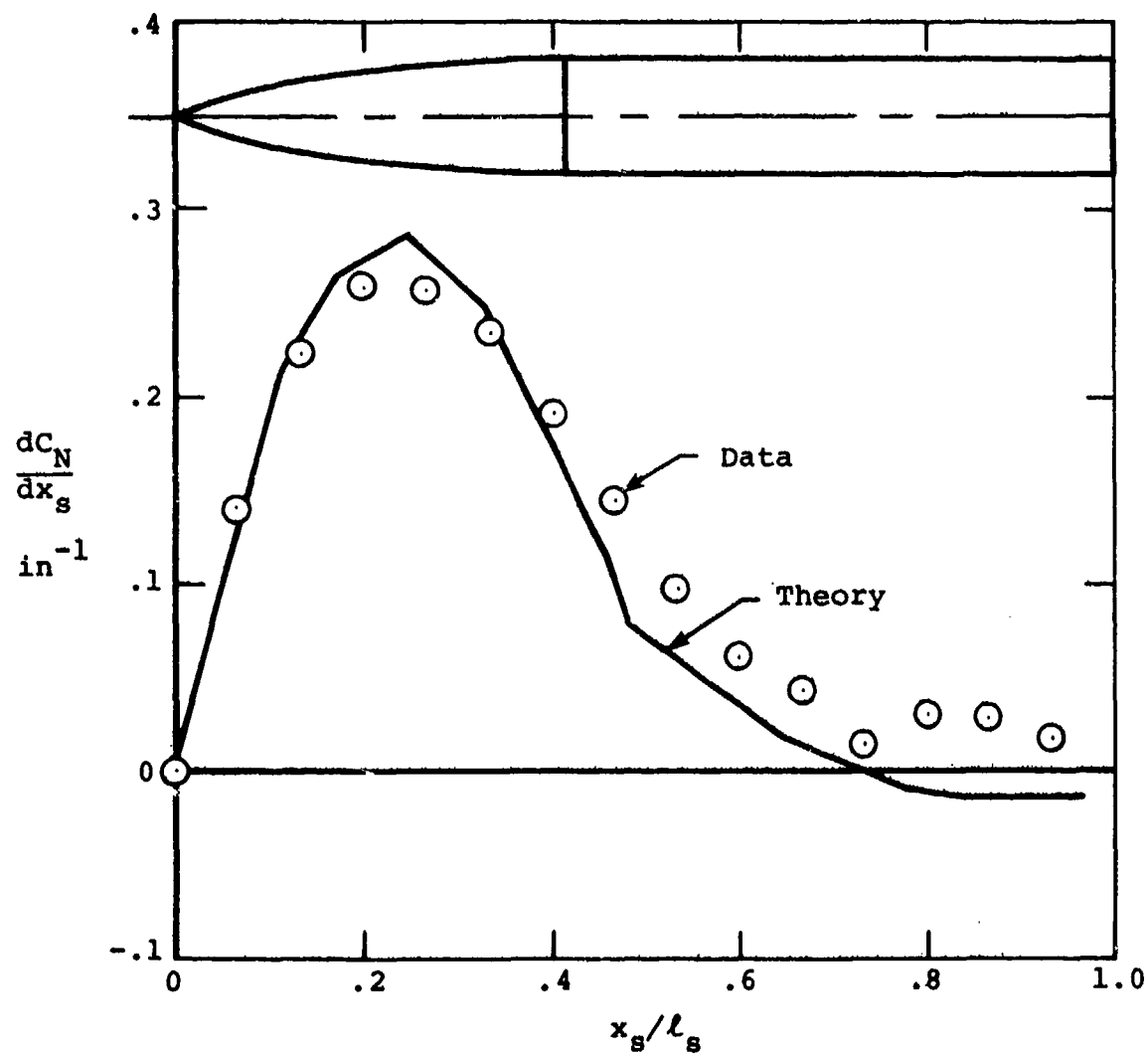
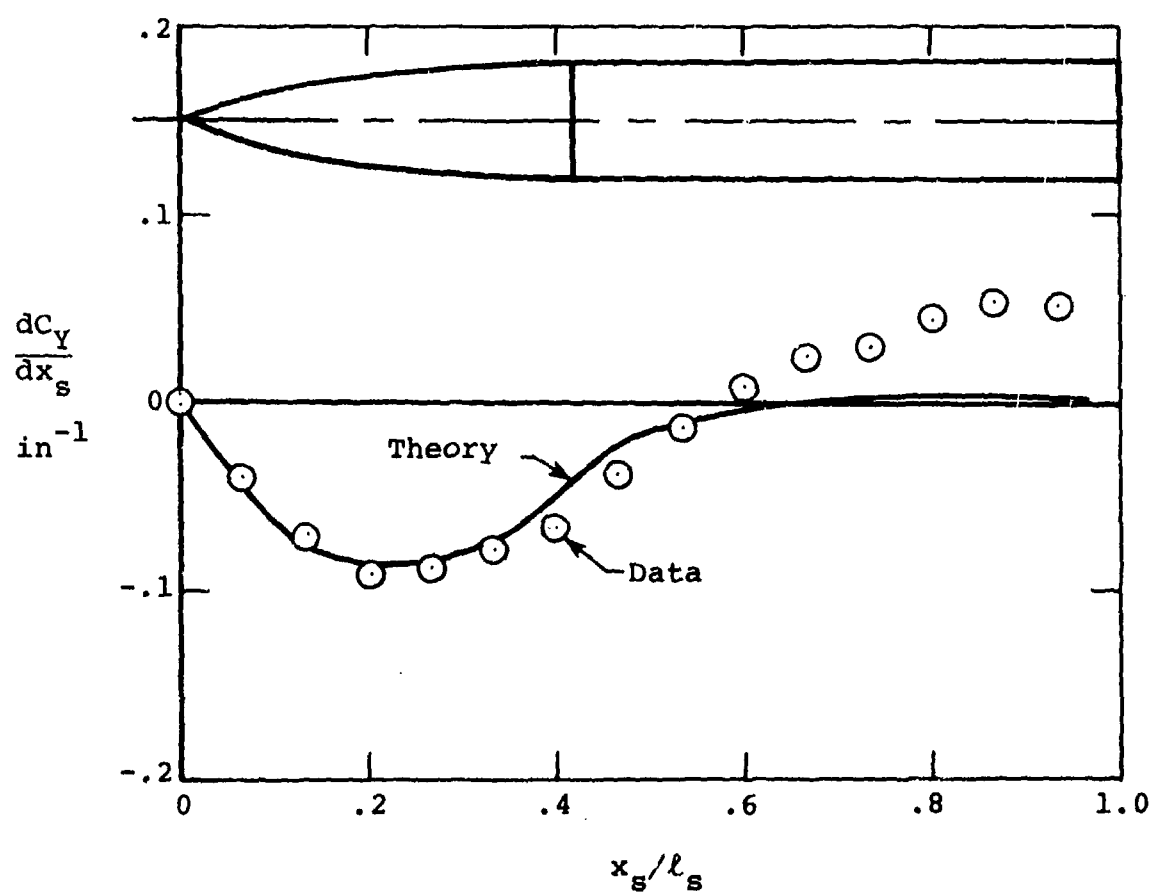


Figure 64.- Normal-force distribution on the elliptic store in the free-stream; $M_\infty = 1.5$, $\alpha_c = 10^\circ$, $\phi_s = 0^\circ$.



(a) Normal-force distribution.

Figure 65.- Load distributions on the elliptic store in the free-stream; $M_\infty = 1.5$, $\alpha_c = 10^\circ$, $\phi_s = 45^\circ$.



(b) Side-force distribution.

Figure 65.- Concluded.

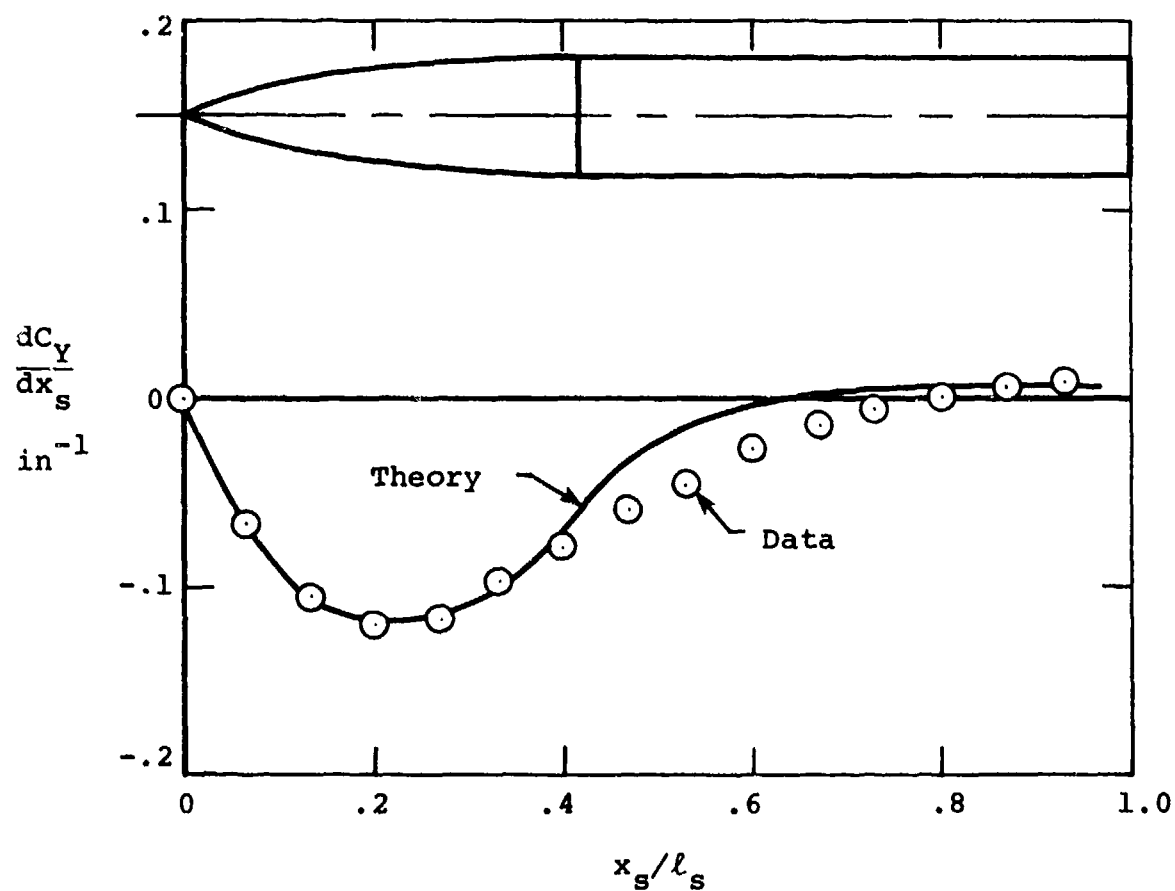
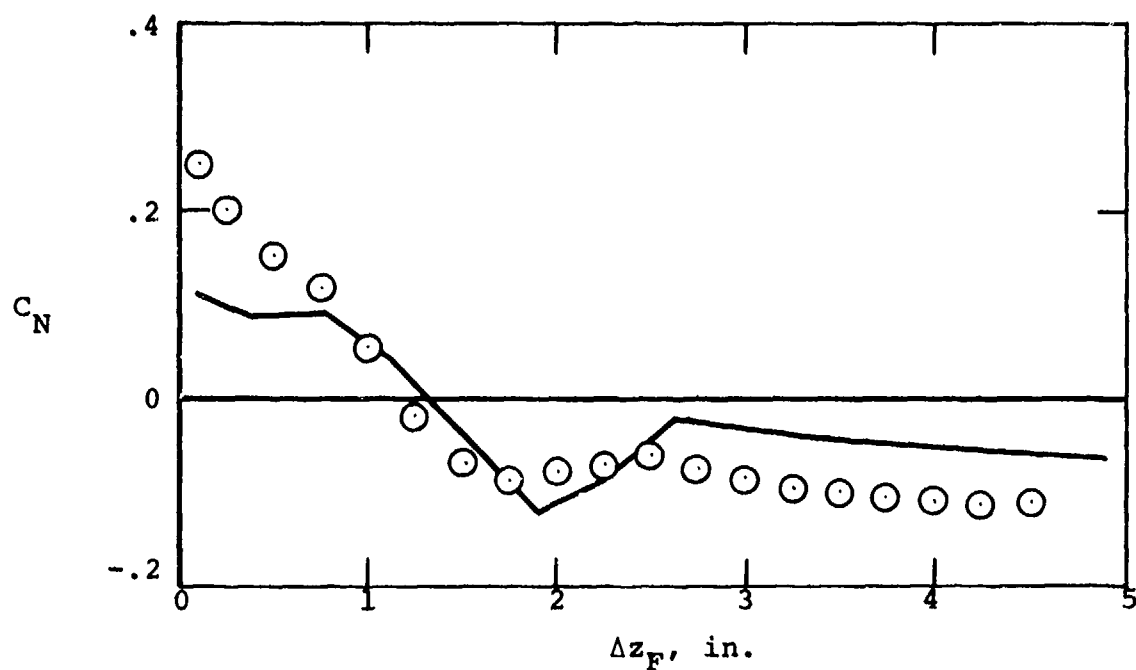
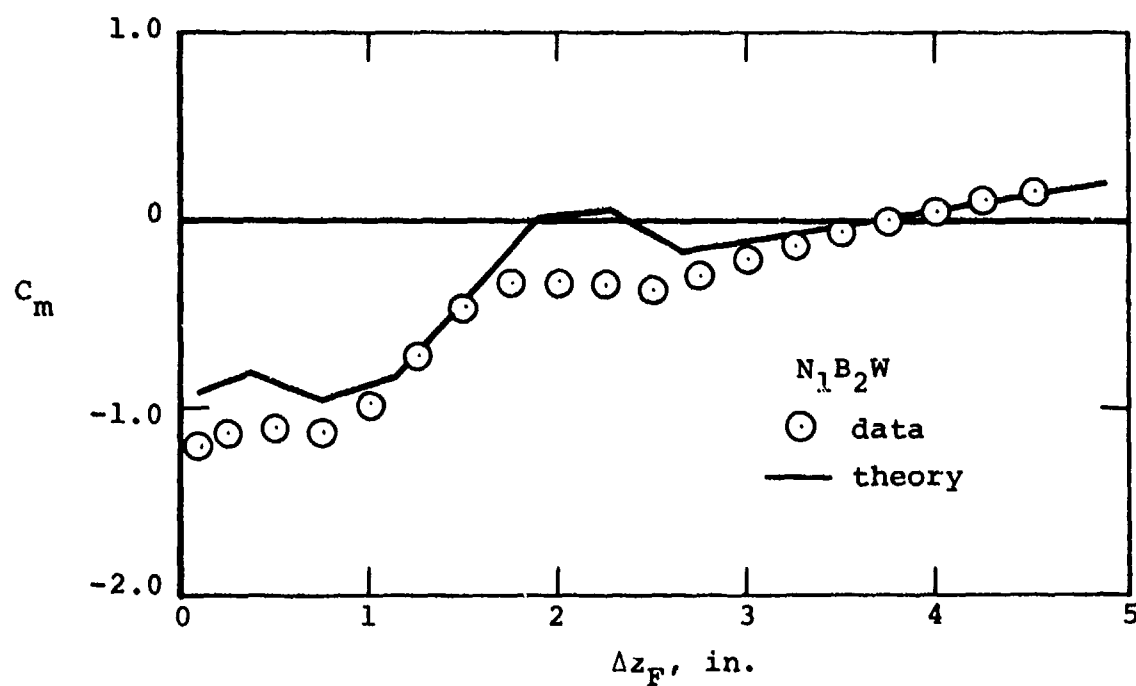


Figure 66.- Side-force distribution on the elliptic store
in the free stream; $M_\infty = 1.5$,
 $\alpha_c = 10^\circ$, $\phi_s = 90^\circ$.

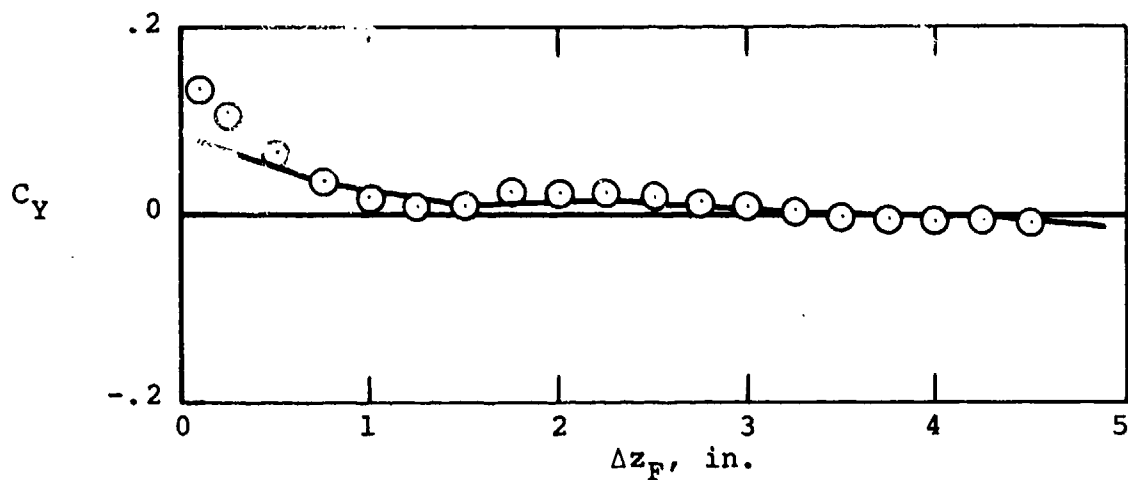


(a) Normal-force coefficient.

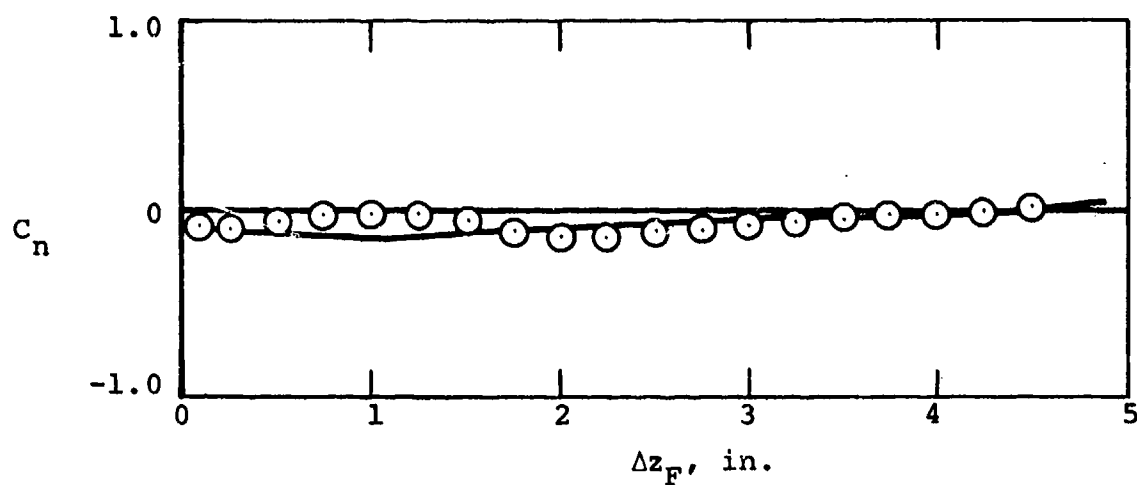


(b) Pitching-moment coefficient.

Figure 67.- Forces and moments on the ogive-cylinder store at the one-third semispan location; $M_\infty = 1.5$, $\alpha_F = 0^\circ$.

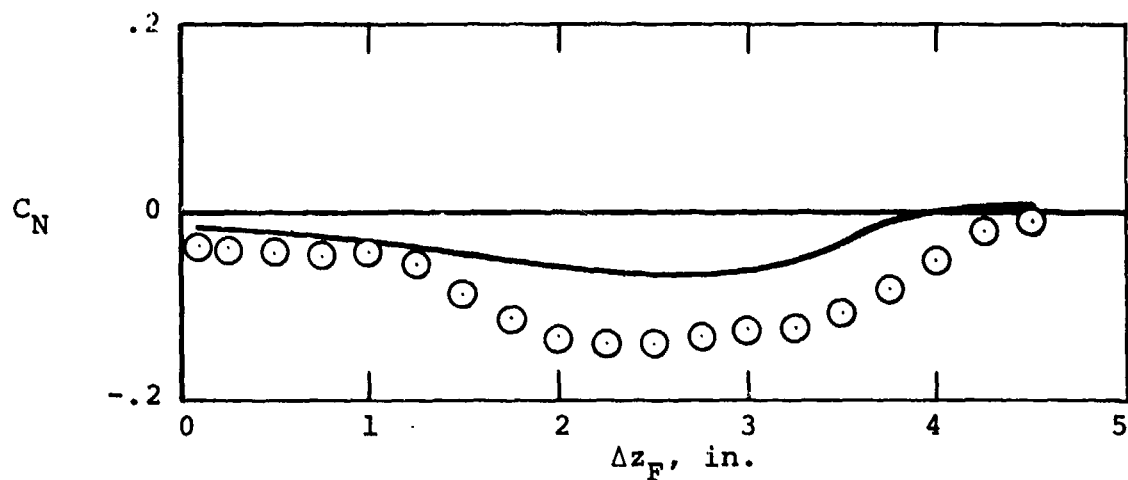


(c) Side-force coefficient.

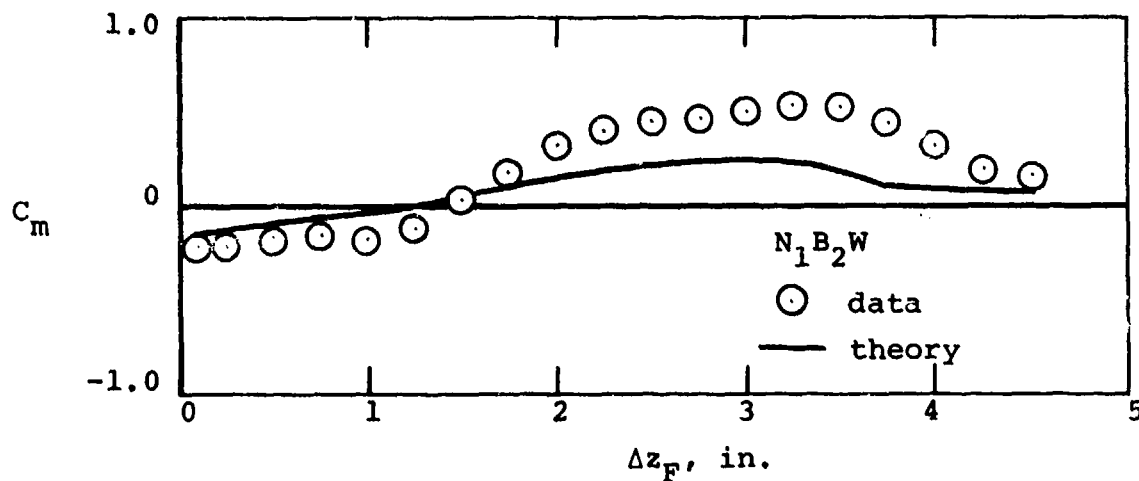


(d) Yawing-moment coefficient.

Figure 67.- Concluded.

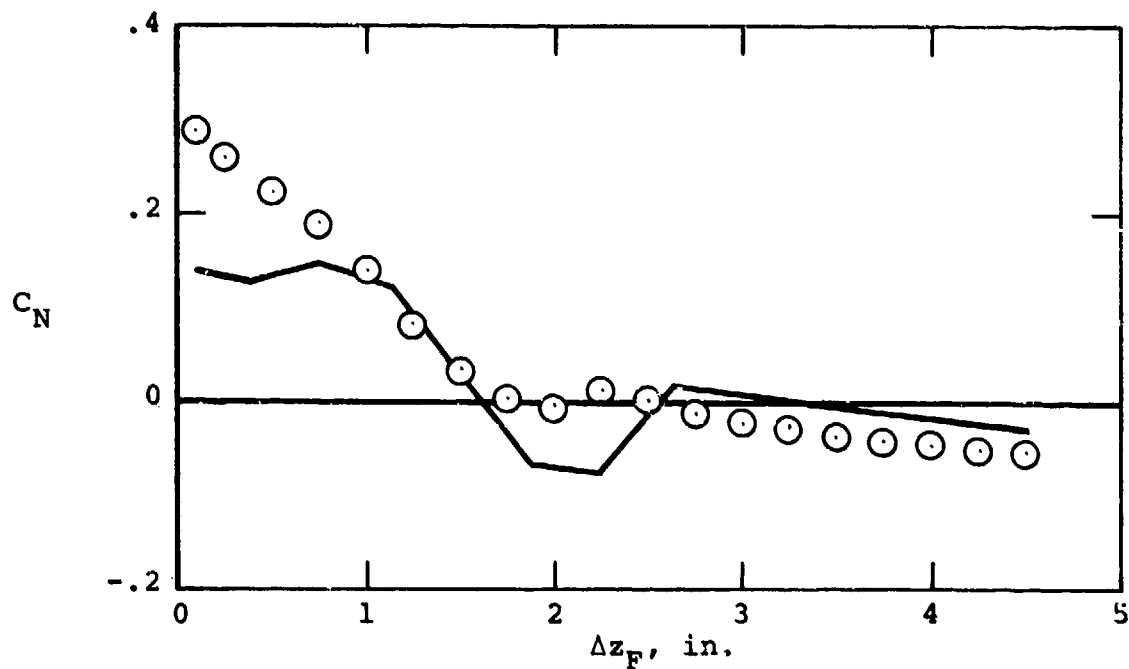


(a) Normal-force coefficient.

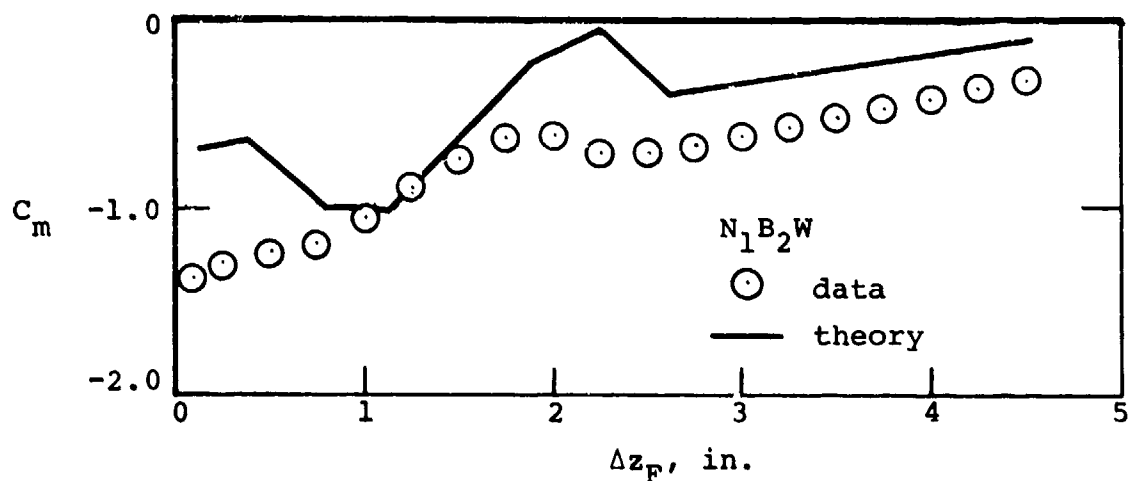


(b) Pitching-moment coefficient.

Figure 68.- Forces and moments on the ogive-cylinder store under the fuselage centerline; $M_\infty = 1.5$, $\alpha_F = 0^\circ$.

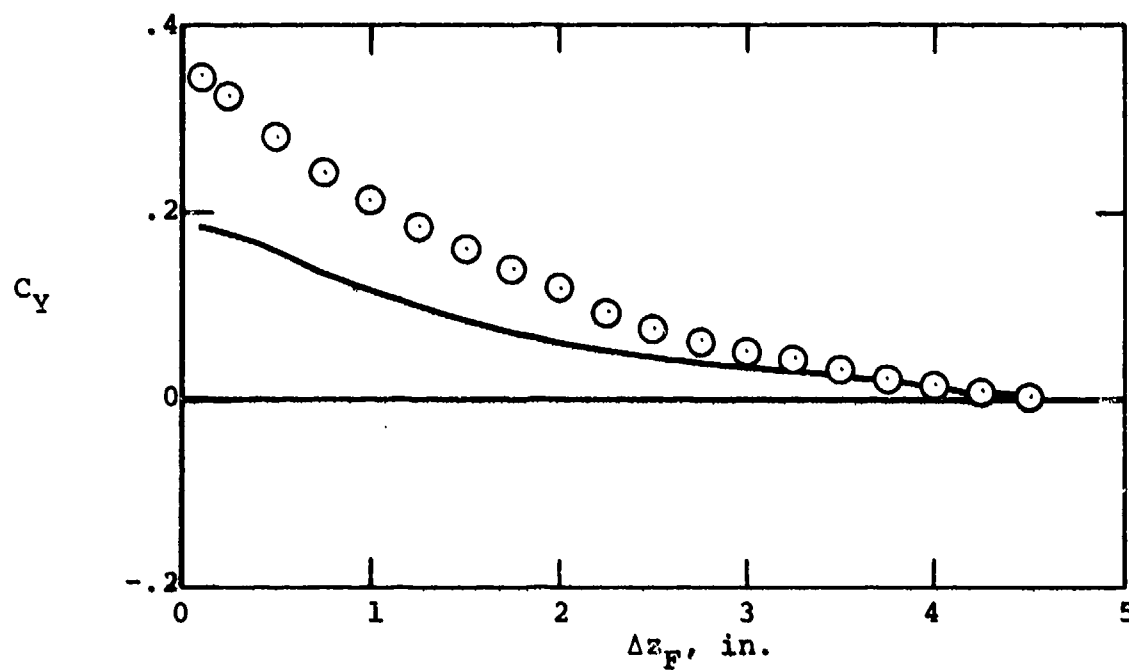


(a) Normal-force coefficient.

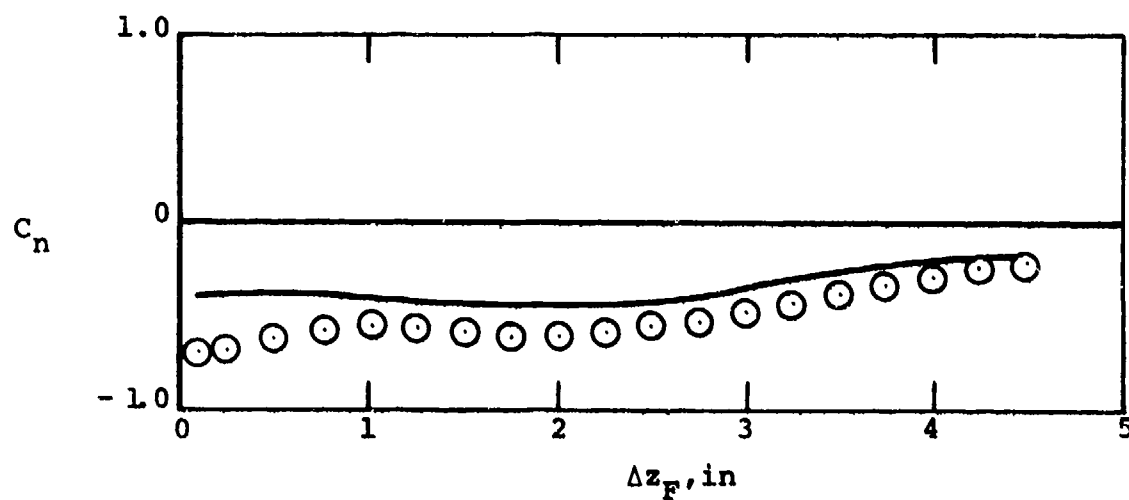


(b) Pitching-moment coefficient.

Figure 69.- Forces and moments on the ogive-cylinder store at the two-third semispan location; $M_\infty = 1.5$, $\alpha_F = 0^\circ$.

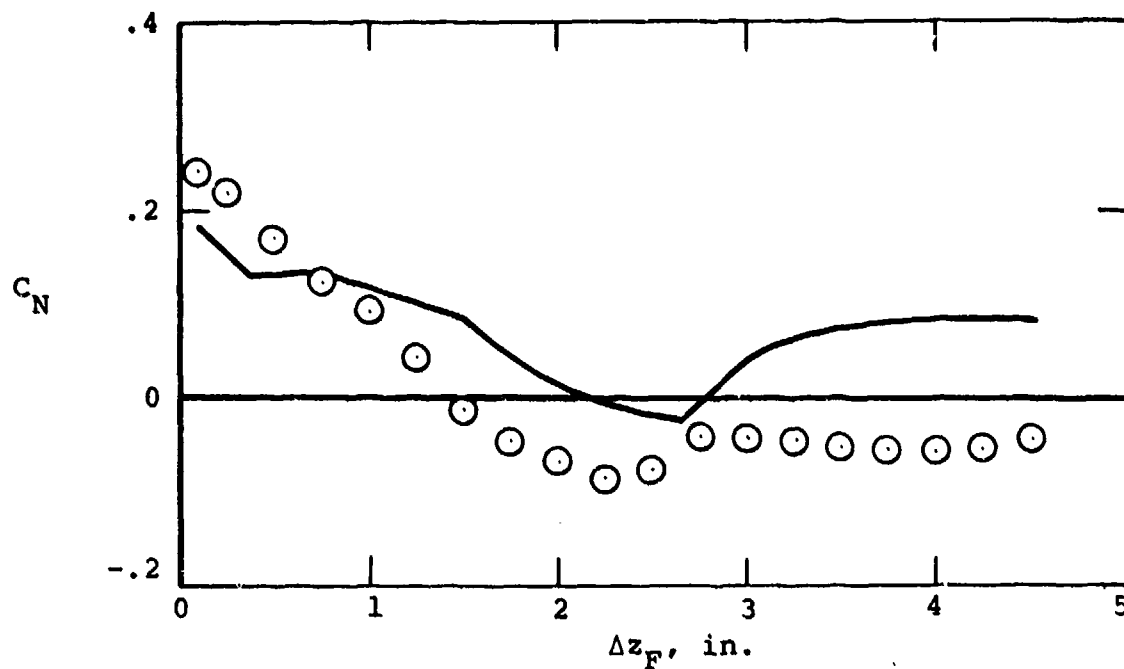


(c) Side-force coefficient.

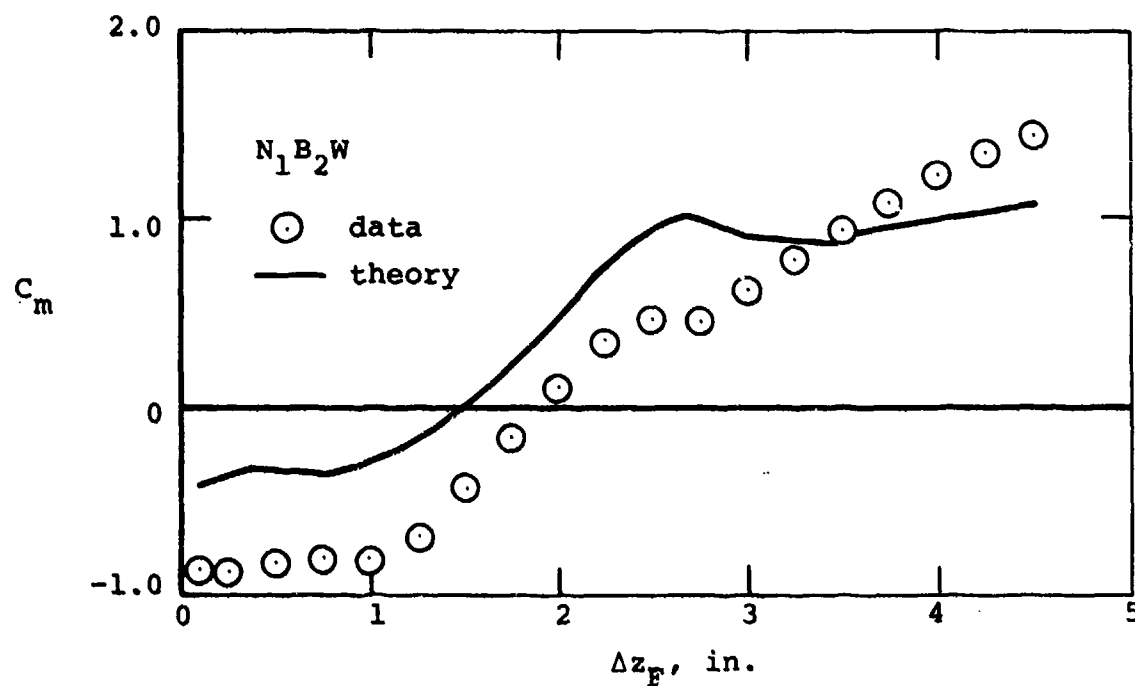


(d) Yawing-moment coefficient.

Figure 69.- Concluded.

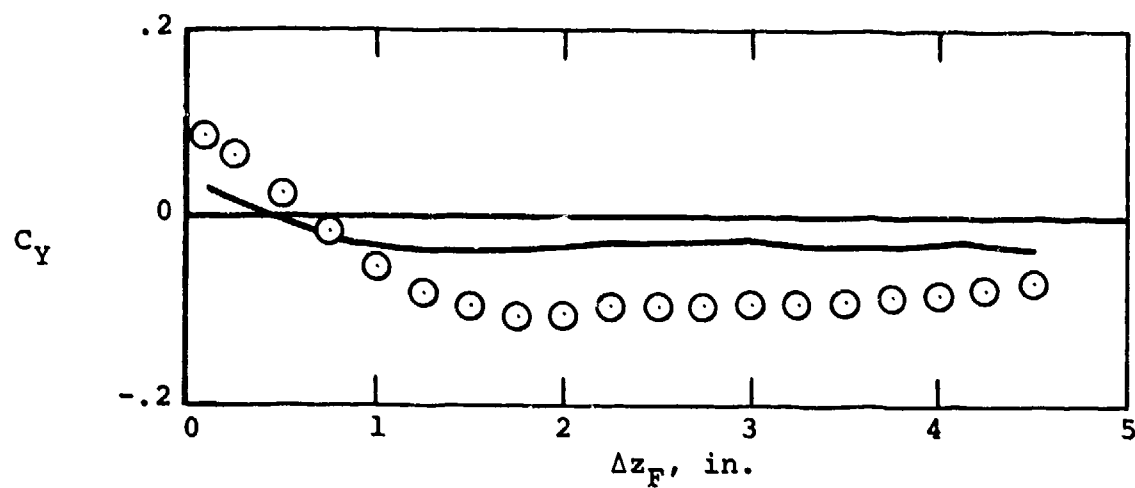


(a) Normal-force coefficient.

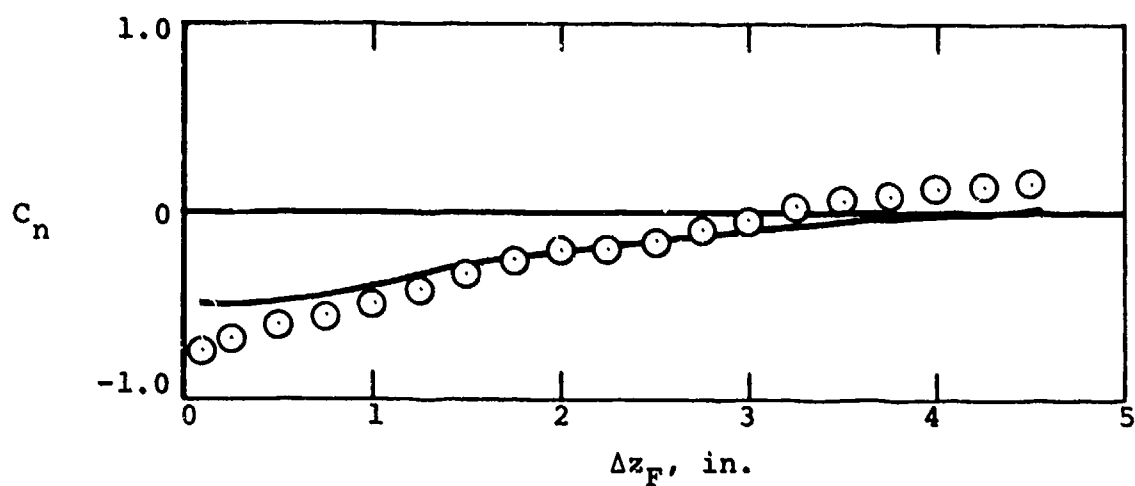


(b) Pitching-moment coefficient.

Figure 70.- Forces and moments on the ogive-cylinder store at the one-third semispan location; $M_\infty = 1.5$, $\alpha_F = 5^\circ$.

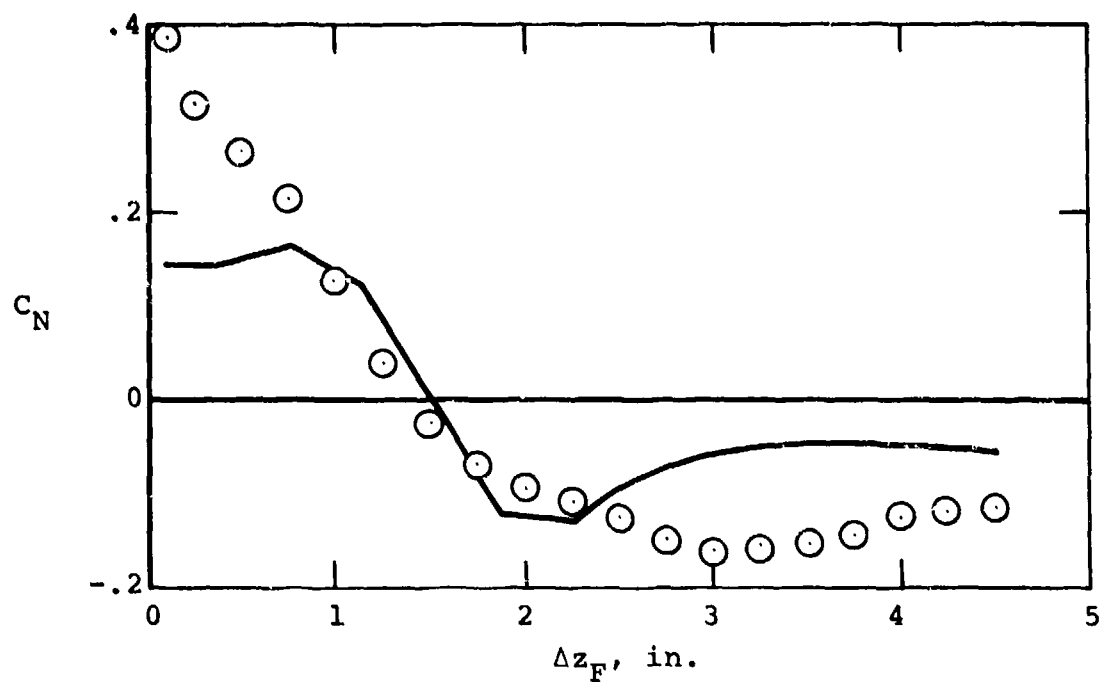


(c) Side-force coefficient.

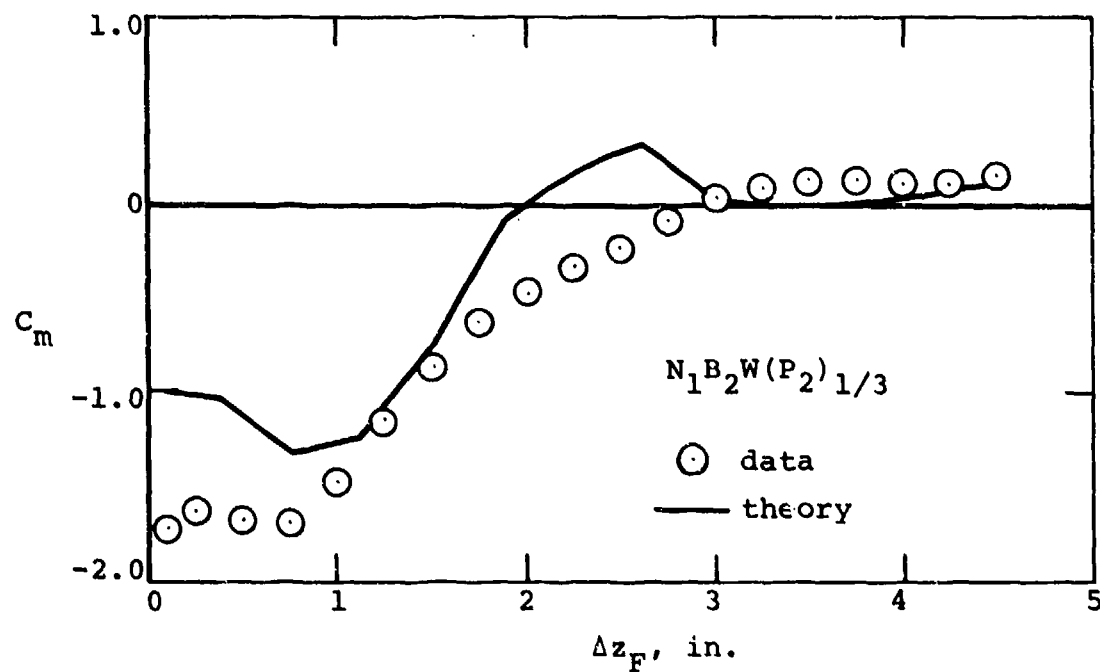


(d) Yawing-moment coefficient.

Figure 70.- Concluded.

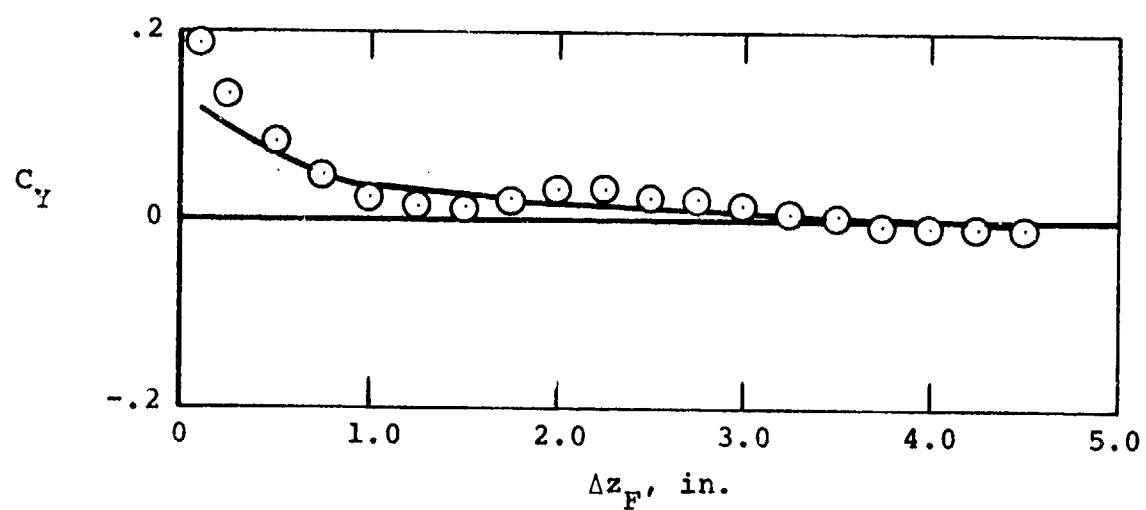


(a) Normal-force coefficient.

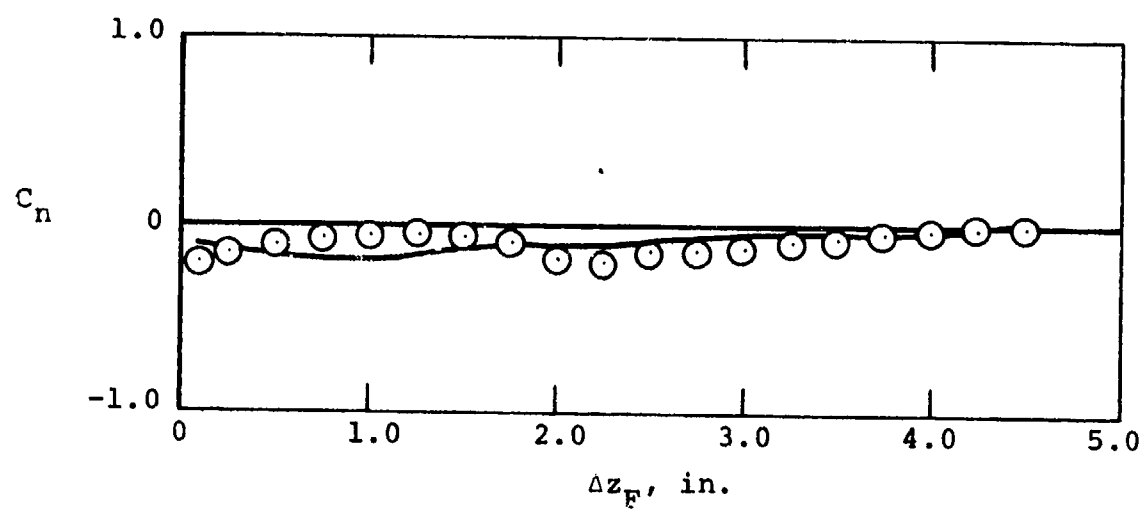


(b) Pitching-moment coefficient.

Figure 71. Forces and moments on the ogive-cylinder store under the pylon at the one-third semispan location; $M_\infty = 1.5$, $\alpha_F = 0^\circ$.

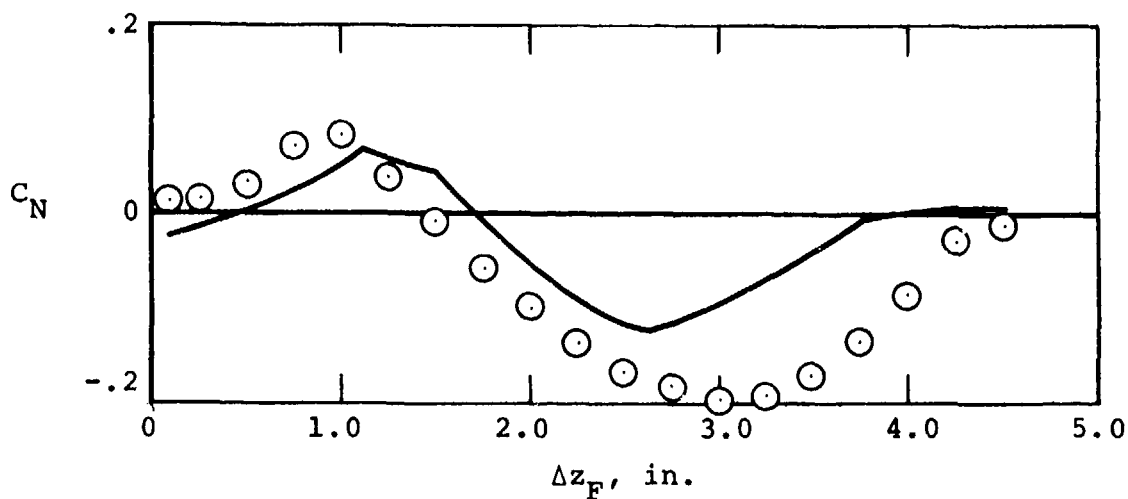


(c) Side-force coefficient.

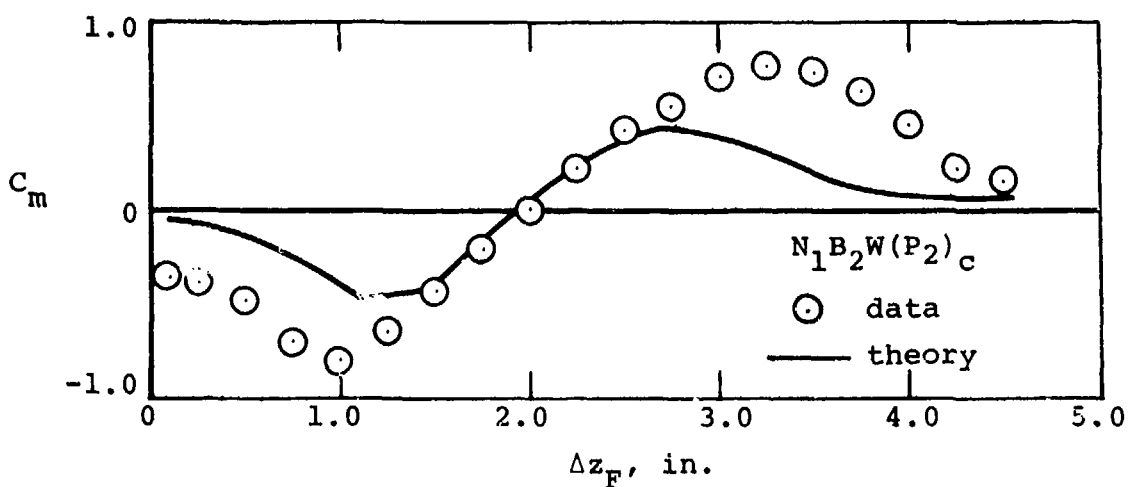


(d) Yawing-moment coefficient.

Figure 71.- Concluded.

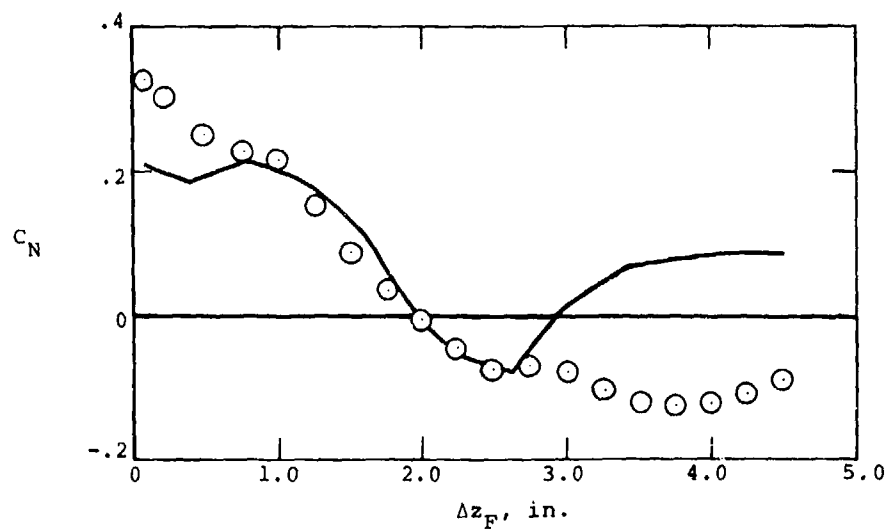


(a) Normal-force coefficient.

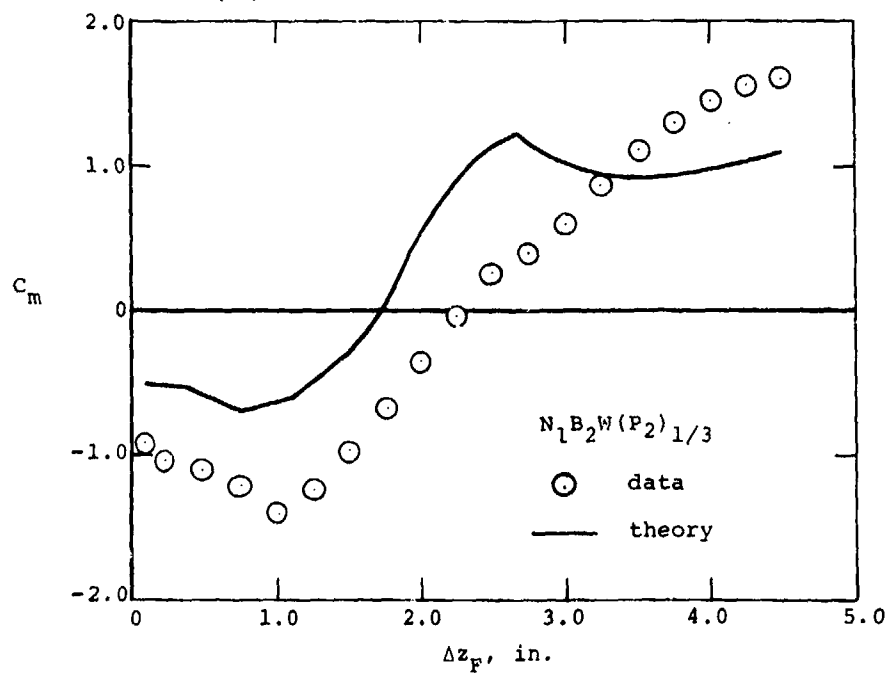


(b) Pitching-moment coefficient.

Figure 72.- Forces and moments on the ogive-cylinder store under the pylon at the fuselage centerline;
 $M_\infty = 1.5$, $\alpha_F = 0^\circ$.

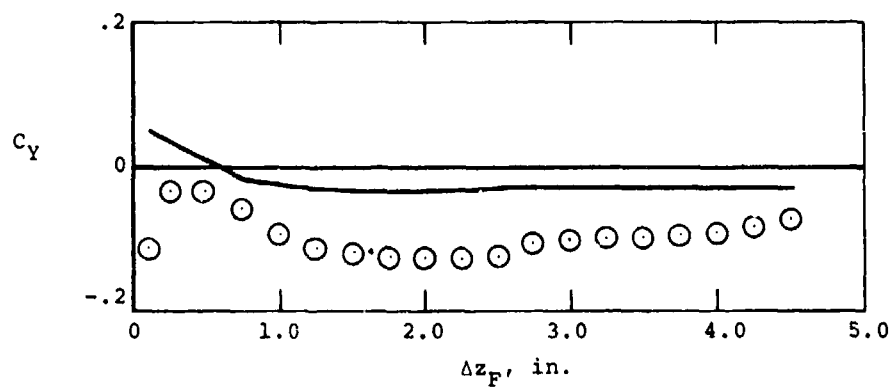


(a) Normal-force coefficient.

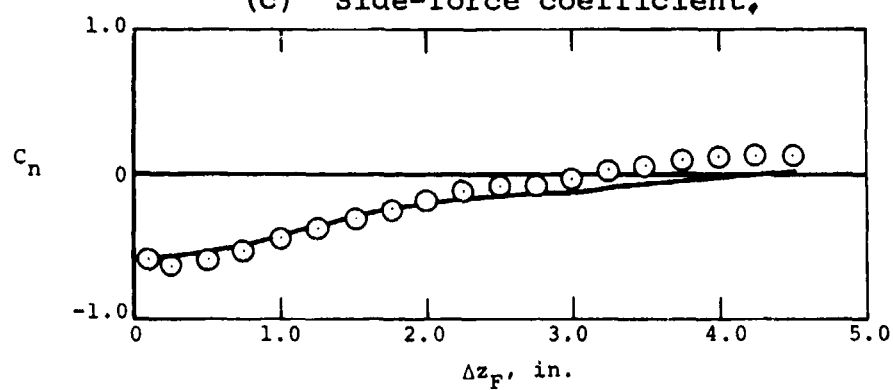


(b) Pitching-moment coefficient.

Figure 73.- Forces and moments on the ogive-cylinder store under the pylon at the one-third semispan location; $M_\infty = 1.5$, $\alpha_F = 5^\circ$.

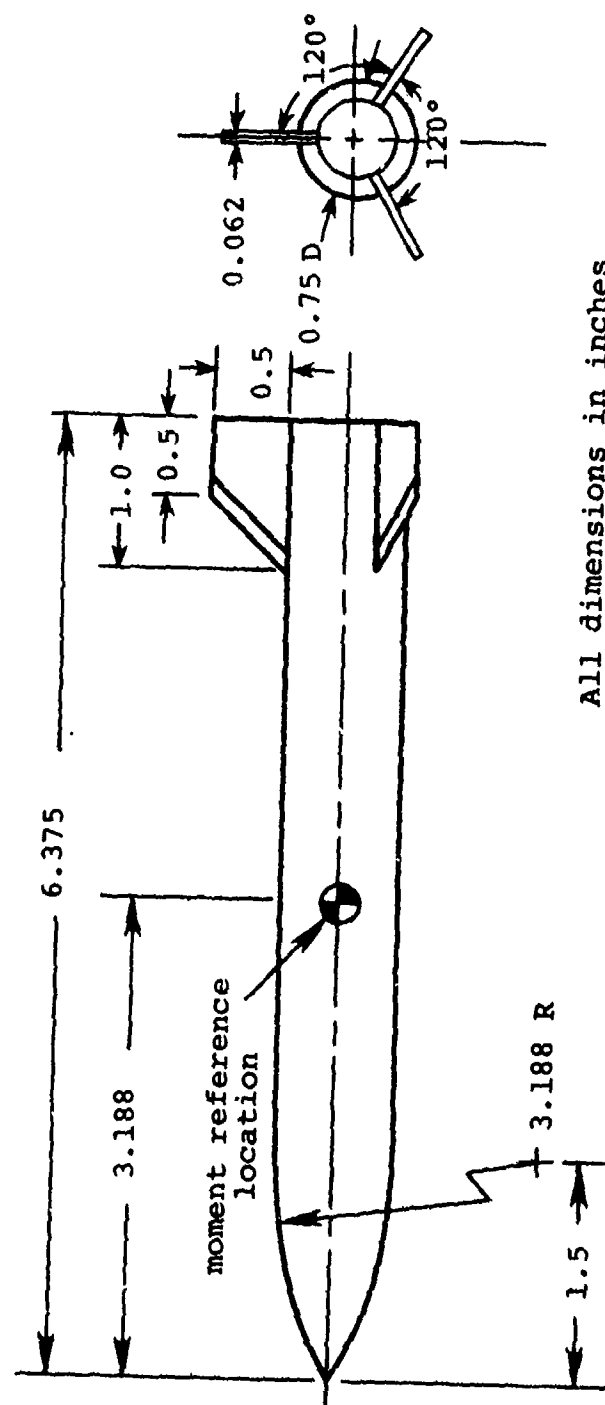


(c) Side-force coefficient,



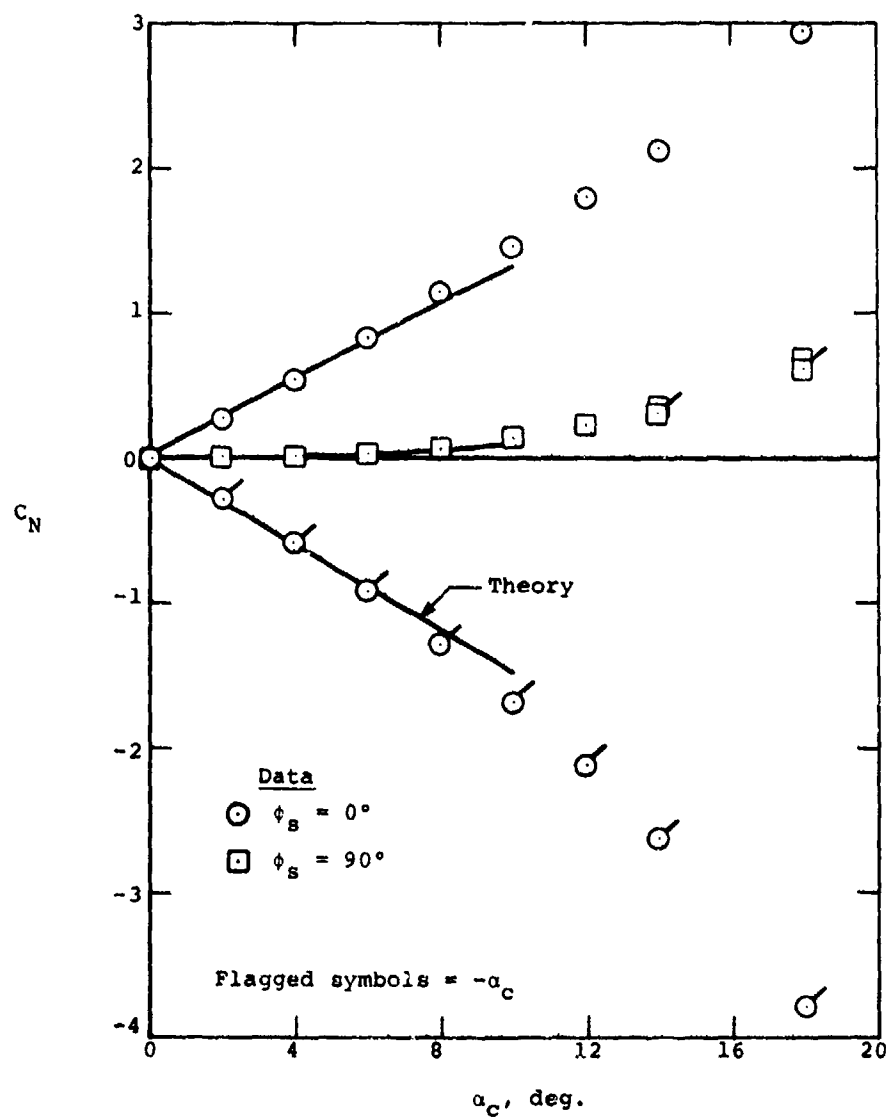
(d) Yawing-moment coefficient.

Figure 73.- Concluded.



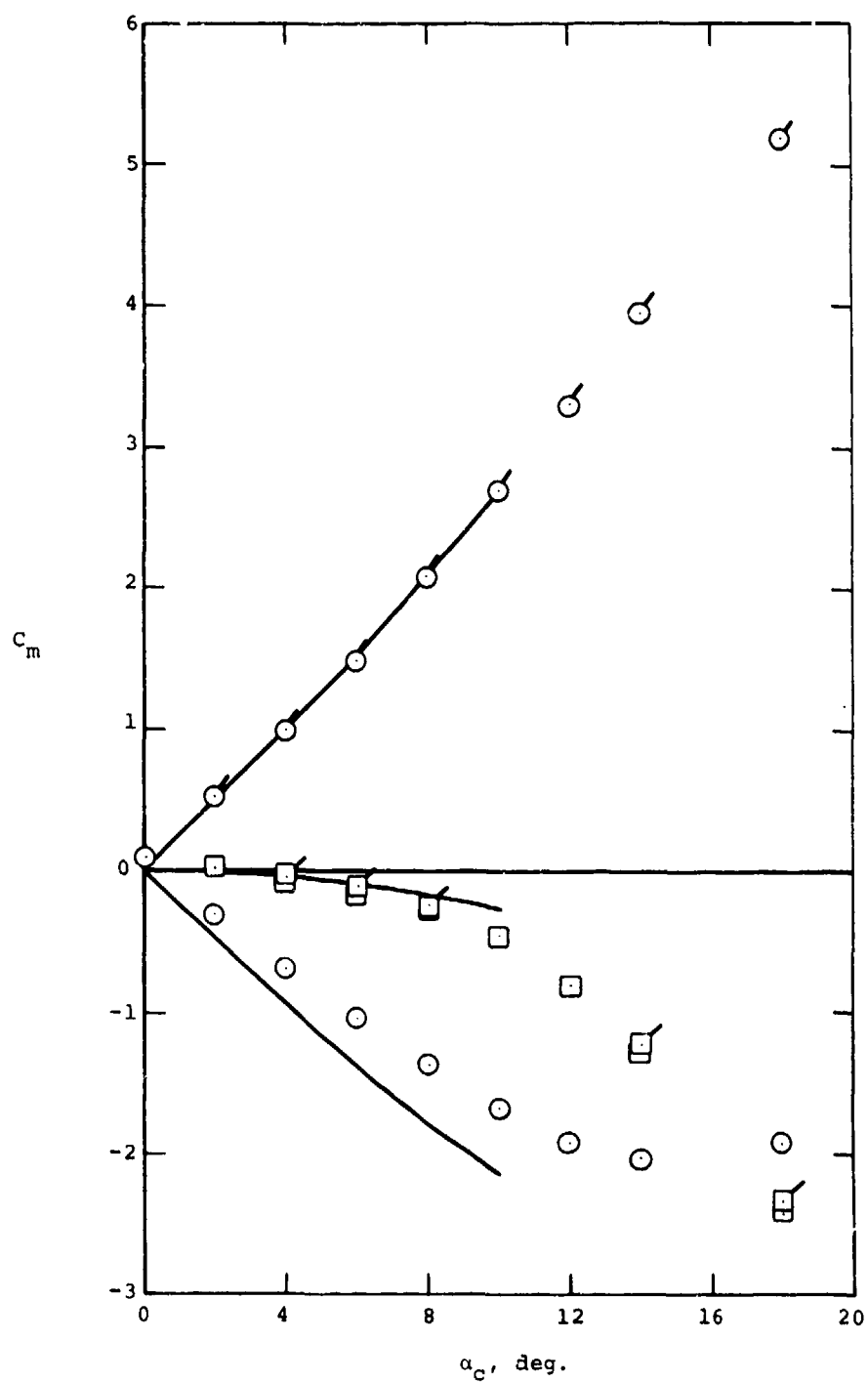
All dimensions in inches

Figure 74.- Triform ogive-cylinder store.



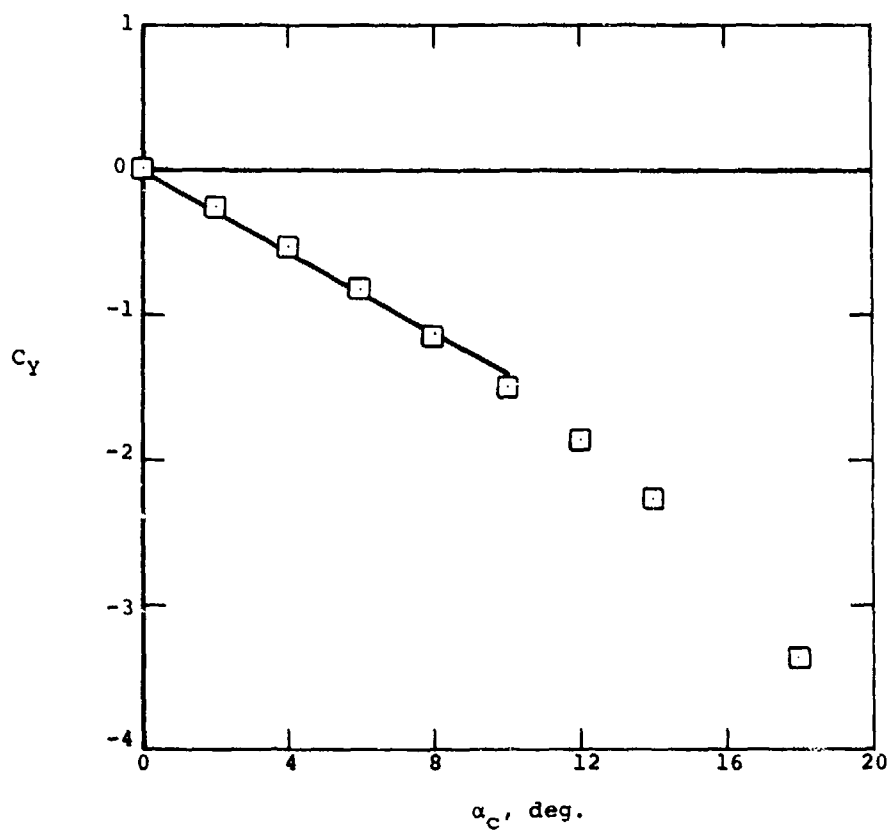
(a) Normal-force coefficient.

Figure 75.- Forces and moments on triform store in free stream, $M_\infty = 1.5$.



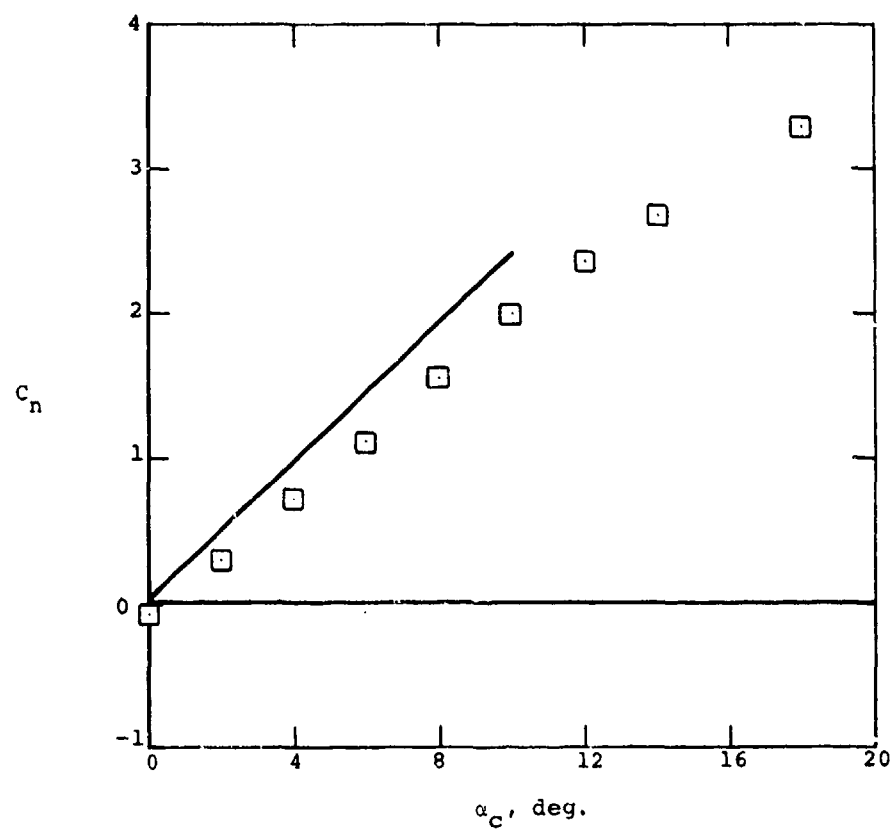
(b) Pitching-moment coefficient.

Figure 75.- Continued.



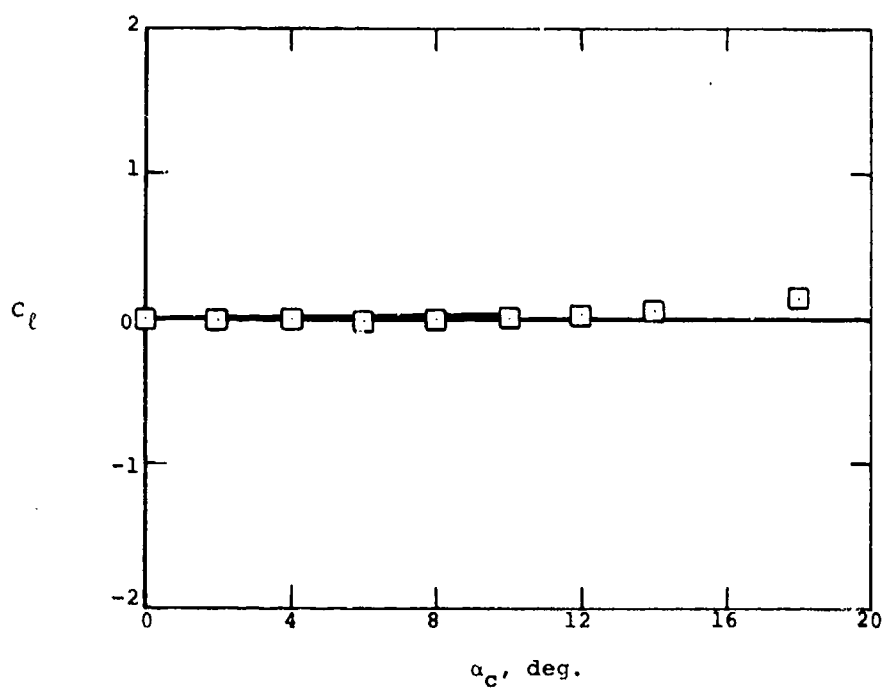
(c) Side-force coefficient.

Figure 75.- Continued.



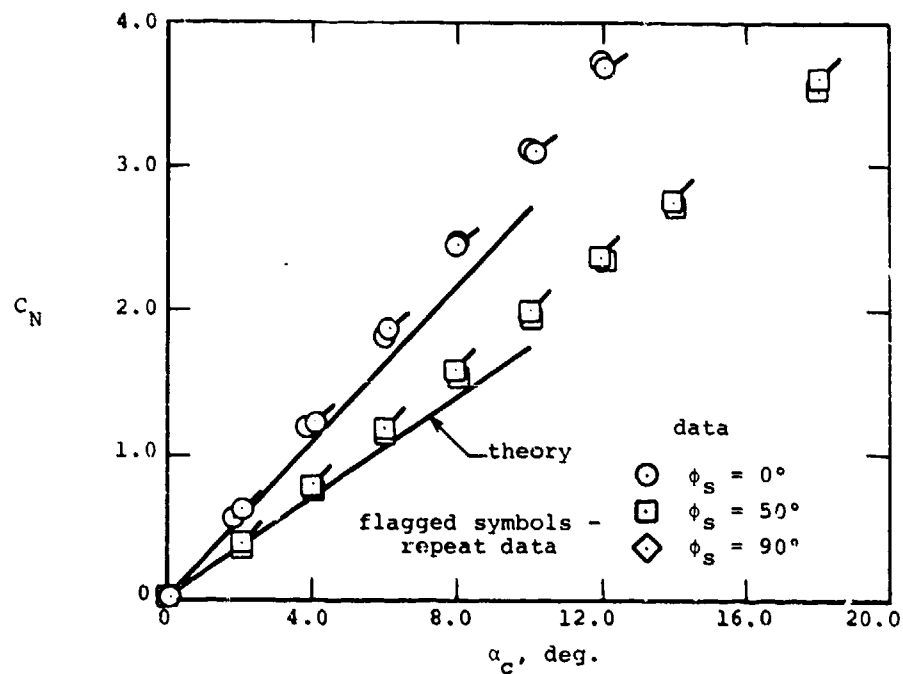
(d) Yawing-moment coefficient.

Figure 75.- Continued.

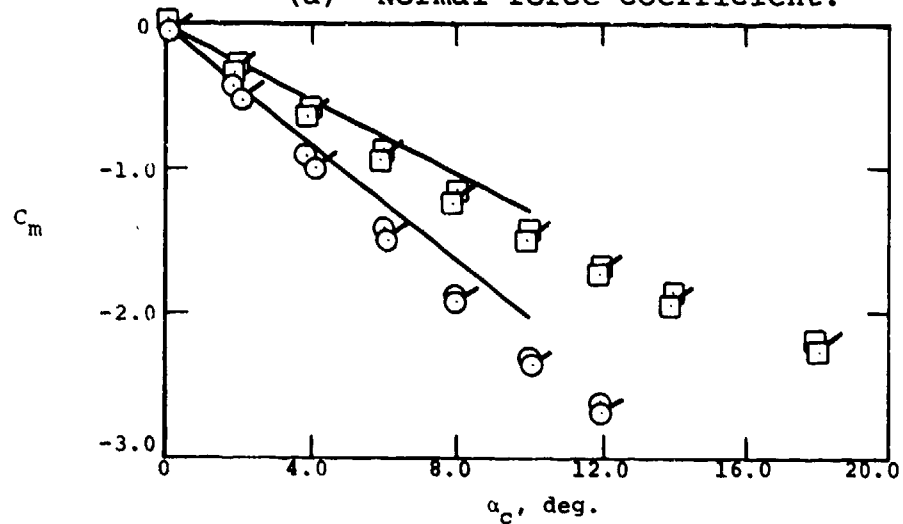


(e) Rolling-moment coefficient.

Figure 75.- Concluded.

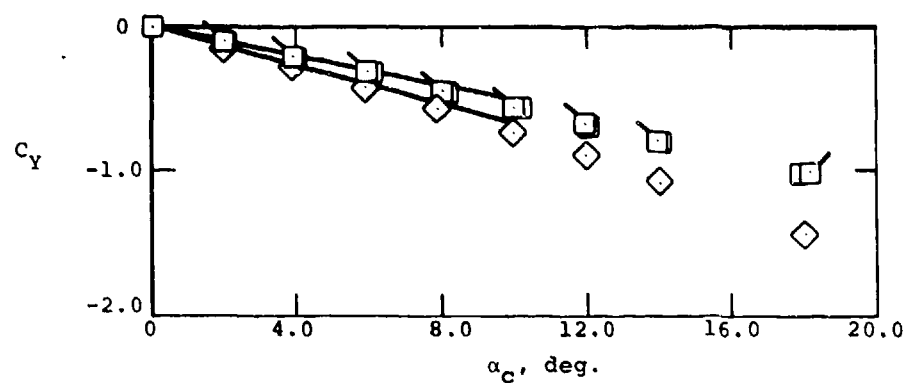


(a) Normal-force coefficient.

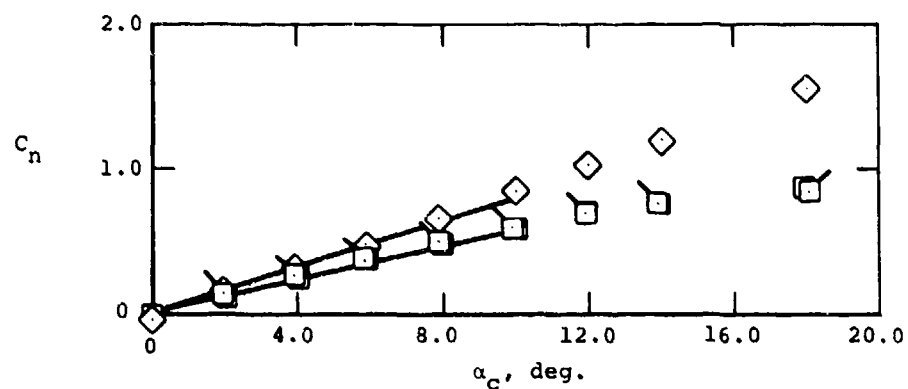


(b) Pitching-moment coefficient.

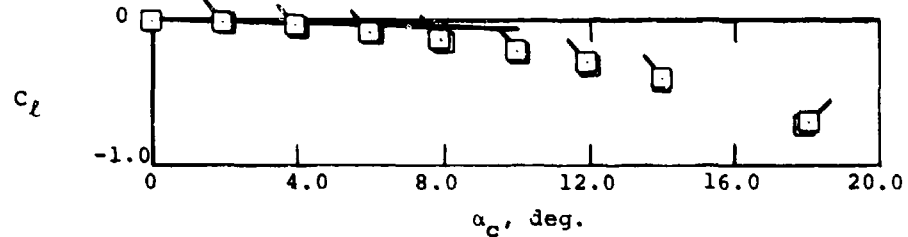
Figure 76.-- Forces and moments on the elliptic store with wing and tail in the free stream, $M_\infty = 1.5$.



(c) Side-force coefficient.



(d) Yawing-moment coefficient.



(e) Rolling-moment coefficient.

Figure 76.- Concluded.

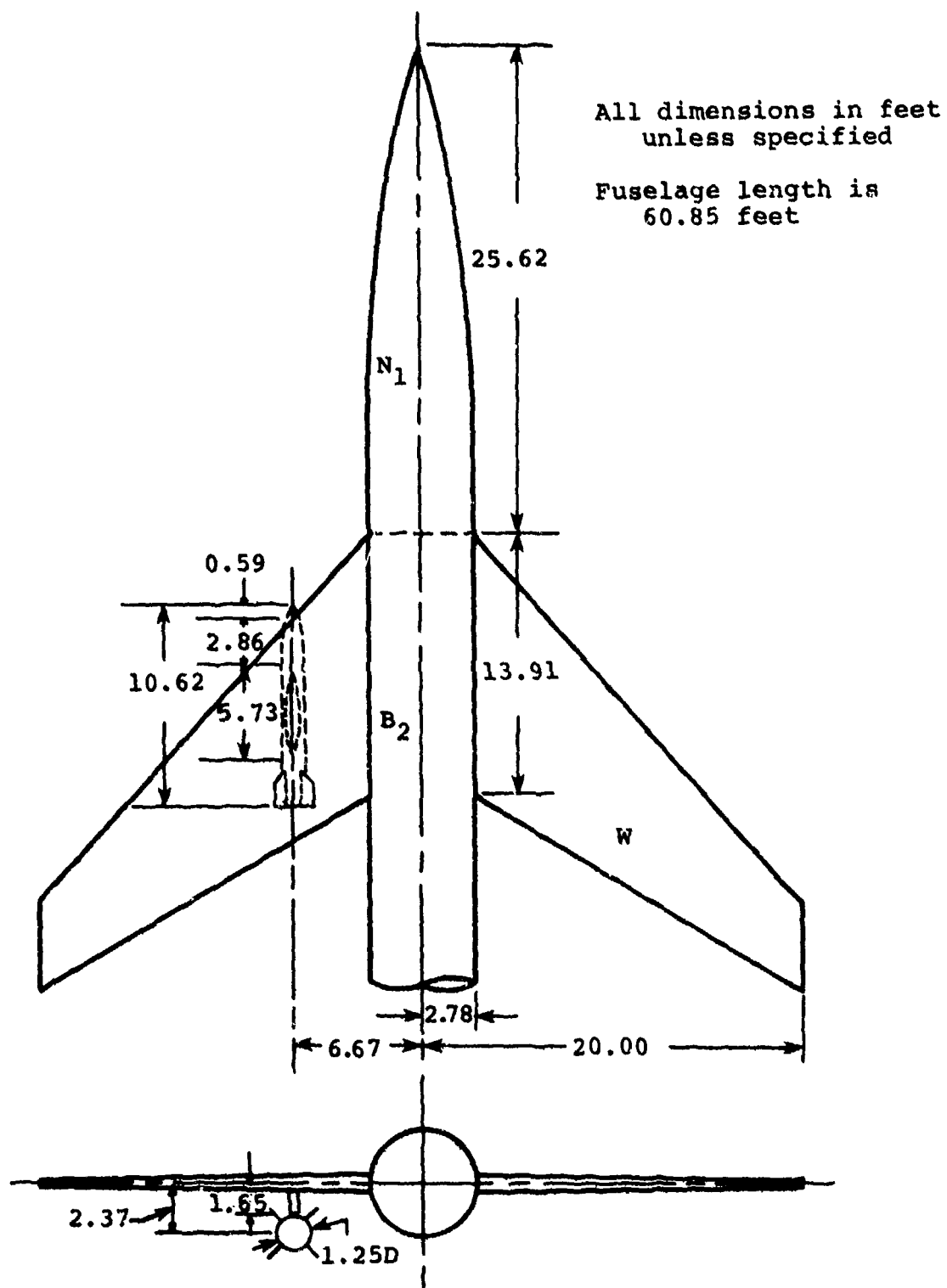
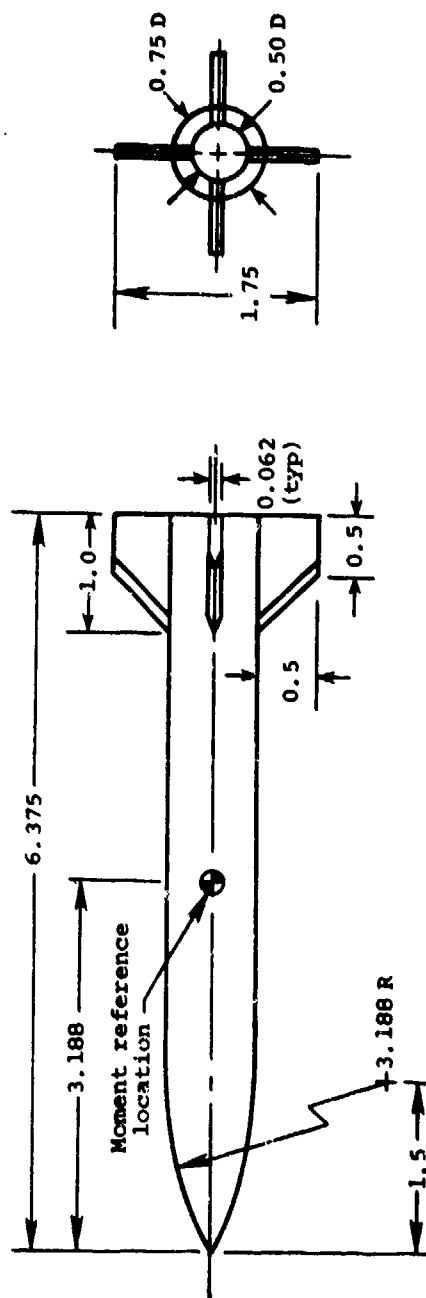


Figure 77.- Configuration for trajectory of ogive-cylinder store with cruciform fins.



All dimensions in inches

Figure 78.- Cruciform ogive-cylinder store.

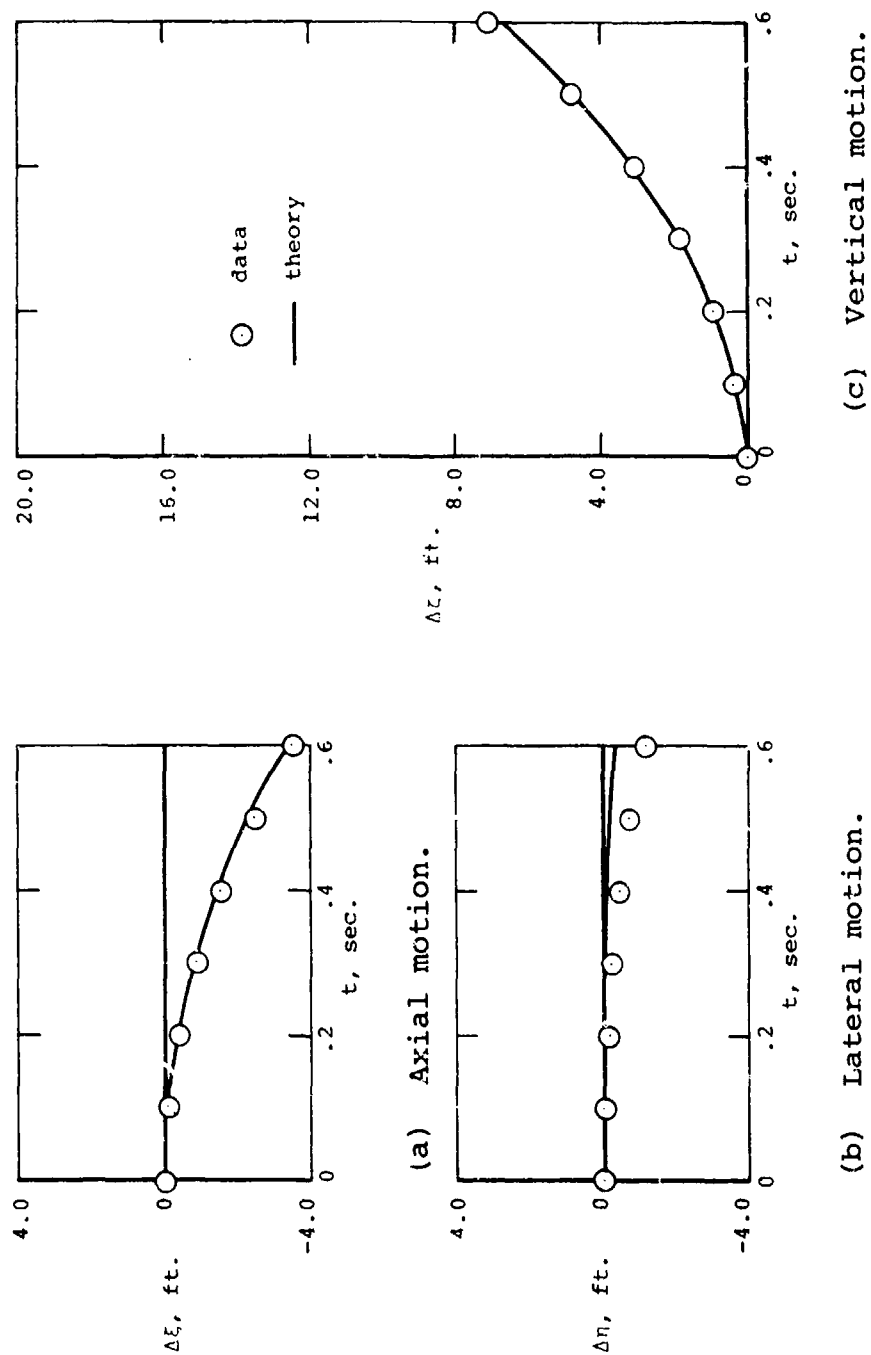


Figure 79.- Trajectory of ogive-cylinder store with cruciform fins released at one-third semispan location;
 $M_{\infty} = 1.5$, $\alpha_F = 5^\circ$.

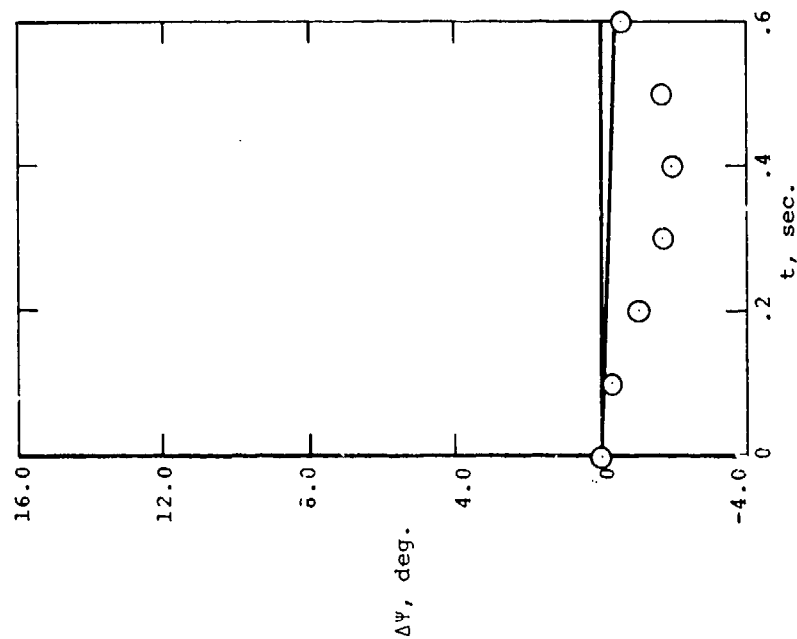
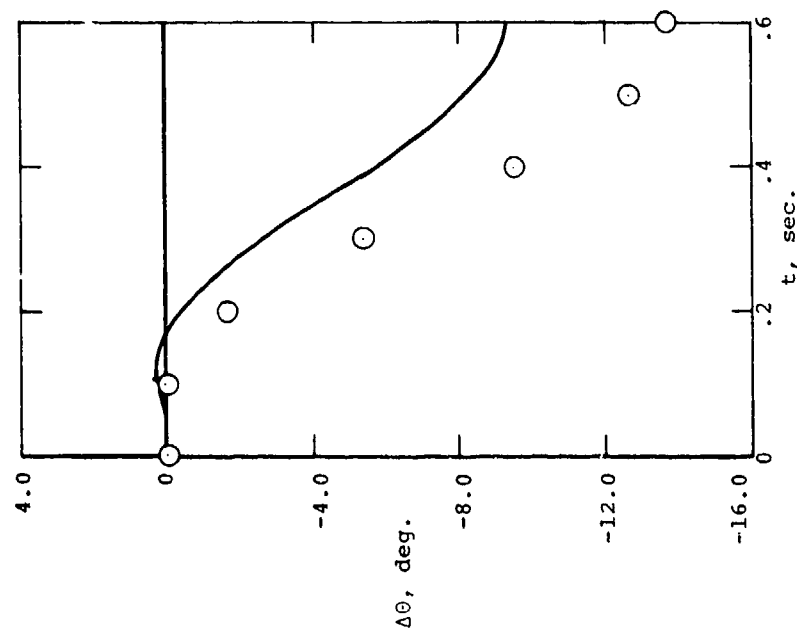
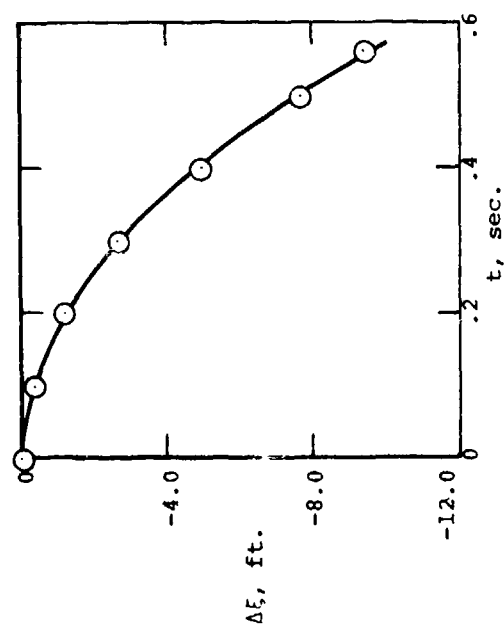
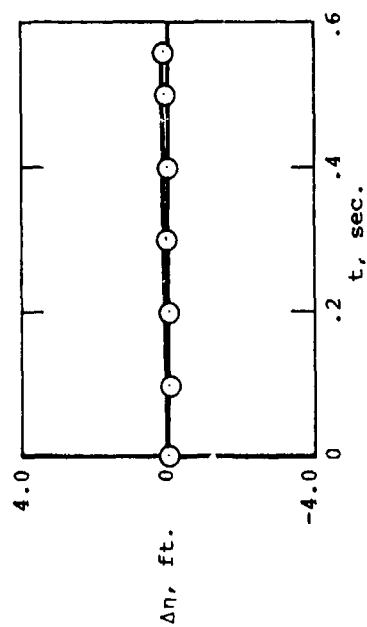


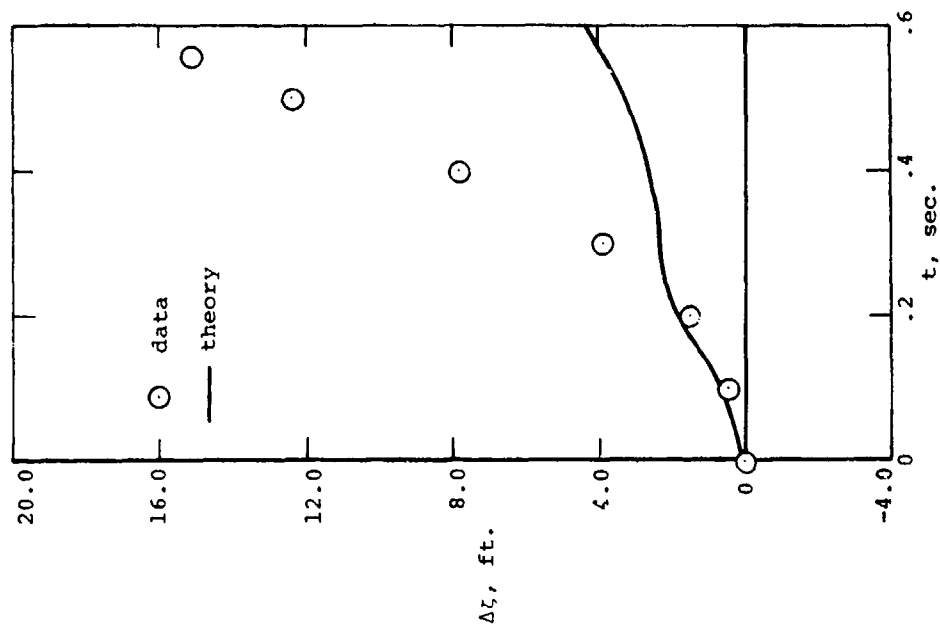
Figure 79.- Concluded.



(a) Axial motion.

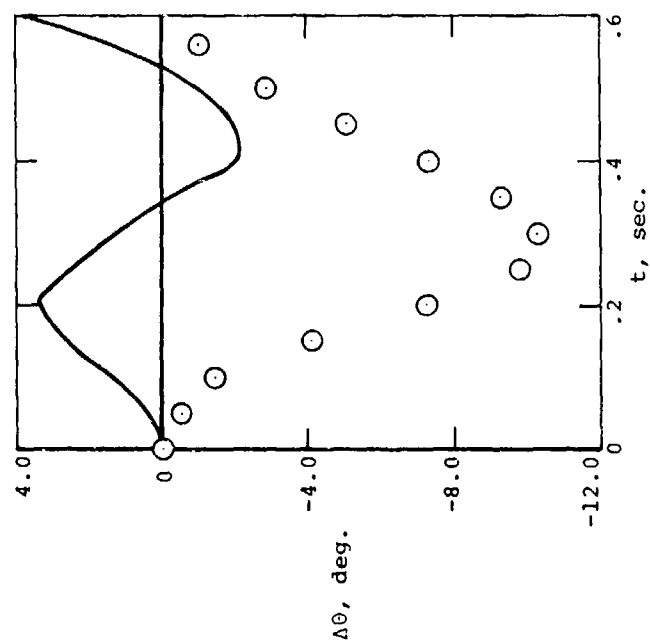


(b) Lateral motion.



(c) Vertical motion.

Figure 81.- Trajectory of elliptic store released under the fuse, age centerline; $M_\infty = 1.5$, $\alpha_F = 5^\circ$.



(1) Pitch motion.

Figure 81.- Concluded.

APPENDIX A

NORMAL- AND SIDE-FORCE DISTRIBUTIONS ACTING ON AN AXISYMMETRIC STORE IN SUPERSONIC, NONUNIFORM FLOW

A-1 INTRODUCTION

A three-dimensional method for calculating load distributions and overall forces and moments acting on a store in supersonic, nonuniform flow in the vicinity of the parent aircraft is presented. The procedure is summarized as follows.

The parent aircraft is flow modeled first and the strengths of the singularities used to model the fuselage, wing, pylon, ejector rack, and other stores are known. Since the separated store-to-parent aircraft interference is accounted for by means of an imaging scheme described in Section 4.4, the strengths of the aforementioned singularities are not affected by the separated store. If this interference were to be included in the boundary condition applied at points on the aircraft, the singularity strengths would be affected by store position. The store is immersed in the nonuniform flow field induced by the parent aircraft and the store image(s). The store is flow modeled in this nonuniform flow field and the pressures on the store are determined.

The next step is to flow model the store in the nonuniform flow field. In order to account for volume effects, supersonic line sources and sinks are disturbed along the store centerline. Appendix I of Reference 1 describes a solution representing volume effects of an axisymmetric body in supersonic, uniform flow. The solution can be extended to account for nonuniform axial flow. The constants in the linearly varying source or sink strengths expressions are obtained from the flow tangency

condition for the store aligned with the local flow streamlines. As a consequence, the constants are related to the product of the body slope measured in a meridional plane and the local axial velocity at a control point on the body surface.

In order to cancel effects due to nonuniform upwash and sidewash, supersonic line doublets are distributed along the store axis. The solution for the cross flow problem associated with an axisymmetric body in supersonic uniform flow is also given in Appendix I of Reference 1. This solution can be extended to account for varying upwash and sidewash at points along the store centerline induced by the parent aircraft and store image(s). The constants in the linearly varying doublet strength equations are determined from an application of the flow tangency condition at control points on the surface of the store body.

The velocities induced by the parent aircraft and store image(s) are computed at points along the centerline. Nonlinear corrections are applied in this process as described in Section 4 of this report. These velocities are transferred to the body surface for use in the flow tangency conditions associated with the axial and crossflow problems. This constitutes an approximation to the flow tangency condition in that the velocities to be cancelled at the surface point are taken equal to the velocities on the centerline. Thus as far as the singularity strengths are concerned, no account is taken of the lateral variation of axial velocity, upwash and sidewash in the region occupied by the store. The error introduced by this approximation is a function of the extent of nonuniformity of the flow coupled with the slenderness of the store. The procedure used to calculate velocities induced by the store image(s) is described in Section 4.4. The image of the store is represented by the same singularities as the real store. On account of the step-by-step solution procedure to be described below, the effects from the image store required in the boundary condition of the real store are induced by singularities with known strengths.

Once the strengths of the singularities representing the store are known, velocities induced by the singularities are computed at the control points on the store surface. Pressures are computed from the velocities including free stream components using the Bernoulli relationship. Normal- and side-force distributions are obtained by integrating the pressures along the circumference of a store body cross section.

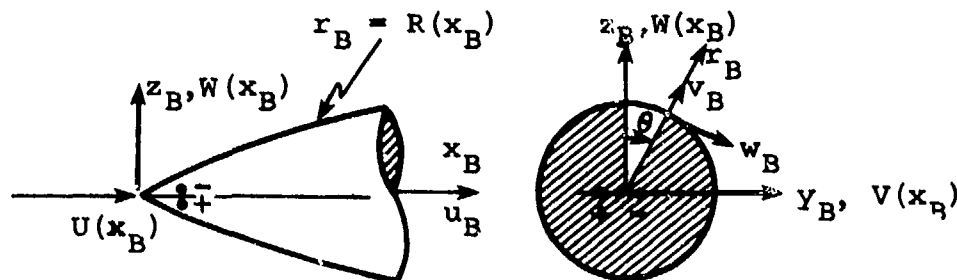
The store modeling technique will be described in detail. This is followed by a discussion of the pressure calculation method and the procedures used to calculate the force distributions and overall forces and moments acting on the store.

A-2 FLOW MODEL FOR AXISYMMETRIC BODY IN NONUNIFORM FLOW

In accordance with the earlier work (References 1 and 20) in supersonic store separation and missile aerodynamics, bodies of revolution with pointed noses in uniform, supersonic flow are represented by the following sets of singularities. Supersonic line sources account for volume effects and supersonic line doublets model effects of upwash and sidewash. In this report the solutions to the source and doublet problems are modified to include effects of nonuniform flow. The modifications affect the flow tangency conditions as described in the following section.

A-2.1 Flow Tangency Boundary Condition at the Body Surface

The sketch below shows a body of revolution in a flow field characterized by velocity components U, V, W which depend on the axial coordinate x_B only. In the application of the method to an ejected store, these velocity components include effects due to store pitch and yaw damping, translational velocities of the store c.g. and store angle of pitch and sideslip in addition to the perturbation velocity components induced by the parent aircraft and store image. The rectangular coordinates x_B, y_B, z_B



with origin at the store nose and a cylindrical coordinate system x_B, r_B, θ are indicated in the sketch. Also shown are the nonuniform free-stream velocity components $U(x_B), V(x_B), W(x_B)$ in the x_B, y_B, z_B directions, respectively. Perturbation velocities u_B, v_B, w_B are in the x_B, r_B , and θ directions. In a meridional plane, the body contour is given by $r_B = R(x_B)$. The flow tangency condition given by Equation (4) in Reference 1 is now restated with the inclusion of variable velocities U, V , and W . Note that the free-stream velocity V_∞ is the resultant flow velocity, with components $U_{s_\infty}, V_{s_\infty}$, and W_{s_∞} , as seen by the store. In the application to an ejected store, the resultant velocity at infinity as seen by the store includes effects due to store angle of pitch and sideslip and translational velocities of the store c.g. The resultant velocity has components $U_{s_\infty}, V_{s_\infty}, W_{s_\infty}$. $M_{\infty a}$ is related to U_{s_∞} . The boundary condition states that the resultant flow vector at the body is aligned with the local body slope.

$$\frac{v_B}{V_\infty} + \frac{W}{V_\infty} \cos \theta + \frac{V}{V_\infty} \sin \theta = \left(\frac{U}{V_\infty} + \frac{u_B}{V_\infty} \right) \frac{dR}{dx_B} \quad (A-1)$$

The equation governing the flow potential, ϕ , is expressed in the cylindrical coordinate system shown in the previous sketch.

$$(M_\infty^2 - 1) \frac{\partial^2 \phi}{\partial x_B^2} - \frac{1}{r_B} \frac{\partial \phi}{\partial r_B} - \frac{1}{r_B^2} \frac{\partial^2 \phi}{\partial \theta^2} - \frac{\partial^2 \phi}{\partial r_B^2} = 0 \quad (A-2)$$

Because Equation (A-2) is linear in ϕ , the solution can be composed as the sum of three potentials

$$\phi(x_B, r_B, \theta) = \phi_a(x_B, r_B) + \phi_{c_W}(x_B, r_B, \theta) + \phi_{c_V}(x_B, r_B, \theta) \quad (A-3)$$

which satisfies Equation (A-2). Potential ϕ_a is the axial potential. Potentials ϕ_{cW} and ϕ_{cV} are crossflow potentials associated with upwash W and sidewash V, respectively. In terms of cylindrical coordinates, the perturbation velocities are related to the two potentials in accordance with the following expressions.

$$\left. \begin{aligned} \frac{u_B}{V_\infty} &= \frac{\partial \phi_a}{\partial x_B} + \frac{\partial \phi_{cW}}{\partial x_B} + \frac{\partial \phi_{cV}}{\partial x_B} \\ \frac{v_B}{V_\infty} &= \frac{\partial \phi_a}{\partial r_B} + \frac{\partial \phi_{cW}}{\partial r_B} + \frac{\partial \phi_{cV}}{\partial r_B} \\ \frac{w_B}{V_\infty} &= \frac{1}{r_B} \frac{\partial \phi_{cW}}{\partial \theta} + \frac{1}{r_B} \frac{\partial \phi_{cV}}{\partial \theta} \end{aligned} \right\} \quad (A-4)$$

Substituting for the perturbation velocities in Equation (A-1) gives the following result.

$$\begin{aligned} \frac{\partial \phi_a}{\partial r_B} + \frac{\partial \phi_{cW}}{\partial r_B} + \frac{\partial \phi_{cV}}{\partial r_B} + \frac{W}{V_\infty} \cos \theta + \frac{V}{V_\infty} \sin \theta = \\ \left(\frac{U}{V_\infty} + \frac{\partial \phi_a}{\partial x_B} + \frac{\partial \phi_{cW}}{\partial x_B} + \frac{\partial \phi_{cV}}{\partial x_B} \right) \frac{dR}{dx_B} \end{aligned} \quad (A-5)$$

This expression for the flow tangency condition can be split into three parts for bodies of revolution.

$$\frac{\partial \phi_a}{\partial r_B} = \left(\frac{U}{V_\infty} + \frac{\partial \phi_a}{\partial x_B} \right) \frac{dR}{dx_B}; \text{ axial flow boundary condition} \quad (A-6a)$$

$$\frac{\partial \phi_{cW}}{\partial r_B} + \frac{W}{V_\infty} \cos \theta = \left(\frac{\partial \phi_{cW}}{\partial x_B} \right) \frac{dR}{dx_B}; \text{ upwash boundary condition} \quad (A-6b)$$

$$\frac{\partial \phi_{cV}}{\partial r_B} + \frac{V}{V_\infty} \sin \theta = \left(\frac{\partial \phi_{cV}}{\partial x_B} \right) \frac{dR}{dx_B}; \text{ sidewash boundary condition} \quad (A-6c)$$

Equation (A-6a) is the boundary condition for the axial flow problem with the axial flow velocity U a function of x_B . Similarly, Equations (A-6b) and (A-6c) involve only crossflow velocities associated with upwash W and sidewash V , respectively. The sum of the three equations yields the complete flow tangency condition, Equation (A-5). Thus, the first term on the right-hand side of Equation (A-3) together with Equation (A-6a) constitute the axial problem. According to Reference 21, the reference velocity for the axial problem is the velocity far from the body parallel to the body axis U_∞ and the associated Mach number is $M_{\infty a}$. The second term on the right-hand side of Equation (A-3) and Equation (A-6b) represent the upwash problem. The third term on the right-hand side of Equation (A-3) and Equation (A-6c) are the sidewash problem. For these two problems, the reference velocity refers to the full free-stream velocity, V_∞ and the Mach number is M_∞ .

The three problems will now be discussed in detail. Where convenient, reference will be made to the pertinent work in Reference 1.

A-2.2 Axial Flow Problem

The technique for modeling the volume effects due to a body of revolution in uniform flow is described in Appendix I, Section I-2.1, of Reference 1. The analysis presented there needs to be modified to include the effect of the variation of the longitudinal velocity component U with coordinate x_B , the distance along the body centerline.

The axial flow potential ϕ_a is governed by Equation (A-2) after omitting the angular dependence term. The result is

$$\left(M_{\infty a}^2 - 1 \right) \frac{\partial^2 \phi_a}{\partial x_B^2} - \frac{1}{r_B} \frac{\partial \phi_a}{\partial r_B} - \frac{\partial^2 \phi_a}{\partial r_B^2} \quad (A-7)$$

In accordance with Section 9.13 in Reference 21, the reference flow associated with the axial flow problem corresponds to the flow parallel to the body axis at infinity, U_{s_∞} , as seen by the store. The boundary condition given by Equation (A-6a) must be satisfied at points on the body surface. It is rewritten below.

$$\frac{\frac{U(x_B)}{U_{s_\infty}} \frac{dR}{dx_B}}{\frac{\partial \phi_a}{\partial r_B} - \frac{\partial \phi_a}{\partial x_B} \left(\frac{dR}{dx_B} \right)} = 1 \quad (A-8)$$

From Equation (I-10) in Appendix I of Reference 1,

$$\left. \begin{aligned} \frac{\partial \phi_a}{\partial x_B} &= \frac{u_{B,a}}{U_{s_\infty}} = -K \cosh^{-1} \left(\frac{x_B}{\beta_a r_B} \right) \\ \frac{\partial \phi_a}{\partial r_B} &= \frac{v_{B,a}}{U_{s_\infty}} = K \beta_a \sqrt{\left(\frac{x_B}{\beta_a r_B} \right)^2 - 1} \\ \beta_a &= \left(M_{\infty a}^2 - 1 \right)^{1/2} \end{aligned} \right\} \quad (A-9)$$

Substituting Equation (A-9) into (A-8) gives the following general result for constant K

$$K = \frac{\frac{U(x_B)}{U_{s_\infty}} \frac{dR}{dx_B}}{\beta_a \sqrt{\left(\frac{x_B}{\beta_a r_B} \right)^2 - 1} + \cosh^{-1} \left(\frac{x_B}{\beta_a r_B} \right) \frac{dR}{dx_B}} \quad (A-10)$$

For body slope dR/dx_B and axial flow velocity U specified at some x_B station, Equations (A-9) and (A-10) describe the flow field due to one line source resulting in a conical flow field.

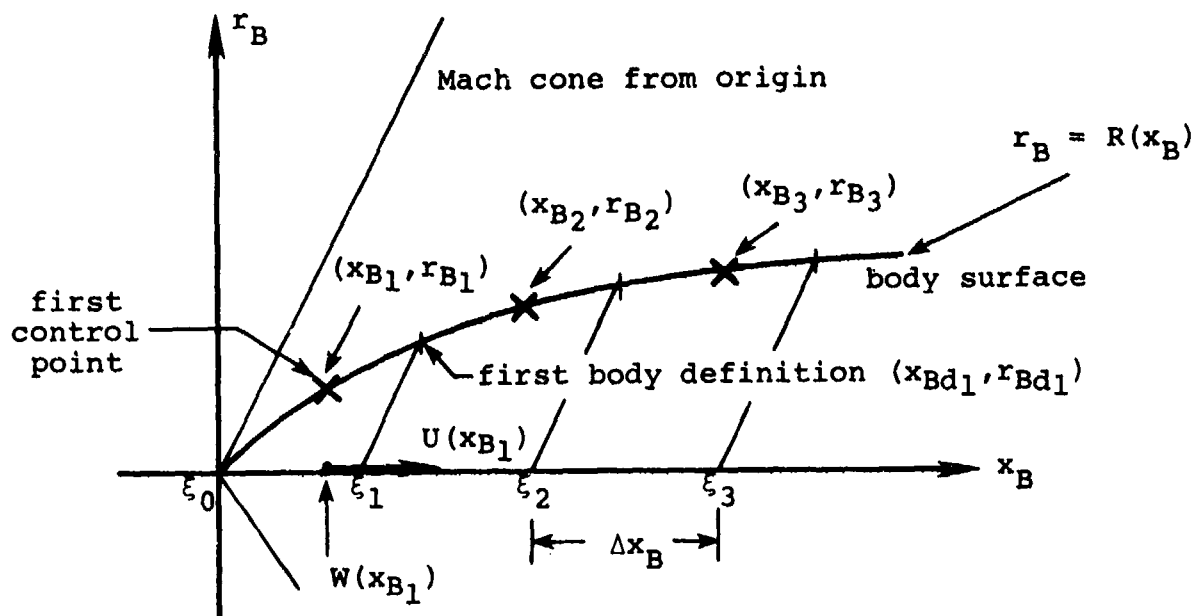
The velocities are functions of parameter $x_B/\beta_a r_B$ only and thus are invariant along lines for which x_B/r_B are constant.

Following the analysis described in Reference 21, the axial flow around an axisymmetric body aligned with the flow can be obtained from a superposition of conical solutions of the type discussed above. The composite source distribution for the axial flow solution is given by a superposition of linearly varying line sources. In fact, the distribution corresponds to a superposition of basic cone solutions

$$f(\xi) + K_0 \xi + K_1 (\xi - \xi_1) + K_2 (\xi - \xi_2) \dots \quad (A-11)$$

In this specification, constants K_1 and K_2 are negative for a typical nose shape and $\xi_0 = 0$, $\xi_1 = x_{Bd1} - \beta_a r_{Bd1}$, $\xi_2 = x_{Bd2} - \beta_a r_{Bd2}$, etc. are the origins of the line singularities expressed in terms of body definition points (x_{Bd}, r_{Bd}) to be discussed next. The constants are evaluated in a step-by-step manner as described in Appendix I of Reference 1. Note that the numerator in Equation (A-10) can be viewed as a modified body slope. Thus, the axial flow analysis for a body of revolution in uniform flow can be directly adapted to the case involving non-uniform flow.

Let NXBODY be the number of line sources with origins equally spaced on the body centerline. The number of control points also equals NXBODY. The x_B coordinates of the control points are half-way in between the x_{Bd} coordinates assigned to the body definition points. Line source origins $\xi_0, \xi_1, \xi_2 \dots$, are related to the body definition point coordinates as mentioned above. Geometrically, the line-source origins are the intersections of the Mach lines drawn from the body definition points with the body or x_B axis. The relative positions of the body definition points, line-source origins, control points, and Mach lines are shown in the following sketch.



In accordance with Equation (A-10), the first constant K_0 is calculated from

$$K_0 = \frac{\frac{U(x_B)}{U_{s_\infty}} \frac{dR}{dx_B}}{\beta_a \sqrt{\left(\frac{x_B}{\beta_a r_B}\right)^2 - 1} + \left[\cosh^{-1} \left(\frac{x_B}{\beta_a r_B} \right) \right] \frac{dR}{dx_B}} \quad \left| \begin{array}{l} x_B = x_{B1} = (\Delta x_B / 2) \\ r_B = r_{B1} = R(x_{B1}) \end{array} \right.$$

(A-12)

where x_{B1} and r_{B1} are the coordinates of the first control point. The n^{th} constant associated with the $(n+1)^{\text{th}}$ line source, K_n , is determined from the flow tangency condition applied at the $(n+1)^{\text{th}}$ control point (x_{Bn+1}, r_{Bn+1}) . The boundary condition

includes the effects of the line sources with known constants K_{k-1} and origins ξ_{k-1} positioned ahead of the origin ξ_n of the line source under consideration ($1 \leq k \leq n$). These effects are added to the axial flow term in the numerator of Equation (A-10). Thus, constant K_n is given by

$$K_n = \frac{a}{b} ; \quad n = 1, 2, \dots (NXBODY-1) \quad (A-13)$$

where

$$a = \frac{U(x_{B_{n+1}})}{U_{s_\infty}} \left. \frac{dR}{dx_B} \right|_{x_{B_{n+1}}} - \sum_{k=1}^n K_{k-1} \left\{ \beta_a \sqrt{\left(\frac{x_{B_{n+1}} - \xi_{k-1}}{\beta_a r_{B_{n+1}}} \right)^2 - 1} + \left[\cosh^{-1} \left(\frac{x_{B_{n+1}} - \xi_{k-1}}{\beta_a r_{B_{n+1}}} \right) \right] \left. \frac{dR}{dx_B} \right|_{x_{B_{n+1}}} \right\}$$

$$b = \beta_a \sqrt{\left(\frac{x_{B_{n+1}} - \xi_n}{\beta_a r_{B_{n+1}}} \right)^2 - 1} + \left[\cosh^{-1} \left(\frac{x_{B_{n+1}} - \xi_n}{\beta_a r_{B_{n+1}}} \right) \right] \left. \frac{dR}{dx_B} \right|_{x_{B_{n+1}}}$$

The terms in the above equation are specified as follows:

$$\left. \begin{aligned} \beta_a &= (M_{\infty a}^2 - 1)^{1/2} \\ M_{\infty a} &= \text{Mach number associated with flow velocity } U_{s_\infty} \text{ parallel to body axis at infinity} \\ \xi_0 &= 0 \\ \xi_{k-1} &= x_{Bd_{k-1}} - \beta_a r_{Bd_{k-1}} ; \quad k = 2, 3, \dots \\ \xi_n &= x_{Bd_n} - \beta_a r_{Bd_n} ; \quad n = 1, 2, \dots \\ x_{B_{n+1}} &= x_{B_n} + \Delta x_B \end{aligned} \right\} \quad (A-14)$$

[Equation (A-14) continued]

$$\begin{aligned}\Delta x_B &= \frac{\text{Body length}}{\text{NXBODY}} \\ r_{B_{n+1}} &= R(x_{B_{n+1}}) \\ \left. \frac{dR}{dx_B} \right|_{n+1} &= R'(x_{B_{n+1}}) \\ U(x_{B_{n+1}}) &= \text{axial flow velocity along the body centerline} \\ &\quad \text{at } x_{B_{n+1}}\end{aligned}$$

After completion of the step-by-step procedure for calculating constants K_0 and K_n where $n = 1, 2, \dots, (\text{NXBODY}-1)$, the axial and radial perturbation velocities induced at a field point with coordinates (x_B, r_B) by the line sources associated with the axial flow problem are

$$\left. \begin{aligned}\frac{u_{B,a}}{U_{s_\infty}} &= \sum_{n=0}^{\text{NXBODY}-1} \left[-K_n \cosh^{-1} \left(\frac{x_B - \xi_n}{\beta_a r_B} \right) \right] \\ \frac{v_{B,a}}{U_{s_\infty}} &= \sum_{n=0}^{\text{NXBODY}-1} \left[K_n \beta_a \sqrt{\left(\frac{x_B - \xi_n}{\beta_a r_B} \right)^2 - 1} \right]\end{aligned} \right\} \quad (\text{A-15})$$

The upwash and sidewash crossflow problems and the associated line-doublet solutions will now be described.

A-2.3 Crossflow Problems Due to Upwash and Sidewash

The analysis presented here is an extension to the cross-flow analysis in Appendix I of Reference 1. The added features are:

- (1) Separate sets of doublets for upwash and sidewash
- (2) Allowance for variation with distance along the body centerline of the upwash and sidewash

A-2.3.1 Solution for Upwash Line Doublets

The crossflow potential ϕ_{CW} for upwash must satisfy Equation (A-2) subject to the boundary condition given by Equation (A-6b). It is shown in Reference 1 that the solution can be constructed from the general (not the cone solution discussed previously) axisymmetric solution. The result is a linearly varying doublet solution for upwash with the doublet axis parallel to the z_B axis shown in the sketch of Section A-2.1.

$$\phi_{CW}(x_B, r_B, \theta) = K_{dW} \cos \theta \left[\frac{x_B}{2r_B} \sqrt{x_B^2 - \beta^2 r_B^2} - \frac{\beta^2 r_B}{2} \cosh^{-1} \left(\frac{x_B}{\beta r_B} \right) \right] \quad (A-16)$$

The reference flow Mach number is M_∞ associated with the free stream velocity V_∞ seen by the store. Factor β is therefore specified as

$$\beta = \sqrt{M_\infty^2 - 1} \quad (A-17)$$

The crossflow around an arbitrary body of revolution can be obtained by a superposition of doublet solutions in the same manner used for the axial flow problem. Thus, the composite doublet distribution for the upwash crossflow solution is obtained by generating a superposition of linearly varying line doublets

$$d_W(\xi) = K_{d_{W,0}} \xi + K_{d_{W,1}} (\xi - \xi_1) + K_{d_{W,2}} (\xi - \xi_2) + \dots \quad (A-18)$$

in terms of constants $K_{dW,0}$, $K_{dW,1}$, $K_{dW,2}$ and origins $\xi_0 = 0$, $\xi_1 = x_{Bd1} - \beta r_{Bd1}$, $\xi_2 = x_{Bd2} - \beta r_{Bd2}$ of the line singularities. These constants are also evaluated in the same step-by-step manner employed in the axial flow problem but with the boundary condition specified by Equation (A-6b). This flow tangency condition must be satisfied at the control points on the surface of the body shown in the sketch of Section A-2.2 concerned with the axial flow problem. Equation (A-6b) is rewritten as

$$\frac{W(x_B)}{V_\infty} \cos \theta = 1 \quad (A-19)$$

$$\frac{\partial \phi_{cW}}{\partial x_B} \frac{dR}{dx_B} - \frac{\partial \phi_{cW}}{\partial r_B}$$

Direct differentiation of the crossflow potential, Equation (A-16), gives the perturbation velocities associated with the line doublet for upwash.

$$\left. \begin{aligned} \frac{u_{B,dW}}{V_\infty} &= \frac{\partial \phi_{cW}}{\partial x_B} = K_{dW} \beta \cos \theta \sqrt{\frac{x_B^2}{\beta^2 r_B^2} - 1} \\ \frac{v_{B,dW}}{V_\infty} &= \frac{\partial \phi_{cW}}{\partial r_B} = - \frac{K_{dW} \beta^2 \cos \theta}{2} \left[\cosh^{-1} \left(\frac{x_B}{\beta r_B} \right) + \frac{x_B}{\beta r_B} \sqrt{\frac{x_B^2}{\beta^2 r_B^2} - 1} \right] \\ \frac{w_{B,dW}}{V_\infty} &= \frac{1}{r_B} \frac{\partial \phi_{cW}}{\partial \theta} = - \frac{K_{dW} \sin \theta}{r_B} \left[\frac{x_B}{2r_B} \sqrt{x_B^2 - \beta^2 r_B^2} - \frac{\beta^2 r_B}{2} \cosh^{-1} \left(\frac{x_B}{\beta r_B} \right) \right] \end{aligned} \right\} (A-20)$$

Note that the partial differentials (representing perturbation velocities) in Equation (A-19) are given by the first two of Equation (A-20) and contain the factor $\cos \theta$. Consequently, the $\cos \theta$ factor is cancelled in Equation (A-19). Referring again to the sketch in Section A-2.2, the first constant $K_{dW,0}$ is obtained from the boundary condition applied to the first control point (x_{B_1}, r_{B_1}) with a substitution from Equation (A-20)

$$K_{dW,0} = \frac{W(x_{B_1})}{V_\infty} \div \frac{\beta^2}{2} \left[\cosh^{-1} \left(\frac{x_{B_1}}{\beta r_{B_1}} \right) + \frac{x_{B_1}}{\beta r_{B_1}} \sqrt{\frac{x_{B_1}^2}{\beta^2 r_{B_1}^2} - 1} \right] + \left. \frac{dR}{dx_B} \right|_{x_{B_1}} \beta \sqrt{\frac{x_{B_1}^2}{\beta^2 r_{B_1}^2} - 1} \quad (A-21)$$

where

$$x_{B_1} = \frac{\Delta x_B}{2}$$

$$r_{B_1} = R(x_{B_1})$$

Let NXBODY be the number of line doublets for upwash with origins equally spaced on the body centerline. In general, the n^{th} constant is explicitly determined from the boundary condition applied at the $(n+1)^{\text{th}}$ control point as follows

$$K_{dW,n} = \frac{a}{b} ; \quad n = 1, 2, \dots (NXBODY-1) \quad (A-22)$$

where

$$a = \frac{W(x_{B_{n+1}})}{V_\infty} - \sum_{k=1}^n K_{d_{W,k-1}} \left\{ \frac{\beta^2}{2} \left[\cosh^{-1} \left(\frac{x_{B_{n+1}} - \xi_{k-1}}{\beta r_{B_{n+1}}} \right) + \left(\frac{x_{B_{n+1}} - \xi_{k-1}}{\beta r_{B_{n+1}}} \right) \right. \right. \\ \left. \left. \times \sqrt{\frac{(x_{B_{n+1}} - \xi_{k-1})^2}{\beta^2 r_{B_{n+1}}^2} - 1} \right] + \frac{dR}{dx_B} \Big|_{x_{B_{n+1}}} \beta \sqrt{\frac{(x_{B_{n+1}} - \xi_{k-1})^2}{\beta^2 r_{B_{n+1}}^2} - 1} \right\}$$

$$b = \frac{\beta^2}{2} \left[\cosh^{-1} \left(\frac{x_{B_{n+1}} - \xi_n}{\beta r_{B_{n+1}}} \right) + \left(\frac{x_{B_{n+1}} - \xi_n}{\beta r_{B_{n+1}}} \right) \sqrt{\frac{(x_{B_{n+1}} - \xi_n)^2}{\beta^2 r_{B_{n+1}}^2} - 1} \right] \\ + \frac{dR}{dx_B} \Big|_{x_{B_{n+1}}} \beta \sqrt{\frac{(x_{B_{n+1}} - \xi_n)^2}{\beta^2 r_{B_{n+1}}^2} - 1}$$

and

$$\left. \begin{aligned} \beta^2 &= M_\infty^2 - 1 \\ \xi_0 &= 0 \\ \xi_{k-1} &= x_{B_{d_{k-1}}} - \beta r_{B_{d_{k-1}}}; \quad k = 2, 3, \dots \\ \xi_n &= x_{B_{d_n}} - \beta r_{B_{d_n}}; \quad n = 1, 2, \dots \\ x_{B_{n+1}} &= x_{B_n} + \Delta x_B \\ \Delta x_B &= \frac{\text{Body length}}{NXBODY} \end{aligned} \right\} \quad (A-23)$$

[Equation (A-23) continued]

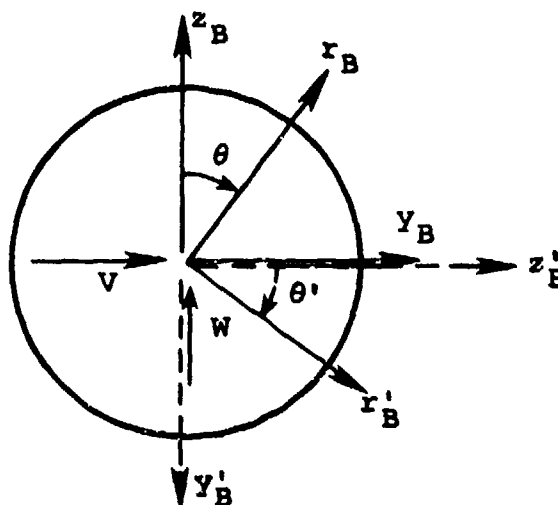
$$\left. \begin{aligned} r_{B_{n+1}} &= R(x_{B_{n+1}}) \\ \left. \frac{dR}{dx_B} \right|_{n+1} &= R'(x_{B_{n+1}}) \\ w(x_{B_{n+1}}) &= \text{upwash along the body centerline at } x_{B_{n+1}} \end{aligned} \right\}$$

The step-by-step procedure indicated by Equation (A-22) together with Equation (A-21) provides the solution for constants $K_{dW,0}$, $K_{dW,n}$, where $n = 1, 2, \dots (NXBODY - 1)$. The axial, radial, and tangential perturbation velocities induced by the line doublets associated with the upwash problem at a field-point (x_B, r_B, θ) are

$$\left. \begin{aligned} \frac{u_{B,dW}}{V_\infty} &= \sum_{n=0}^{NXBODY-1} K_{dW,n} \beta \cos \theta \sqrt{\frac{(x_B - \xi_n)^2}{\beta^2 r_B^2} - 1} \\ \frac{v_{B,dW}}{V_\infty} &= \sum_{n=0}^{NXBODY-1} -K_{dW,n} \beta^2 \frac{\cos \theta}{2} \left[\cosh^{-1} \left(\frac{x_B - \xi_n}{\beta r_B} \right) \right. \\ &\quad \left. + \left(\frac{x_B - \xi_n}{\beta r_B} \right) \sqrt{\left(\frac{x_B - \xi_n}{\beta r_B} \right)^2 - 1} \right] \\ \frac{w_{B,dW}}{V_\infty} &= \sum_{n=0}^{NXBODY-1} -\frac{K_{dW,n} \sin \theta}{r_B} \left[\left(\frac{x_B - \xi_n}{2r_B} \right) \right. \\ &\quad \left. \times \sqrt{(x_B - \xi_n)^2 - \beta^2 r_B^2} - \frac{\beta^2 r_B}{2} \cosh^{-1} \left(\frac{x_B - \xi_n}{\beta r_B} \right) \right] \end{aligned} \right\} (A-24)$$

A-2.3.2 Solution for Sidewash Line Doublets

For this problem, the doublet axis is parallel to the direction of the y_B axis shown in the first sketch of Section A-2.1. The solution can be related to the solution for the upwash by a rotation of coordinate axes y_B and z_B as shown in the following sketch. It is seen that the relation of the y'_B, z'_B or r'_B, θ' system to the V vector is the same as the relation of the y_B, z_B or r_B, θ system to the vector W . In fact, the former can be derived from the latter by means of a clockwise rotation in



angle θ through 90° . As a consequence, Equations (A-20) and (A-24) for perturbation velocities due to upwash, replace $\cos \theta$ with $\sin \theta$, and $\sin \theta$ with $-\cos \theta$. The resulting expressions represent the perturbation velocities induced by sidewash. The values for constants $K_{dV,0}$ through $K_{dV,n}$ are obtained from Equations (A-21) and (A-22) replacing $W(x_{B1})/V_\infty$ and $W(x_{B_{n+1}})/V_\infty$ with $V(x_{B1})/V_\infty$ and $V(x_{B_{n+1}})/V_\infty$.

Alternatively, it can be shown that the cross-flow potential for sidewash can be related to the general axisymmetric solution as follows

$$\phi_{cV}(x_B, r_B, \theta) = \sin \theta \frac{\partial \phi_a}{\partial r_B} \quad (A-25)$$

For the upwash problem the $\sin \theta$ factor is replaced with $\cos \theta$. The potential for the sidewash problem can then be derived in the manner used for the upwash problem as summarized in Appendix I of Reference 1.

The composite doublet distribution for the sidewash cross-flow solution is given by a superposition of linearly varying line doublets

$$d_V(\xi) = K_{d_{V,0}} \xi + K_{d_{V,1}} (\xi - \xi_1) + K_{d_{V,2}} (\xi - \xi_2) + \dots \quad (A-26)$$

in the same manner used for the upwash case, Equation (A-18). The first constant $K_{d_{V,0}}$ is obtained from the boundary condition given by Equation (A-6c) which is rewritten below

$$\frac{\frac{V(x_B)}{V_\infty} \sin \theta}{-\frac{\partial \phi_{c_V}}{\partial r_B} + \frac{\partial \phi_{c_V}}{\partial x_B} \frac{dR}{dx_B}} = 1 \quad (A-27)$$

In accordance with the transformations mentioned above, the perturbation velocities associated with one line doublet for sidewash can be obtained from Equation (A-20). The result is

$$\left. \begin{aligned} \frac{u_{B,d_V}}{V_\infty} &= \frac{\partial \phi_{c_V}}{\partial x_B} = K_{d_V} \beta \sin \theta \sqrt{\frac{x_B^2}{\beta^2 r_B^2} - 1} \\ \frac{v_{B,d_V}}{V_\infty} &= \frac{\partial \phi_{c_V}}{\partial r_B} = -K_{d_V} \frac{\beta^2 \sin \theta}{2} \left[\cosh^{-1} \left(\frac{x_B}{\beta r_B} \right) + \frac{x_B}{\beta r_B} \sqrt{\frac{x_B^2}{\beta^2 r_B^2} - 1} \right] \end{aligned} \right\} \quad (A-28)$$

[Equation (A-28) continued]

$$\frac{w_{B,dV}}{V_\infty} = \frac{1}{r_B} \frac{\partial \phi_{cV}}{\partial \theta} = \frac{K_{dV} \cos \theta}{r_B} \left[\frac{x_B}{2r_B} \sqrt{x_B^2 - \beta^2 r_B^2} - \frac{\beta^2 r_B}{2} \cosh^{-1} \left(\frac{x_B}{\beta r_B} \right) \right]$$

In Equation (A-27), the partial differentials representing perturbation velocities are given by the first two of Equation (A-28) and contain the factor $\sin \theta$. Thus, the factor $\sin \theta$ is canceled in Equation (A-27). The first constant $K_{dV,o}$ is obtained from the boundary condition applied to the first control point (x_{B1}, r_{B1}) shown in the sketch of Section A-2.2

$$K_{dV,o} = \frac{\frac{V(x_{B1})}{V_\infty}}{\frac{\beta^2}{2} \left[\cosh^{-1} \left(\frac{x_{B1}}{\beta r_{B1}} \right) + \frac{x_{B1}}{\beta r_{B1}} \sqrt{\frac{x_{B1}^2}{\beta^2 r_{B1}^2} - 1} \right] + \left. \frac{dR}{dx_B} \right|_1 \beta \sqrt{\frac{x_{B1}^2}{\beta^2 r_{B1}^2} - 1}}$$

(A-29)

where

$$x_{B1} = \Delta x_B / 2$$

$$r_{B1} = R(x_{B1})$$

Let NXBODY be the number of line doublets for sidewash with origins equally spaced on the body centerline. In general, the n^{th} constant is explicitly determined from the boundary condition applied at the $(n+1)^{\text{th}}$ control point as follows.

$$K_{dV,n} = \frac{a}{b}; \quad n = 1, 2, \dots, (\text{NXBODY}-1) \quad (\text{A-30})$$

where

$$a = \frac{V(x_{B_{n+1}})}{V_{\infty}} - \sum_{k=1}^n K_{dV,k-1} \left\{ \frac{\beta^2}{2} \left[\cosh^{-1} \left(\frac{x_{B_{n+1}} - \xi_{k-1}}{\beta r_{B_{n+1}}} \right) + \left(\frac{x_{B_{n+1}} - \xi_{k-1}}{\beta r_{B_{n+1}}} \right) \right. \right. \\ \left. \left. \times \sqrt{\frac{(x_{B_{n+1}} - \xi_{k-1})^2}{\beta^2 r_{B_{n+1}}^2} - 1} \right] + \frac{dR}{dx_B} \Big|_{x_{B_{n+1}}} \beta \sqrt{\frac{(x_{B_{n+1}} - \xi_{k-1})^2}{\beta^2 r_{B_{n+1}}^2} - 1} \right\}$$

$$b = \frac{\beta^2}{2} \left[\cosh^{-1} \left(\frac{x_{B_{n+1}} - \xi_n}{\beta r_{B_{n+1}}} \right) + \left(\frac{x_{B_{n+1}} - \xi_n}{\beta r_{B_{n+1}}} \right) \sqrt{\frac{(x_{B_{n+1}} - \xi_n)^2}{\beta^2 r_{B_{n+1}}^2} - 1} \right] \\ + \frac{dR}{dx_B} \Big|_{x_{B_{n+1}}} \beta \sqrt{\frac{(x_{B_{n+1}} - \xi_n)^2}{\beta^2 r_{B_{n+1}}^2} - 1}$$

and

$$\left. \begin{aligned} \beta^2 &= M_{\infty}^2 - 1 \\ \xi_0 &= 0 \\ \xi_{k-1} &= x_{Bd_{k-1}} - \beta r_{Bd_{k-1}}, \quad k = 2, 3, \dots \\ \xi_n &= x_{Bd_n} - \beta r_{Bd_n}, \quad n = 1, 2, \dots \end{aligned} \right\} \quad (\text{A-31})$$

[Equation (A-31) continued]

$$x_{B_{n+1}} = x_{B_n} + \Delta x_B$$

$$\Delta x_B = \frac{\text{Body length}}{NXBODY}$$

$$r_{B_{n+1}} = R(x_{B_{n+1}})$$

$$\left. \frac{dR}{dx_B} \right|_{n+1} = R'(x_{B_{n+1}})$$

$$V(x_{B_{n+1}}) = \text{sidewash along the body centerline at } x_{B_{n+1}}$$

The step-by-step procedure indicated by Equation (A-30), together with Equation (A-29) provides the solution for constants $K_{dV,0}$, $K_{dV,n}$ where $n = 1, 2, \dots, (NXBODY-1)$. The axial, radial, and tangential perturbation velocities induced by the line doublets associated with the side-wash problem at a fieldpoint (x_B, r_B, θ) can be determined from Equation (A-24) with the transformations discussed earlier. The results are

$$\frac{u_{B,dV}}{V_\infty} = \sum_{n=0}^{NXBODY-1} K_{dV,n} \beta \sin \theta \sqrt{\frac{(x_B - \xi_n)^2}{\beta^2 r_B^2} - 1}$$

$$\frac{v_{B,dV}}{V_\infty} = \sum_{n=0}^{NXBODY-1} -K_{dV,n} \beta^2 \frac{\sin \theta}{2} \left[\cosh^{-1} \left(\frac{x_B - \xi_n}{\beta r_B} \right) \right.$$

$$\left. + \left(\frac{x_B - \xi_n}{\beta r_B} \right) \sqrt{\frac{(x_B - \xi_n)^2}{\beta^2 r_B^2} - 1} \right]$$

(A-32)

[Equation (A-32) continued]

$$\frac{w_{B,d_V}}{V_\infty} = \sum_{n=0}^{NXBODY-1} \frac{K_{d_{V,n}} \cos \theta}{r_B} \left[\left(\frac{x_B - \xi_n}{2r_B} \right) \right. \\ \left. \times \sqrt{(x_B - \xi_n)^2 - \beta^2 r_B^2} - \frac{\beta^2 r_B}{2} \cosh^{-1} \left(\frac{x_B - \xi_n}{r_B} \right) \right]$$

Knowing the strengths of the line sources, sinks, and doublets, the pressure can now be computed at points on the surface of the store body. The pressures are then integrated to yield the force distribution on the store. The technique used will now be described.

A-3 CALCULATION OF LOADS ON THE STORE IN SUPERSONIC, NONUNIFORM FLOW

This section is concerned with the methods used to compute the pressure distributions, load distributions, and forces and moments acting on an axisymmetric store in nonuniform, supersonic flow. The strengths of the singularities used to represent the store in such a flow field have been determined by the methods described in the previous section. Velocities induced by the store singularities at points on the store body surface are calculated. The Bernoulli velocity-pressure relationship is then used to compute pressure coefficients at points on the body surface. Integration around the body circumference yields the axial distributions of normal and side forces and the pitching and yawing moments. Finally, the axial distributions are integrated to obtain overall forces and moments.

In the calculation of pressures on the store body summarized above, velocity components induced by the store image and parent aircraft are not included. In Section 6.2.1 it was shown that this assumption improves agreement between the theory and data for the store pressure distribution. Over the region of the store where shock waves impinge, this assumption is rationalized on the basis of pressure bleed-off by the strong boundary-layer cross-flow. A description of these viscous effects is given in Section 5.4 of Reference 1. Note that the strengths of the singularities modeling the store in the nonuniform flow field are affected by effects from the image store(s) and parent aircraft. Away from the shock impingement regions, their effects should probably be included in the pressure calculations. At the present time, only the sources or sinks and the doublets associated with the store itself induce velocities at the points on the body surfaces where pressures are calculated.

A-3.1 Effects Due to Store Volume

Store volume is represented by a distribution of linearly varying line sources (supersonic cone solutions) along the store body axis. The strengths of the line sources are related to the store body surface slopes measured in a meridional plane. The reference velocity used in the line source strength calculation is the component, $U_{s\infty}$ measured along the store axis of the free-stream velocity as seen by the store. This free-stream velocity, designated V_∞ , includes effects of translation of the store relative to the parent aircraft.

At a point (x_B, y_B, z_B) on the surface of the store, the perturbation velocities induced by the line sources representing store volume are calculated. Thus, at a point (x_B, y_B, z_B) on the surface of the store, the perturbation velocity components are expressed as follows.

$$\left. \begin{aligned} \frac{u_B}{V_\infty}(x_B, y_B, z_B) &= \frac{u_{B,a}}{U_{s\infty}} \frac{U_{s\infty}}{V_\infty} \\ \frac{v_B}{V_\infty}(x_B, y_B, z_B) &= \frac{v_{B,a}}{U_{s\infty}} \frac{U_{s\infty}}{V_\infty} \\ \frac{w_B}{V_\infty}(x_B, y_B, z_B) &= \frac{w_{B,a}}{U_{s\infty}} \frac{U_{s\infty}}{V_\infty} \end{aligned} \right\} \quad (A-33)$$

Note that these perturbation velocities are expressed in terms of the axial, radial, and tangential components aligned with the cylindrical coordinate system (x_B, r_B, θ) indicated in the sketch of Section A-2.1. Also, the reference velocity is the one actually seen by the store, V_∞ , mentioned earlier. Terms subscripted with "a" pertain to the volume effects of the store (axial solution) and are given by Equation (A-15). In that equation, the reference velocity, $U_{s\infty}$, must be scaled up to V_∞ as shown in Equation (A-33).

At this stage, the perturbation velocities specified in Equation (A-33) include effects of the store volume. However, at the point (x_B, y_B, z_B) on the body, a net flow normal to the surface exists which must be counteracted by additional singularities distributed along the store body axis. Their contributions will be discussed in the next section.

A-3.2 Effects Due to Crossflow

The line sources distributed along the store axis satisfy the condition of no flow through the body surface provided the store is aligned with the flow. This case is dealt with in the previous section. In general, the store is not aligned and therefore subjected to crossflow as well. In order to cancel flow normal to its surface, line doublets are distributed along the store axis in addition to the line sources.

The crossflow is associated with the nonuniform, supersonic flow field induced by the parent aircraft in which the store is immersed. It includes effects of store pitch and yaw damping. In addition, store translational velocities are accounted for in the specification of the crossflow. All these contributions are combined into a crossflow velocity vector whose variation with distance x_B along the store axis can be specified. This vector can be resolved into components along the z_B and y_B axes of the store resulting in upwash component, $W(x_B)$, and sidewash component, $V(x_B)$. Subject to these crossflow velocity components, the strengths of the line doublets for upwash and sidewash are then determined using the methods described in detail in Section A.2.3.

At a point (x_B, y_B, z_B) on the surface of the store, the perturbation velocities induced by the upwash and sidewash doublets are calculated using Equations (A-24) for u_B, d_W , v_B, d_W , and w_B, d_W and Equation (A-32) for u_B, d_V , v_B, d_V , and w_B, d_V . They are added to the store volume perturbation velocities to give

$$\left. \begin{aligned}
 \frac{u_B}{V_\infty} (x_B, y_B, z_B) &= \frac{u_{B,a}}{V_\infty} + \frac{u_{B,d_W}}{V_\infty} + \frac{u_{B,d_V}}{V_\infty} \\
 \frac{v_B}{V_\infty} (x_B, y_B, z_B) &= \frac{v_{B,a}}{V_\infty} + \frac{v_{B,d_W}}{V_\infty} + \frac{v_{B,d_V}}{V_\infty} \\
 \frac{w_B}{V_\infty} (x_B, y_B, z_B) &= \frac{w_{B,a}}{V_\infty} + \frac{w_{B,d_W}}{V_\infty} + \frac{w_{B,d_V}}{V_\infty}
 \end{aligned} \right\} \quad (A-34)$$

Components (u_B, v_B, w_B) are the axial, radial, and tangential velocity components in the cylindrical coordinate system shown in the sketch of Section A-2.1. For use in the Bernoulli pressure equation, to be described next, these perturbation velocity components will be transformed into the components aligned with the rectangular coordinate system (x_B, y_B, z_B) . The reference velocity, V_∞ , is the free-stream velocity as seen by the store. As mentioned before in connection with Equation (A-33), the perturbation velocities induced by the line sources and sinks associated with the store volume are given by Equation (A-15), but the reference velocity must be scaled up to V_∞ as indicated in Equation (A-33).

A-3.3 Pressure Coefficient Calculation

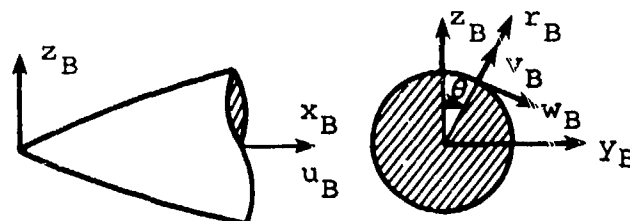
At a point (x_B, y_B, z_B) on the surface of the store, the pressure coefficient is calculated using the Bernoulli relationship. For compressible, isentropic flow, the Bernoulli equation is given by

$$C_P = \frac{p - p_\infty}{\frac{1}{2} \rho_\infty V_\infty^2} = \frac{2}{\gamma M_\infty^2} \left\{ \left[1 + \frac{\gamma - 1}{2} M_\infty^2 \left(1 - \frac{V^2}{V_\infty^2} \right) \right]^{\gamma/\gamma-1} - 1 \right\} \quad (A-35)$$

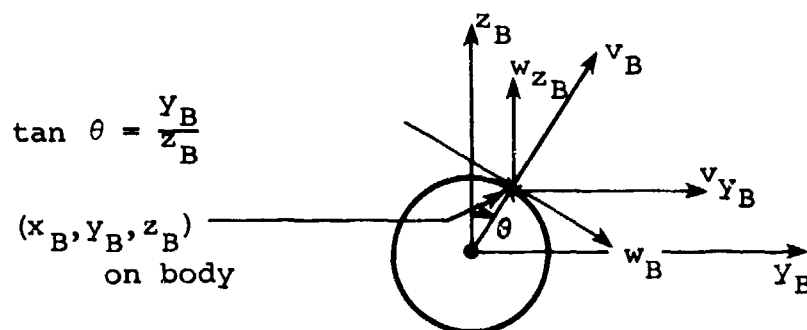
The ratio of specific heats for air is γ and equals 1.4. Reference velocity, V_∞ , and Mach number, M_∞ , are as seen by the

store at infinity. The magnitude of the resultant velocity, V , at a point on the body surface can be obtained in the following manner.

The perturbation velocities are now known at the point (x_B, y_B, z_B) on the surface of the store through Equation (A-34) in terms of components aligned with the cylindrical coordinate system (x_B, r_B, θ) attached to the store as shown in the sketch of Section A-2.1 and repeated below for convenience. A transformation converts the perturbation velocity components of Equation (A-34) into components aligned with rectangular coordinate system



(x_B, y_B, z_B) with origin at the store nose and directions along the major axes of the store also shown in the sketch above. Longitudinal component u_B remains as is. Let v_{y_B} and w_{z_B} denote the perturbation velocity components in the y_B and z_B directions, respectively. As such, all three perturbation



velocity components are specified in a body axis coordinate system (as opposed to the wind axis system aligned with the free-stream direction). Components v_{y_B} and w_{z_B} are related to v_B and w_B as follows.

$$\left. \begin{aligned} \frac{u_{x_B}}{V_\infty} &= \frac{u_B}{V_\infty} \\ \frac{v_{y_B}}{V_\infty} &= \frac{v_B}{V_\infty} \sin \theta + \frac{w_B}{V_\infty} \cos \theta \\ \frac{w_{z_B}}{V_\infty} &= \frac{v_B}{V_\infty} \cos \theta - \frac{w_B}{V_\infty} \sin \theta \end{aligned} \right\} \quad (A-36)$$

The perturbation velocities specified in the above equation are now specified in the cartesian, body coordinate system. The magnitude of the resultant velocity, V , required in Equation (A-35) can be expressed in terms of the perturbation velocities in the body axis system by the following equation.

$$\begin{aligned} \frac{V^2}{V_\infty^2} &= 1 + \frac{2u_{x_B}}{V_\infty} \cos \alpha_{c,s} - \frac{2v_{y_B}}{V_\infty} \sin \beta_s \\ &\quad + \frac{2w_{z_B}}{V_\infty} \sin \alpha_s + \frac{u_{x_B}^2 + v_{y_B}^2 + w_{z_B}^2}{V_\infty^2} \end{aligned} \quad (A-37)$$

Angles $\alpha_{c,s}$, β_s , and α_s are the included angle of attack, side-slip angle, and pitch angle, respectively, associated with the store. In accordance with page 5 of Reference 19, the angles can be related to the components along the body coordinate system of the free-stream velocity, V_∞ , as seen by the store.

$$\left. \begin{aligned}
 \sin \alpha_s &= \frac{W_{s,\infty}}{V_\infty} \\
 \sin \beta_s &= \frac{-V_{s,\infty}}{V_\infty} \\
 \sin^2 \alpha_{c,s} &= \sin^2 \alpha_s + \sin^2 \beta_s
 \end{aligned} \right\} \quad (A-38)$$

Special care must be taken with the term inside the square brackets in Equation (A-35) and raised to the power $\gamma/(\gamma - 1)$. It is possible that numerical inaccuracies can occur in the determination of the perturbation velocities. In certain cases, the inaccuracies can cause the bracketed term to be negative resulting in a negative pressure in the flow. This is physically impossible and the bracketed term must therefore be limited to values which are equal to or larger than zero.

A-3.4 Loading Distributions Along the Store Axis

At a given axial location, the pressure coefficients are calculated at points on the circumference of a cross section of the store body using the method described above. In terms of length x_B along the store axis from the nose, and the store frontal area as reference area, expressions for the rate of change of normal and side force with the axial length can be written. The normal and side forces act along the z_B and y_B axes, respectively.

$$\left. \begin{aligned}
 \frac{dC_N}{dx_B} &= - \frac{r(x_B)}{S_{ref}} \int_0^{2\pi} C_p \cos \theta \, d\theta \\
 \frac{dC_Y}{dx_B} &= - \frac{r(x_B)}{S_{ref}} \int_0^{2\pi} C_p \sin \theta \, d\theta
 \end{aligned} \right\} \quad (A-39)$$

In these expressions, angle θ (radians) is as shown in the previous sketch and is positive clockwise from the positive z_B axis.

The distributions of pitching and yawing moments are given by

$$\left. \begin{aligned} \frac{dC_m}{dx_B} &= - \frac{x_B - x_m}{d} \frac{dC_N}{dx_B} \\ \frac{dC_n}{dx_B} &= - \frac{x_B - x_m}{d} \frac{dC_Y}{dx_B} \end{aligned} \right\} \quad (A-40)$$

In Equation (A-40), d is the maximum diameter of the store and x_m is the location on the body axis of the moment center.

Due to the nonlinear dependence of the pressure coefficient on the resultant velocity, V , analytical integration of Equation (A-39) is laborious but not necessarily impossible. It is convenient to integrate Equation (A-39) numerically. At a finite number of discrete points on the circumference of a body cross section, the pressure coefficient is calculated from the perturbation velocities by means of Equations (A-35) and (A-37). The products $C_p \cos \theta$ and $C_p \sin \theta$ are formed at the discrete points. An integration scheme based on a Simpson's rule takes in the products and the $\Delta \theta$ interval between points and provides the numerical answers.

A-3.5 Overall Forces and Moments Acting on the Store

The overall force and moment coefficients can be determined by multiplying Equations (A-39) and (A-40) by Δx_B and summing over the length of the body. The interval Δx_B is given by the spacing between the axial stations at which the loading distributions are calculated. Thus, the normal-force, side-force, pitching-moment and yawing-moment coefficients are then given by the following expressions, respectively.

$$\left. \begin{aligned}
 C_N &= \sum_{i=1}^N \left. \frac{dC_N}{dx_B} \right|_i \Delta x_{B_i} \\
 C_Y &= \sum_{i=1}^N \left. \frac{dC_Y}{dx_B} \right|_i \Delta x_{B_i} \\
 C_m &= \sum_{i=1}^N \left. \frac{dC_m}{dx_B} \right|_i \Delta x_{B_i} \\
 C_n &= \sum_{i=1}^N \left. \frac{dC_n}{dx_B} \right|_i \Delta x_{B_i}
 \end{aligned} \right\} \quad (A-41)$$

where N is the number of axial stations on the body centerline at which the circumferential pressure distributions are calculated.

APPENDIX B

EQUATIONS OF MOTION OF A RIGID BODY WITH MASS AND INERTIA ASYMMETRIES

B-1 INTRODUCTION

The purpose of this appendix is to present the derivation of the equations of motion of a rigid body, the store, with mass and inertia asymmetries. By mass asymmetry we mean that the center of mass is not at the origin of the coordinate system fixed in the body and used in the equations of motion. Generally the external store will have axes of geometrical symmetry which will be used in determining the forces and moments acting on it, but the center of mass in certain applications will not lie on these axes of symmetry. By inertia asymmetry, we mean that the principal axes of inertia do not coincide with the geometric axes of symmetry of the store. For these geometric axes, the tensor of inertia will thus possess off-diagonal terms, the so-called products of inertia.

B-2 AXIS SYSTEMS AND EULERIAN ANGLES

In the derivation of the equations of motion consider first an inertial set of axes, (ξ, η, ζ) , fixed in the aircraft which is in rectilinear flight at uniform velocity. Then a system of axes (x, y, z) fixed in the store is defined. The x axis is forward along the store longitudinal axis, the y axis is positive to the right looking forward, and the z axis is vertical downward so that a right-handed system exists. The ξ, η, ζ system is an airplane fixed system with ξ measured forward along the fuselage longitudinal axis, η laterally to the right and, ζ vertically downward. The origin is at the fuselage nose.

In order to determine the orientation of the store with respect to the ξ, η, ζ axes, a system of angles will be introduced. The system of angles to be used is that shown in Figure 14. The origins of the inertial and store axis systems are taken at the same point to show the angular orientation. The system consists of three rotations in the yaw, pitch, roll sequence. This order is important. The three angles will be designated

Ψ yaw
 Θ pitch
 Φ roll

B-3 DIFFERENTIAL EQUATIONS FOR THE ORIENTATION ANGLES

In specifying the position and orientation of the store relative to the aircraft, we will determine the coordinates ξ , η , and ζ of the origin of the x , y , z coordinate system and the angular quantities Ψ , θ , and ϕ . The equations of motion will, however, be written in terms of the following quantities and their time derivatives: ξ , η , ζ , p , q , r . Here p , q , and r are the components of the store angular velocity about the x , y , and z axes, respectively. A set of differential equations is required for Ψ , θ , and ϕ in terms of p , q , and r which are to be integrated along with the equations of motion to keep track of the angular orientation of the store. These equations are from Reference 16.

$$\left. \begin{aligned} \dot{\Psi} &= (q \sin \phi + r \cos \phi) / \cos \theta \\ \dot{\theta} &= q \cos \phi - r \sin \phi \\ \dot{\phi} &= p + q \sin \phi \tan \theta + r \cos \phi \tan \theta \end{aligned} \right\} \quad (B-1)$$

With initial values of the orientation parameters Ψ , θ , and ϕ , the foregoing equation can be integrated to obtain the variations of these quantities with time.

From the values of Ψ , θ , and ϕ it is possible to determine the orientation of the x , y , z axes with respect to the ξ , η , ζ in the usual direction cosine way. That is

$$\begin{bmatrix} \xi \\ \eta \\ \zeta \end{bmatrix} = [A] \begin{bmatrix} x \\ y \\ z \end{bmatrix}$$

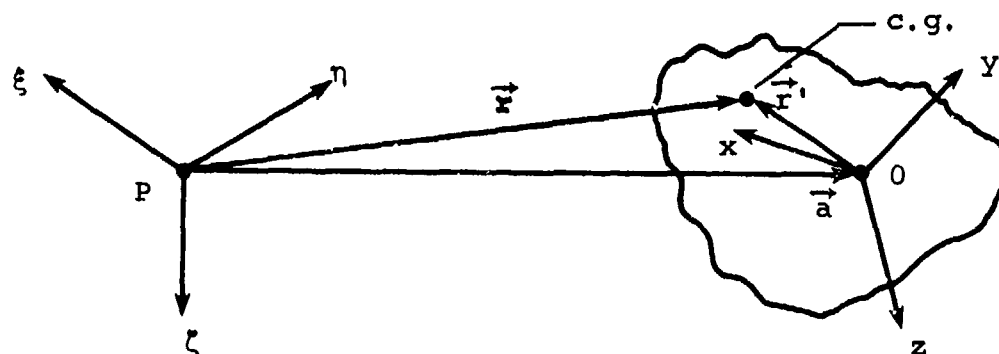
where (Reference 16)

$$[A] = \begin{bmatrix} \cos \theta \cos \psi & \sin \phi \sin \theta \cos \psi & \cos \phi \sin \theta \cos \psi \\ \cos \theta \sin \psi & \sin \phi \sin \theta \sin \psi & \cos \phi \sin \theta \sin \psi \\ -\sin \theta & \sin \phi \cos \theta & \cos \phi \cos \theta \end{bmatrix} \quad (B-2)$$

These data are also necessary in converting forces calculated in the x, y, z system to the ξ, η, ζ system.

B-4 TRANSLATIONAL EQUATIONS OF MOTION

We will now write the equations of motion for translation of the origin of the x, y, z body axes. The origin is not assumed to be at the body center of mass. Consider the following sketch.



Let \vec{a} be the vector from the origin of the inertial system point P , to the origin of the body system, point O . Let \vec{r}' be the vector from the origin of the body axes to the body center of mass.

$$\vec{r}' = \vec{e}_x \bar{x} + \vec{e}_y \bar{y} + \vec{e}_z \bar{z} \quad (\text{B-3})$$

Let \vec{r} be the vector from the origin of the inertial system to the body center of mass. Then

$$\vec{r} = \vec{a} + \vec{r}' \quad (\text{B-4})$$

If \vec{F} is the vector force acting on the body the equation of translational motion is

$$\vec{F} = m \frac{d^2 \vec{r}}{dt^2} \quad (\text{B-5})$$

This equation will now be expressed in terms of the force components (F_x, F_y, F_z) along x, y , and z ; the position coordinates

$(\bar{x}, \bar{y}, \bar{z})$ of the body center of mass; and the components of the body angular velocity $\vec{\omega}$ given by

$$\vec{\omega} = \vec{e}_x \dot{p} + \vec{e}_y \dot{q} + \vec{e}_z \dot{r} \quad (B-6)$$

To establish the acceleration vector Equation (B-4) is differentiated with respect to time

$$\frac{d\vec{r}}{dt} = \frac{d\vec{a}}{dt} + \frac{d\vec{r}'}{dt} \quad (B-7)$$

$$= \frac{d\vec{a}}{dt} + \vec{\omega} \times \vec{r}' \quad (B-8)$$

Differentiating again yields

$$\frac{d^2\vec{r}}{dt^2} = \frac{d^2\vec{a}}{dt^2} + \frac{d\vec{\omega}}{dt} \times \vec{r}' + \vec{\omega} \times \frac{d\vec{r}'}{dt} \quad (B-9)$$

Since

$$\frac{d\vec{\omega}}{dt} = \vec{e}_x \ddot{p} + \vec{e}_y \ddot{q} + \vec{e}_z \ddot{r} \quad (B-10)$$

we find

$$\begin{aligned} \frac{d^2\vec{r}}{dt^2} &= \frac{d^2\vec{a}}{dt^2} + (\vec{e}_x \ddot{p} + \vec{e}_y \ddot{q} + \vec{e}_z \ddot{r}) \times \vec{r}' + \vec{\omega} \times (\vec{\omega} \times \vec{r}') \\ &= \frac{d^2\vec{a}}{dt^2} + (\vec{e}_x \ddot{p} + \vec{e}_y \ddot{q} + \vec{e}_z \ddot{r}) \times \vec{r}' + \vec{\omega}(\vec{\omega} \cdot \vec{r}') - \vec{r}'(\vec{\omega} \cdot \vec{\omega}) \end{aligned}$$

or

$$\begin{aligned} \frac{d^2\vec{r}}{dt^2} &= \frac{d^2\vec{a}}{dt^2} + \vec{e}_x \left[(pq - \dot{r})\bar{y} + (pr + \dot{q})\bar{z} - \bar{x}(q^2 + r^2) \right] \\ &\quad + \vec{e}_y \left[(pq + \dot{r})\bar{x} + (qr - \dot{p})\bar{z} - \bar{y}(p^2 + r^2) \right] \\ &\quad + \vec{e}_z \left[(pr - \dot{q})\bar{x} + (qr + \dot{p})\bar{y} - \bar{z}(p^2 + q^2) \right] \quad (B-11) \end{aligned}$$

which from Equation (B-5) is equal to

$$\frac{d^2 \vec{r}}{dt^2} = \frac{1}{m} \left[F_x \vec{e}_x + F_y \vec{e}_y + F_z \vec{e}_z \right] \quad (\text{B-12})$$

The acceleration of O relative to P can be expressed in terms of the moving body coordinate system as follows:

$$\frac{d^2 \vec{a}}{dt^2} = \ddot{x}_O \vec{e}_x + \ddot{y}_O \vec{e}_y + \ddot{z}_O \vec{e}_z + \vec{\omega} \times \frac{d\vec{a}}{dt} \quad (\text{B-13})$$

where $\frac{d\vec{a}}{dt}$ is the velocity of O relative to P and may be expressed in terms of components along the moving body coordinate system \dot{x}_O , \dot{y}_O , and \dot{z}_O . The body angular velocity $\vec{\omega}$ is given by Equation (B-6). Therefore

$$\begin{aligned} \frac{d^2 \vec{a}}{dt^2} = & \ddot{x}_O \vec{e}_x + \ddot{y}_O \vec{e}_y + \ddot{z}_O \vec{e}_z + (\dot{q}\dot{z}_O - \dot{y}_O r) \vec{e}_x \\ & + (\dot{x}_O r - p\dot{z}_O) \vec{e}_y + (p\dot{y}_O - \dot{x}_O q) \vec{e}_z \end{aligned} \quad (\text{B-14})$$

Combining Equations (B-11), (B-12), and (B-14) gives

$$\begin{aligned} \ddot{x}_O + (\dot{q}\dot{z}_O - r\dot{y}_O) &= \frac{F_x}{m} - \left[-(q^2 + r^2)\bar{x} + (pq - \dot{r})\bar{y} + (pr + \dot{q})\bar{z} \right] \\ \ddot{y}_O + (r\dot{x}_O - p\dot{z}_O) &= \frac{F_y}{m} - \left[(pq + \dot{r})\bar{x} - (p^2 + r^2)\bar{y} + (qr - \dot{p})\bar{z} \right] \\ \ddot{z}_O + (p\dot{y}_O - q\dot{x}_O) &= \frac{F_z}{m} - \left[(pr - \dot{q})\bar{x} + (qr + \dot{p})\bar{y} - (p^2 + q^2)\bar{z} \right] \end{aligned} \quad (\text{B-15})$$

The accelerations along the inertial axes are then

$$\begin{bmatrix} \ddot{\xi} \\ \ddot{\eta} \\ \ddot{\zeta} \end{bmatrix} = [A] \begin{bmatrix} \ddot{x}_0 + (q\dot{z}_0 - r\dot{y}_0) \\ \ddot{y}_0 + (r\dot{x}_0 - p\dot{z}_0) \\ \ddot{z}_0 + (p\dot{y}_0 - q\dot{x}_0) \end{bmatrix}$$

where the transformation matrix is given by Equation (B-2).

The final equations of translational motion in the inertial coordinate system are now written using the following direction cosine notation for the [A] matrix of Equation (B-2)

$$[A] = \begin{bmatrix} \cos(\xi, x) & \cos(\xi, y) & \cos(\xi, z) \\ \cos(\eta, x) & \cos(\eta, y) & \cos(\eta, z) \\ \cos(\zeta, x) & \cos(\zeta, y) & \cos(\zeta, z) \end{bmatrix}$$

$$\begin{aligned} \ddot{\xi} &+ \left[\bar{y} \cos(\xi, z) - \bar{z} \cos(\xi, y) \right] \dot{p} + \left[\bar{z} \cos(\xi, x) - \bar{x} \cos(\xi, z) \right] \dot{q} \\ &+ \left[\bar{x} \cos(\xi, y) - \bar{y} \cos(\xi, x) \right] \dot{r} \end{aligned}$$

$$\begin{aligned} &= \left[\frac{F_x}{m} + \bar{x}(q^2 + r^2) - \bar{y}pq - \bar{z}pr \right] \cos(\xi, x) \\ &+ \left[\frac{F_y}{m} - \bar{x}pq + \bar{y}(p^2 + r^2) - \bar{z}qr \right] \cos(\xi, y) \\ &+ \left[\frac{F_z}{m} - \bar{x}pr - \bar{y}qr + \bar{z}(p^2 + q^2) \right] \cos(\xi, z) \end{aligned}$$

(B-16)

$$\begin{aligned}
\ddot{\eta} &+ \left[\bar{y} \cos (\eta, z) - \bar{z} \cos (\eta, y) \right] \dot{p} + \left[\bar{z} \cos (\eta, x) - \bar{x} \cos (\eta, z) \right] \dot{q} \\
&+ \left[\bar{x} \cos (\eta, y) - \bar{y} \cos (\eta, x) \right] \dot{r} \\
&= \left[\frac{F_x}{m} + \bar{x}(q^2 + r^2) - \bar{y}pq - \bar{z}pr \right] \cos (\eta, x) \\
&+ \left[\frac{F_y}{m} - \bar{x}pq + \bar{y}(p^2 + r^2) - \bar{z}qr \right] \cos (\eta, y) \\
&+ \left[\frac{F_z}{m} - \bar{x}pr - \bar{y}qr + \bar{z}(p^2 + q^2) \right] \cos (\eta, z)
\end{aligned}$$

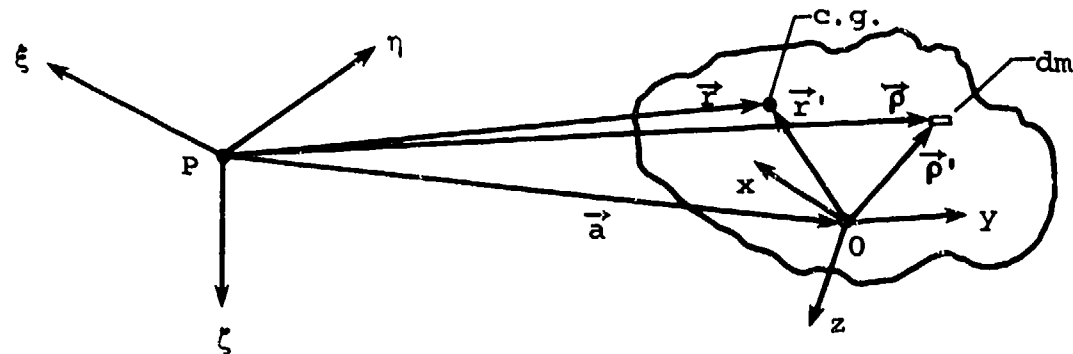
(B-17)

$$\begin{aligned}
\ddot{\zeta} &+ \left[\bar{y} \cos (\zeta, z) - \bar{z} \cos (\zeta, y) \right] \dot{p} + \left[\bar{z} \cos (\zeta, x) - \bar{x} \cos (\zeta, z) \right] \dot{q} \\
&+ \left[\bar{x} \cos (\zeta, y) - \bar{y} \cos (\zeta, x) \right] \dot{r} \\
&= \left[\frac{F_x}{m} + \bar{x}(q^2 + r^2) - \bar{y}pq - \bar{z}pr \right] \cos (\zeta, x) \\
&+ \left[\frac{F_y}{m} - \bar{x}pq + \bar{y}(p^2 + r^2) - \bar{z}qr \right] \cos (\zeta, y) \\
&+ \left[\frac{F_z}{m} - \bar{x}pr + \bar{y}qr + \bar{z}(p^2 + q^2) \right] \cos (\zeta, z)
\end{aligned}$$

(B-18)

B-5 EQUATIONS OF ROTATIONAL MOTION

The equations of rotational motion will be written in terms of body axes because the moments and products of inertia are not functions of time in these axes. Also, the moments due to aerodynamic forces are calculated in this axis system which is an additional convenience. Consider a general body with axes x, y, z having its origin at point O and an inertial system ξ, η, ζ having its origin at point P . Let $\vec{\rho}$ be the position vector of an element of mass in the inertial system and $\vec{\rho}'$ be the position vector in the body system.



Let \vec{L}_P be the torque of the forces acting on the body with respect to point P . Then the law of the conservation of angular momentum in inertial coordinates is

$$\vec{L}_P = \frac{d\vec{H}_P}{dt} \quad (B-19)$$

where the angular momentum vector is given by

$$\vec{H}_P = \int \vec{\rho} \times \frac{d\vec{\rho}}{dt} dm \quad (B-20)$$

the integral being taken over the body mass.

For the store the origin O , of the body system, will generally be offset from the body center of gravity by position vector

\vec{r}' , and the tensor of inertia for the x, y, z axes will generally contain products of inertia. The torque will be known with respect to the origin O, and the angular velocity is given by Equation (B-6) in terms of components p, q, and r in body axes. We will now transform Equation (B-19) to body axes in terms of the foregoing quantities. The angular momentum becomes

$$\vec{H}_p = \int (\vec{a} + \vec{\rho}') \times \frac{d}{dt} (\vec{a} + \vec{\rho}') dm \quad (B-21)$$

Let

$$\vec{H}_o \equiv \int \vec{\rho}' \times \frac{d\vec{\rho}'}{dt} dm \quad (B-22)$$

so that

$$\vec{H}_p = \vec{a} \times \int \frac{d\vec{\rho}}{dt} dm + \int \vec{\rho}' \times \frac{d\vec{a}}{dt} dm + \vec{H}_o$$

and

$$\begin{aligned} \frac{d}{dt} \vec{H}_p &= \vec{a} \times \int \frac{d^2 \vec{\rho}}{dt^2} dm + \frac{d\vec{a}}{dt} \times \int \frac{d\vec{\rho}}{dt} dm + \frac{d\vec{H}_o}{dt} \\ &\quad + \int \frac{d\vec{\rho}'}{dt} dm \times \frac{d\vec{a}}{dt} + \int \vec{\rho}' dm \times \frac{d^2 \vec{a}}{dt^2} \end{aligned} \quad (B-23)$$

Certain simplifications arise in the foregoing expression from the property of the center of mass

$$\int (\vec{\rho}' - \vec{r}') dm = 0 \quad (B-24)$$

so that

$$\int \vec{\rho}' dm = \vec{r}' m \quad (B-25)$$

and

$$\int \frac{d\vec{\rho}'}{dt} dm = \frac{d}{dt} \int \vec{\rho}' dm = m \frac{d\vec{r}'}{dt} \quad (B-26)$$

Also

$$\begin{aligned}
 \frac{d^2 \vec{p}}{dt^2} dm &= \frac{d^2}{dt^2} \int \vec{p}' dm + \frac{d^2}{dt^2} \int \vec{a} dm \\
 &= m \frac{d^2 \vec{r}'}{dt^2} + m \frac{d^2 \vec{a}}{dt^2} \\
 &= m \frac{d}{dt} (\vec{\omega} \times \vec{r}') + m \frac{d^2 \vec{a}}{dt^2} \\
 &= m \left[\vec{\omega} \times \frac{d\vec{r}'}{dt} + \frac{d\vec{\omega}}{dt} \times \vec{r}' + \frac{d^2 \vec{a}}{dt^2} \right] \\
 &= m \frac{d^2 \vec{r}}{dt^2} = \vec{F} \tag{B-27}
 \end{aligned}$$

Accordingly, we find from Equation (B-19) that

$$\vec{L}_p = \vec{a} \times \vec{F} + m \frac{d\vec{a}}{dt} \times \left(\frac{d\vec{a}}{dt} + \frac{d\vec{r}'}{dt} \right) + m \frac{d\vec{r}'}{dt} \times \frac{d\vec{a}}{dt} + m \vec{r}' \times \frac{d^2 \vec{a}}{dt^2} + \frac{d\vec{H}_o}{dt}$$

which becomes

$$\vec{L}_p = \vec{a} \times \vec{F} + m \vec{r}' \times \frac{d^2 \vec{a}}{dt^2} + \frac{d\vec{H}_o}{dt} \tag{B-28}$$

Now define

$$\vec{L}_o = m \vec{r}' \times \frac{d^2 \vec{a}}{dt^2} + \frac{d\vec{H}_o}{dt} \tag{B-29}$$

where \vec{L}_o is the torque with respect to the O origin so that

$$\vec{L}_o = \vec{L}_p - \vec{a} \times \vec{F} \tag{B-30}$$

Equation (B-29) for the conservation of angular momentum with respect to origin O has the same form as that with respect to origin P plus an additional term.

With regard to the three terms of Equation (B-29), the torque \vec{L}_O will have three components along the x, y, z axes

$$\vec{L}_O = \vec{e}_x M_x + \vec{e}_y M_y + \vec{e}_z M_z \quad (B-31)$$

The acceleration vector $d^2\vec{a}/dt^2$ has components ξ , η , and ζ which can be related to the components of $d^2\vec{a}/dt^2$ given by Equation (B-14) as follows

$$\left. \begin{aligned} \ddot{x}_O + (q\dot{z}_O - r\dot{y}_O) &= \xi \cos(x, \xi) + \eta \cos(x, \eta) + \zeta \cos(x, \zeta) \\ \ddot{y}_O + (r\dot{x}_O - p\dot{z}_O) &= \xi \cos(y, \xi) + \eta \cos(y, \eta) + \zeta \cos(y, \zeta) \\ \ddot{z}_O + (p\dot{y}_O - q\dot{x}_O) &= \xi \cos(z, \xi) + \eta \cos(z, \eta) + \zeta \cos(z, \zeta) \end{aligned} \right\} \quad (B-32)$$

The direction cosines in the above equation are obtained from the transpose of [A], Equation (B-2).

With the following notation

$$\vec{r}' = \vec{e}_x \bar{x} + \vec{e}_y \bar{y} + \vec{e}_z \bar{z} \quad (B-33)$$

and Equation (B-14) we have

$$\begin{aligned} m\vec{r}' \times \frac{d^2\vec{a}}{dt^2} &= m\vec{e}_x \left[\bar{y}(\ddot{z}_O + p\dot{y}_O - q\dot{x}_O) - \bar{z}(\ddot{y}_O + r\dot{x}_O - p\dot{z}_O) \right] \\ &+ m\vec{e}_y \left[\bar{z}(\ddot{x}_O + q\dot{z}_O - r\dot{y}_O) - \bar{x}(\ddot{z}_O + p\dot{y}_O - q\dot{x}_O) \right] \\ &+ m\vec{e}_z \left[\bar{x}(\ddot{y}_O + r\dot{x}_O - p\dot{z}_O) - \bar{y}(\ddot{x}_O + q\dot{z}_O - r\dot{y}_O) \right] \end{aligned} \quad (B-34)$$

With regard to the remaining term in Equation (B-29), we have from Equation (B-22)

$$\frac{d\vec{H}_O}{dt} = \frac{d}{dt} \int \vec{\rho}' \times \frac{d\vec{\rho}'}{dt} dm$$

We first evaluate \vec{H}_O and then differentiate

$$\begin{aligned} \vec{H}_O &= \int \vec{\rho}' \times \frac{d\vec{\rho}'}{dt} dm = \int \vec{\rho}' \times (\vec{\omega} \times \vec{\rho}') dm = \int [\vec{\omega}(\vec{\rho}' \cdot \vec{\rho}') - \vec{\rho}'(\vec{\rho}' \cdot \vec{\omega})] dm \\ &= \int \vec{\omega}(x^2 + y^2 + z^2) dm - \int (\vec{e}_x x + \vec{e}_y y + \vec{e}_z z)(px + qy + rz) dm \\ &= \vec{e}_x \left[p \int (y^2 + z^2) dm - q \int xy dm - r \int xz dm \right] \\ &\quad + \vec{e}_y \left[-p \int xy dm + q \int (x^2 + z^2) dm - r \int yz dm \right] \\ &\quad + \vec{e}_z \left[-p \int xz dm - q \int yz dm + r \int (x^2 + y^2) dm \right] \end{aligned} \quad (B-35)$$

The moments and products of inertia are defined as follows:

$$\left. \begin{aligned} I_{xx} &= \int (y^2 + z^2) dm & I_{xy} &= \int xy dm \\ I_{yy} &= \int (x^2 + z^2) dm & I_{xz} &= \int xz dm \\ I_{zz} &= \int (x^2 + y^2) dm & I_{yz} &= \int yz dm \end{aligned} \right\} \quad (B-36)$$

so that Equation (B-35) becomes

$$\begin{aligned} \vec{H}_O &= \vec{e}_x [pI_{xx} - qI_{xy} - rI_{xz}] \\ &\quad + \vec{e}_y [-pI_{xy} + qI_{yy} - rI_{yz}] \\ &\quad + \vec{e}_z [-pI_{xz} - qI_{yz} + rI_{zz}] \end{aligned} \quad (B-37)$$

In body coordinates the moments and products of inertia are not functions of time for a rigid body. With the help of the relationships

$$\left. \begin{aligned} \frac{d\vec{e}_x}{dt} &= \vec{e}_y r - \vec{e}_z q = \vec{\omega} \times \vec{e}_x \\ \frac{d\vec{e}_y}{dt} &= \vec{e}_z p - \vec{e}_x r = \vec{\omega} \times \vec{e}_y \\ \frac{d\vec{e}_z}{dt} &= \vec{e}_x q - \vec{e}_y p = \vec{\omega} \times \vec{e}_z \end{aligned} \right\} \quad (B-38)$$

we find

$$\begin{aligned} \frac{d\vec{H}_c}{dt} &= \vec{e}_x \left[\dot{p}I_{xx} - \dot{q}I_{xy} - \dot{r}I_{xz} + rq(I_{zz} - I_{yy}) \right. \\ &\quad \left. - (q^2 - r^2)I_{yz} - p(qI_{xz} - rI_{xy}) \right] \\ &\quad + \vec{e}_y \left[-\dot{p}I_{xy} + \dot{q}I_{yy} - \dot{r}I_{yz} + rp(I_{xx} - I_{zz}) \right. \\ &\quad \left. - (r^2 - p^2)I_{xz} - q(rI_{xy} - pI_{yz}) \right] \\ &\quad + \vec{e}_z \left[-\dot{p}I_{xz} - \dot{q}I_{yz} + \dot{r}I_{zz} + pq(I_{yy} - I_{xx}) \right. \\ &\quad \left. - (p^2 - q^2)I_{xy} - r(pI_{yz} - qI_{xz}) \right] \end{aligned} \quad (B-39)$$

Equating the components of Equation (B-31) to the sum of Equations (B-34) and (B-39) yields the three desired equations of rotational motion

$$M_x = m \left[\bar{y}(\ddot{z}_0 + p\dot{y}_0 - q\dot{x}_0) - \bar{z}(\ddot{y}_0 + r\dot{x}_0 - p\dot{z}_0) \right] + \dot{p}I_{xx} - \dot{q}I_{xy} - \dot{r}I_{xz} \\ + rq(I_{zz} - I_{yy}) - (q^2 - r^2)I_{yz} - p(qI_{xz} - rI_{xy})$$

$$M_y = m \left[\bar{z}(\ddot{x}_0 + q\dot{z}_0 - r\dot{y}_0) - \bar{x}(\ddot{z}_0 + p\dot{y}_0 - q\dot{x}_0) \right] - \dot{p}I_{xy} + \dot{q}I_{yy} - \dot{r}I_{yz} \\ + rp(I_{xx} - I_{zz}) - (r^2 - p^2)I_{xz} - q(rI_{xy} - pI_{yz})$$

$$M_z = m \left[\bar{x}(\ddot{y}_0 + r\dot{x}_0 - p\dot{z}_0) - \bar{y}(\ddot{x}_0 + q\dot{z}_0 - r\dot{y}_0) \right] - \dot{p}I_{xz} - \dot{q}I_{yz} + \dot{r}I_{zz} \\ + pq(I_{yy} - I_{xx}) - (p^2 - q^2)I_{xy} - r(pI_{yz} - qI_{xz})$$

(B-40)

The rotational equations of motion in the inertial coordinate system, using Equation (B-32), are

$$m \left[\bar{y} \cos(z, \xi) - \bar{z} \cos(y, \xi) \right] \ddot{\xi} + m \left[\bar{y} \cos(z, \eta) - \bar{z} \cos(y, \eta) \right] \ddot{\eta} \\ + m \left[\bar{y} \cos(z, \zeta) - \bar{z} \cos(y, \zeta) \right] \ddot{\zeta} + I_{xx}\dot{p} - I_{xy}\dot{q} - I_{xz}\dot{r} \\ = M_x - rq(I_{zz} - I_{yy}) + (q^2 - r^2)I_{yz} + p(qI_{xz} - rI_{xy})$$

(B-41)

$$m \left[\bar{z} \cos(x, \xi) - \bar{x} \cos(z, \xi) \right] \ddot{\xi} + m \left[\bar{z} \cos(x, \eta) - \bar{x} \cos(z, \eta) \right] \ddot{\eta} \\ + m \left[\bar{z} \cos(x, \zeta) - \bar{x} \cos(z, \zeta) \right] \ddot{\zeta} - I_{xy}\dot{p} + I_{yy}\dot{q} - I_{yz}\dot{r} \\ = M_y - rp(I_{xx} - I_{zz}) + (r^2 - p^2)I_{xz} + q(rI_{xy} - pI_{yz})$$

(B-42)

$$m \left[\bar{x} \cos (y, \xi) - \bar{y} \cos (x, \xi) \right] \ddot{\xi} + m \left[\bar{x} \cos (y, \eta) - \bar{y} \cos (x, \eta) \right] \ddot{\eta}$$

$$+ m \left[\bar{x} \cos (y, \zeta) - \bar{y} \cos (x, \zeta) \right] \ddot{\zeta} - I_{xz} \dot{p} - I_{yz} \dot{q} + I_{zz} \dot{r}$$

$$= M_z - pq(I_{yy} - I_{xx}) + (p^2 - q^2)I_{xy} + r(pI_{yz} - qI_{xz})$$

(B-43)

B-6 OVERALL SOLUTION OF EQUATIONS OF MOTION

Certain input data and initial conditions are to be specified before any integration of the equations of motion can be performed. First the input data must include the body mass, m , and the moments and products of inertia. Secondly, the offset of the origin of the body coordinate system from the center of mass must be specified. We also need the initial body orientation as specified by the three initial angles. With regard to initial conditions, the initial position (ξ, η, ζ) of the origin of the body coordinate system and its velocity $(\dot{\xi}, \dot{\eta}, \dot{\zeta})$ must be specified together with the initial angular velocity components $p, q,$ and r . We may then integrate Equations (B-16) through (B-18) and Equations (B-41) through (B-43) to determine $\xi, \eta, \zeta, p, q,$ and r as functions of time. Simultaneously we must integrate Equation (B-1) to keep track of the body orientation. The aerodynamic force and moment components are calculated step-by-step during the integration of the trajectory.

REFERENCES

1. Dillenius, M. F. E., Goodwin, F. K., and Nielsen, J. N.: Prediction of Supersonic Store Separation Characteristics. Vol. I - Theoretical Methods and Comparisons with Experiment. Tech. Report AFFDL-TR-76-41, Vol. I, May 1976.
2. Goodwin, F. K., Keirstead, M. M., and Dillenius, M. F. E.: Prediction of Supersonic Store Separation Characteristics. Vol. II - Users Manual for the Computer Program. Tech. Report AFFDL-TR-76-41, Vol. II, May 1976.
3. Mullen, J., Jr., Goodwin, F. K., and Dillenius, M. F. E.: Prediction of Supersonic Store Separation Characteristics Including Fuselage and Stores of Noncircular Cross Section. Vol. II - Users Manual for the Computer Program. Tech. Report AFWAL-TR-80-3032, Vol. II, Nov. 1980.
4. Mullen, J., Jr., Goodwin, F. K., and Dillenius, M. F. E.: Prediction of Supersonic Store Separation Characteristics Including Fuselage and Stores of Noncircular Cross Section. Vol. III - Appendices A and B, Details of Program I. Tech. Report AFWAL-TR-80-3032, Vol. III, Nov. 1980.
5. Mullen, J., Jr., Goodwin, F. K., and Dillenius, M. F. E.: Prediction of Supersonic Store Separation Characteristics Including Fuselage and Stores of Noncircular Cross Section. Vol. IV - Appendices C and D, Details of Program II. Tech. Report AFWAL-TR-80-3032, Vol. IV, Nov. 1980.
6. Goodwin, F. K. and Dyer, C. L.: Data Report for an Extensive Store Separation Test Program Conducted at Supersonic Speeds. Tech. Report AFFDL-TR-79-3130, Dec. 1979.
7. Dillenius, M. F. E. and Nielsen, J. N.: Computer Program for Calculating Pressure Distributions Including Vortex Effects on Supersonic Monoplane or Cruciform Wing-Body-Tail Combinations with Round or Elliptical Bodies. NASA CR-3122, Apr. 1979.
8. Woodward, F. A.: An Improved Method for the Aerodynamic Analysis of Wing-Body-Tail Configurations in Subsonic and Supersonic Flow, Part I - Theory and Applications. NASA CR-2228, Part I, May 1973.
9. Woodward, F. A.: An Improved Method for the Aerodynamic Analysis of Wing-Body-Tail Configurations in Subsonic and Supersonic Flow, Part II - Computer Program Description. NASA CR-2228, Part II, May 1973.

REFERENCES (Concluded)

10. Sharp, B. M., Howe, J. P.: Procedures for Estimating Inlet External and Internal Performance. NWC TP 5555, Apr. 1974.
11. NACA Ames Research Staff: Equations, Tables, and Charts for Compressible Flow. NACA Report 1135, 1953.
12. Hall, I. M.: Inversion of the Prandtl-Meyer Relation. Aero. Journal, Roy. Aero. Soc., UK, Sept. 1975, pp. 417-418.
13. Kutler, P., Reinhardt, W. A., and Warming, R. F.: Multi-Shocked, Three-Dimensional Supersonic Flow Fields with Red Gas Effects. AIAA Journal, Vol. 11, May 1973, pp. 657-664.
14. Krasnov, N. F.: Aerodynamics of Bodies of Revolution. Edited by D. N. Morris, Elsevier, New York, 1970, pp. 220, 221, 232, and 233.
15. Milne-Thomson, L. M.: Theoretical Hydrodynamics. Fifth Edition, The MacMillan Company, New York, 1968, pp. 222 and 230.
16. Etkin, B.: Dynamics of Flight. John Wiley & Sons, Inc., New York, N.Y., 1959, pp. 100-103.
17. Morkovin, M. V., Migotsky, E., Baily, H. E., and Phinney, R. E.: Experiments on Interaction of Shock Waves and Cylindrical Bodies at Supersonic Speeds. J. Aero. Sci., 19, No. 4, Apr. 1952.
18. Goodwin, F. K., Dillenius, M. F. E., and Nielsen, J. N.: Prediction of Six-Degree-of-Freedom Store Separation Trajectories at Speeds Up to the Critical Speed. Vol. I - Theoretical Methods and Comparisons with Experiment. Tech. Report AFFDL-TR-72-83, Vol. I, Oct. 1974.
19. Nielsen, J. N.: Missile Aerodynamics. McGraw-Hill Book Co., Inc., New York, N.Y. 1960.
20. Dillenius, M. F. E., and Nielsen, J. N.: Supersonic Lifting-Surface Computer Program for Cruciform Wing-Body Combinations in Combined Pitch and Sideslip. Office of Naval Research, Annual Report, Dec. 1974 (also NEAR TR 74).
21. Lipmann, H. W. and Roshko, A.: Elements of Gasdynamics. John Wiley & Sons, Inc., New York, N.Y. 1957, Ch. 9, pp. 248-251.